Doctoral Thesis

Relationships between seismicity and slow slip events at New Zealand's northern and central Hikurangi subduction zone inferred from detailed spatiotemporal earthquake analysis

Kazuya Tateiwa

Department of Geophysics
Graduate School of Science
Tohoku University

Thesis Committee Members

Associate Professor	Tomomi Okada (Chair, Supervisor)
Professor	Toru Matsuzawa
Professor	Satoshi Miura
Professor	Takeshi Nishimura
Professor	Ryota Hino
Professor	Martha Savage (Victoria University of Wellington)
Lecturer	Calum Chamberlain (Victoria University of Wellington)
Assistant Professor	Ryota Takagi

2023

博士論文

詳細な時空間解析によって推定された
ニュージーランド ヒクランギ沈み込み帯北部および中央部の
地震活動とスロースリップイベントとの関係

立岩　和也

東北大学大学院理学研究科
地球物理学専攻

論文審査委員

岡田　知己　准教授（指導教員・主査）
松澤　　暢　教授
三浦　　哲　教授
西村　太志　教授
日野　亮太　教授
Martha Savage　教授（ヴィクトリア大学ウェリントン）
Calum Chamberlain　講師（ヴィクトリア大学ウェリントン）
髙木　涼太　助教

令和５年

Abstract

The Hikurangi subduction zone is located at the south end of the 300 km-long Tonga-Kermadec-Hikurangi subduction system, where the Pacific plate subducts westward under the Australian plate beneath the North Island of New Zealand. Previous works have identified that slow slip events (SSEs) along the plate boundary are sometimes accompanied with seismic swarms and that the two phenomena may be related by fluid movement. Although previous studies proposed fluid movement from the subducting oceanic crust before SSEs to the upper plate after SSEs as a trigger for swarms in the central and northern Hikurangi margin, they did not identify where the swarms occurred. That is, they did not classify the location of earthquakes in the upper Australian plate, the lower Pacific plate, or the plate boundary, making the physical relationship among swarms, SSEs, and fluids uncertain. The regional dependency of mechanisms of shallow SSEs showed that the earthquake-triggering mechanism varied spatially; however, the previous studies did not investigate such a spatial variation of the triggering mechanisms. Thus, this thesis aims to determine (1) what types of earthquakes are activated relative to SSE occurrence and (2) how the activation pattern and triggering mechanisms differ between the northern and central Hikurangi margins.

We generated a revised earthquake catalog for this region with well-constrained locations and magnitudes. We started with the earthquake catalog and seismic waveform data from New Zealand's nationwide geological hazard monitoring network, GeoNet. We relocated earthquakes greater than the magnitude of completeness (2.8 for 2004-2007, 2.6 for 2008-2011, and 2.5 for 2012-2020) within the shallow Hikurangi margin using the NonLinLoc program and a 3-D velocity model. We also determined focal mechanisms using the first P-wave polarities. Based on relocated hypocenters, focal mechanisms, and waveform cross-correlation, the earthquakes were classified into six types: AUS (earthquakes in the Australian plate), PAC (earthquakes in the Pacific plate), INT (earthquakes at the plate interface), maybe_AUS (earthquakes possibly in the Australian plate or maybe at the plate interface), maybe_PAC (earthquakes possibly in the Pacific plate or maybe at the plate interface), and unknown (earthquakes which cannot be classified into above five types due to large uncertainties). After the classification, we obtained 433 AUS, 469 INT, 9,065 PAC, 820 maybe_AUS, 3,273 maybe_PAC, and 2,872 unknown earthquakes. The AUS events showed a concentration and a gap in the northern Hikurangi margin. The INT events were mainly located outside or on the periphery of SSE sources, which might reflect a difference in frictional properties on the megathrust. The PAC events were widely distributed throughout the study area, and their focal mechanisms showed some depth dependencies.

We detected SSE signals using eastward displacements recorded at GNSS stations of GeoNet in the study area. This study detected all shallow SSEs previously published, as well as new

ones that were not located. After retaining only the earliest event in each sequence (swarms and mainshock-aftershock sequences) based on the space-time distance between each pair of two events, we evaluated the number of earthquakes relative to SSE timing. In and around the northern SSE source area (the northern Hikurangi margin), AUS events were somewhat activated just after SSEs ended (0-10 days); maybe_AUS, INT, and maybe_PAC events were activated during SSEs; and PAC events were activated just before SSEs started (0-20 days before). In contrast, in and around the southern shallow SSE source area (the central Hikurangi margin), maybe_AUS events were activated just after SSEs ended (0-10 days); maybe_PAC events were activated during SSEs and just after SSEs ended (0-10 days). Such regional difference in activation patterns between the northern and central Hikurangi margins suggests a difference in driving force(s) of SSE-related earthquakes.

We investigated fluid movement inferred from swarm migration and Coulomb stress change induced by SSEs to explain the observed activation patterns. Ten out of twelve diffusion-consistent swarm sequences, which appeared to migrate according to the fluid diffusion equation, were located in the northern Hikurangi margin. If we assume that these swarms are related to fluid migration, the swarm activity indicates that fluid movement occurs more easily in the northern Hikurangi margin than in the central Hikurangi margin. Temporal relationships between swarms and SSEs suggested that fluid might migrate within the Australian plate after SSEs, at the plate boundary during SSEs, and within the Pacific plate before SSEs. The Coulomb stress analysis revealed that the AUS events activated immediately after SSEs in the northern Hikurangi margin might not have been triggered by SSE-induced Coulomb stress change and that INT events (including maybe_AUS and maybe_PAC events) during or immediately after SSEs might have been triggered by SSE-induced Coulomb stress change.

From these results, we propose that fluid movement from before SSEs to after SSEs is a possible mechanism of earthquake-triggering in the northern Hikurangi margin and that SSE-induced stress loading is a possible mechanism of earthquake-triggering in the central Hikurangi margin. The difference we infer in earthquake-triggering mechanisms between the northern and central Hikurangi margins is consistent with other geological and geophysical features. More detailed studies along the Hikurangi subduction zone would allow us to test the interpretations of this study and its comparison with other subduction zones worldwide.

Acknowledgments

First and foremost, I would like to thank Tomomi Okada for being an incredibly enthusiastic, knowledgeable, inspiring, patient, and kind supervisor. He imparted a lot of knowledge to me. He also provided me with opportunities for researching overseas and fieldwork, which allowed me to grow as a scientist.

I would like to express my gratitude to Martha Savage and Calum Chamberlain for their kind and careful supervising. They introduced me to many papers and taught me how to analyze the data. They also supported my stay in Wellington.

Thanks go to thesis committee members, Toru Matsuzawa, Satoshi Miura, Takeshi Nishimura, Ryota Hino, and Ryota Takagi. They gave me much advice on research methods and interpretation of results, which was indispensable for writing this thesis, at conference presentations, rehearsals, and seminars.

Acknowledgments must be given to Naoki Uchida, with whom I shared a room at the Research Center for Prediction of Earthquakes and Volcanic Eruptions (RCPEVE). He was a great help to me in using the computers and in discussions about my research.

I would like to thank RCPEVE and Solid Earth Physics Laboratory professors for their guidance on a wide range of solid earth physics topics through seminars, lectures, zassi-kai, and conference rehearsals. I also would like to thank the graduate and undergraduate students of RCPEVE and Solid Earth Physics Laboratory for their discussions at seminars and their support in my daily life.

Huge thanks to the staff of RCPEVE for their help with conference registration and fieldwork.

I was financially supported by the International Joint Graduate Program in Earth and Environment Sciences (GP-EES) program. Special mentions go to Shinobu Okuyama and Shin Ozawa for supporting my life as a GP-EES student. They supported my visit to Wellington and provided me with a lot of wonderful lectures by world-leading scientists.

This study used Generic Mapping Tool provided by Wessel & Smith (1998) to plot figures and seismic and geodetic data provided by GNS Science. I would like to express my gratitude to all of them.

Contents

Chapter 1.
Introduction

1.1. Slow earthquakes and related seismic activity

Subduction zones, where plates converge, produce various phenomena due to dynamic interaction between the subducting plate and the overlying plate. An earthquake cycle consists of a sequence of large similar earthquakes that rupture the same portion of the plate boundary, which may be locked and accumulate stress until the next large earthquake. In addition to ordinary earthquakes, slow earthquakes, some of them called slow slip events or SSEs, that are not felt have been discovered recently (Obara, 2020). Understanding the relationship between these different types of earthquakes is essential to consider the occurrence of large interplate earthquakes in the future.

Slow earthquakes have been observed worldwide, mainly in the subduction zone, since 1990 (Figure 1.1; Obara, 2020). Slow earthquake is a general term for a phenomenon in which fault rupture proceeds more slowly than regular earthquakes and has a very wide range of duration and moment (Figure 1.2; Ide et al., 2007). In order of the characteristic duration, slow earthquakes are classified into low-frequency earthquakes (~ a few seconds), low-frequency tremors, or tremors (~ a few tens of seconds), very low-frequency earthquakes (from 10 seconds to a few minutes), short-term slow slip events (from a few days to a few tens of days), and long-term slow slip events (from a few months to a few years). Many slow earthquakes are observed at the updip or downdip of slip area of great plate boundary earthquakes (Figure 1.3).

Since the slip of slow earthquakes relaxes the strain at the plate boundary, just like interplate earthquakes, researchers have considered relationships between the activity of slow earthquakes and great plate boundary earthquakes. About a month before the 2011 M9 Tohoku-oki earthquake in northeast Japan, two sequences of SSE migrated toward the rupture initiation point of the Tohoku-oki mainshock, indicating that the slow slip unlocked the plate interface (Kato et al., 2012). Before the 2014 M8.2 Iquique earthquake in northern Chile, multiple sequences of earthquake migrations, indicating SSEs, occurred (Kato and Nakagawa, 2014). The last sequence and SSE migrated toward the nucleation point of the Iquique mainshock. Obara and Kato (2016) pointed out the possibility that SSEs can periodically load onto the plate boundary fault and modulate the recurrence time of large earthquakes. Since slow earthquakes are sensitive to surrounding stress change (Miyazawa & Mori, 2005; Ide, 2010), Obara and Kato (2016) suggested that slow earthquakes can be used as stress meters for megathrust patches adjacent to slow earthquake regions.

SSE-related seismic activities were also detected for smaller interplate and other earthquakes, not only for great plate boundary earthquakes. Fukuda (2018) found that earthquake swarms occurred

during SSEs in the Boso-oki region, Japan. They concluded that the stress loading triggered the swarms due to the SSEs because very few swarms were observed before SSEs there. Nakajima and Uchida (2018) found that seismicity rates and seismic attenuation above the subducting Philippine Sea plate changed cyclically in the Kanto region, Japan, in response to accelerated slow slip, which was interpreted as fluid migration into the permeable overlying plate after SSEs. In the Hikurangi subduction zone, east of the North Island, New Zealand, changes in stress ratio (Warren-Smith et al., 2019), seismicity rate (Nishikawa et al., 2021; Yarce et al., 2023), seismic velocity (Wang et al., 2022), and delay time of shear-wave splitting (Zal et al., 2020) were observed related with SSEs (details in section 1.3).

These studies indicate that understanding the process of SSEs and related phenomena provides essential knowledge for the earthquake cycle in subduction zones.

1.2. Tectonic setting of the Hikurangi margin

The Hikurangi subduction zone is located at the south end of the 300 km-long Tonga-Kermadec-Hikurangi subduction system, where the Pacific plate subducts westward under the Australian plate beneath the North Island of New Zealand (Figure 1.4). The forearc block, east coast of the North Island, rotates clockwise by ~3.8 deg/Myr, making varying convergence rates along the Hikurangi margin: ~60 mm/yr in the northern margin and ~20 mm/yr in the southern margin (Wallace et al., 2004). The convergence of the Pacific plate relative to the Australian plate is highly oblique. The margin-parallel component of the plate motion is accommodated by forearc rotation and right-lateral strike-slip motion in North Island Fault Belt (Beanland and Haines, 1998; Wallace et al., 2004).

A part of the subducting Pacific plate consists of the Hikurangi plateau, which has a thickness of ~10-15 km (Mortimer and Parkinson, 1996). The Hikurangi plateau is formed from the decompression melting of the low-density subcontinental mantle (Mochizuki et al., 2019). The plateau has undergone two subduction histories (Reyners et al., 2017): southward convergence with Gondwana in 105-100 Ma and the current westward convergence between the Pacific plate and the Australian plate. The buoyant Hikurangi plateau produces a subaerial forearc. The depth to the subduction interface on the east coast of the North Island is about 12-20 km (Williams et al., 2013), making the conditions ideal for analyzing seismic phenomena in subduction zones using seismometers and GNSS stations inland.

Sediments and seamounts are also subducting from the Hikurangi trough. The thickness of sediments on the Hikurangi plateau decreases from the southern margin (~5 km) to the northern margin (< 1 km) (Barnes et al., 2010). Seamounts are buried beneath the thick sediments in the southern margin and protrude over the sediment in the northern margin. Three layers of high seismic reflectivity along the subduction interface are found off Gisborne, interpreted as fluid-rich sediments entrained by subducting seamounts (Bell et al., 2010).

The subaerial forearc of the Hikurangi margin makes it easier to analyze SSEs and related seismic activity using seismometers and GNSS stations on land than other subduction zones (e.g., Japan trench) with further offshore trenches. Taking advantage of this feature, many studies have been conducted, and various types of slip phenomena, including repeating earthquakes (Shaddox and Schwartz, 2019; Hughes et al., 2021), earthquake swarms (Nishikawa et al., 2021), SSEs (Wallace and Beavan, 2010; Wallace et al., 2012; Wallace and Eberhart-Phillips, 2013; Wallace et al., 2016; Wallace et al., 2017; Wallace et al., 2018; Wallace, 2020; Woods, 2022), and tremors (Todd and Schwartz, 2016; Todd et al., 2018; Romanet and Ide, 2019) were observed in the Hikurangi subduction zone, which is considered to be related to the tectonic features above.

1.3. SSEs and related seismic activity in the Hikurangi margin

Both deep and shallow SSEs have been detected in the Hikurangi margin (Figure 1.5a) (e.g., Wallace, 2020). Here we summarize Wallace's (2020) paper. Shallow SSEs frequently occur in the northern and central Hikurangi margin with a typical recurrence interval of about 1-2 years, varying along the margin. The recurrence interval of SSEs near Cape Turnagain in the central Hikurangi margin is about five years, and 1-2 SSEs occur every year near Tolaga Bay in the northern Hikurangi margin. Despite contrasts in recurrence interval, the shallow SSEs typically last 2–3 weeks. Deep SSEs are mainly detected in the southern and central Hikurangi margins, with longer recurrence intervals and durations than shallow SSEs. The Kapiti and Manawatu deep SSEs last 1–2 years and recur approximately every 4–5 years. The Kaimanawa deep SSEs occurred downdip of the shallow SSEs in the Hawkes Bay region and were most clearly observed in 2006 and 2008. Their duration is about 2-3 months, shorter than other deep Hikurangi margin SSEs (i.e., the Kapiti and Manawatu deep SSEs).

Several Hikurangi margin SSEs were studied for their generation mechanisms. Warren-Smith et al. (2019) examined the temporal change in stress ratio before and after the 2014-2015 Hikurangi margin SSEs near Gisborne and Hawkes Bay (SSE A in Figure 1.5b), the northern Hikurangi margin, using intraslab earthquakes. They computed the stress ratio (R) as

$$R = \frac{\sigma_1 - \sigma_2}{\sigma_1 - \sigma_3}, \tag{1.1}$$

where σ_1, σ_2, and σ_3 are maximum, intermediate, and minimum principal stress, respectively. Warren-Smith et al. (2019) found a decrease in the retrieved stress ratio before SSEs and an increase in the retrieved stress ratio during SSEs (Figure 1.6a). Since the bending-related fractures within subducting oceanic crust strike margin-parallel with their poles in the σ_1/σ_3 plane (Figure 1.6b), the retrieved stress ratio should be inversely related to pore fluid pressure. Warren-Smith et al. (2019) interpreted the decrease in the retrieved stress ratio before SSEs as an increase in the pore fluid pressure and the increase in the retrieved stress ratio during SSEs as a decrease in the pore fluid pressure. They proposed that the accumulation and release of fluid pressure within overpressured

subducting oceanic crust may influence the timing of SSEs (Figures 1.6c, d). Deep, long-term SSEs and shallow short-term SSEs continuously occurred from 2010 to 2011 (Wallace et al., 2012). Firstly, the Manawatu deep SSE started in mid-2010 and lasted until late September 2011. It loaded stress along the shallow plate interface and induced a shallow SSE in June 2011, just updip of the deep SSE source (SSE B in Figure 1.5b). The 2016 Mw7.8 Kaikōura earthquake (e.g., Okada et al., 2019; Chamberlain et al., 2021; Matsuno et al., 2022), which occurred in the north of the South Island, New Zealand, triggered shallow SSEs from the central to northern Hikurangi margin (SSE C in Figure 1.5b) due to a significant dynamic stress change caused by the Kaikōura mainshock (Wallace et al., 2017). These results, in addition to the variety of interevent times of shallow SSEs along the Hikurangi margin, might indicate that the mechanisms of shallow SSEs can vary from event to event and probably depend on the region.

Several studies support the idea of fluid movement before, during, and after SSEs proposed by Warren-Smith et al. (2019): analysis of temporal change in Vp/Vs and delay time of shear-wave splitting (Zal et al., 2020), temporal change in seismic velocity (Wang et al., 2022), and earthquake swarms (Nishikawa et al., 2021). Zal et al. (2020) found that Vp/Vs increased and the delay time of shear-wave splitting decreased during the 2014 SSE near Gisborne using ocean bottom seismometers deployed by the Hikurangi Ocean Bottom Investigation of Tremor and Slow Slip (HOBITSS) (Figure 1.7a, b). They interpreted the Vp/Vs increase and the delay time decrease as caused by the interconnection of cracks in the upper plate, which allowed the fluid movement from below the overpressured oceanic crust, and by the rounder (larger aspect ratio) and more randomly oriented cracks (Figure 1.7c). Wang et al. (2022) applied scattered wave interferometry to ambient noise data acquired by nine HOBITSS ocean bottom seismometers to investigate the seismic velocity variations related to the SSE. They found a decrease in the average velocity variations displayed on the order of 0.05% during the 2014-2015 SSEs (Figure 1.8a). One of the possibilities to explain the decrease of the velocity during SSEs is the fluid migration into the upper plate, which increases the pore fluid volume in the upper plate (Figure 1.8b). Nishikawa et al. (2021) detected earthquake swarms, which were assumed to be related to fluid movement, in the northern and central Hikurangi margin between 1997-2015 and determined the occurrence timing of SSEs using GNSS data (Figure 1.9a). They found that swarms occurred not only during SSEs but also before and after SSEs (Figure 1.9b). From these results and the previously proposed fluid movement model, they proposed a modified fluid migration model, where fluid migration within the subducting oceanic crust before SSEs triggers pre-SSE swarms, then the occurrence of the SSE along the plate boundary induces post-SSE fluid migration in the upper plate, which may potentially trigger post-SSE swarms (Figure 1.9c). This SSE-related swarm activity in the Hikurangi margin differs from that in the Boso-oki region, where swarms were activated only during SSEs, indicating SSE-induced stress loading triggered swarms (Fukuda, 2018). All these studies support the idea that fluid migration is a critical factor for the occurrence of SSEs and related

earthquakes in the Hikurangi margin.

1.4. Objective

Although Nishikawa et al. (2021) suggested that the fluid migrated from the subducting oceanic crust before SSEs to the upper plate after SSEs, triggering swarms, they did not identify where the swarms occurred. That is, they did not determine the location of earthquakes in the upper Australian plate, the lower Pacific plate, or at the plate boundary. As mentioned in section 1.3, the mechanisms of shallow SSEs might vary depending on the region, indicating that the earthquake-triggering mechanism might vary spatially. However, Nishikawa et al. (2021) used earthquakes in the northern and central Hikurangi margins (the black dashed box in Figure 1.5b) for their analysis. They did not investigate such a spatial variation of the triggering mechanisms. Yarce et al. (2023) located small earthquakes using inland seismometers and HOBITSS ocean bottom seismometers to investigate the temporal relationship between the 2014 SSE and earthquakes. They found that the seismicity rate of small earthquakes increased during the SSE and gradually returned to their baseline after the SSE stopped. However, they also did not identify what type of earthquakes, earthquakes in the upper plate, in the lower plate, or at the plate boundary, were activated during SSEs. The seismicity rate of tremors off Gisborne also increased during and after the 2014 SSE (Todd et al., 2018). To summarize, what is not revealed in the previous studies are (1) what type of earthquakes are activated relative to SSE occurrence and (2) how the activation pattern and triggering mechanisms differ between the northern and central Hikurangi margin. This study aims to reveal the answers to the two questions above. These answers will contribute to understanding the earthquake cycle in subduction zones and its spatial variation.

The content of each chapter is as follows. In Chapter 1, we have described the background and objective of this study. Chapter 2 describes how earthquakes are classified based on relocated hypocenters, computed focal mechanisms, and waveform similarities. Chapter 3 describes how the SSE signals are detected at each GNSS station, how the seismicity rate is evaluated relative to SSE occurrence, and activation patterns in the northern and central Hikurangi margins. Chapter 4 describes how the observed activation patterns are introduced from the perspective of earthquake swarm activity and Coulomb stress change and proposes an earthquake-triggering model along the Hikurangi margin. In Chapter 5, we summarize the study and suggest further avenues of research.

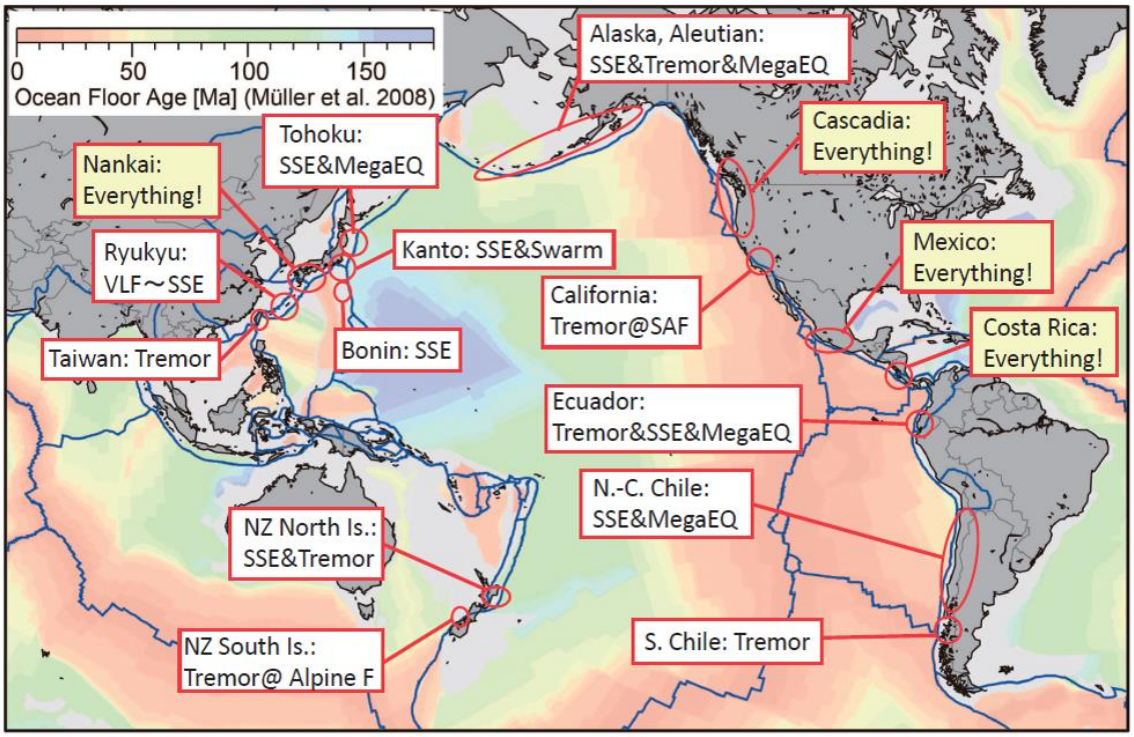

Figure 1.1. Worldwide slow and fast earthquake activity in subduction zones (Obara, 2020; Figure 1). The characteristic slow earthquake activity (tremor, very low-frequency earthquakes (VLFEs), and slow slip events (SSEs)) and regular earthquake activity (megathrust earthquakes (MegaEQ) and swarm) along each major fault system are indicated. Everything! indicates that three types of slow earthquakes (tremors, VLFEs, and SSEs) are detected. Blue lines indicate the tectonic plate boundaries. The background image shows the seafloor age (Müller et al., 2008).

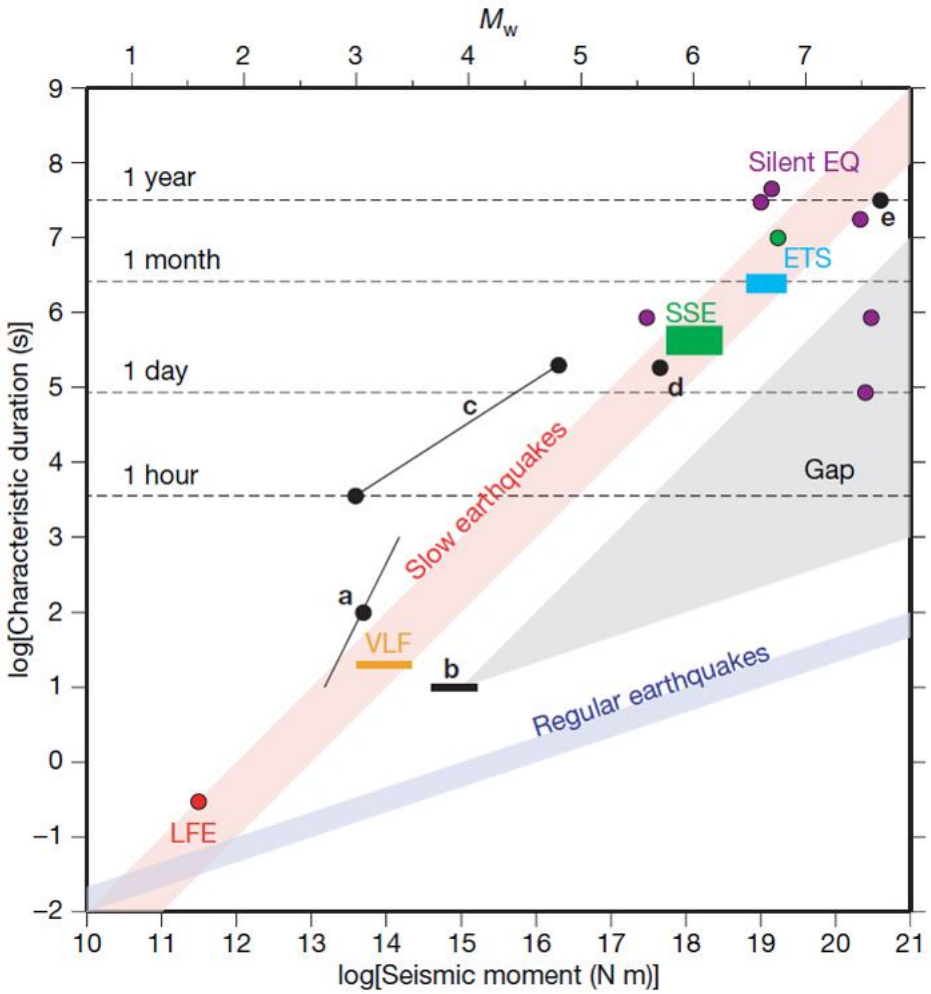

Figure 1.2. Scaling law for regular earthquakes and slow earthquakes (Ide et al., 2007; Figure 2). LFE: Low-Frequency Earthquake; VLF: Very Low-Frequency earthquake; SSE: Slow Slip Event; ETS: Episodic Tremor and Slip.

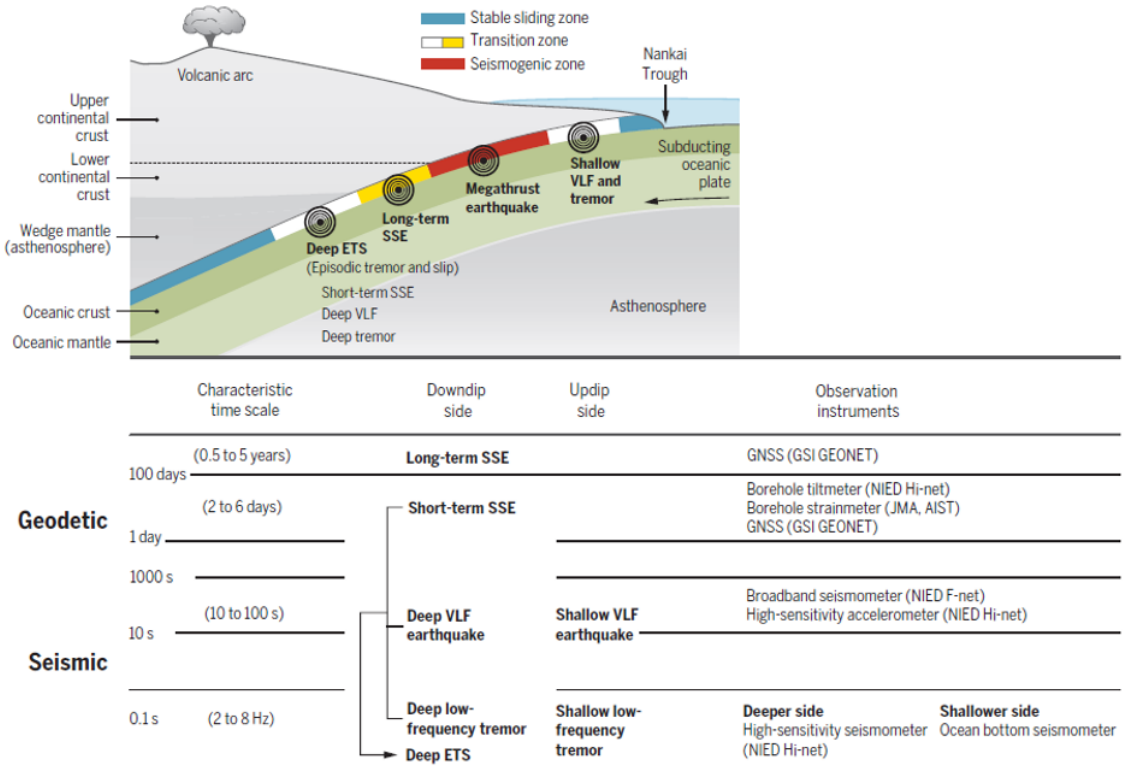

Figure 1.3. Cross section of the Nankai subduction zone, Japan, and spatial distribution of the megathrust earthquake and slow earthquakes (Obara and Kato, 2016).

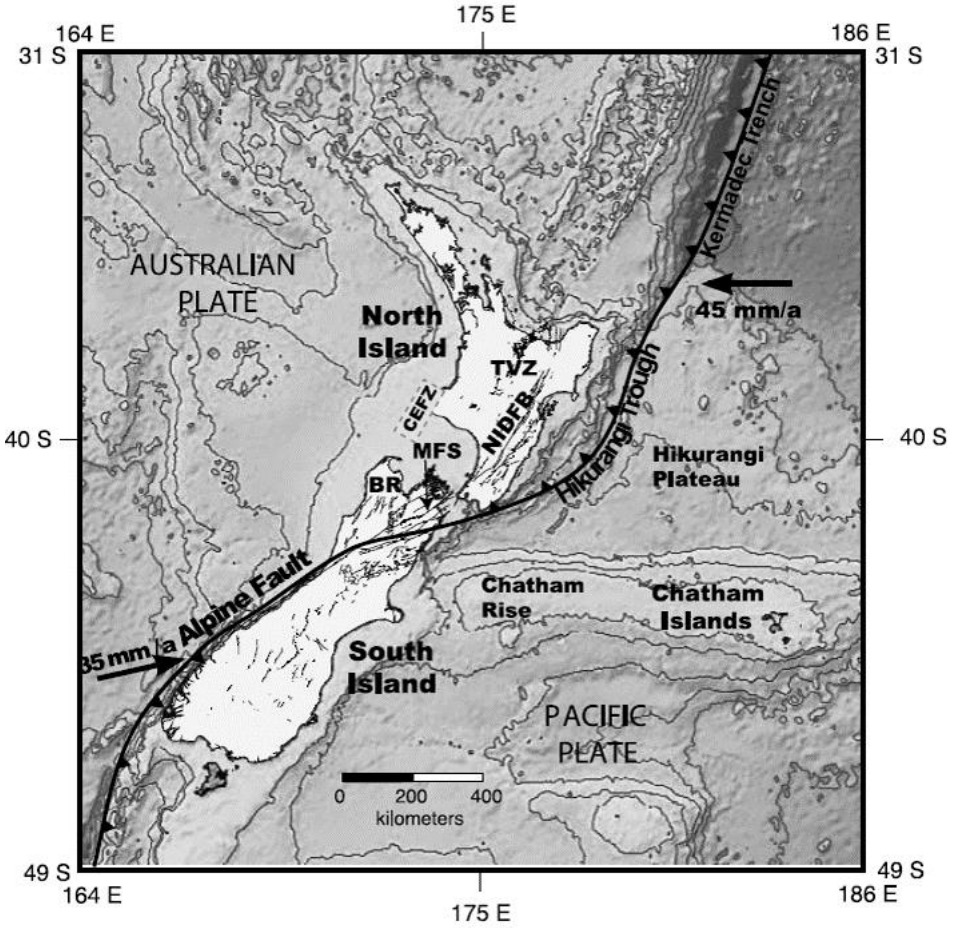

Figure 1.4. Regional tectonic setting of New Zealand (Wallace et al., 2004; Figure 1). MFS, Marlborough Fault System; NIDFB, North Island Dextral Fault Belt; TVZ, Taupo Volcanic Zone; BR, Buller region where shortening-related faults are located, and CEFZ, Cape Egmont Fault Zone where extensional faulting occurs. The bold black line indicates the Kermadec Trench, the Hikurangi Trough, and the Alpine Fault. Arrows show the relative motion of the Pacific plate / Australian plate at each location.

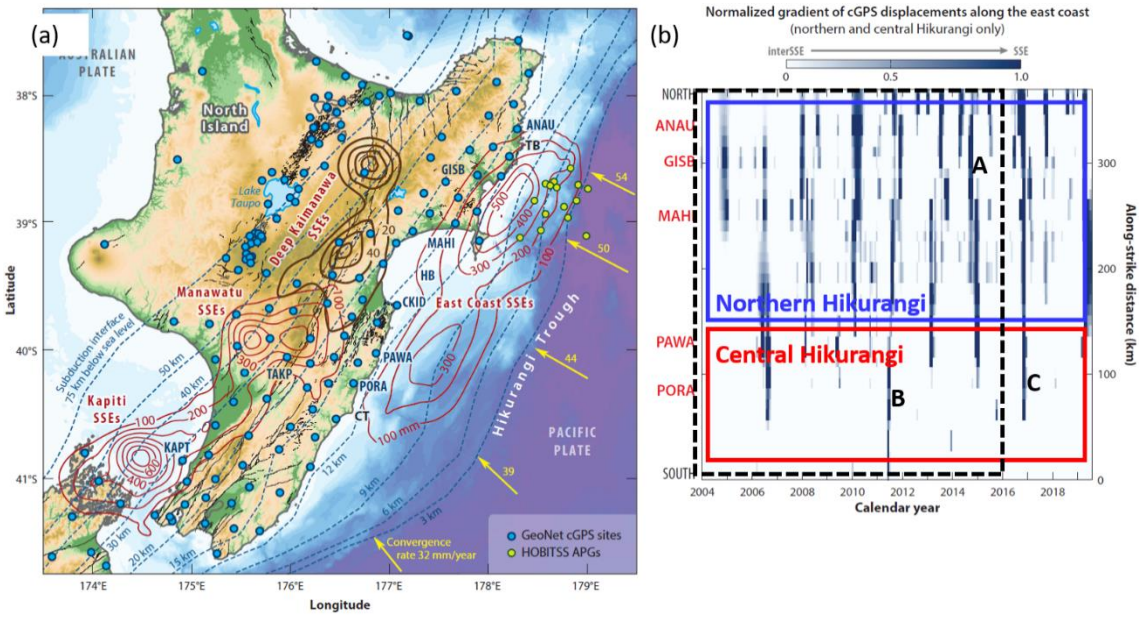

Figure 1.5. (a) Cumulative slow slip between 2002 and 2014 in the Hikurangi subduction zone (Wallace, 2020; Figure 2). Labeled dashed blue lines indicate the depths of the plate interface (in km below sea level) (data from Williams et al., 2013) (b) Change in rate of motion at GeoNet continuously operating global positioning system (cGPS) sites along the east coast of the North Island (modified from Wallace, 2020; Figure 4). Darker colors show periods with the fastest rates of position change in the cGPS time series. Letters A, B, and C indicate SSEs in which previous studies examined mechanisms. The blue and red boxes indicate the northern and central Hikurangi margin areas defined in this study. The black dashed box shows the study area and period of Nishikawa et al. (2021) (see Figure 1.9).

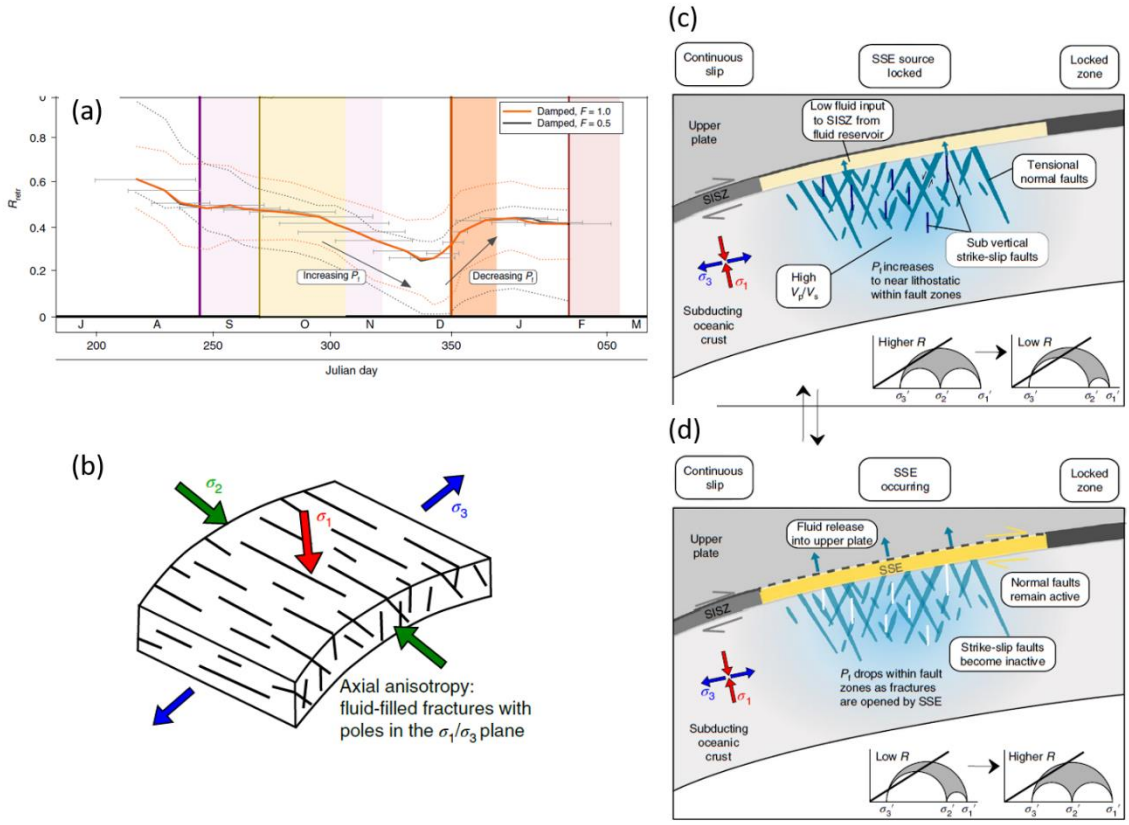

Figure 1.6. (a) Temporal change in retrieved stress ratio. Black and red lines show F = 0.5 and F = 1.0 probability of correct nodal plane selection. Vertical errors (dashed lines) indicate 95% confidence intervals. Horizontal errors show the period of events used to calculate each retrieved stress ratio. Shaded areas indicate SSE occurrence periods. (b) Schematic of tensional, bending-related fractures in subducting oceanic crust. (c, d) SSE occurrence model from fluid accumulation in the subducting oceanic crust. P_f, fluid pressure; σ_1, maximum principal stress; σ_2, intermediate principal stress; σ_3, minimum principal stress; R, stress ratio; V_p/V_s, ratio of seismic compressional and shear-wave velocities. The figures are from Warren-Smith et al. (2019).

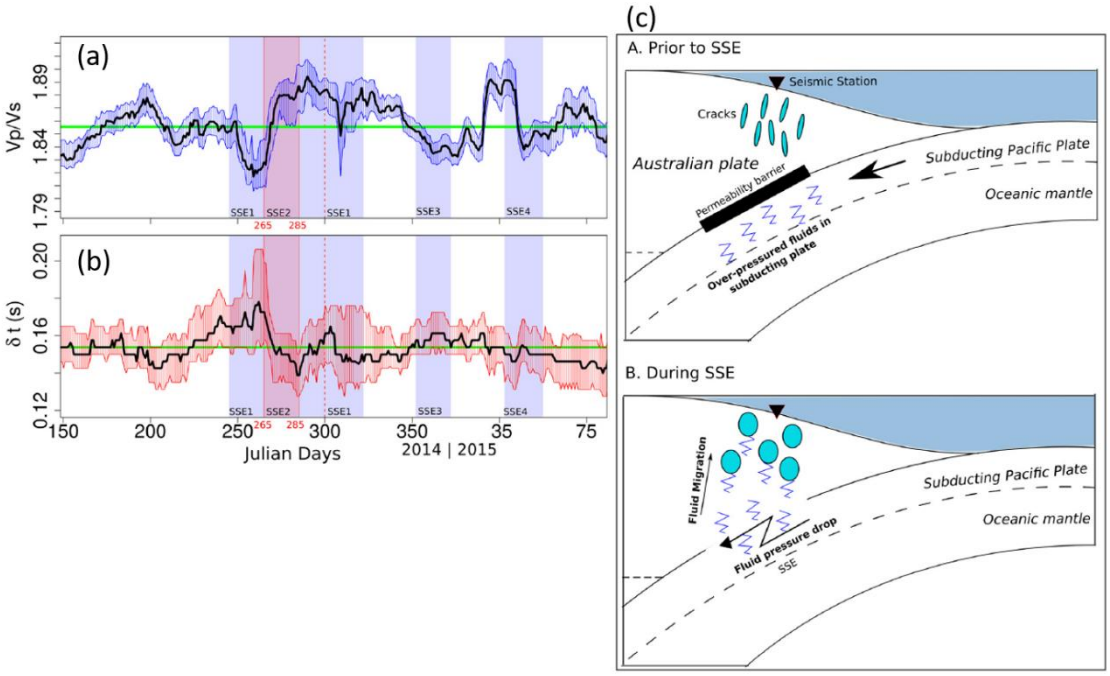

Figure 1.7. (a) Temporal change in Vp/Vs and (b) delay time of shear-wave splitting. Shaded areas indicate the period of SSE occurrence. (c) Fluid migration model to explain the temporal change in Vp/Vs and delay time. The figures are from Zal et al. (2020).

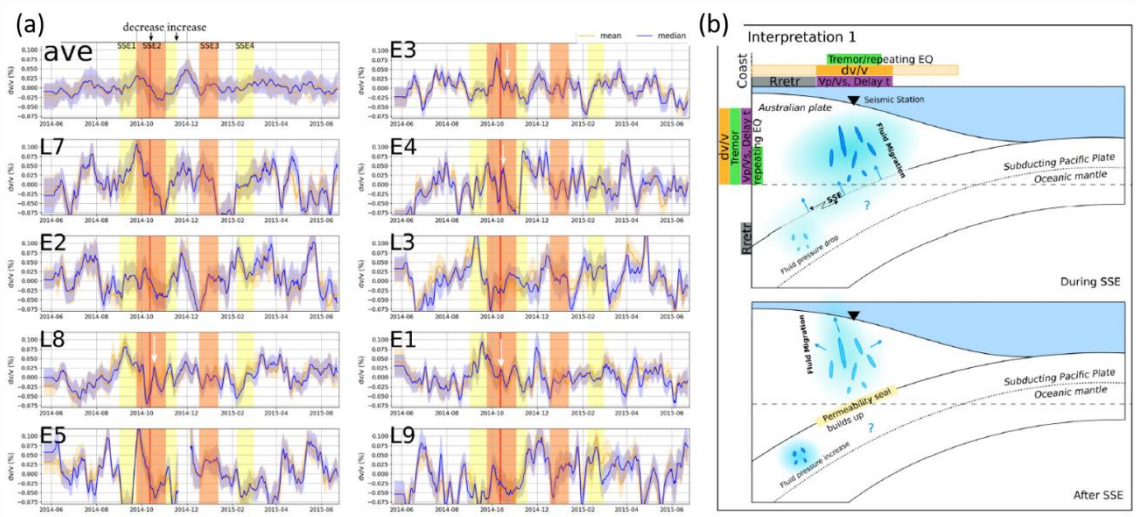

Figure 1.8. (a) Temporal change in seismic velocity recorded at each ocean bottom seismometer and averaged one. Shaded areas indicate the period of SSE occurrence. (b) One of the interpretations for temporal change in seismic velocity. The figures are from Wang et al. (2022).

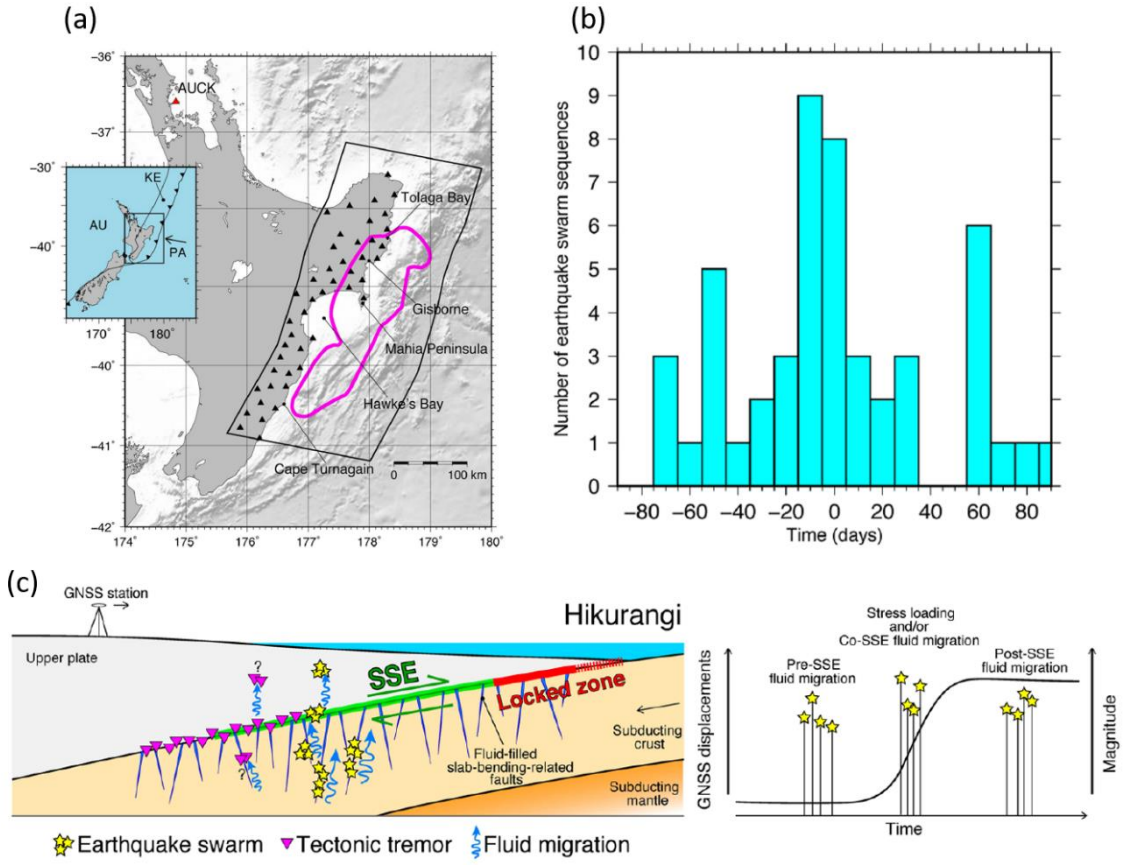

Figure 1.9. (a) The study area of Nishikawa et al. (2021). (b) Histogram of detected earthquake swarm sequences. The horizontal axis indicates the lag time between the swarm sequences and SSEs. (c) Schematic model for fluid migration and swarm occurrence in the Hikurangi margin. The figures are from Nishikawa et al. (2021).

Chapter 2.

Earthquake classification

2.1. GeoNet's earthquake catalog

GeoNet provides the nationwide earthquake catalog in New Zealand (GNS Science, 2023a). The catalog includes hypocenter locations and their uncertainties and magnitudes. We can use this catalog to classify whether an earthquake is occurring in the Pacific plate, in the Australian plate, or at the plate interface, but there are two major problems. The first one is the depth type of "operator assigned": these depths are not determined by calculations but assigned by operators. The second one is the different location algorithms and seismic velocity models used before and after 2012. Between 1987 and 2011, the GROPE technique (GeoNet, no date a), a part of the CUSP (Caltech-USGS Seismic Processing system) package that was distributed by the USGS (Eaton, 1996; Euan Smith, personal communication), which utilizes P and S phases and weights reviewed by earthquake analysts, was used with 1-D velocity models specific to certain regions within the country. Since 2012 the LocSAT technique (Bratt and Nagy, 1991) with a 1-D velocity model (iaspei91: Kennett, 1991) and the NonLinLoc (Non-Linear Location) technique (Lomax et al., 2000) with the 3-D velocity model (Eberhart-Phillips et al., 2010) have been used. This makes it difficult to evaluate the uncertainties of hypocenters equally before and after 2012. These facts demonstrate the utility and necessity of hypocenter relocation using one algorithm throughout the entire period of this study. The methods to estimate earthquake magnitudes also differ before and after 2012, and GeoNet provides different magnitude types. Thus it is necessary to recalculate magnitudes to be considered equal before and after 2012. In the following sections, we describe how magnitudes are corrected, how earthquakes are relocated, and how earthquakes are classified.

2.2. Reconstructing earthquake catalog

GeoNet's catalog provides local magnitudes (M_L) (Haines, 1981) before 2012 (GeoNet, no date a). After 2012, the catalog provides local magnitude (M_L, not for all earthquakes); local magnitude calculated on the vertical component using a correction term to fit with M_L (M_{Lv}, not for all earthquakes); estimation of the moment magnitude based on using the moment magnitude (M_w) vs. the body wave magnitude (mB) regression of Bormann and Saul (2008) ($M_{w(mB)}$); and summary magnitude, weighted mean of M_{Lv} and $M_{w(mB)}$ (M_{sum}, not for all earthquakes) (GeoNet, no date b). Since GeoNet's moment tensor solution catalog (Ristau, 2013; GNS Science, 2023b) provides seismic moment and moment magnitude (M_w) for moderate to large earthquakes, we corrected earthquake magnitudes (M_L, M_{Lv}, and M_{sum}) to M_w by following three steps. Here, we used earthquakes shallower

than 100 km in the northern and central Hikurangi margin between 2004 and 2020 (Figure 2.1a). The number of earthquakes in the GeoNet catalog within this area and period was 67,116.

1. We compared M_L and M_w. GeoNet's moment magnitudes were used if the variance reductions (VR) of moment tensor inversion were 70% or greater (Figure 2.1b). The regression line shows the empirical relationship between M_L and M_w (Figure 2.2a) as

$$M_w = 0.822 * M_L + 0.504. \quad (2.1)$$

2. We investigated the relationships between M_{sum} and M_L, and between M_{Lv} and M_L. We fitted a two-part piecewise linear function and obtained empirical relationships (Figure 2.2b, c) as

$$M_L = \begin{cases} 0.875 * M_{sum} + 0.475 \cdots \text{for } M_{sum} < 2.029 \\ 1.054 * M_{sum} + 0.111 \cdots \text{for } M_{sum} \geq 2.029 \end{cases} \quad (2.2)$$

and

$$M_L = \begin{cases} 0.874 * M_{Lv} + 0.475 \cdots \text{for } M_{Lv} < 2.025 \\ 1.052 * M_{Lv} + 0.114 \cdots \text{for } M_{Lv} \geq 2.025. \end{cases} \quad (2.3)$$

The points where the two linear functions meet were determined by a grid search to minimize the misfit.

3. We corrected M_{sum} and M_{Lv} to M_L and then M_L to M_w. Unless otherwise noted, magnitude shall refer to the converted moment magnitude using Equations (2.1-2.3).

We calculated the magnitude of completeness (Mc) using the maximum curvature method (Wiemer and Wyss, 2000) and added a correction value of 0.2, as recommended by Woessner and Wiemer (2005). The magnitude of completeness decreases with time (red lines in Figure 2.2d), probably due to an increase in the number of seismic stations and automated picking procedure of arrival time. We set the lower limits of magnitude (M_w) to be analyzed so that they were greater than Mc: we used lower limits of 2.8 between 2004 and 2007, 2.6 between 2008 and 2011, and 2.5 between 2012 and 2020 (yellow lines in Figure 2.2d). Thus the earthquakes analyzed in this study occurring between 2004 and 2020 within the study area (red lines in Figure 2.3) were shallower than 100 km and had magnitudes greater than the lower limits as defined above (Figure 2.3). The depths of some earthquakes were fixed (operator assigned) in the GeoNet's catalog (Figure 2.4). The number of earthquakes that satisfied these criteria was 17,359.

We relocated the earthquakes that satisfied the criteria above using the NonLinLoc technique (Lomax et al., 2000) with the NZ-wide 3-D velocity model (version 2.2) (Eberhart-Phillips et al., 2020). We used P- and S-wave pick data at short-period seismic stations (EH) and broadband seismic stations (HH) of the GeoNet network (Petersen et al., 2011; Gale et al., 2015) for relocation (Figure 2.5a). Here, we selected only stations within 200 km of the earthquake epicenters. We used pick data from GeoNet's catalog and Hughes et al. (2021) and also used pick data manually read in this study. The difference in pick-time between this study and GeoNet (this study minus GeoNet) was 0.01 ± 0.04 s for P-wave (N=5,144) and -0.07 ± 0.27 s for S-wave (N=9,232), where our pick data were different

from those used for the relocation and read only for this comparison. Our picks were mainly for the "operator assigned" earthquakes by GeoNet so that the number of pick data increased. The number of pick data is listed in Table 2.1. Figure 2.6 shows the distribution of relocated earthquakes, where only earthquakes within the study area are plotted. Relocated earthquakes show clearer structures along and below the plate boundary than those from GeoNet's catalog (Figures 2.4 and 2.7). Most of the relocated earthquakes had horizontal and depth one-sigma uncertainties of less than 5 km (Figure 2.8). The uncertainties decreased with time (Figure 2.8c, d), probably due to the increased number of used seismic stations (Figure 2.5b). Earthquakes of which horizontal or depth uncertainty was less than 5 km and within the study area were used for the classification in further analysis. The number of such earthquakes was 14,060. Depth uncertainty obtained by this study was 4.9 km smaller than that from the GeoNet catalog, comparing the same events after 2012.

Not only earthquake locations but also focal mechanisms are useful for determining and classifying where the earthquakes occurred. Using the P-wave first motion polarity obtained by GeoNet, Hughes et al. (2021), and this study, we estimated earthquake focal mechanisms with the HASH program (Hardebeck and Shearer, 2002, 2003). This study picked polarities for some events of which P- and S-wave onsets were picked. The increase in pick data decreases the uncertainty of locations and focal mechanisms. The number of polarity data is listed in Table 2.1. Outputs from HASH include root mean square (RMS) and misfit of estimated focal mechanisms, where RMS is computed as a root mean square difference of the acceptable nodal planes from the preferred planes, which ranges between 0° and 60°, and misfit is the weighted fraction of misfit polarities between the observation and the preferred mechanism, which ranges between 0 and 0.5. We used the double-couple components of the GeoNet's moment tensor for which VR of moment tensor inversion was 70% or greater to evaluate focal mechanisms obtained by this study. We utilized Kagan angles (Kagan, 1991) to compare our focal mechanisms with GeoNet's moment tensor solutions. The Kagan angle is a measure of the angular difference between two focal mechanisms, which ranges between 0° and 120°. The obtained Kagan angles between focal mechanisms from the GeoNet's catalog and HASH (this study) were slightly smaller for inland earthquakes than those nearshore or offshore (Figure 2.9a), which might be due to the difference in station coverage. The Kagan angles were small for smaller RMS of HASH's focal mechanisms (Figure 2.9b). Since earthquakes with RMS $\leq$ 35° and misfit $\leq$ 0.2 had relatively small Kagan angles, we used only earthquakes satisfying these RMS and misfit criteria for the further focal mechanism analysis. Figure 2.10 shows the distribution of the 483 earthquakes satisfying these criteria and their focal mechanisms. We generated a new reconstructed earthquake catalog using corrected magnitudes, relocated hypocenters, and focal mechanisms calculated by HASH and used it for classification.

2.3. Classification of earthquakes using the reconstructed catalog

After the catalog reconstruction mentioned above, we classified earthquakes into six types: AUS (earthquakes in the Australian plate), PAC (earthquakes in the Pacific plate), INT (earthquakes at the plate interface), maybe_AUS (earthquakes maybe in the Australian plate or maybe at the plate interface), maybe_PAC (earthquakes maybe in the Pacific plate or maybe at the plate interface), and unknown (earthquakes which cannot be classified into above five types due to large uncertainties). The classification consists of three steps: classification based on relocated hypocenters, focal mechanisms calculated by HASH, and waveform cross-correlation. These steps and the classification criteria used are described below.

2.3.1. Classification based on relocated hypocenters

Firstly, we classified the relocated earthquakes with horizontal uncertainties greater than 5 km or depth uncertainty greater than 5 km as "unknown." The number of unknown earthquakes was 2,872 (Table 2.2). Then, other earthquakes were classified into AUS, PAC, maybe_AUS, or maybe_PAC based on the relative depth to the plate interface modeled by Williams et al. (2013) (Figure 2.11). We considered the depth uncertainty of the plate interface model as 5 km in this study, much larger than the uncertainty in interface depth (2 km) estimated by Williams et al. (2013). If an earthquake was shallower than 5 km above the plate interface, it was classified into AUS; if the event was deeper than 5 km below the interface, it was classified into PAC. Earthquakes within 5 km of the plate interface were tentatively grouped maybe_AUS if shallower than the interface and maybe_PAC if deeper. In this step, we obtained 350 AUS, 8,559 PAC, 1,046 maybe_AUS, and 4,105 maybe_PAC earthquakes (Table 2.2; Figure 2.12). The maybe_AUS and maybe_PAC earthquakes were further used in the next step to be classified into AUS, PAC, or INT based on their focal mechanisms.

2.3.2. Classification based on focal mechanisms

Earthquake focal mechanisms can be classified into seven types (Figure 2.13): strike-slip (SS), oblique strike-slip – normal (SS-N), oblique strike-slip – reverse (SS-R), normal (N), oblique normal – strike-slip (N-SS), reverse (R), and oblique reverse – strike-slip (R-SS). INT earthquakes are expected to have focal mechanisms of R or R-SS. In other words, earthquakes that are not R or R-SS are expected to be classified into AUS or PAC. We examined focal mechanism types of AUS, PAC, maybe_AUS, and maybe_PAC with Álvarez-Gómez (2019)'s software that returns a focal mechanism type from strike, dip, and rake (Table 2.3). Only about 13% of AUS and 6% of PAC had a focal mechanism type of R or R-SS. In contrast, about 71% of maybe_AUS and 58% of maybe_PAC had a focal mechanism type of R or R-SS, which indicates that many of maybe_AUS and maybe_PAC would be classified into INT. We considered that maybe_AUS and maybe_PAC earthquakes with focal mechanism types of SS, SS-N, SS-R, N, or N-SS did not occur on the subduction interface. Thus, we classified earthquakes initially classified as maybe_AUS and maybe_PAC that did not have R or R-

SS types into AUS or PAC, respectively. We compared other maybe_AUS and maybe_PAC earthquakes with R or R-SS focal mechanisms to synthetic INT focal mechanisms. The synthetic INT focal mechanisms have strike and dip corresponding to the plate interface model of Williams et al. (2013) and rake corresponding to the relative plate motion vector (Wallace et al., 2004; Wallace et al., 2009) (Figure 2.14). In this study, the plate motion of the Pacific plate relative to the Australian plate is fixed to 280° measured clockwise from north. If the Kagan angle (Kagan, 1991) between calculated focal mechanisms of maybe_AUS or maybe_PAC and those of synthetic INT was 60° or less, the earthquakes were classified into INT. We examined the Kagan angle between synthetic INT focal mechanisms and AUS and PAC focal mechanisms, where the distance between the hypocenters and the plate interface model was less than 10 km (Figure 2.15a, b). The distribution of obtained INT earthquakes did not essentially change even assuming a larger or smaller Kagan angle threshold (Figure 2.16), suggesting that INT earthquakes were likely detected correctly by setting the threshold of 60°. In this step, 18 AUS, 69 PAC, and 127 INT earthquakes were newly classified (Table 2.2; Figure 2.17).

2.3.3. Classification based on waveform similarities

We were unable to compute high-quality locations and focal mechanisms for all events. To classify the remaining events, we considered that similar waveforms between two earthquakes probably indicate that they occurred close to each other (e.g., Uchida, 2019) and have identical focal mechanisms. In this step, we calculated the cross-correlation coefficient (CC) between earthquakes and classified the pairs into the same type if they had a large CC value. We selected only seismic stations within 150 km of the earthquakes' epicenters for calculating CC and used vertical component waveforms bandpass filtered between 1 and 10 Hz. We cut waveforms, provided by GeoNet (GNS Science, 2023c), from 1 s before the P-wave onset to 19 s after so that the trace contains both P-wave and S-wave. We calculated the CC values between two earthquakes, of which epicentral separation was 20 km or shorter, where hypocenter locations were from the GeoNet's catalog. Figure 2.18 shows an example of CC calculation. We used waveforms with a signal-to-noise amplitude ratio greater than two to compute cross-correlation, where signal and noise amplitudes were defined as the maximum absolute amplitude between P-wave onset and 19 s after the onset, and between 1 s before and 0.01 s before the onset, respectively. The CC values with a lag time of less than 1.5 s were used. We confirmed that many of the high CC values (74% of CC ≥ 0.95; 66% of CC ≥ 0.8; 59% of CC ≥ 0.65) were within a very short lag time of ±0.1 s (Figure 2.19a). The number of obtained CC was 15,899,352 (Figure 2.19b, c). We paired the two earthquakes if CC values were greater than or equal to the threshold value (cross-correlation threshold) of 0.65 at two or more stations. The idea that two earthquakes with high CC at two or more stations are paired was also used in the study of repeating earthquake detection (e.g., Hughes et al., 2021; Igarashi, 2010; Uchida and Matsuzawa, 2013). If some pairs shared the

same earthquake, the pairs were grouped; if events A and B and events A and C satisfy the criteria, but not for events B and C, all events (A, B, and C) are grouped. Then, we classified earthquakes in each pair and group into the same type as the type of the youngest event among those already classified into AUS, INT, or PAC. When all earthquakes in a pair or group were maybe_AUS or maybe_PAC, these earthquakes were not re-classified.

The cross-correlation threshold was 0.65 in this study, which was determined based on CC distribution in two ways. Firstly, CC had large values if the two earthquakes occurred close in space (Figure 2.19d), where earthquakes whose depth uncertainties were less than 3 km were used. About 78% of CCs greater than 0.65 were from earthquake pairs with inter-event distances less than 5 km. This indicates that the two strongly correlated earthquakes are probably of the same type. The CC values computed at each station did not show large dependence on the distance between the epicenter and the seismic station (Figure 2.19e), indicating that the high attenuation (e.g., Sato, 1967) due to the large travel distance did not contribute to the high CC values. From these results, we considered a cross-correlation threshold of 0.65 as a reasonable threshold, which might prevent the process from making pairs for two earthquakes that were actually not of the same type. Secondly, we conducted a random test. Under the assumption that CC has an x% probability of exceeding the cross-correlation threshold (> 0) by chance, we calculated the expected value of the number of earthquake pairs (N) that satisfied CC > cross-correlation threshold at two or more stations. Considering the probability x as the probability of CC exceeding the threshold, what is needed is to find x and the cross-correlation threshold such that N is less than one (to eliminate false detections). We tested several x and obtained N for each x, and N became less than one when x was 0.0167% (Table 2.4). Since the positive and negative CCs should show a similar distribution for two independent waveforms, we assumed that the number of CCs exceeding a value z (> 0) by chance was the same as the number of CCs falling below -z by chance. Under this assumption, the probability of CC randomly exceeding *threshold* is equivalent to the probability of CC randomly falling below -1* *threshold*. The relationship between x and the cross-correlation threshold is expressed as

$$x = \frac{n(-1 \le CC < (-1 * threshold))}{n(-1 \le CC \le 1)} \times 100, \tag{2.4}$$

where $n(CC)$ is the number of CC data. This equation shows how small the probability of randomly exceeding the cross-correlation threshold becomes with increasing the assumed threshold. The probability x, calculated from Equation (2.4) and obtained CC data (Figure 2.19b, c), decreases with the cross-correlation threshold and falls below 0.0167% for cross-correlation threshold > 0.64 (Figure 2.19f), indicating that the threshold above 0.64 detects no earthquake pairs (N) which satisfied CC > cross-correlation threshold by chance at two or more stations. Therefore, the cross-correlation threshold value of 0.65 is expected to almost eliminate the possibility of detecting false earthquake pairs, and we can reduce the number of false detections to less than one.

In this step, 66 AUS, 447 PAC, and 347 INT earthquakes were newly classified (Table 2.2; Figure 2.20). After three classification steps, we obtained 433 AUS, 469 INT, 9,065 PAC, 820 maybe_AUS, 3,273 maybe_PAC, and 2,872 unknown earthquakes (Table 2.2; Figure 2.21). In the next section, we describe the space-time distribution of classified earthquakes.

2.4. Spatial distribution of classified earthquakes

The AUS earthquakes were concentrated in the north of our study area (Figure 2.22a), and many of AUS's focal mechanisms were strike-slip type (Figure 2.23a). There was a small gap where no AUS earthquakes were detected in the north of our study region (marked by a black circle in Figure 2.22f). The P-axis of the estimated focal mechanism and the direction of maximum contraction (Haines and Wallace, 2020) were nearly parallel in the south of the study area (Figure 2.23f). In contrast, AUS events had a variety of focal mechanisms in the north of the study area, making the direction of the P-axis and maximum contraction not aligned (Figure 2.23f, g). The gap and dense region of AUS earthquakes correspond to extensional and contractional regions of areal strain rates (Dimitrova et al., 2016; Haines and Wallace, 2020) in the north of our study area, respectively, which suggests that areal strain rates might play a role in the occurrence of AUS earthquakes here (discussed in section 4.2.4).

The INT earthquakes were mainly located outside or periphery of SSE sources (Figure 2.22b). However, we note that detection bias will tend to provide the best locations for earthquakes close to and beneath the land and that earthquakes offshore might not be detected. The location difference between INT events and SSEs may reflect a difference in frictional properties on the megathrust: SSEs are thought to occur in transitional frictional zones in the presence of high fluid pressure (e.g., Liu and Rice, 2007), and INT, or regular interplate earthquakes, require velocity weakening friction. Such a difference in frictional properties might be explained by the properties of subducting rocks, pressure, and temperature (Boulton et al., 2019; Shreedharan et al., 2022).

The PAC earthquakes were widely distributed throughout the study area (Figure 2.22c), and their focal mechanisms showed some regional dependencies (Figure 2.23c). There was a small seismicity gap in the northern Hikurangi margin (a red circle in Figure 2.22c), also reported by previous studies (e.g., Yarce et al., 2019). A double seismicity zone can be seen, especially in the north of our study region (B-B' and C-C' in Figure 2.24), and a large PAC cluster was observed in the central Hikurangi margin (x = 60-90 km for cross-sections F-F' and G-G' in Figure 2.24). Focal mechanisms of PAC earthquakes showed different types depending on their depth relative to the plate interface. Shallow PAC events (0-30 km deep from the plate interface) were mainly normal fault type for both planes of the double seismic zone as shown by Reyners and McGinty (1999), and deep PAC events (30-40 km deep from the plate interface) were mainly reverse type (Figure 2.25), as commonly seen in plate bending (e.g., Evanzia et al., 2019).

2.5. Relationships between regular earthquakes and tremors

Tremors were detected in a wide region of the North Island by Romanet and Ide (2019), the north of our study area by Todd and Schwartz (2016), and the north offshore of our study area by Todd et al. (2018). Relocated earthquakes showed some space-time correlation with tremors. Tremors and INT earthquakes showed a weak visual correlation in space (Figure 2.26). This may also indicate the small-scale differences in frictional properties if tremors occurred at the plate interface (Nishikawa et al., 2019; Takahashi, 2021). Tremors and regular earthquakes sometimes occurred in very short time intervals: AUS and INT earthquakes seemed to have occurred just before and after tremors occurred in the middle of 2010 (oval A in Figure 2.27), and PAC and INT earthquakes and tremors occurred almost at the same time in the middle of 2011 (oval B in Figure 2.27). We note that a random dataset of tremors and earthquakes will also be able to produce such synchronization, indicating that observed synchronization of tremors and INT earthquakes are apparent. If these space-time correlations between regular earthquakes and tremors are not apparent, some relationships between the earthquakes and other slow earthquakes, including SSEs, should appear. Todd et al. (2018) detected and located shallow tremors and local earthquakes offshore Gisborne in the northern Hikurangi margin. The rate of detected tremors increased during and after the 2014 SSE (white dots in an oval in Figure 2.28b). They also showed a small seismicity rate increase accompanying the 2014 SSE. The earthquake catalog used in this study did not show such an increase in seismicity rate (Figure 2.28) probably due to the small number of used earthquakes: this study used only ~3% of earthquakes detected by Todd et al. (2018). The next chapter examines and describes such relationships between earthquakes and SSEs.

Table 2.1. The number of P- and S- wave pick data used for relocating earthquakes and polarities for computing focal mechanisms.

	GeoNet (manual)	GeoNet (auto)	Hughes et al. (2021)	This study		Total of adopted
				Added	Adopted	
P-wave	48,259	334,749	357	33,747	22,690	406,055
S-wave	78,130	282	268	27,968	14,312	92,992
Polarity	12,799	20,585	353	24,311	15,833	49,570

Table 2.2. The number of newly classified earthquakes at each step.

	Hypocenter	Focal mechanism	Waveform cross-correlation	Total
AUS	350	18	66	433
INT	0	127	347	469
PAC	8,559	69	447	9,065
maybe_AUS	1,046	-	-	820
maybe_PAC	4,105	-	-	3,273
unknown	2,872	-	-	2,872

Table 2.3. The number of focal mechanism types using Álvarez-Gómez (2019)'s software: strike-slip (SS), strike-slip – normal (SS-N), strike-slip – reverse (SS-R), normal (N), normal – strike-slip (N-SS), reverse (R), and reverse – strike-slip (R-SS). Numbers in parentheses indicate percentages (%).

	SS	SS-N	SS-R	N	N-SS	R	R-SS
AUS	3 (20)	4 (27)	0 (0)	3 (20)	3 (20)	2 (13)	0 (0)
PAC	3 (3)	11 (12)	7 (7)	54 (57)	14 (15)	3 (3)	3 (3)
maybe_AUS	4 (6)	4 (6)	6 (10)	0 (0)	4 (6)	28 (45)	16 (26)
maybe_PAC	6 (4)	13 (8)	6 (4)	34 (21)	10 (6)	82 (50)	13 (8)

Table 2.4. Relationship between probability (x) and obtained expected value of the number of pairs (N).

x (%)	N
100	4,064,175
10	147,315
1	1,855
0.1	22
0.03	2
0.0167	0

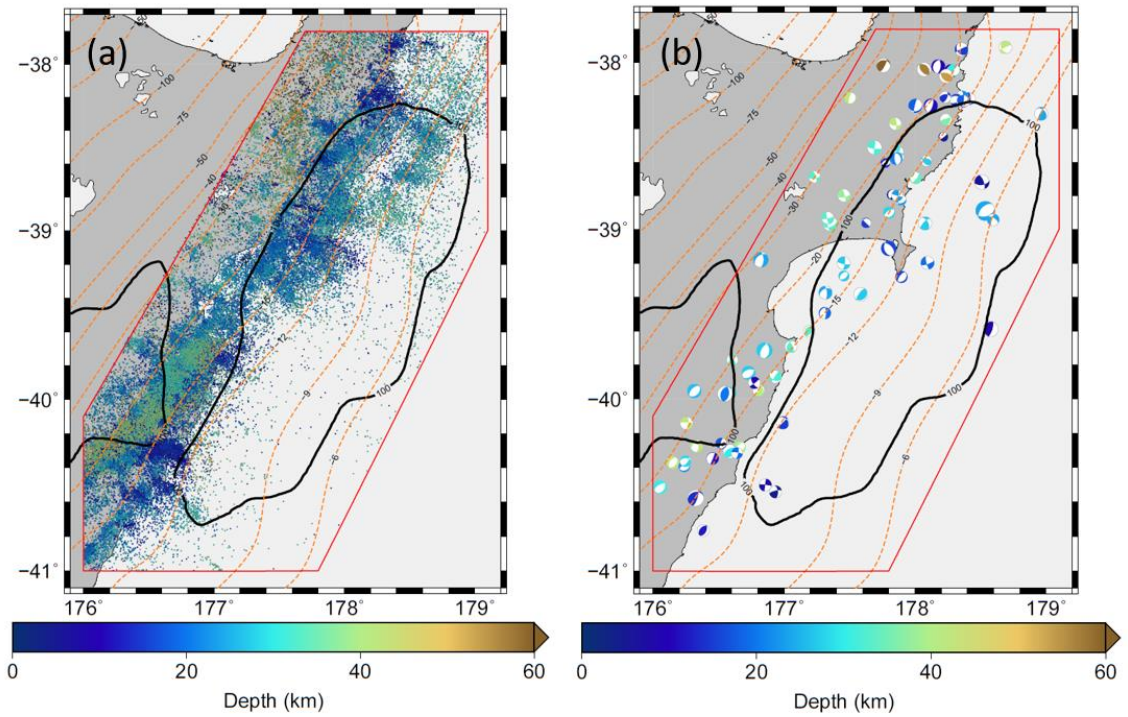

Figure 2.1. Earthquakes that were used to correct magnitudes. (a) Spatial distribution of earthquakes. The colors correspond to the depth of hypocenters. Black contours are cumulative SSE slips of 100 mm between 2002-2020 (Wallace, 2020; Woods, 2022). Orange dashed line contours are the iso-depth of the subducted Pacific plate surface (in kilometers) estimated by Williams et al. (2013). The red line indicates the study area. (b) Spatial distribution of earthquakes and their focal mechanisms that were used to examine the relationship between ML and Mw. The colors correspond to the focal depth.

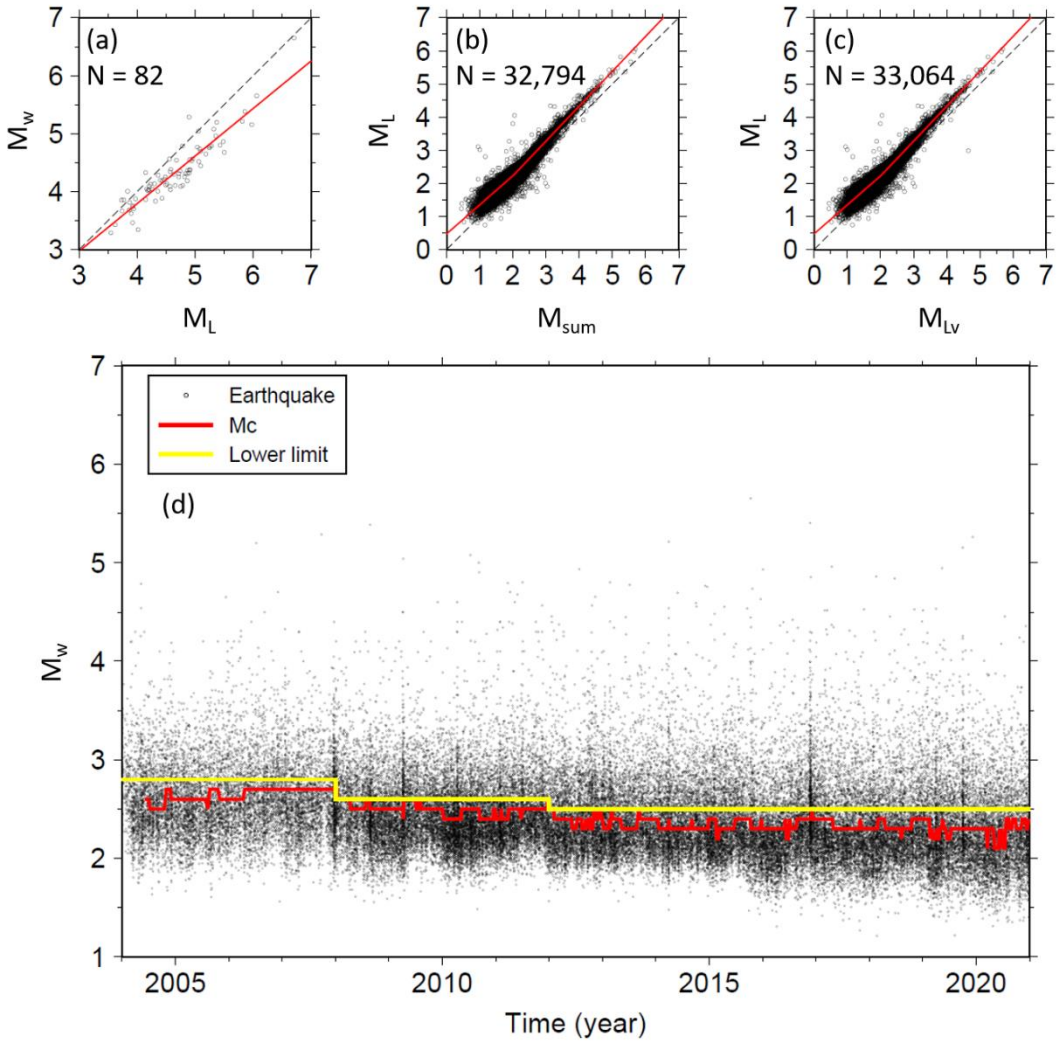

Figure 2.2. (a), (b), (c) Relationships between M_L and M_w, M_{sum} and M_L, and M_{Lv} and M_L. Black dashed lines indicate the same magnitude. Red lines are estimated regression lines. (d) The magnitude of completeness (Mc) and lower limits of magnitude used. Circles are earthquake magnitude within the study area. Here magnitudes computed from Equations (2.1-2.3) are used. The red line is a temporal change of Mc. Mc is calculated for every 1,000 earthquakes. The yellow lines are lower limits of magnitude in three periods for analysis.

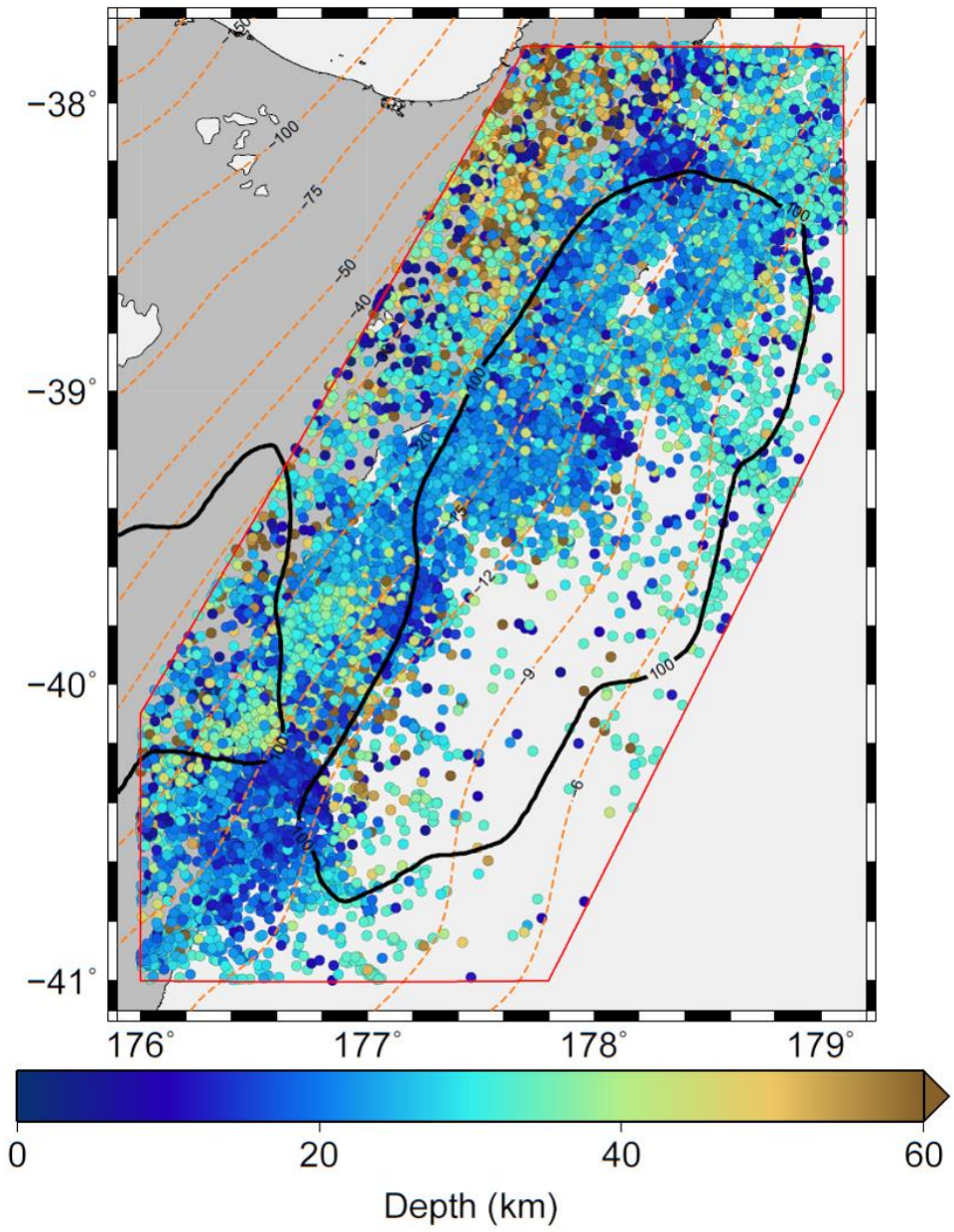

Figure 2.3. Spatial distribution of earthquakes to be relocated. The colors correspond to the depth of hypocenters. Black contours are cumulative SSE slips of 100 mm between 2002-2020 (Wallace, 2020; Woods, 2022). Orange dashed line contours are the iso-depth of the subducted Pacific plate surface (in kilometers) estimated by Williams et al. (2013). The red line indicates the study area.

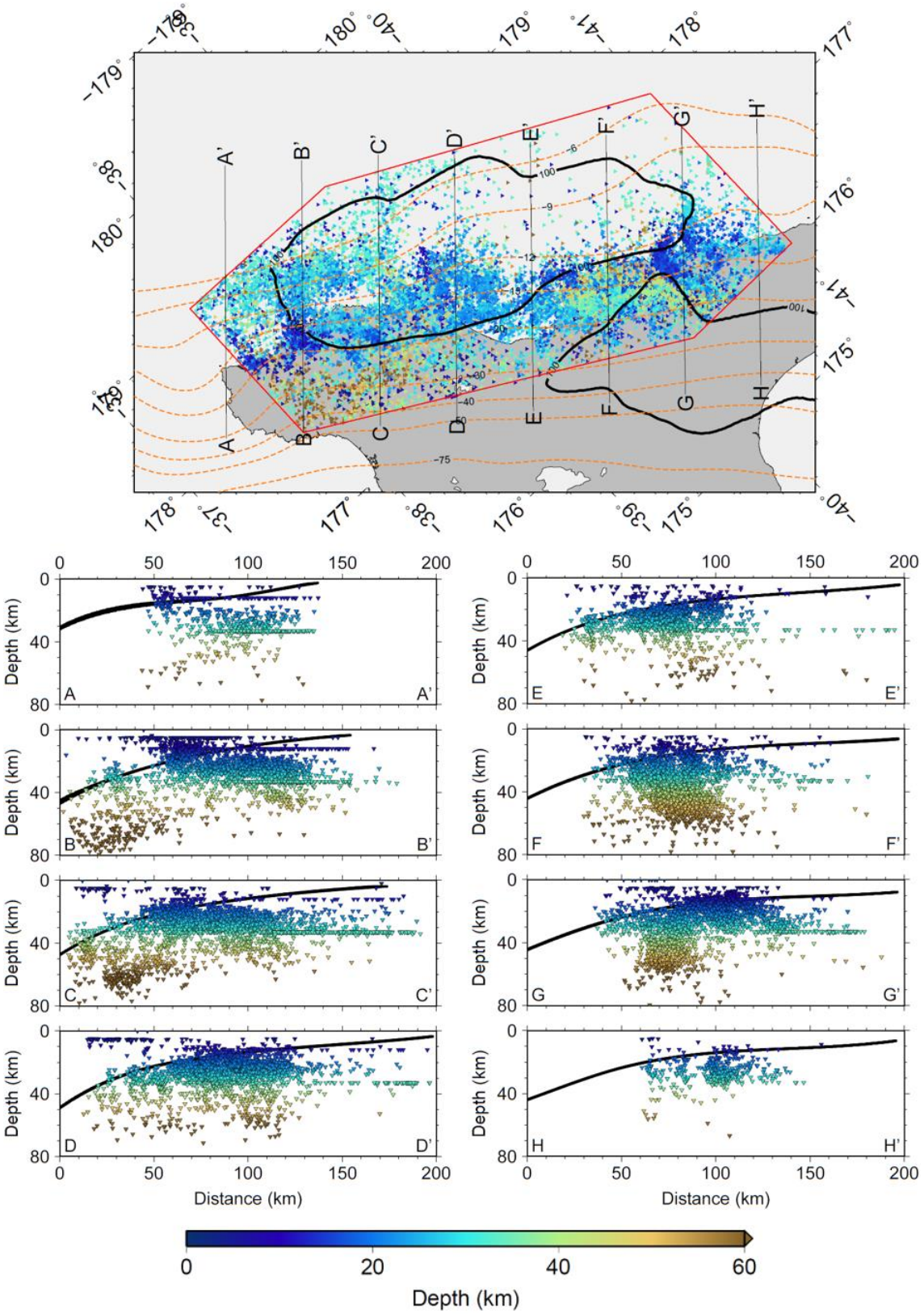

Figure 2.4. Cross sections for Figure 2.3. The colors correspond to the depth of hypocenters. Black contours are cumulative SSE slips of 100 mm between 2002-2020 (Wallace, 2020; Woods, 2022).

Orange dashed line contours are the iso-depth of the subducted Pacific plate surface (in kilometers) estimated by Williams et al. (2013). The red line indicates the study area. Bold black lines indicate the plate interface. Note that the depths of some earthquakes are operator assigned (fixed).

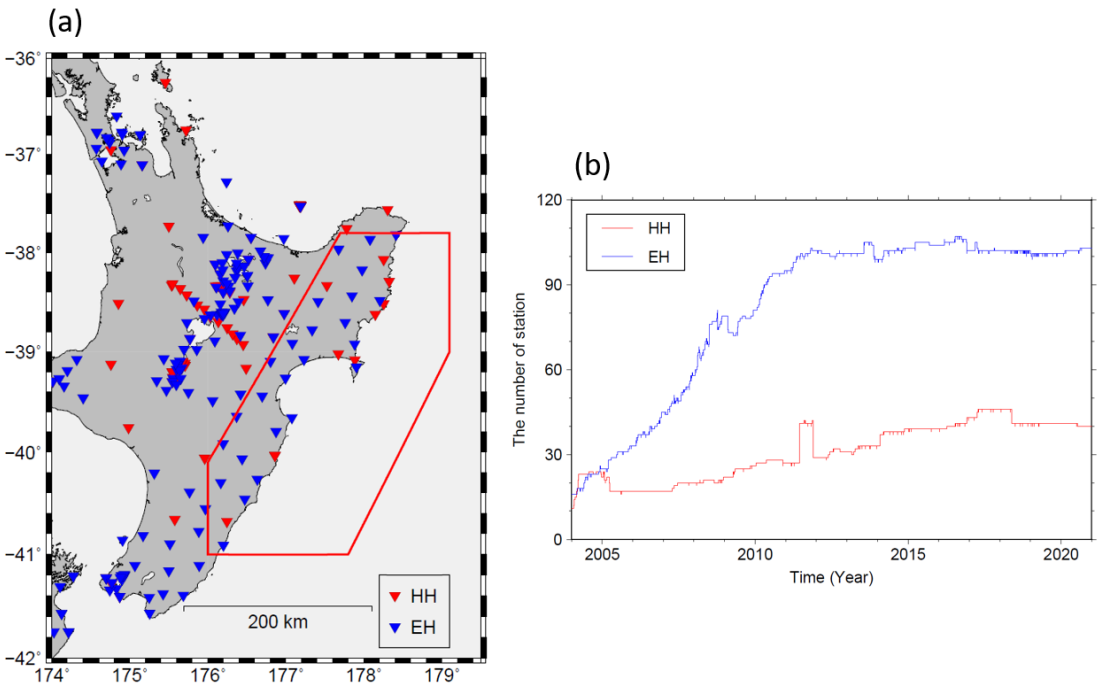

Figure 2.5. (a) Distribution of seismic stations. Red and blue inverted triangles represent broadband seismic stations (HH) and short-period seismic stations (EH), respectively. The red line is the study area. (b) The number of operated seismic stations in Figure 2.5a. The red and blue lines represent HH and EH, respectively.

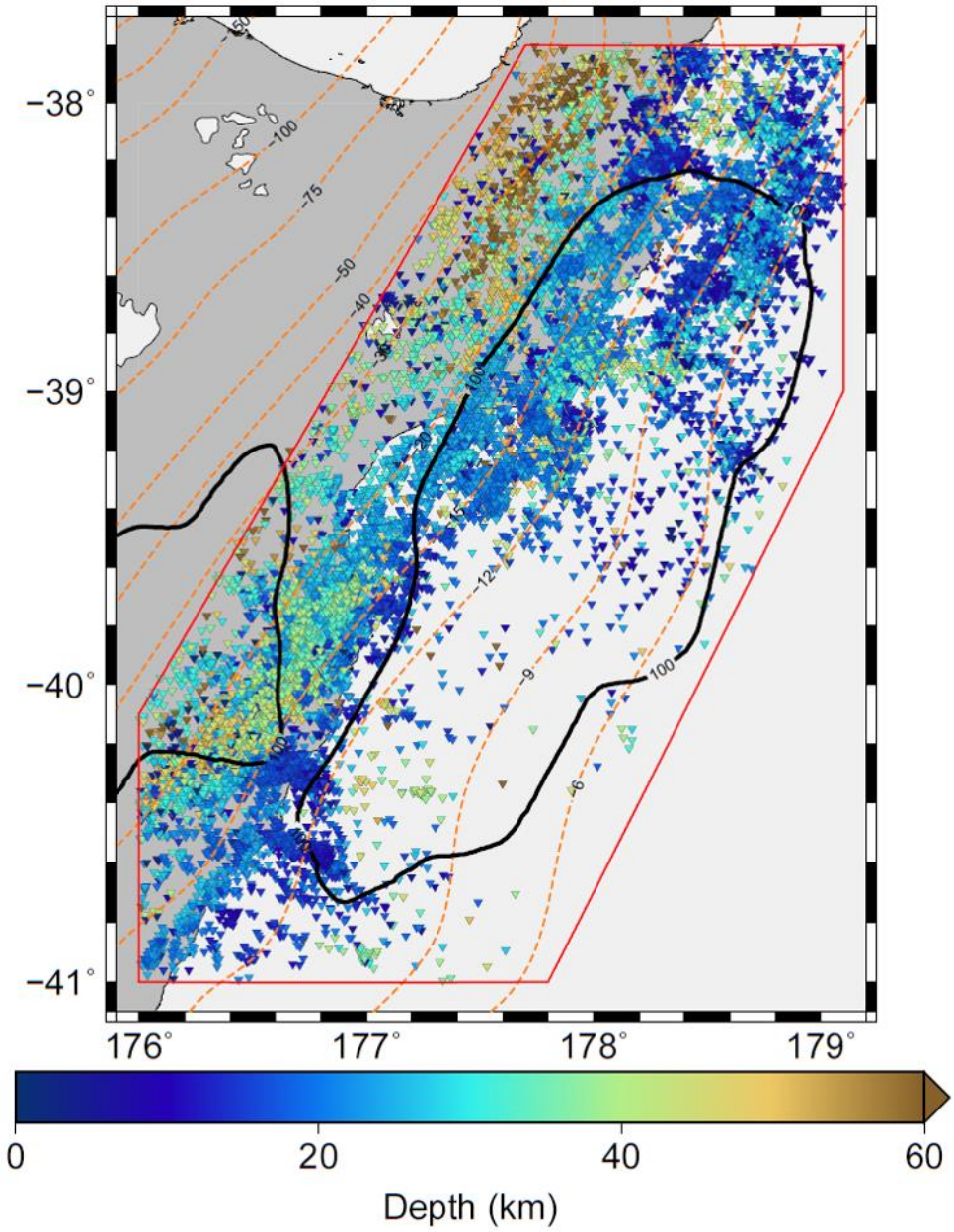

Figure 2.6. Spatial distribution of relocated earthquakes. The colors correspond to the depth of hypocenters. Black contours are cumulative SSE slips of 100 mm between 2002-2020 (Wallace, 2020; Woods, 2022). Orange dashed line contours are the iso-depth of the subducted Pacific plate surface (in kilometers) estimated by Williams et al. (2013). The red line indicates the study area.

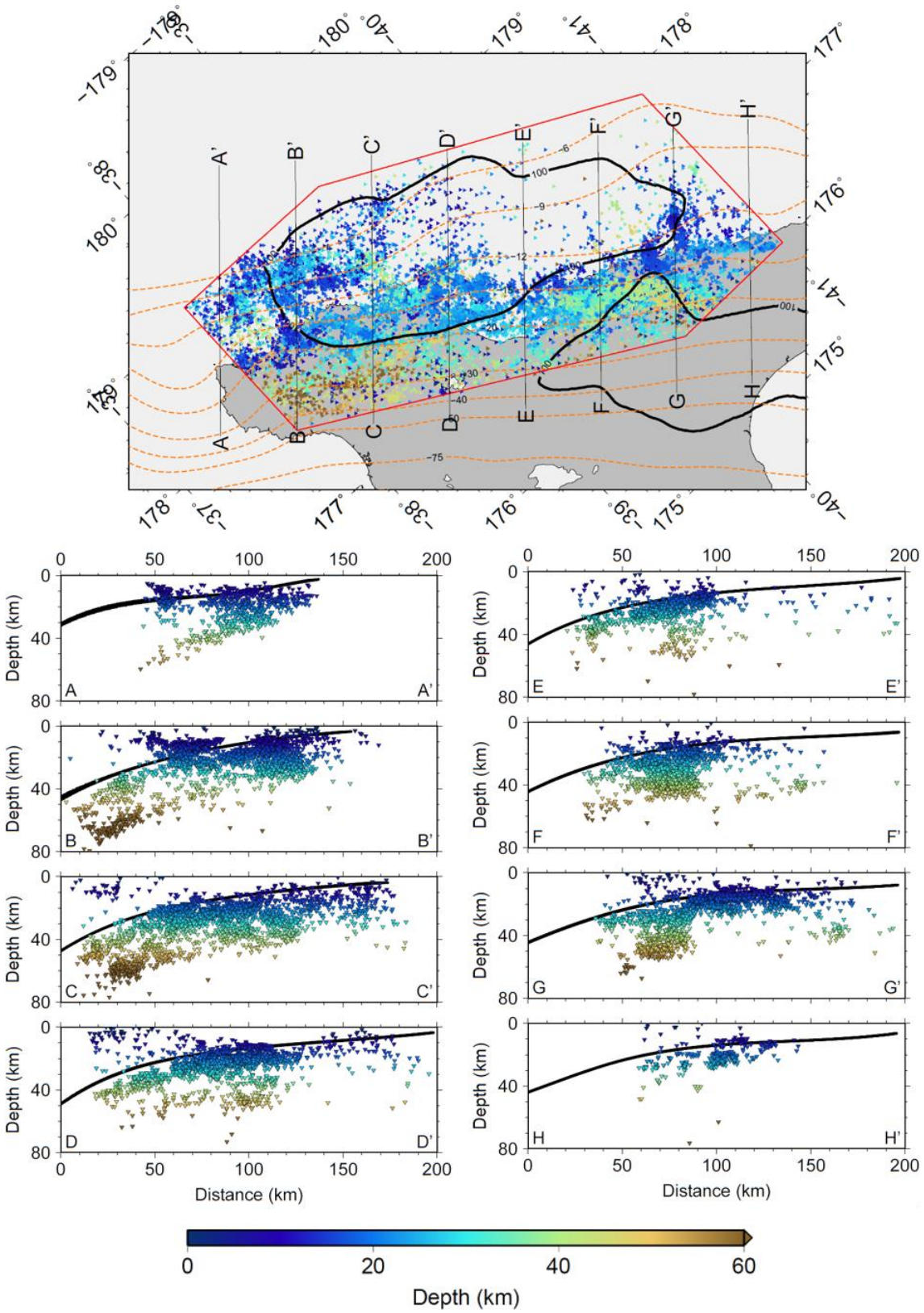

Figure 2.7. Cross sections for Figure 2.6. The colors correspond to the depth of hypocenters. Black contours are cumulative SSE slips of 100 mm between 2002-2020 (Wallace, 2020; Woods, 2022).

Orange dashed line contours are the iso-depth of the subducted Pacific plate surface (in kilometers) estimated by Williams et al. (2013). The red line indicates the study area. Bold black lines indicate the plate interface. Note that the depths of some earthquakes are operator assigned (fixed).

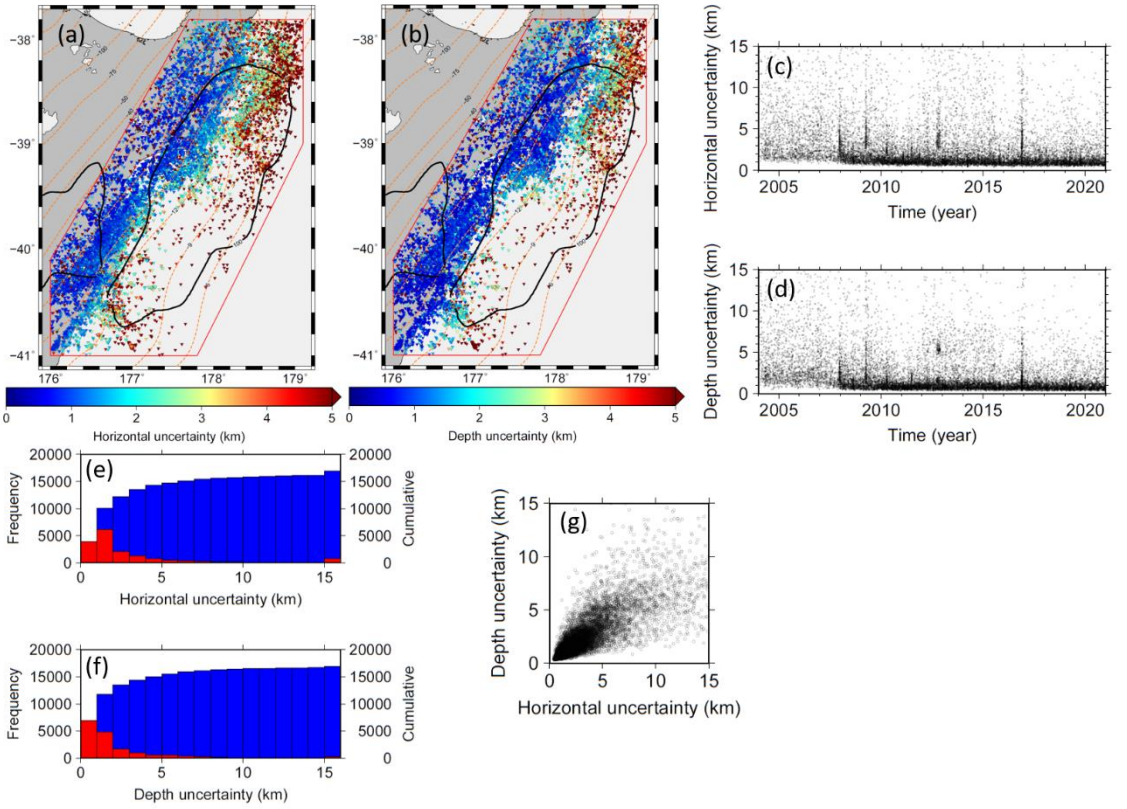

Figure 2.8. Uncertainties of relocated earthquakes. (a), (b) Horizontal and depth uncertainties of relocated earthquakes, respectively. The colors correspond to the uncertainties. Black contours are cumulative SSE slips of 100 mm between 2002-2020 (Wallace, 2020; Woods, 2022). Orange dashed line contours are the iso-depth of the subducted Pacific plate surface (in kilometers) estimated by Williams et al. (2013). The red line indicates the study area. (c), (d) Temporal changes in horizontal and depth uncertainties of relocated earthquakes, respectively. (e), (f) Histograms of horizontal and depth uncertainties of relocated earthquakes, respectively. The red and blue bars are the number of events in each 1 km bin and the cumulative number of events, respectively. This figure shows uncertainties greater than 15 km as "15 km." (g) Relationships between horizontal and depth uncertainties.

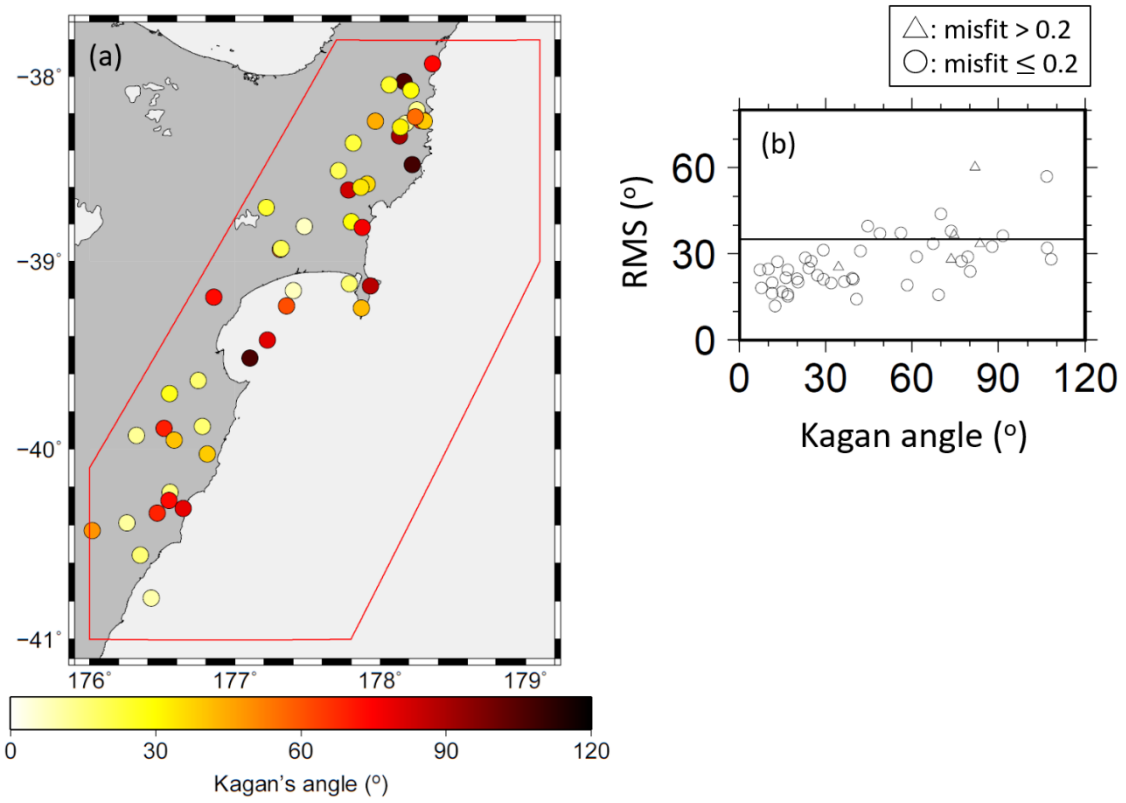

Figure 2.9. Kagan angle between the HASH program's focal mechanisms and GeoNet's moment tensor catalog. (a) Spatial distribution of Kagan angle plotted at relocated epicenters. The red line indicates the study area. (b) Relationships between Kagan angle and RMS of HASH's focal mechanisms. Circles and triangles are misfits of 0.2 or less and greater than 0.2, respectively.

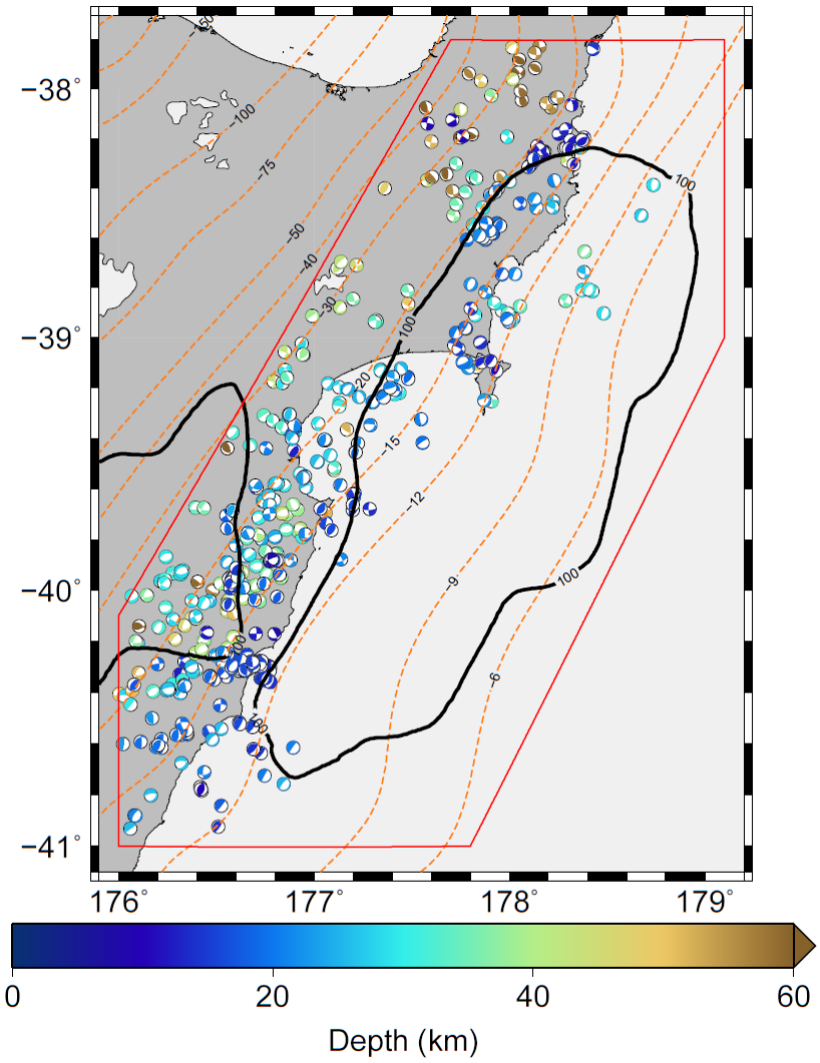

Figure 2.10. Focal mechanisms calculated by the HASH program of which RMS ≤ 35° and misfit ≤ 0.2. The colors correspond to the depths. Black contours are cumulative SSE slips of 100 mm between 2002-2020 (Wallace, 2020; Woods, 2022). Orange dashed line contours are the iso-depth of the subducted Pacific plate surface (in kilometers) estimated by Williams et al. (2013). The red line indicates the study area.

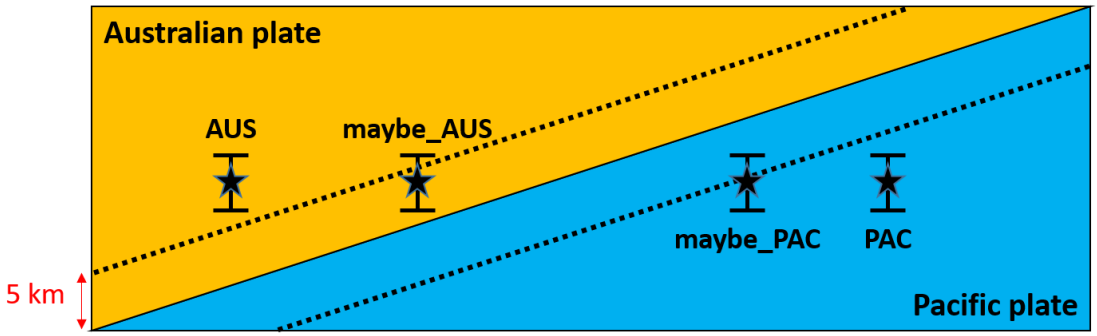

Figure 2.11. Schematic diagram of classification based on the relocated hypocenters. Orange and light blue triangles indicate the Australian plate and the Pacific plate, respectively. Two dashed lines are the plate interface considering its uncertainty of 5 km. Four stars are relocated hypocenters. An earthquake shallower than 5 km above the plate interface is classified into AUS (the first star from the left). An earthquake deeper than 5 km above the plate interface is classified into maybe_AUS (the second star from the left). An earthquake shallower than 5 km below the plate interface is classified into maybe_PAC (the second star from the right). An earthquake deeper than 5 km below the plate interface is classified into PAC (the first star from the right).

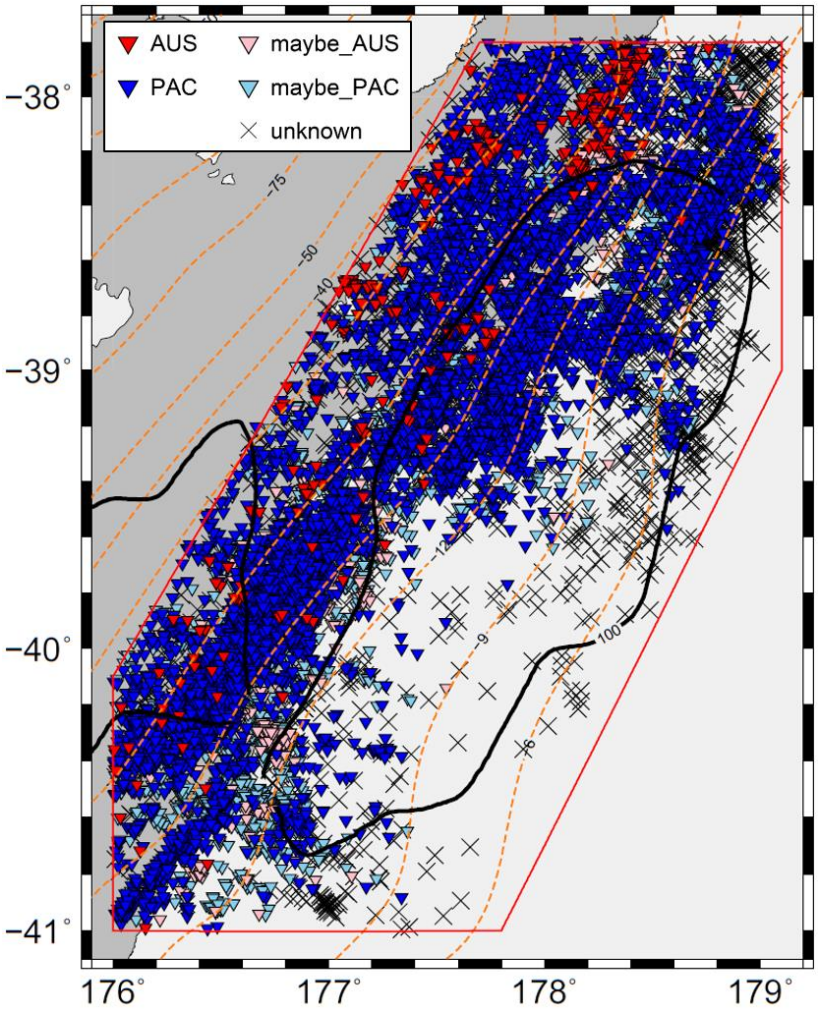

Figure 2.12. Results of classification based on relocated hypocenters. Red, blue, pink, and light blue inverted triangles are AUS, PAC, maybe_AUS, and maybe_PAC earthquakes. Black crosses are unknown earthquakes. Black contours are cumulative SSE slips of 100 mm between 2002-2020 (Wallace, 2020; Woods, 2022). Orange dashed line contours are the iso-depth of the subducted Pacific plate surface (in kilometers) estimated by Williams et al. (2013). The red line indicates the study area.

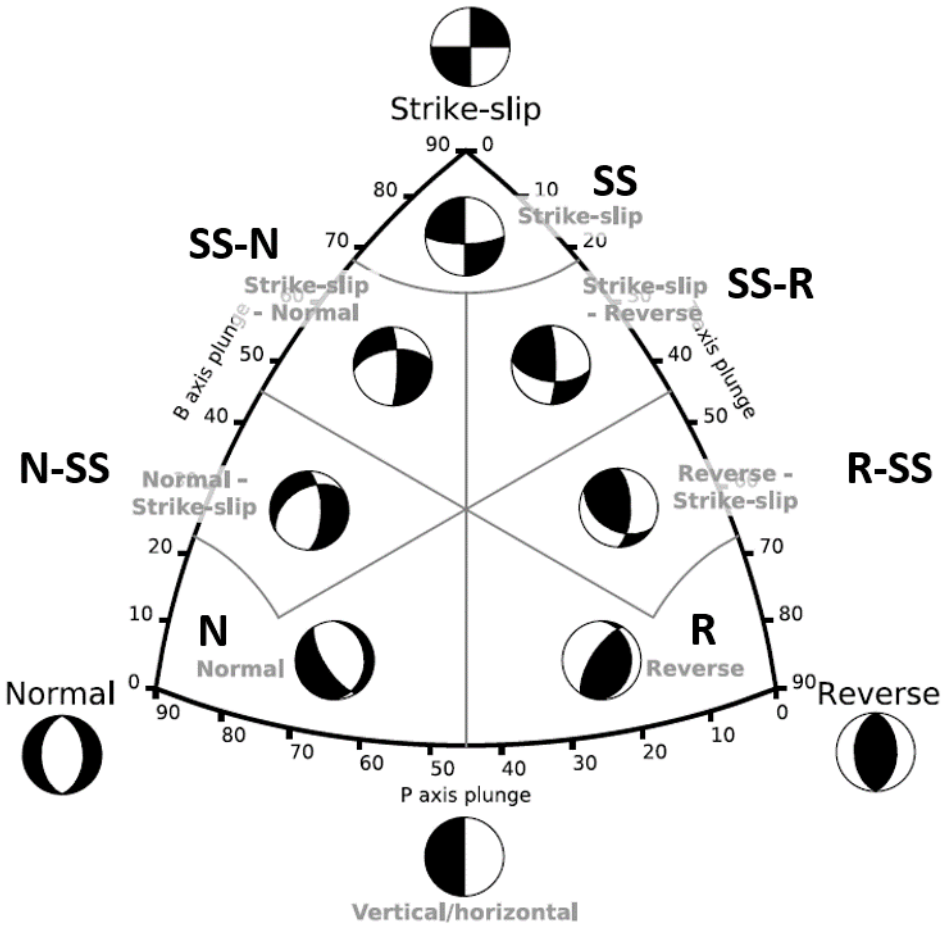

Figure 2.13. Seven focal mechanism types (modified from Álvarez-Gómez, 2019).

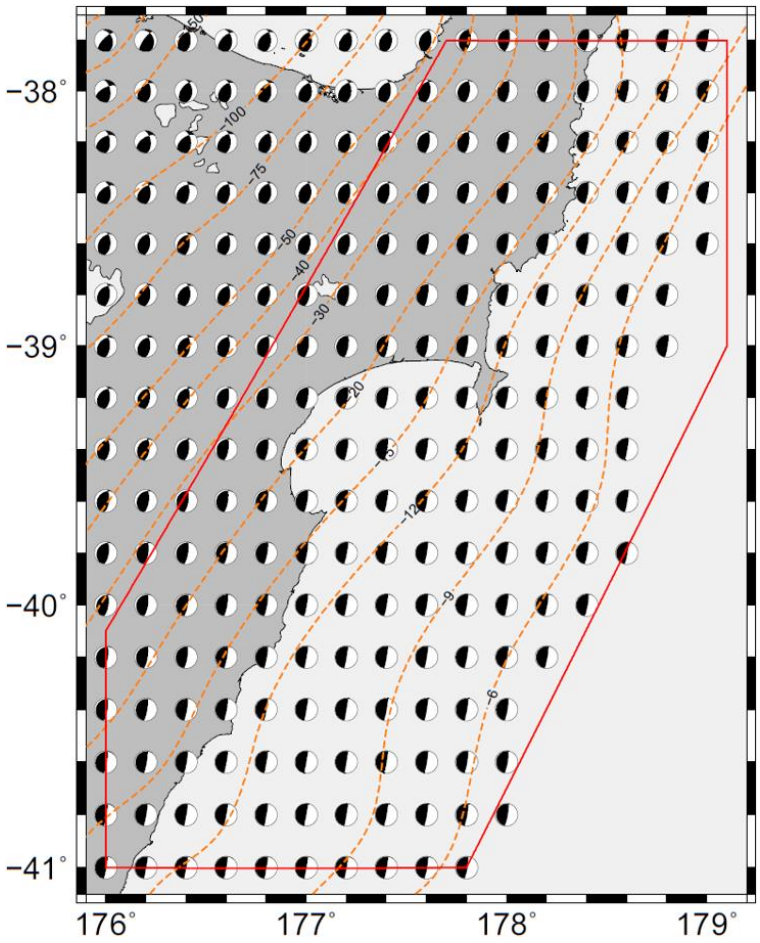

Figure 2.14. Synthetic INT focal mechanisms. Orange dashed line contours are the iso-depth of the subducted Pacific plate surface (in kilometers) estimated by Williams et al. (2013). The red line indicates the study area.

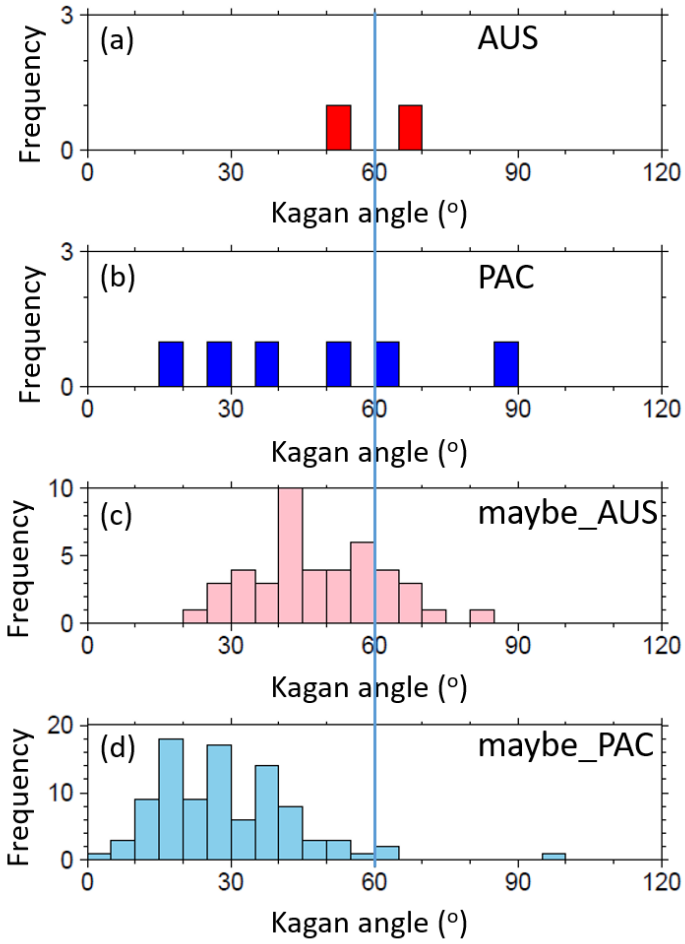

Figure 2.15. Histograms of Kagan angle between focal mechanisms of R or R-SS types and those of synthetic INT. (a) Histogram for AUS of which distance to the plate interface is less than 10 km. (b) Histogram for PAC of which distance to the plate interface is less than 10 km. (c) Histogram for maybe_AUS. (d) Histogram for maybe_PAC. The vertical line indicates a threshold of 60° to classify into INT.

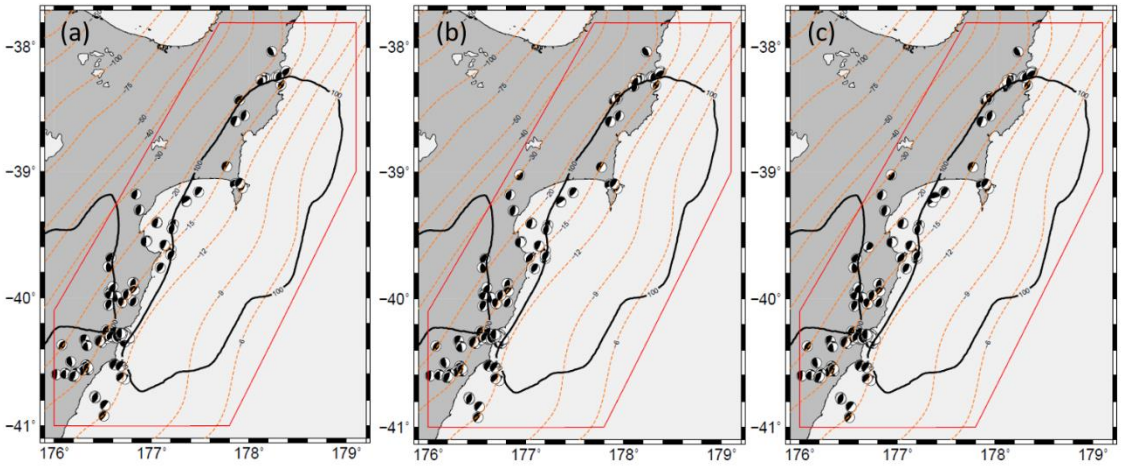

Figure 2.16. Spatial distribution and focal mechanisms of INT for each Kagan angle threshold. (a) The case of threshold = 50°. (b) The case of threshold = 60°. (c) The case of threshold = 70°. Black contours are cumulative SSE slips of 100 mm between 2002-2020 (Wallace, 2020; Woods, 2022). Orange dashed line contours are the iso-depth of the subducted Pacific plate surface (in kilometers) estimated by Williams et al. (2013). The red line indicates the study area.

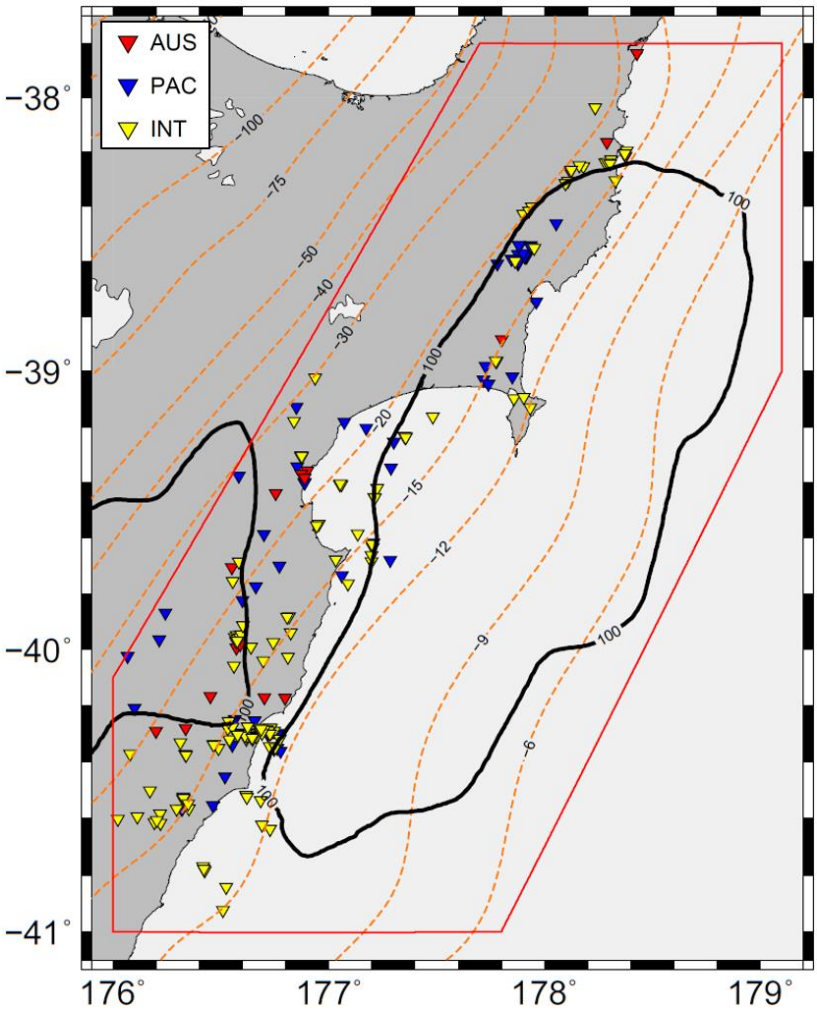

Figure 2.17. Results of classification based on focal mechanisms. Red, blue, and yellow inverted triangles are AUS, PAC, and INT earthquakes. Black contours are cumulative SSE slips of 100 mm between 2002-2020 (Wallace, 2020; Woods, 2022). Orange dashed line contours are the iso-depth of the subducted Pacific plate surface (in kilometers) estimated by Williams et al. (2013). The red line indicates the study area.

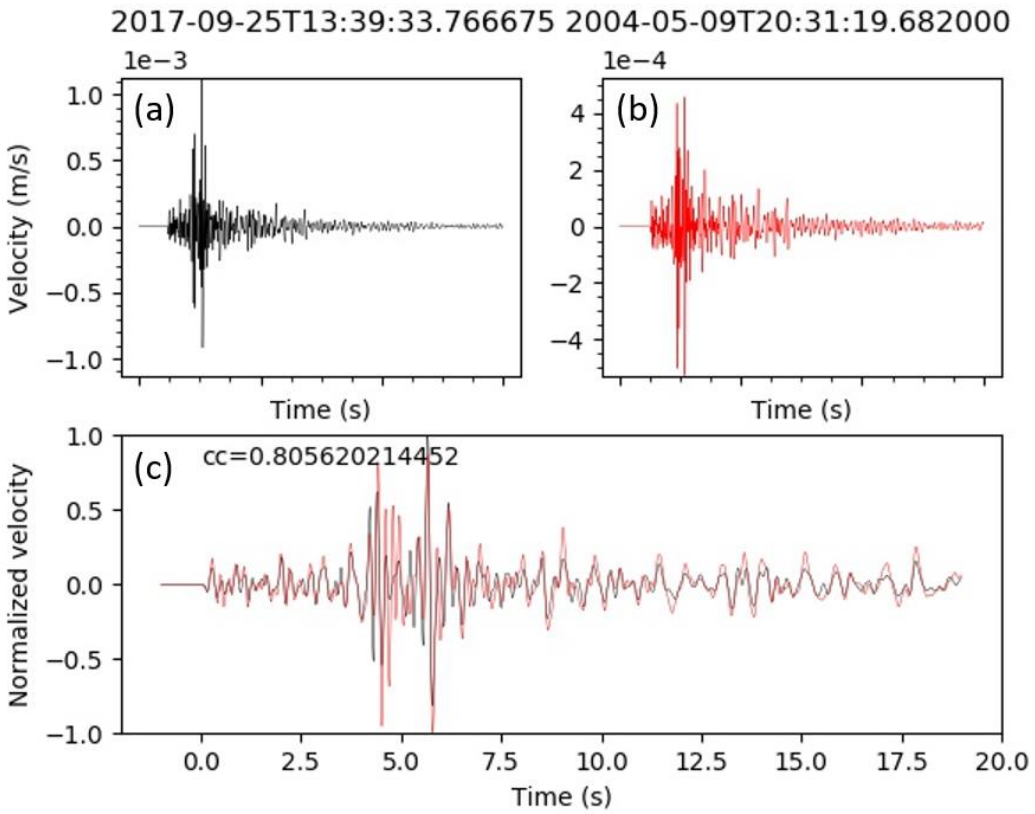

Figure 2.18. An example of CC calculation. (a) A waveform of template event. (b) A waveform of paired events at the same station. (c) Normalized waveforms of template event (black) and paired event (red). Waveforms are filtered between 1-10 Hz.

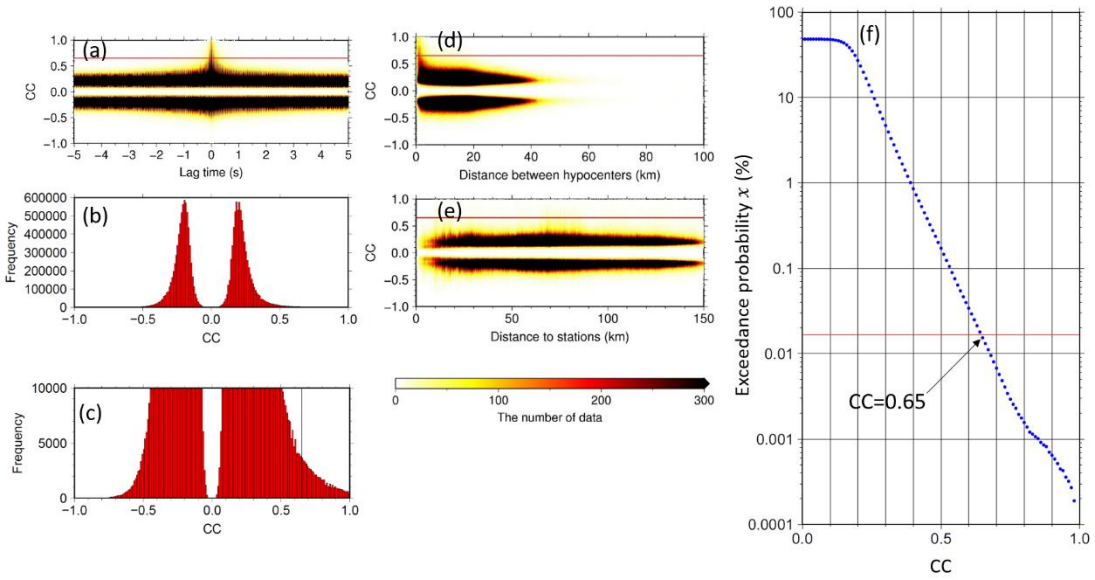

Figure 2.19. Waveform cross-correlation results. (a) Relationships between lag time and cross-correlation coefficient (CC). Colors correspond to the number of data in the 0.02 s × 0.01 grid. A red horizontal line indicates a CC of 0.65. (b) Histogram of CC values for all data. (c) Enlarged histogram. A black vertical line indicates a CC of 0.65. (d) Relationship between the distance between relocated hypocenters to calculate CC and the CC value, where only earthquakes with small depth error (< 3 km) were used. Colors correspond to the number of data in the 0.2 km × 0.01 grid. A red horizontal line indicates a CC of 0.65. (e) Relationship between distance from the epicenter of template events to the seismic stations and CC value. Colors correspond to the number of data in the 0.3 km × 0.01 grid. (f) Relationship between cross-correlation threshold and probability *x*. A red horizontal line indicates *x* of 0.0167%. An arrow points to data of which the cross-correlation threshold is 0.65.

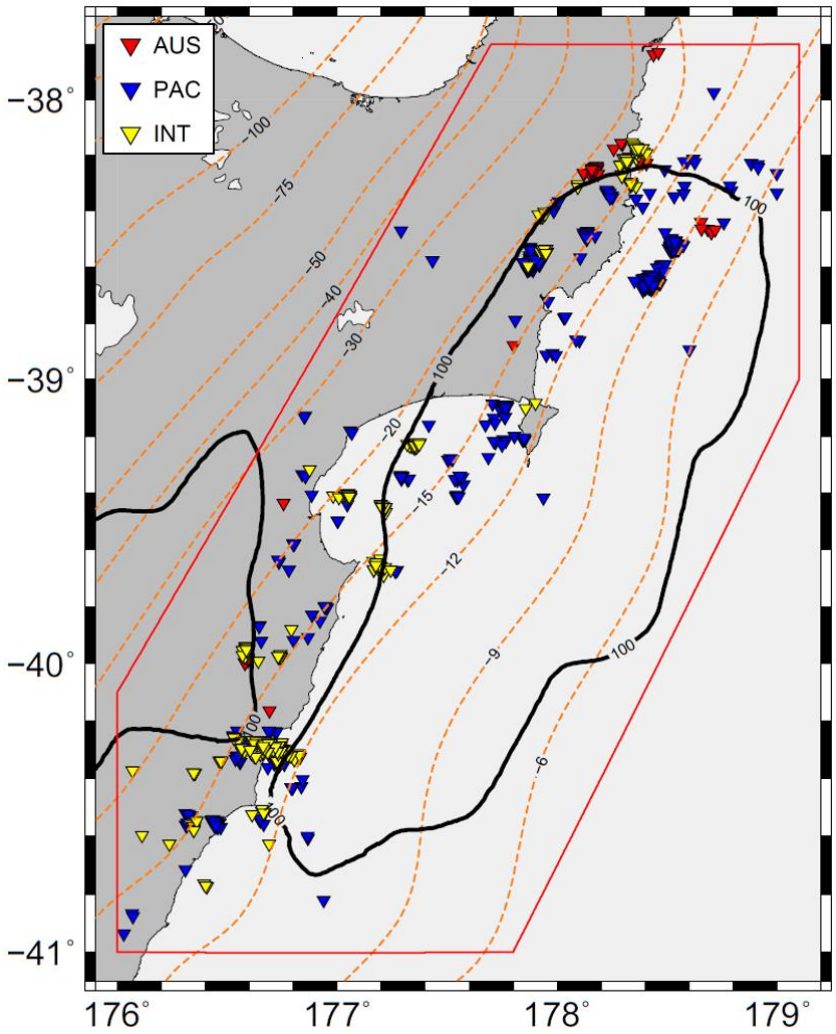

Figure 2.20. Results of classification based on waveform cross-correlations. Red, blue, and yellow inverted triangles are AUS, PAC, and INT earthquakes. Black contours are cumulative SSE slips of 100 mm between 2002-2020 (Wallace, 2020; Woods, 2022). Orange dashed line contours are the iso-depth of the subducted Pacific plate surface (in kilometers) estimated by Williams et al. (2013). The red line indicates the study area.

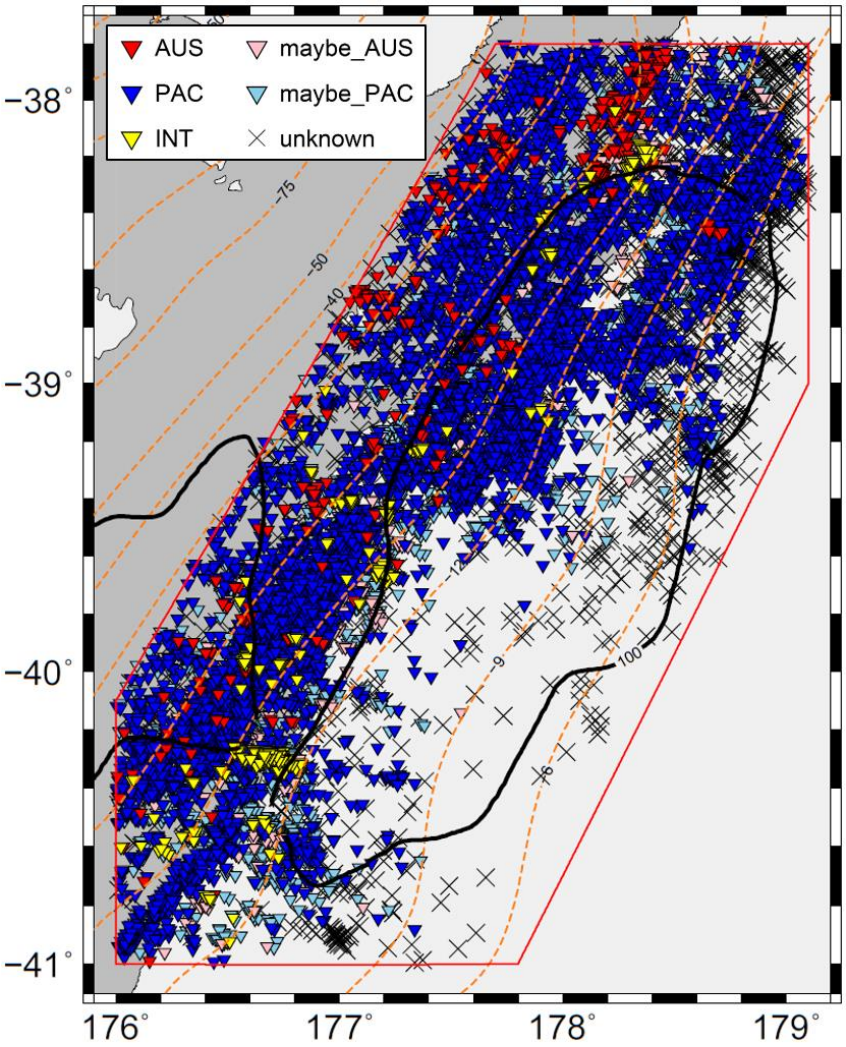

Figure 2.21. Results of classification after all steps processed. Red, blue, yellow, pink, and light blue inverted triangles are AUS, PAC, INT, maybe_AUS, and maybe_PAC earthquakes, respectively. Black crosses are unknown earthquakes. Black contours are cumulative SSE slips of 100 mm between 2002-2020 (Wallace, 2020; Woods, 2022). Orange dashed line contours are the iso-depth of the subducted Pacific plate surface (in kilometers) estimated by Williams et al. (2013). The red line indicates the study area.

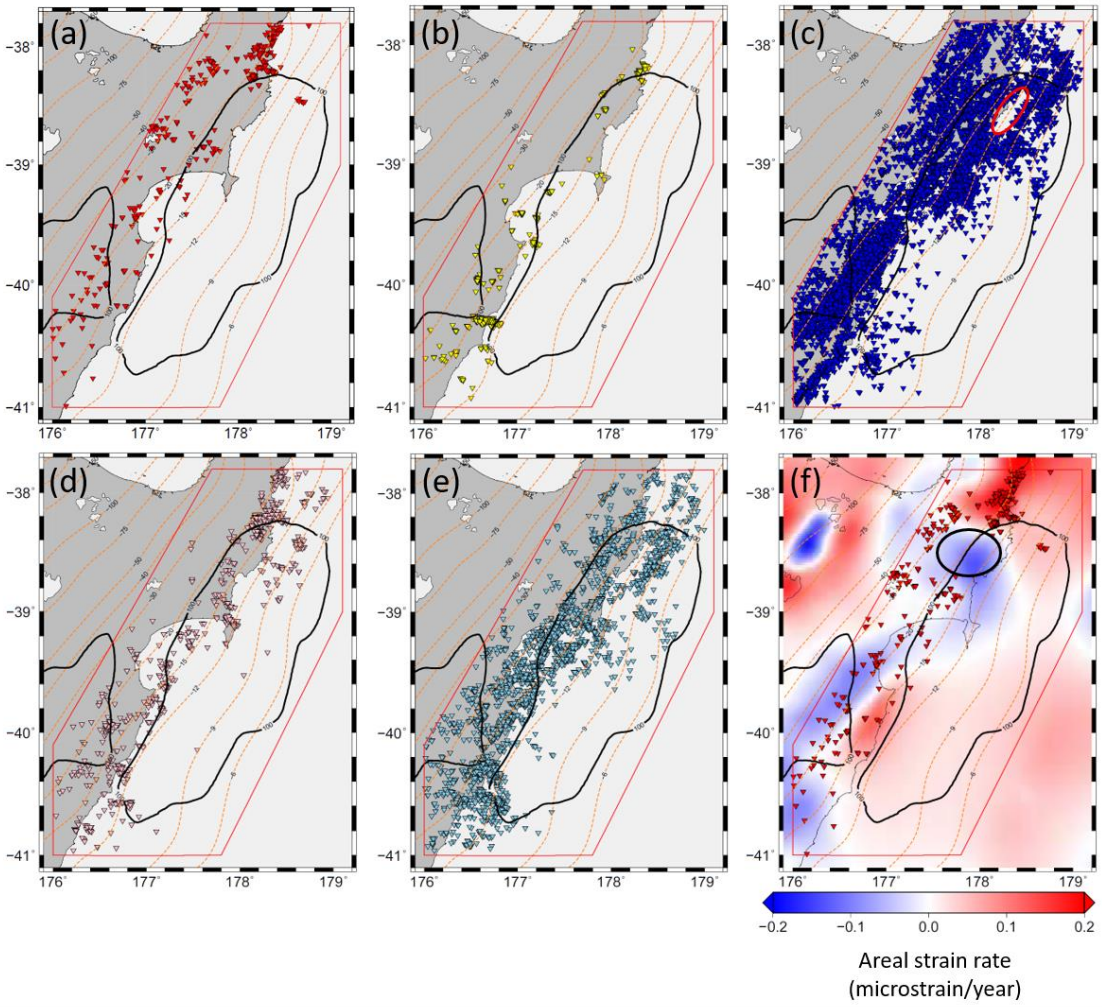

Figure 2.22. Distributions of classification for each type: (a) AUS. (b) INT. (c) PAC. A red circle indicates a gap of PAC earthquakes. (d) maybe_AUS. (e) maybe_PAC. (f) AUS with the areal strain rate, where positive and negative mean extension and contraction, respectively (Haines and Wallace, 2020). A black circle indicates a gap of AUS earthquakes. Black contours are cumulative SSE slips of 100 mm between 2002-2020 (Wallace, 2020; Woods, 2022). Orange dashed line contours are the iso-depth of the subducted Pacific plate surface (in kilometers) estimated by Williams et al. (2013). The red line indicates the study area.

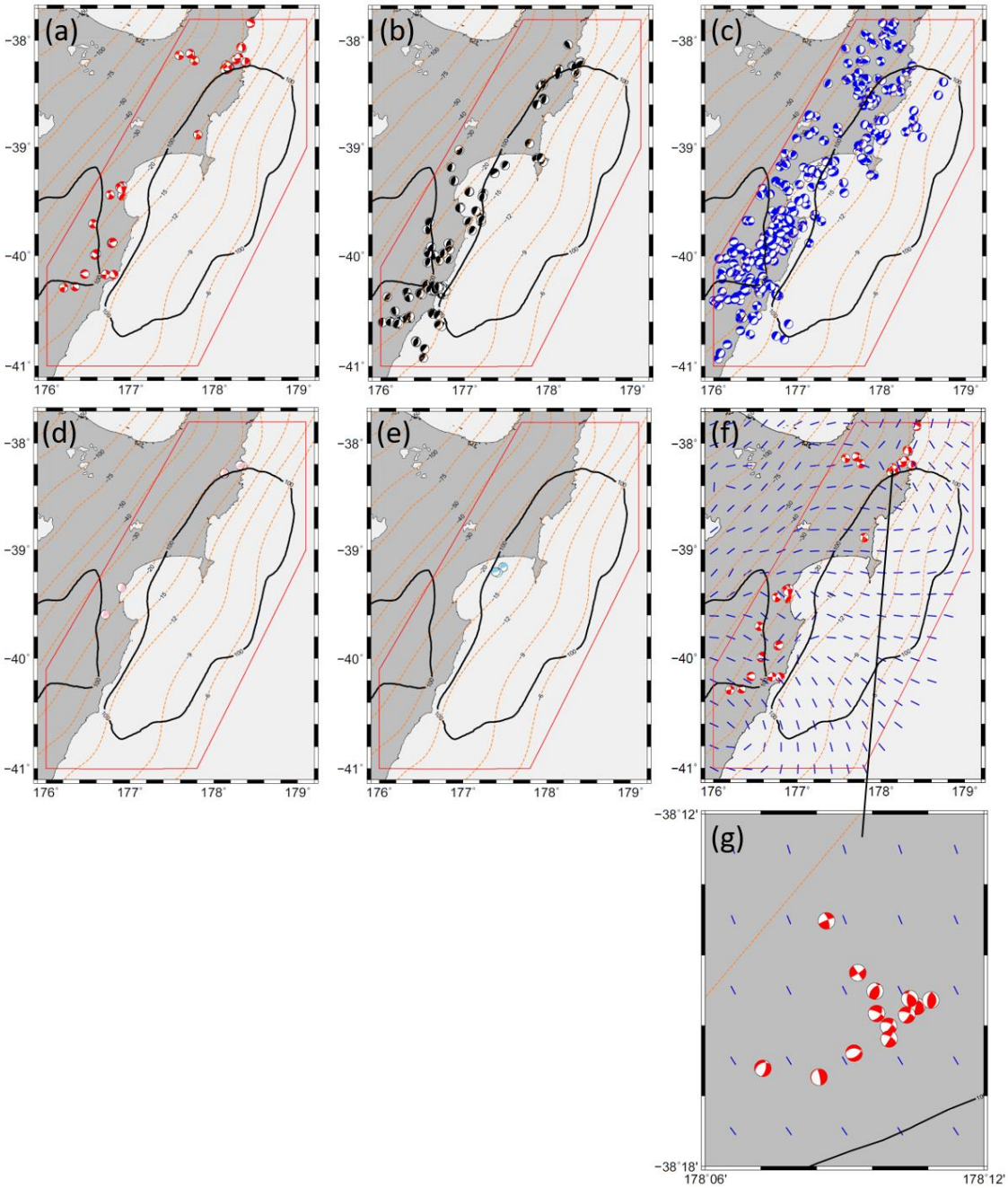

Figure 2.23. Focal mechanisms for each type of earthquake: (a) AUS, (b) INT, (c) PAC, (d) maybe_AUS, and (e) maybe_PAC. (f) AUS with the direction of maximum contraction (Haines and Wallace, 2020). (g) Enlarged one for the northern part of the study area. Black contours are cumulative SSE slips of 100 mm between 2002-2020 (Wallace, 2020; Woods, 2022). Orange dashed line contours are the iso-depth of the subducted Pacific plate surface (in kilometers) estimated by Williams et al. (2013). The red line indicates the study area.

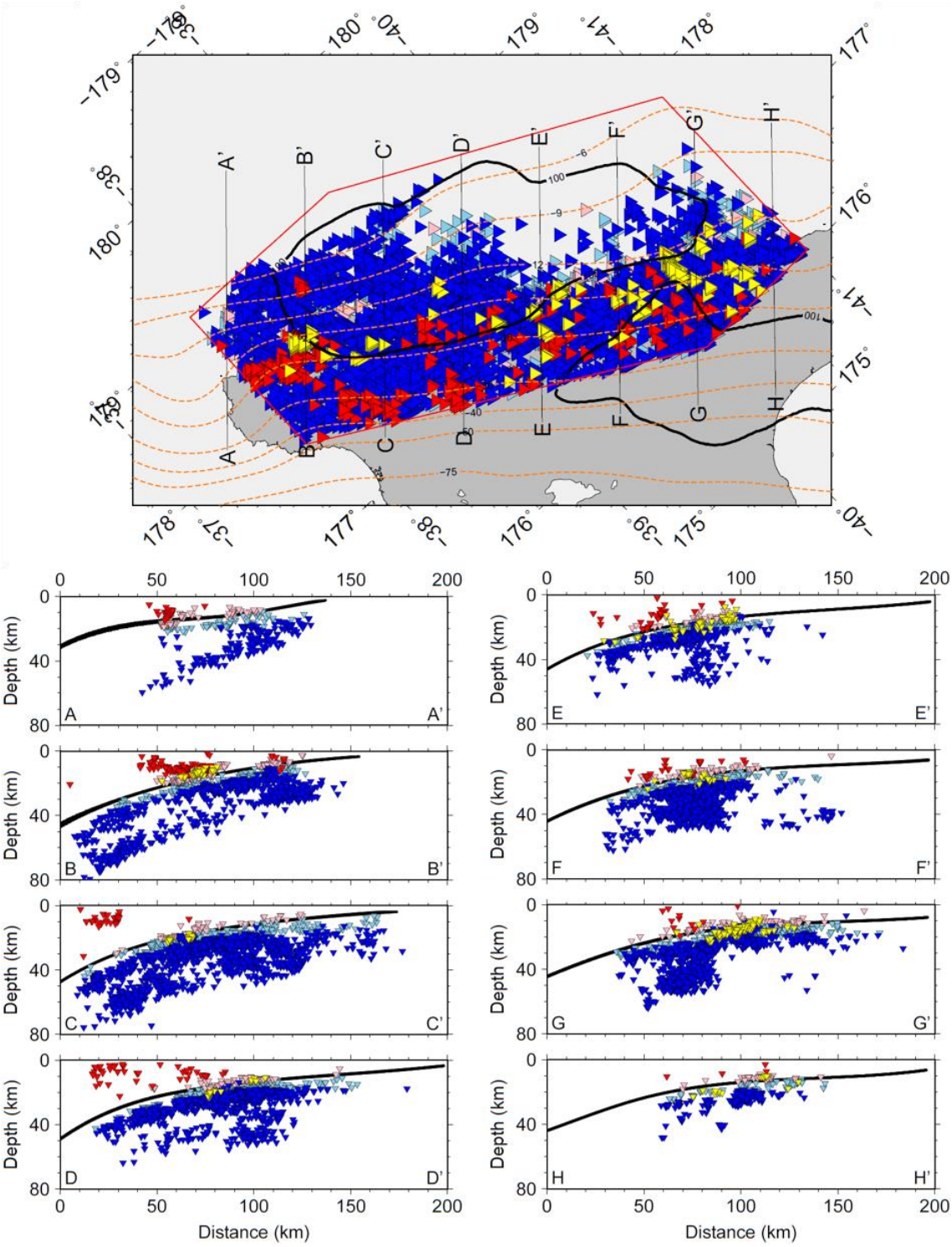

Figure 2.24. Cross section of classification results. Black contours are cumulative SSE slips of 100 mm between 2002-2020 (Wallace, 2020; Woods, 2022). Orange dashed line contours are the iso-depth of the subducted Pacific plate surface (in kilometers) estimated by Williams et al. (2013). The red line indicates the study area. Black curves in the bottom panels show the plate interface.

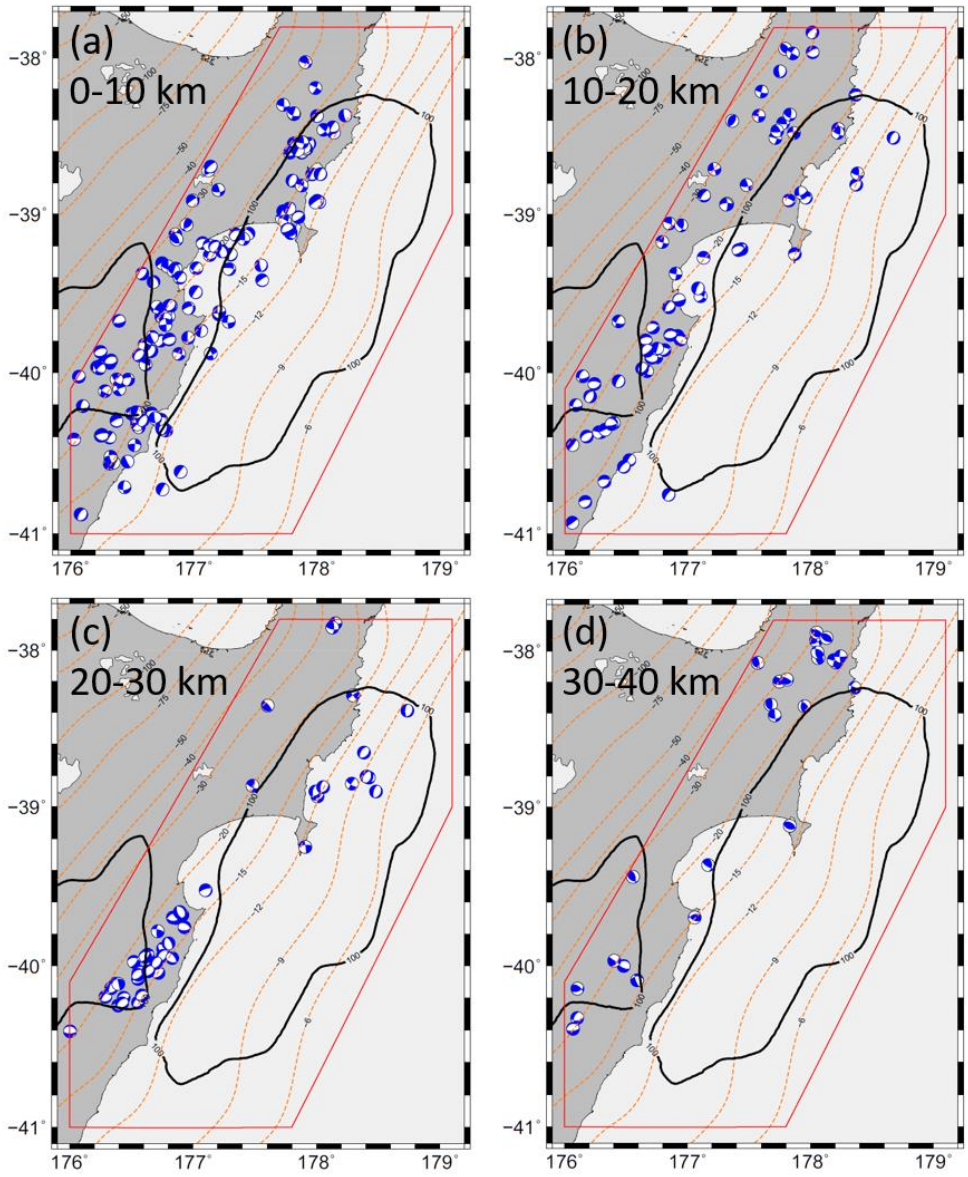

Figure 2.25. Focal mechanism of PAC earthquakes for each depth range relative to the plate interface. (a) 0-10 km, (b) 10-20 km, (c) 20-30 km, and (d) 30-40 km. Black contours are cumulative SSE slips of 100 mm between 2002-2020 (Wallace, 2020; Woods, 2022). Orange dashed line contours are the iso-depth of the subducted Pacific plate surface (in kilometers) estimated by Williams et al. (2013). The red line indicates the study area.

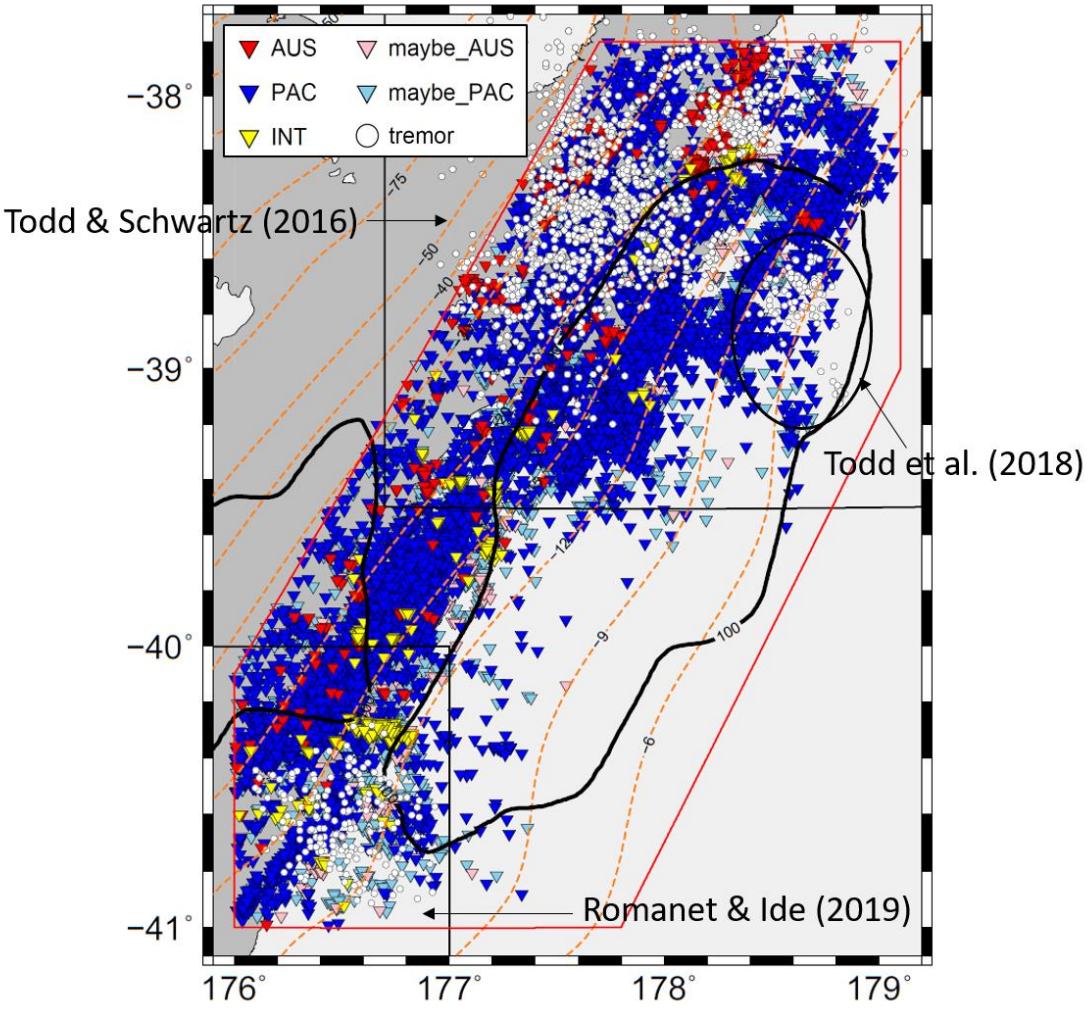

Figure 2.26. Distribution of classified earthquakes and tremors detected by previous studies (Romanet and Ide, 2019; Todd et al., 2018; Todd and Schwartz, 2016). Red, blue, yellow, pink, and light blue inverted triangles are AUS, PAC, INT, maybe_AUS, and maybe_PAC earthquakes. White dots are tremors. Black rectangles are the study areas of previous studies to detect tremors. Black contours are cumulative SSE slips of 100 mm between 2002-2020 (Wallace, 2020; Woods, 2022). Orange dashed line contours are the iso-depth of the subducted Pacific plate surface (in kilometers) estimated by Williams et al. (2013). The red line indicates the study area.

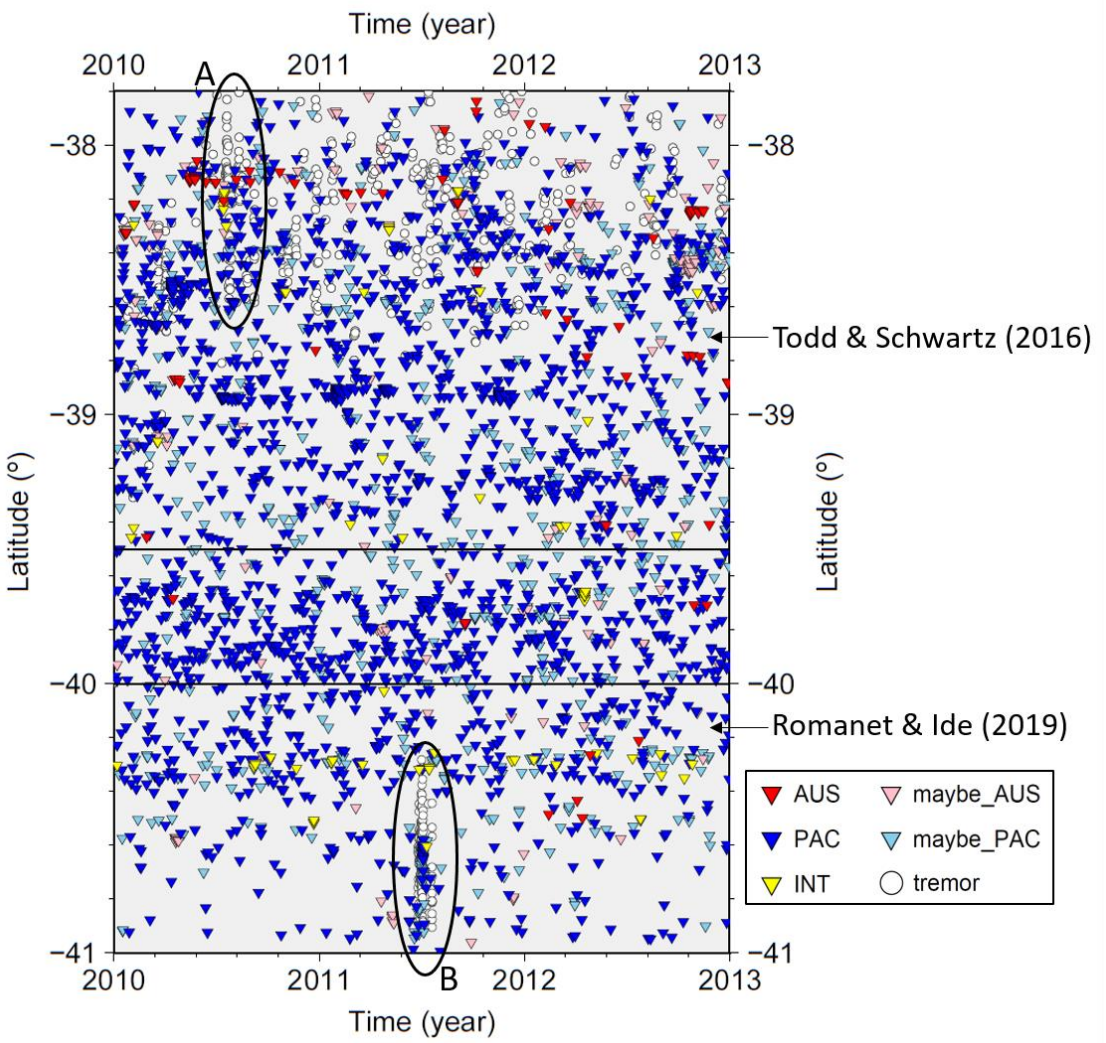

Figure 2.27. The time-space plot of classified earthquakes and tremors detected by previous studies (Romanet and Ide, 2019; Todd et al., 2018; Todd and Schwartz, 2016). The detection period of Romanet and Ide (2019) and Todd and Schwartz (2016) are 2005-2016 and 2010-2015, respectively. The detection period of Todd et al. (2018) is September 2014 - October 2014, which is out of range for this figure. Red, blue, yellow, pink, and light blue inverted triangles are AUS, PAC, INT, maybe_AUS, and maybe_PAC earthquakes. White dots are tremors. Black rectangles are the time-space areas of previous studies to detect tremors. Black ovals indicate the synchronous of earthquakes and tremors.

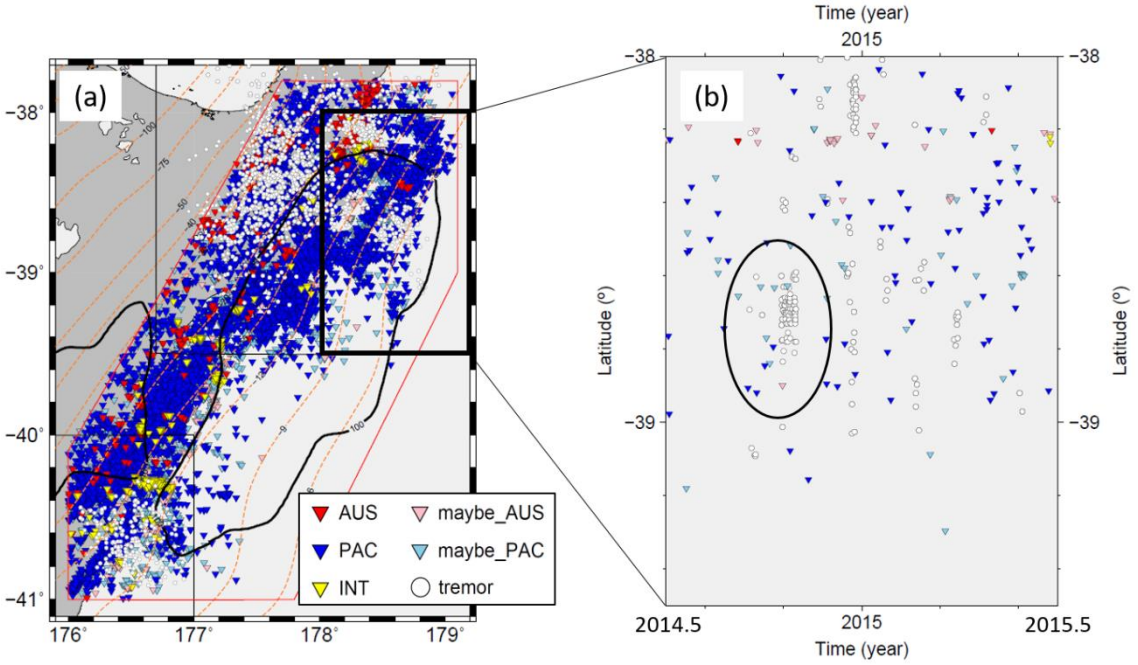

Figure 2.28. (a) Distribution of classified earthquakes and tremors detected by previous studies (same as Figure 2.26). (b) The time-space plot of classified earthquakes and tremors. Earthquakes and tremors in the black box in Figure 2.28a are plotted. The black oval indicates the activated tremors accompanied with the 2014 SSE.

Chapter 3.
Temporal relationship between SSEs and seismicity

3.1. Introduction

Earthquakes' spatiotemporal relation to SSEs has the potential to inform on the mechanism of both SSEs and triggered earthquakes. Delahaye et al. (2009) found an increase in seismicity rate on the subduction interface or just below it near the Mahia Peninsula, New Zealand, during the 2004 SSE for the first time. Nishikawa et al. (2021) showed that earthquake swarms occurred before and after SSEs in the northern and central Hikurangi margins. Yarce et al. (2023) showed that the seismicity of small earthquakes in the northern Hikurangi margin increased during the 2014 SSE. These previous studies did not focus on where these activated earthquakes were located relative to the plate interface. Since earthquakes in the northern and central Hikurangi margins were already classified (AUS, INT, PAC, maybe_AUS, and maybe_PAC) in this study, we can evaluate what types of earthquakes occurred and when they were activated relative to SSE occurrence. In this chapter, we describe how SSEs are detected, how many earthquakes are activated in each time period, and the spatial change of activation patterns.

3.2. Data and method to detect SSE signals

Since SSEs should cause eastward displacement in the upper plate in the study area, they can appear as transient eastward displacement in GNSS time series data (Wallace, 2020). This study considers transient eastward displacements obtained at GNSS stations (GNS Science, 2023d) as SSE signals. GeoNet's GNSS stations in the study area were used (Figure 3.1a). This study used the daily time-series solutions, which are converted into displacement (east, north, up) in millimeters with respect to the ITRF2008 framework (GeoNet, no date c). In the following analysis, we used eastward displacements relative to Auckland station (AUCK), located far from the study area (~250 km) and less affected by the Hikurangi SSEs. Transient eastward displacements caused by SSEs were recorded at all the stations (Figure 3.1b). This study detected the start time and end time of SSE and its duration by comparing the fits of a linear function and a three-part piecewise linear function (Figure 3.2). This is a concept of detecting SSE signals: a linear function might explain the obtained GNSS data well if no SSEs occurred, however, a three-part piecewise linear function might explain well if an SSE occurred. Details of the detection method are as follows (Figure 3.3).

1. Set t_0 as the date that the GNSS station started working.

2. Set the window length (L) as 90 days.
3. Cut GNSS data from t_0 with the window length of L.
4. Fit a linear function to the data and calculate Akaike's Information Criterion (Akaike, 1974) (AIC_{one}). AIC is introduced because we will later determine whether the data fits better to two functions with different numbers of model parameters: a linear function with two model parameters or a three-piecewise function with five model parameters.
5. Set the duration of SSEs (D) as 3 days.
6. Fit a three-piecewise function to data, with the second piece constrained to be length D, with its center at the center of the window of length L, and calculate Akaike's Information Criterion (AIC_{three}).
7. If $D < L$, $D = D + 1$ and go to step 6. If $D = L$, go to step 8.
8. Calculate the difference of AIC ($\Delta AIC = AIC_{three} - AIC_{one}$) using the minimum AIC_{three} in the loop of steps 6 and 7, and record it as ΔAIC^L.
9. Set L as 120 and 150 days and repeat steps 3-9, and then go to step 10.
10. Get ΔAIC^L and D^L by using L that minimizes $AIC_{three}{}^L$ (L = 90, 120, 150 days).
11. Add one day to t_0 ($t_0 = t_0 + 1$) and go to step 2 to get ΔAIC^L and D^L at the center of each time window unless the start time of the data window reaches the year 2021, the end of the study period.
12. When ΔAIC is minimum and less than or equal to -2 in a 30-day time window, the center of the time window is determined as the central date of the SSE occurrence. This procedure can prevent detecting SSE signals with a local minimum of ΔAIC in a short time window of 30 days. The corresponding D is determined as the duration of the SSE.

In this study, AIC was calculated as

$$\mathrm{AIC} = n\ln(2\pi) + n\ln\left(\frac{\sum_{i=1}^{n}(O_i - C_i)^2}{n}\right) + n + 2k, \qquad (3.1)$$

where n is the number of data, k is the number of model parameters (= 2 for a linear function and 5 for a three-piecewise function), O_i is the observed value for the i-th data point, and C_i is the calculated value for i-th data. Our method is similar to previous studies (Nishimura et al., 2013; Nishimura, 2014; Nishikawa et al., 2021) but differs in that this study is able to estimate the duration of SSE signals. We visually checked that detected SSE signals corresponded to transient eastward displacement (Figure 3.4). This method detected 2,296 SSE signals. Out of 2,296 SSE signals, 464 signals were detected by a single station, and 1,832 signals by multiple stations. Here, we defined an SSE signal detected by a single station as a signal detected at a station but not at other stations within 42 km, two times longer than the mean distance of inter-GNSS stations. 267 SSEs are included in 1,832 signals detected by multiple stations.

We calculated the means of SSE durations, intervals defined as the time between each SSE,

and displacements at every station (Figure 3.5). The mean of SSE durations was shorter near the SSE source (< 20 days) than that far from the SSE source (> 25 days) (Figure 3.5a). Intervals between SSEs were shorter in the northern Hikurangi margin (< 200 days) than in the central Hikurangi margin (> 300 days) (Figure 3.5b). Transient ground displacements caused by SSEs were the largest of ~6.8 mm within the 100 mm cumulative slow-slip area between 2002 and 2020 (area A in Figure 3.5c), indicating large signals were detected due to the short distance between the SSE sources and stations. GNSS stations just outside the area of 100 mm cumulative slow-slip detected SSE signals with a ground displacement of about 3.8 mm in the north of the study area (area B in Figure 3.5c) and 5.1 mm in the south of the study area (area C in Figure 3.5c), slightly larger than north (area A). SSE signals detected at GNSS stations along the coastline showed coherent signals at stations close to each other. The signals showed that the number of SSEs in the northern Hikurangi margin was larger than that in the central Hikurangi margin (Figure 3.6) as observed previously (e.g., Wallace, 2020). All SSEs detected by previous studies (Wallace and Beavan, 2010; Wallace et al., 2012; Wallace and Eberhart-Phillips, 2013; Wallace et al., 2016; Wallace et al., 2017; Woods, 2022) were also detected in this study. We note that this method detects SSE signals with a duration of shorter than 150 days, much shorter than deep long-term (1-2 years) Kapiti and Manawatu SSEs (Wallace, 2020), meaning that this method cannot detect such SSEs. The long-term deep Kaimanawa SSEs have durations longer than three months (Wallace and Eberhart-Phillips, 2013), and we confirmed that our method did not detect 2006 and 2008 Kaimanawa SSEs. Thus, detected GNSS signals were probably derived from shallow SSEs, not deep SSEs.

3.3. Removing earthquake sequences

We aimed to investigate the triggering relationship between earthquakes and SSEs. To ensure that we were not biased by inter-earthquake triggering, we removed earthquake sequences (swarms and mainshock-aftershock sequences) and retained only the earliest event in each sequence, as later events were likely to be more strongly affected by inter-earthquake triggering or postseismic creep caused by the earliest earthquake rather than SSE-related phenomena. We removed such sequences based on space-time distance (Zaliapin and Ben-Zion, 2013). Considering two quantitative metrics of the correlation between any two earthquakes, Gutenberg-Richter distribution (Gutenberg and Richter, 1941) and the fractal appearance of earthquake epicenters (Hirata, 1989), the distance between earthquake i and j (where event j follows event i) is defined as

$$\eta_{ij} = t_{ij}(r_{ij})^{d_f} 10^{-bm_i}, \tag{3.2}$$

where $t_{ij} = t_j - t_i$ (> 0) is the inter-occurrence time in years, r_{ij} is the spatial distance between the epicenters in kilometers, d_f is the fractal dimension of the earthquake hypocenter distribution, b is the b-value, and m_i is the magnitude of earthquake i. The b-value was estimated as 1.41±0.02 for M≥2.8 earthquakes (Figure 3.7a) by the method of maximum likelihood (Utsu, 1965):

$$b = \frac{\log_{10} e}{\bar{M} - M_c} \ , \tag{3.3}$$

where $\bar{M}$ is the mean of earthquake magnitude, and M_c is the cutoff magnitude (= 2.8). Using earthquakes magnitude range between 2.8 and 5.6, the goodness-of-fit (e.g., Liu et al., 2017) estimated the b-value as 1.29, which is slightly smaller than that estimated from maximum likelihood (1.41), however, such b-value dependence on estimation method had little effect on results (see section 3.4). The fractal dimension of the earthquake hypocenter distribution (d_f) was estimated following the method of Hirata (1989), which uses the correlation integral. The correlation integral $C(r)$, defined for the epicenter distribution, follows

$$C(r) = \frac{2}{N(N-1)} N(R < r), \tag{3.4}$$

where N is the number of earthquakes in the catalog, and $N(R < r)$ is the number of earthquake pairs with a smaller distance than r. If the epicenter distribution has a fractal structure, $C(r)$ follows

$$C(r) \sim r^{d_f}. \tag{3.5}$$

Thus d_f can be estimated as the slope of $C(r)$ - r if it is plotted on a log-log scale. In this study, d_f was 1.71±0.03 (Figure 3.7b). The η_{ij} is divided into a time component and a space component as

$$T_{ij} = t_{ij} 10^{-qbm_i}; \ R_{ij} = \left(r_{ij}\right)^{d_f} 10^{-(1-q)bm_i}, \tag{3.6}$$

where q (= 0.5) determines the effect of the magnitude on T_{ij} and R_{ij}, which is independent of η_{ij}, and the η_{ij} is represented as $\eta_{ij} = T_{ij} R_{ij}$. Of all the earthquakes preceding the event j, the earthquake i^* that minimizes the η_{ij} is called the nearest-neighbor of event j. Hereafter, η_{ij}, R_{ij}, and T_{ij} of nearest-neighbor are represented as η, R, and T, respectively. Larger η implies that the event pair possibly occurred independently, and smaller η means that the event pair might be a part of foreshock-mainshock-aftershock sequences. Thus, such sequences can be removed from the earthquake catalog by removing earthquakes with small η. The T - R plot shows possibly a cluster and an outlier group (Figure 3.7c). We visually determined the threshold value of η as -6.5 that would split the cluster and the outlier (Figures 3.7c, d). We recognized the earthquakes of which η was smaller than -6.5 as a member of foreshock-mainshock-aftershock sequences and removed them from the catalog. Of all 16,932 earthquakes, 3,972 earthquakes (23.5%) were removed. Figure 3.8 shows the distribution of earthquakes after removing the sequences.

3.4. The number of earthquakes relative to SSE occurrences

In the northern Hikurangi margin, we can see that an AUS earthquake occurred just after an SSE signal appeared (Figure 3.9b), some INT, maybe_AUS, and maybe_PAC earthquakes occurred during SSEs (Figure 3.9b), and some PAC earthquakes occurred just before an SSE signal disappeared (Figure 3.9d). We paired earthquakes to the closest GNSS station. For temporal analysis, we required

the distance between the epicenter and the paired GNSS station to be less than 50 km. To see and evaluate the activated period for each earthquake type more clearly, we stacked events around each detected SSE and counted the number of earthquakes relative to SSE timing.

To evaluate and visualize the number of earthquakes in each time period, the following steps were performed (Figure 3.10):

1. For each earthquake, we determined the closest SSE signal in time from the paired GNSS station. If the earthquake occurred before (after) the SSE started (ended), we calculated the lag time relative to the start (end) signal and counted the number of earthquakes in each 10-day time bin. We counted the number of events if the earthquake occurred during the SSE signal. Histograms of lag times were obtained for each SSE signal in this step (Figure 3.10b).
2. Since the duration (D) of SSEs is not always ten days and differs from event to event, it is not fair to compare the number of earthquakes before (or after) SSEs with those during SSEs. Thus, the number of earthquakes during SSEs was multiplied by $10/D$ so that it was equivalent to a duration of 10 days. This step obtained modified histograms of lag times for each SSE signal (Figure 3.10c).
3. All of the modified histograms in step 2 were stacked to obtain the cumulative number of earthquakes in each 10-day time bin (Figure 3.10d).
4. We created 300 catalogs with the hypocenter location unchanged but with only the origin time randomly changed from 2004 to 2020 according to the uniformly random distribution. For each catalog, we calculated the lag time with SSEs by steps 1 to 3, made a histogram, and obtained the mean and standard deviation for each time bin. This mean value and standard deviation represent the expected number of earthquakes in each time period assuming random occurrence of earthquakes (Figure 3.10e).
5. For clarity, the mean estimated in step 4 was subtracted from the total number of earthquakes in step 3 for each time bin. The number of earthquakes relative to random occurrence in each 10-day time bin (relative histogram) was obtained in this step (Figure 3.10f).
6. Time periods (bins) were shaded if the relative number of earthquakes was smaller than the standard deviation of random occurrence. Since histograms sometimes showed oscillating patterns possibly due to the effect of short time bins (10 days), the time periods (bins) were also shaded if the value obtained by adding the values of adjacent bin values was less than the standard deviation of random occurrence (Figure 3.10g).

We conducted these evaluation and visualization procedures for each earthquake type and each region.

Activation pattern, or activated period and earthquake type, varied from region to region. In and around the northern shallow SSE source (the northern Hikurangi margin; Figure 3.11), AUS earthquakes were somewhat activated just after SSEs ended (0-10 days), maybe_AUS, INT, and maybe_PAC earthquakes were activated during SSEs, and PAC earthquakes were activated just before

SSEs started (0-20 days before). Using only earthquakes occurring 0-10 days before SSEs, during SSEs, and 0-10 days after SSEs, AUS events occurred most frequently (~53%) after SSEs, maybe_AUS events (~51%), INT events (~76%), and maybe_PAC events (~40%) during SSEs (Table 3.1). Using only earthquakes occurring 0-20 days before SSEs, during SSEs, and 0-20 days after SSEs, PAC events occurred most frequently (~38%) before SSEs (Table 3.1).

In and around the southern shallow SSE source (the central Hikurangi margin; Figure 3.12), maybe_AUS earthquakes were activated just after SSEs ended (0-10 days), maybe_PAC earthquakes were activated during SSEs and just after SSEs ended (0-10 days). PAC earthquakes were activated 30-40 days after SSEs ended and 90-100 days before SSEs started, which might not be related to SSEs due to a large lag time. We did not evaluate AUS earthquakes for their activated period due to the small number of data. When considering only earthquakes that occurred just around SSE occurrence in time, maybe_AUS events occurred most frequently (~64%) after SSEs and maybe_PAC events (~40%) after SSEs (Table 3.1).

Other regions also showed different activation patterns (Figures 3.13-3.17), and many of the activated periods had large lag times relative to SSE signals, indicating that they might not be related to SSEs as much as the northern and central Hikurangi margins.

We evaluated how much of the SSE signals were accompanied with characteristic seismicity. In the northern Hikurangi margin, ~2% of SSE signals were accompanied with AUS events 0-10 days after SSEs, ~10% with maybe_AUS events during SSEs, ~9% with INT events during SSEs, ~17% with maybe_PAC events during SSEs, and ~25% with PAC events 0-20 days before SSEs. In the central Hikurangi margin, ~5% of SSE signals were accompanied with maybe_AUS events 0-10 days after SSEs and ~11% with maybe_PAC events 0-10 days after SSEs. These results indicate that not all SSEs were accompanied with characteristic seismicity. We will discuss it in section 4.5.

Detected SSE signals are characterized by their transient ground displacement and duration. We computed the median of detected ground displacements and durations for each GNSS station and re-calculated the activation patterns using the SSE signal with the ground displacement greater (smaller) than the median and the duration greater (smaller) than the median. SSE signals with ground displacement greater than the median were accompanied with the characteristic activation patterns (Figures 3.18, 3.19), as calculated using all SSE signals (Figures 3.11, 3.12). That is, in the northern Hikurangi margin, AUS events were activated 0-10 days after SSEs, maybe_AUS, INT, and maybe_PAC events were activated during SSEs, and PAC events were activated 0-20 days before SSEs; and in the central Hikurangi margin, maybe_AUS events were activated 0-10 days after SSEs, and maybe_PAC events were activated during and 0-10 days after SSEs. However, the activation pattern using SSE signals with ground displacement smaller than the median did not show such a characteristic pattern (Figures 3.20, 3.21). All types of events were activated 20-100 days before or 20-100 days after SSEs in the northern and central Hikurangi margin for small ground displacement

signals. This indicates that large ground displacement signals, or large SSEs, were accompanied with more active seismicity. Another possibility is that the detected signals with small ground displacements are unrelated to SSEs. The duration seemed to affect the observed activation patterns less than the ground displacement (Figures 3.22-3.25).

Figures 3.26-3.30 show the distribution of each type of earthquake every ten days before and after SSEs and during SSEs, and Figures 3.31-3.35 show their focal mechanisms. Yarce et al. (2023) detected small earthquakes in the northern Hikurangi margin from 1 September to 31 October 2014 and found that their rate increased during the 2014 SSE, which is consistent with this study. However, previous studies did not reveal what types of earthquakes (AUS, INT, or PAC) were activated relative to SSEs and how the activation pattern spatially changed. This is the first study to precisely analyze activation patterns and their spatial difference in the northern and central Hikurangi margins.

3.5. Parameter dependence

We examined how the activation patterns in the northern and central Hikurangi margin change with hyperparameters. Here eight parameters were considered: (1) the threshold of Kagan angle to classify INT, (2) the range of bandpass filtering to calculate waveform cross-correlation, (3) the threshold of cross-correlation coefficient (CC), (4) the threshold of GNSS-epicenter distance, (5) b-value for declustering, (6) the fractal dimension (d_f) for declustering, (7) the threshold of η for declustering, and (8) random SSEs and fixed seismicity. Irrespective of hyperparameter choice, PAC events were activated before SSEs, maybe_PAC, INT, and maybe_AUS events were activated during SSEs, and AUS events were activated after SSEs in the northern Hikurangi margin, and maybe_PAC and maybe_AUS events were activated during or after SSEs in the central Hikurangi margin (see Appendix A). This indicates that our results obtained in section 3.4 did not largely depend on the hyperparameters we adopted and that such activation patterns were robust.

Table 3.1. The ratio of earthquakes that occurred during pre-SSE, co-SSE, and post-SSE periods for each earthquake type. The pre-SSE (post-SSE) period is defined as 0-20 days before (after) SSEs for PAC events in the northern Hikurangi margin and 0-10 days before (after) SSEs for other events.

		Pre-SSE	Co-SSE	Post-SSE
Northern Hikurangi margin	AUS	13%	34%	53%
	maybe_AUS	24%	51%	24%
	INT	8%	76%	16%
	maybe_PAC	31%	40%	29%
	PAC	38%	31%	32%
Central Hikurangi margin	AUS	0%	100%	0%
	maybe_AUS	0%	36%	64%
	INT	27%	59%	14%
	maybe_PAC	25%	35%	40%
	PAC	35%	36%	29%

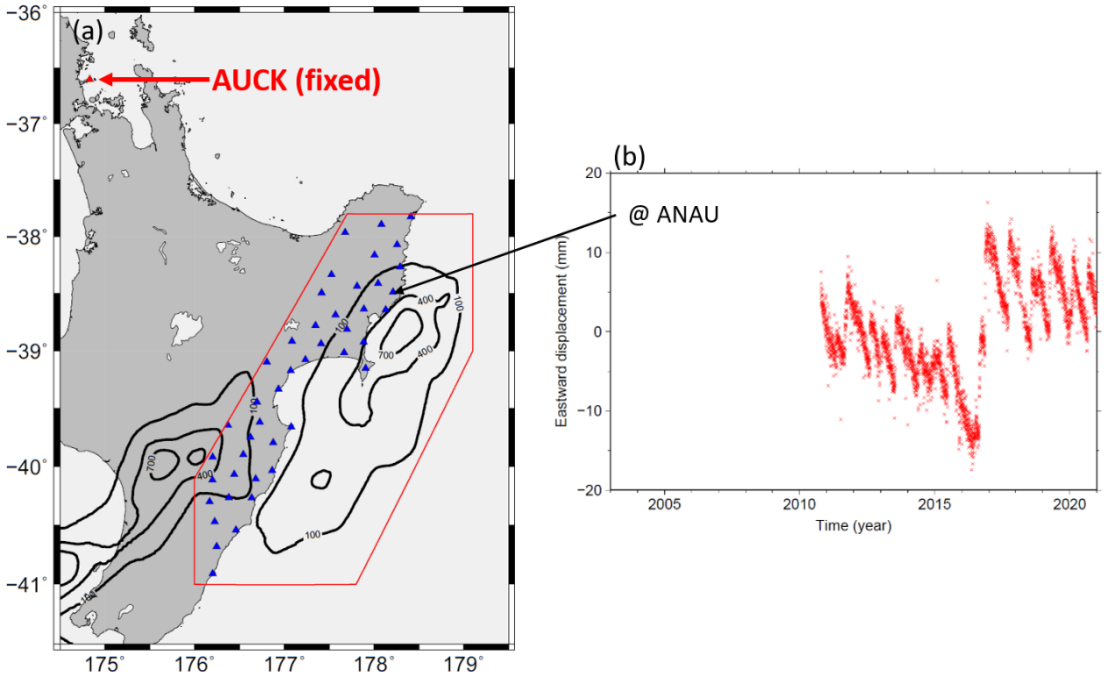

Figure 3.1. GNSS stations used in this study. (a) A red triangle is the fixed AUCK station. Blue triangles are GNSS stations used to detect SSE signals. Red lines indicate the study area. Black contours are cumulative SSE slip of 100 mm, 400 mm, and 700 mm between 2002-2020 (Wallace, 2020; Woods, 2022). (b) An example of eastward displacement recorded at ANAU.

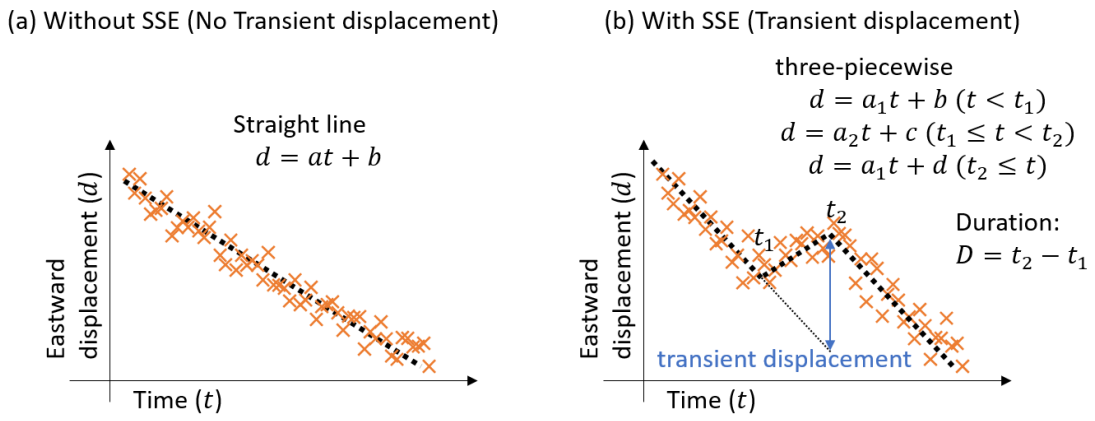

Figure 3.2. Concept of SSE detection. (a) Case of without an SSE. Red crosses are daily data of eastward displacement and fitted well by a straight line. (b) Case of with an SSE. Red crosses are daily data of eastward displacement and fitted well by a three-piecewise line. The duration (D) of SSE at the station is defined by the time between the two inflection points. A blue arrow indicates the ground displacement caused by an SSE at the station.

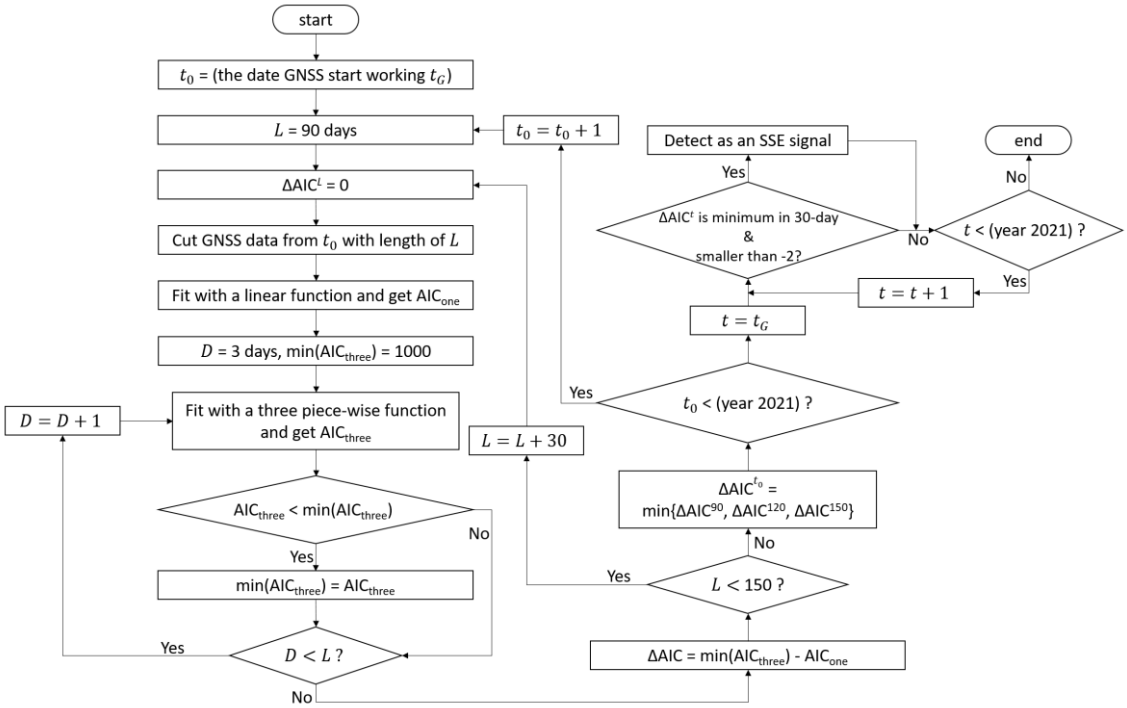

Figure 3.3. A flow chart for detecting SSE signals at a GNSS station.

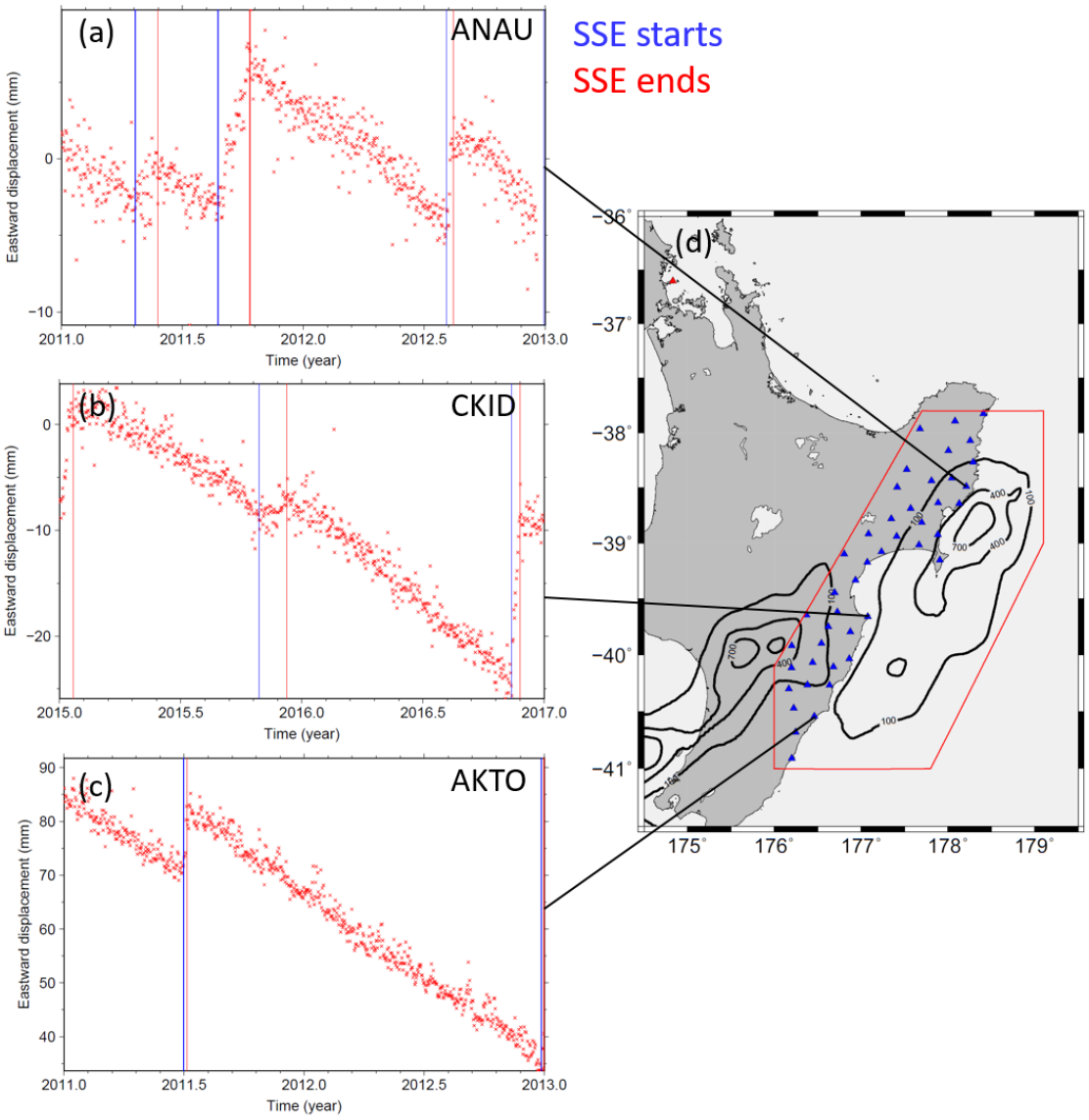

Figure 3.4. Examples of detected SSE signals. (a) Detected at station ANAU. (b) Detected at station CKID. (c) Detected at station AKTO. Blue and red vertical lines indicate SSEs' start and end timing. (d) Distribution of GNSS stations. Black contours are cumulative SSE slips of 100 mm, 400 mm, and 700mm between 2002-2020 (Wallace, 2020; Woods, 2022). The red line indicates the study area.

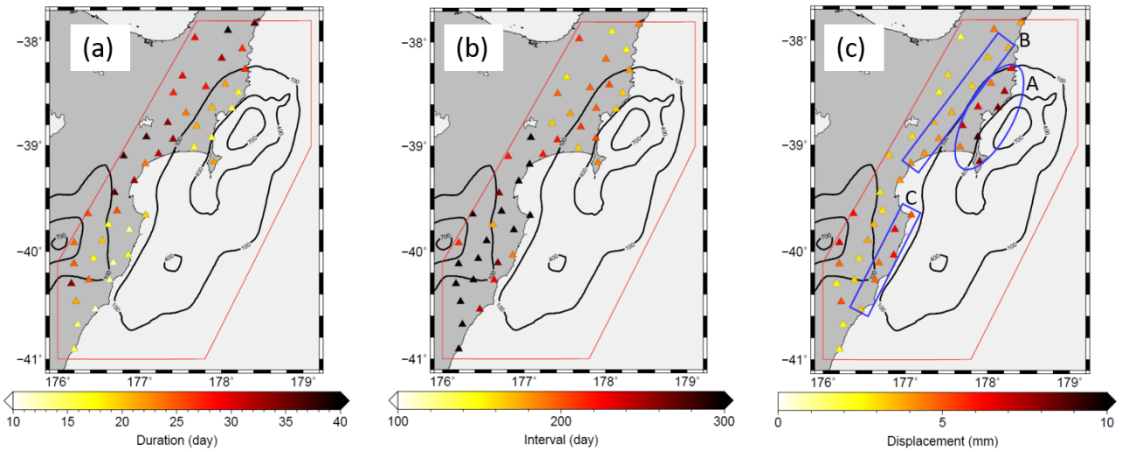

Figure 3.5. Parameters of SSEs detected at each station. (a) The mean of SSE durations. (b) The mean of SSE intervals. (c) The mean of transient ground displacements. The blue circle and rectangles indicate areas A, B, and C. Black contours are cumulative SSE slips of 100 mm, 400 mm, and 700mm between 2002-2020 (Wallace, 2020; Woods, 2022).

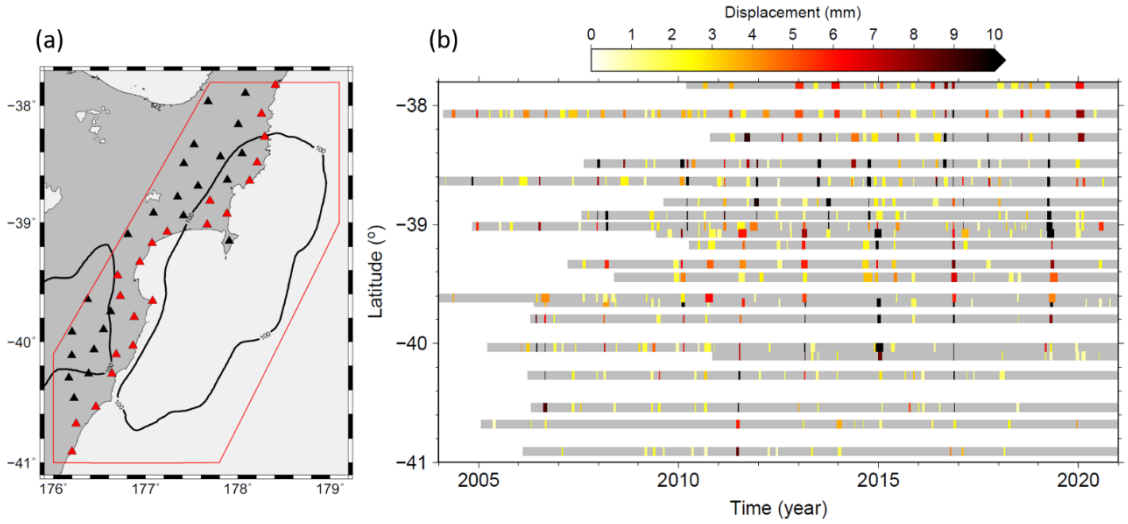

Figure 3.6. Detected SSE signals along the coastline. (a) GNSS stations used for this analysis. Black contours are cumulative SSE slips of 100 mm between 2002-2020 (Wallace, 2020; Woods, 2022). The red line indicates the study area. (b) SSE signals at each station. The length of the bars represents the duration of SSE signals. White shade represents the location where stations do not exist or the period when the GNSS stations are not operated.

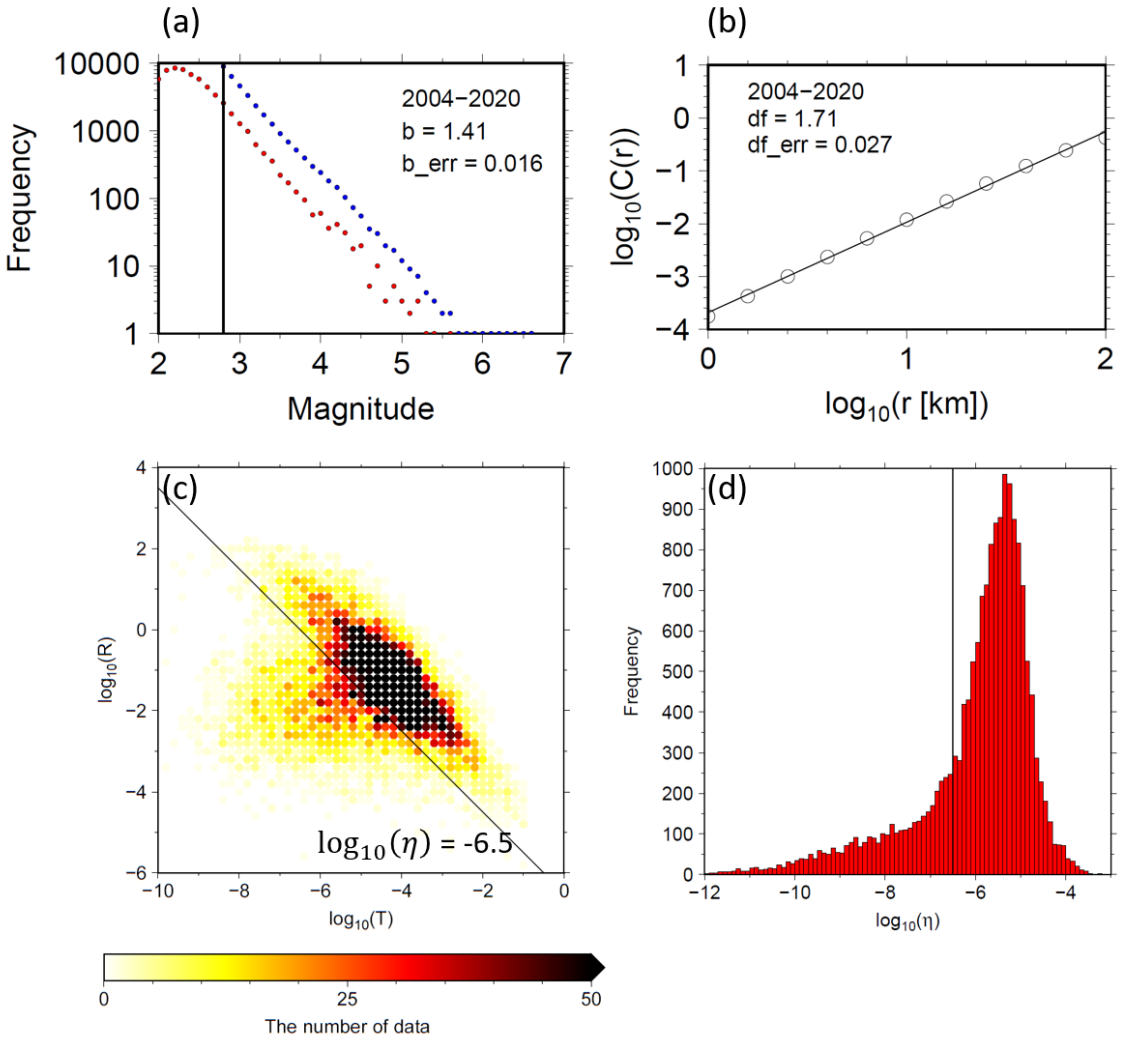

Figure 3.7. Parameters related to space-time distance. (a) The number of earthquakes in the magnitude bin of 0.1 (red dots) and a cumulative number of earthquakes (blue dots). The black vertical line is the cutoff magnitude (M_c) of 2.8. The b-value and its uncertainty are 1.41 and 0.02, respectively. (b) The $\log_{10} C(r)$ - $\log_{10} r$ plot. The slope represents the dimension of the earthquake hypocenter distribution (d_f). The d_f and its uncertainty are 1.71 and 0.03, respectively. (c) The relationship between $\log_{10} T$ and $\log_{10} R$. The color represents the number of data in 0.2×0.2 grid points. The black line represents a constant $\log_{10} \eta$ of -6.5. (d) Histogram of $\log_{10} \eta$. A black vertical line is -6.5.

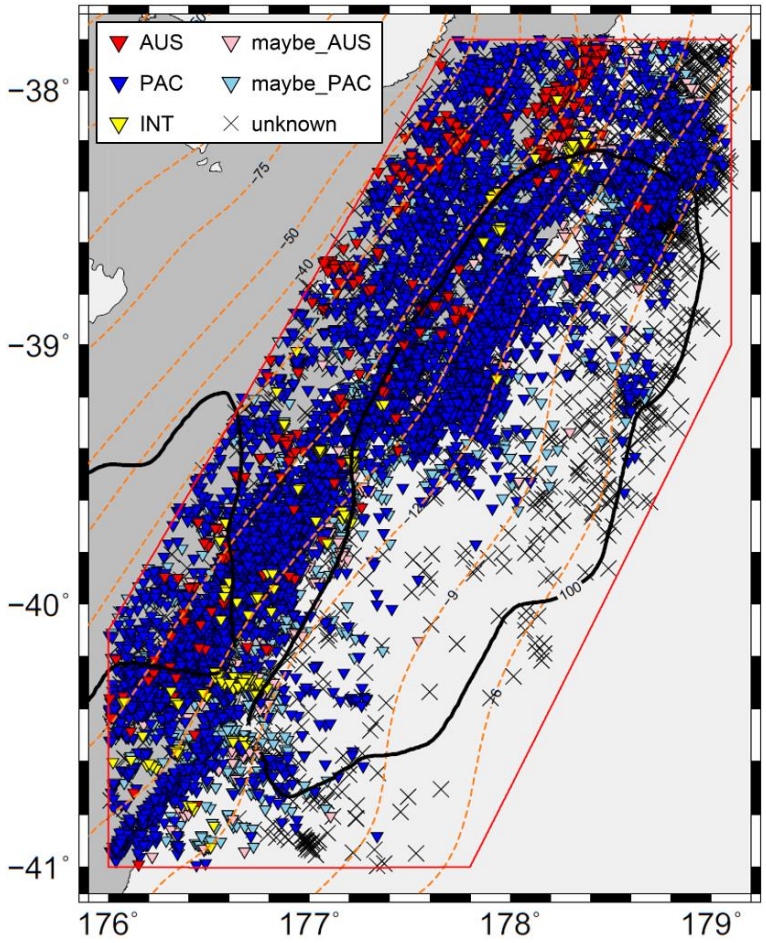

Figure 3.8. Distribution of earthquake after removing the sequences. Red, blue, pink, and light blue inverted triangles are AUS, PAC, maybe_AUS, and maybe_PAC earthquakes. Black crosses are unknown earthquakes. Black contours are cumulative SSE slips of 100 mm between 2002-2020 (Wallace, 2020; Woods, 2022). Orange dashed line contours are the iso-depth of the subducted Pacific plate surface (in kilometers) estimated by Williams et al. (2013). The red line indicates the study area.

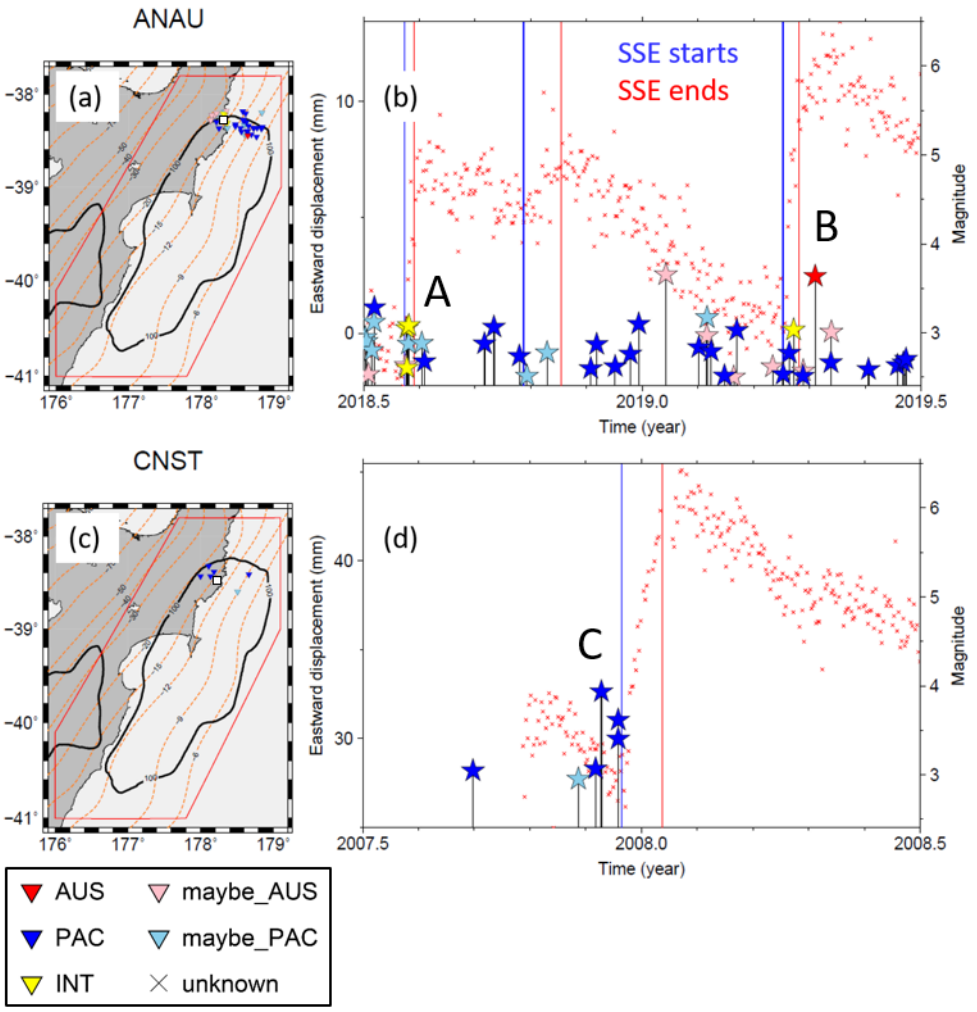

Figure 3.9. Distribution of earthquake epicenters, paired GNSS stations, and occurrence timing of earthquakes and SSE signals. Red, yellow, blue, pink, and light blue inverted triangles are AUS, INT, PAC, maybe_AUS, and maybe_PAC earthquakes. (a) GNSS station ANAU and paired earthquakes that occurred between 2018.5 and 2019.5. The white square is the GNSS station. Black contours are cumulative SSE slips of 100 mm between 2002-2020 (Wallace, 2020; Woods, 2022). Orange dashed line contours are the iso-depth of the subducted Pacific plate surface (in kilometers) estimated by Williams et al. (2013). The red line indicates the study area. (b) Occurrence timing of SSEs and earthquakes in Figure 3.9a. Red crosses are eastward GNSS displacement. Blue and red vertical lines are estimated timing when SSEs started and ended. Stars are earthquakes of which color is the same as in Figure 3.9a. INT and maybe_PAC events were active during SSE A, and one AUS event occurred just after SSE B. (c), (d) Same for Figure 3.9a, b but for the station CNST and period between 2007.5 and 2008.5. PAC events were active before SSE C.

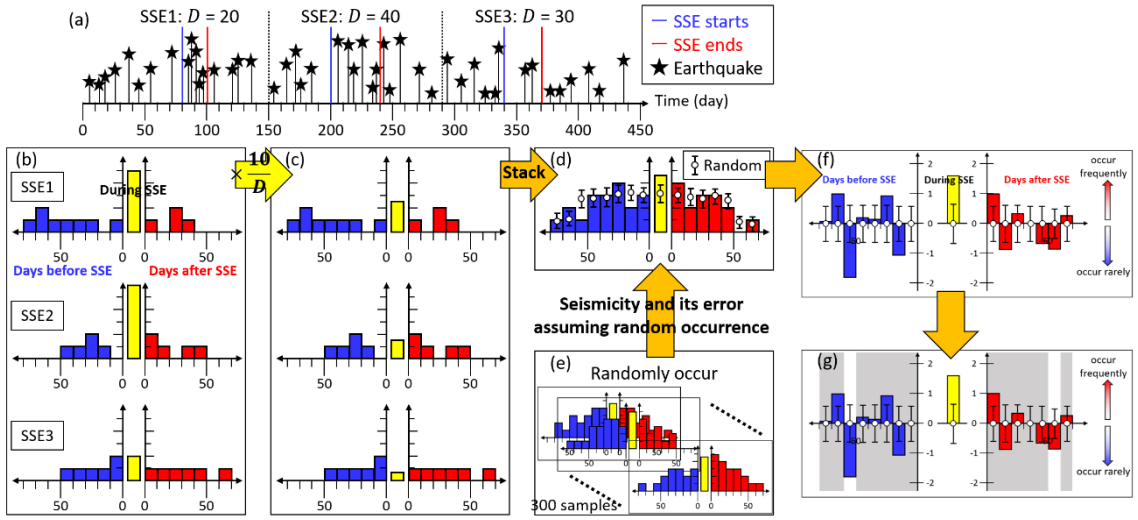

Figure 3.10. An explanation of how to count the number of earthquakes. (a) Synthetic occurrence timing of SSEs and earthquakes. Blue and red lines represent the timing when SSEs start and end, respectively. Black stars are earthquakes. Three SSEs are set and have different durations (D). (b) The cumulative number of earthquakes relative to SSE occurrence timing for SSE1-3. Blue bars and red bars are the numbers of earthquakes in each 10-day bin before SSEs start and after SSE end, respectively. Yellow bars are the number of earthquakes during SSEs. (c) The cumulative number of earthquakes after normalization. Yellow bars in Figure 3.10b are multiplied by $10/D$ so that they can be compared with blue and red bars. (d) The stacked number of earthquakes. Color bars represent the stacked number of earthquakes for SSE1-3. White dots are the number of earthquakes under the assumption of random occurrence of earthquakes. (e) The stacked number of earthquakes if the random occurrence of earthquakes is assumed. The mean and standard deviation are calculated from 300 samples and plotted in Figure 3.10d. (f) Relative numbers of earthquakes (color bars minus white dots). Positively (negatively) large bars mean that earthquakes occur more frequently (rarely) than random occurrences. (g) The relative number of earthquakes with shaded areas where we do not focus on due to the large uncertainty of random sampling.

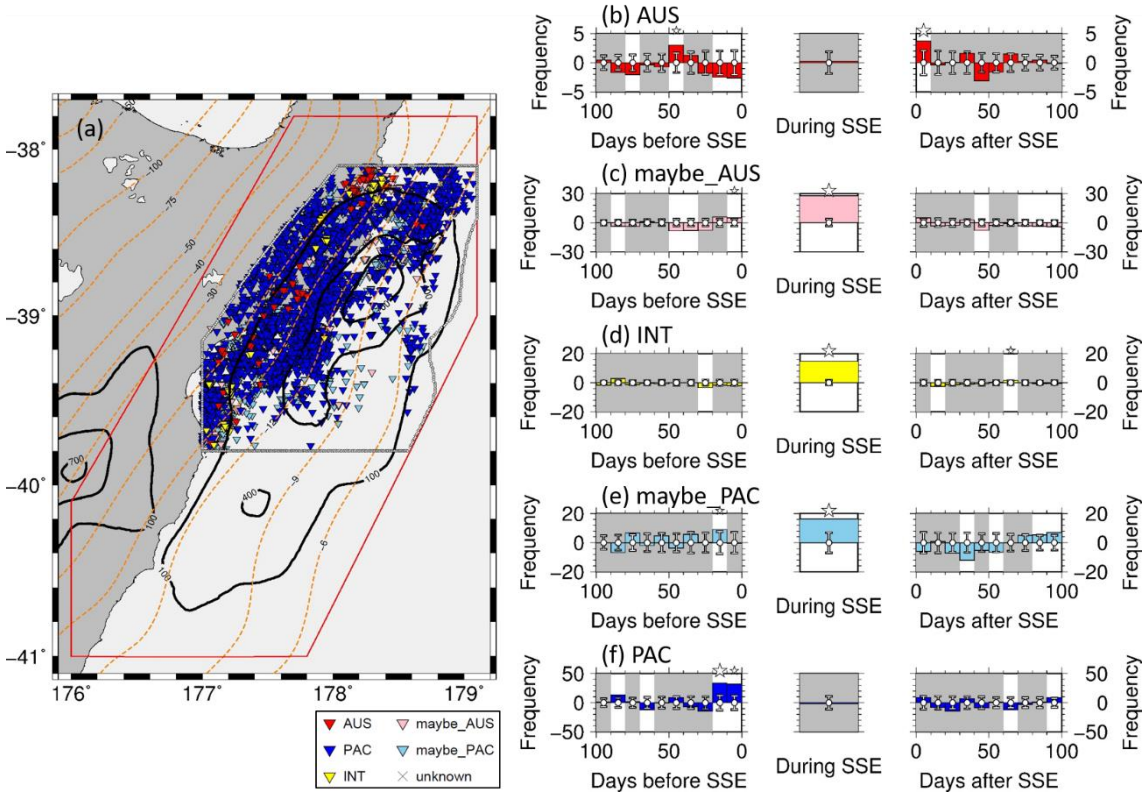

Figure 3.11. The number of earthquakes relative to that under the assumption of random occurrence. Earthquakes in and around the SSE source in the northern Hikurangi margin. (a) Epicenters of used earthquakes. Red, yellow, blue, pink, and light blue inverted triangles are AUS, INT, PAC, maybe_AUS, and maybe_PAC earthquakes. Black contours are cumulative SSE slips of 100 mm, 300 mm, and 700 mm between 2002-2020 (Wallace, 2020; Woods, 2022). Orange dashed line contours are the iso-depth of the subducted Pacific plate surface (in kilometers) estimated by Williams et al. (2013). The red line indicates the study area. (b), (c), (d), (e), (f) The number of observed AUS, maybe_AUS, INT, maybe_PAC, and PAC earthquakes relative to random occurrence in each 10-day, respectively (color bar). The number during SSEs is normalized. The white dot and error bar are the expected number of earthquakes and its error for random seismicity, respectively. Gray and white backgrounds indicate insignificant and significant time period, respectively. Big and small white stars on the top of each panel indicate the time period when earthquakes are most and the second most activated, respectively, among significant time periods.

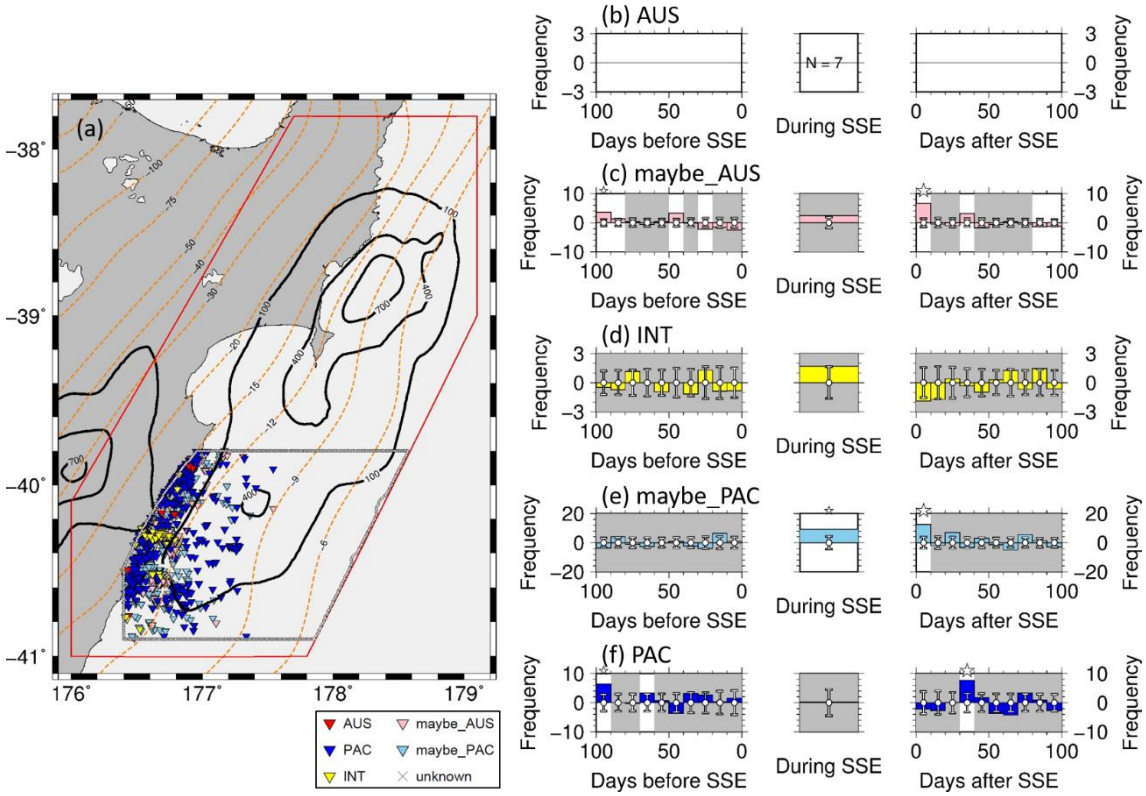

Figure 3.12. Same as Figure 3.11 but for earthquakes in and around the SSE source in the central Hikurangi margin. Histograms are not shown if the number of earthquakes is less than 20.

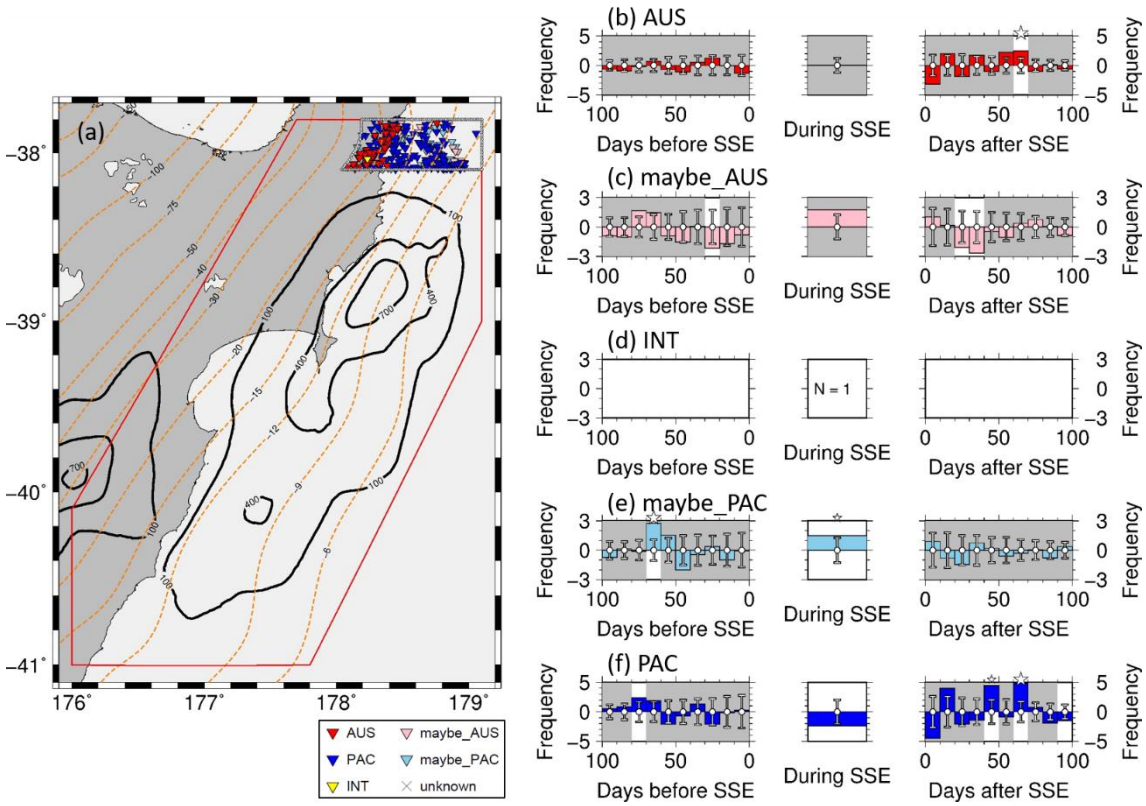

Figure 3.13. Same as Figure 3.11 but for earthquakes north of the SSE source in the northern Hikurangi margin.

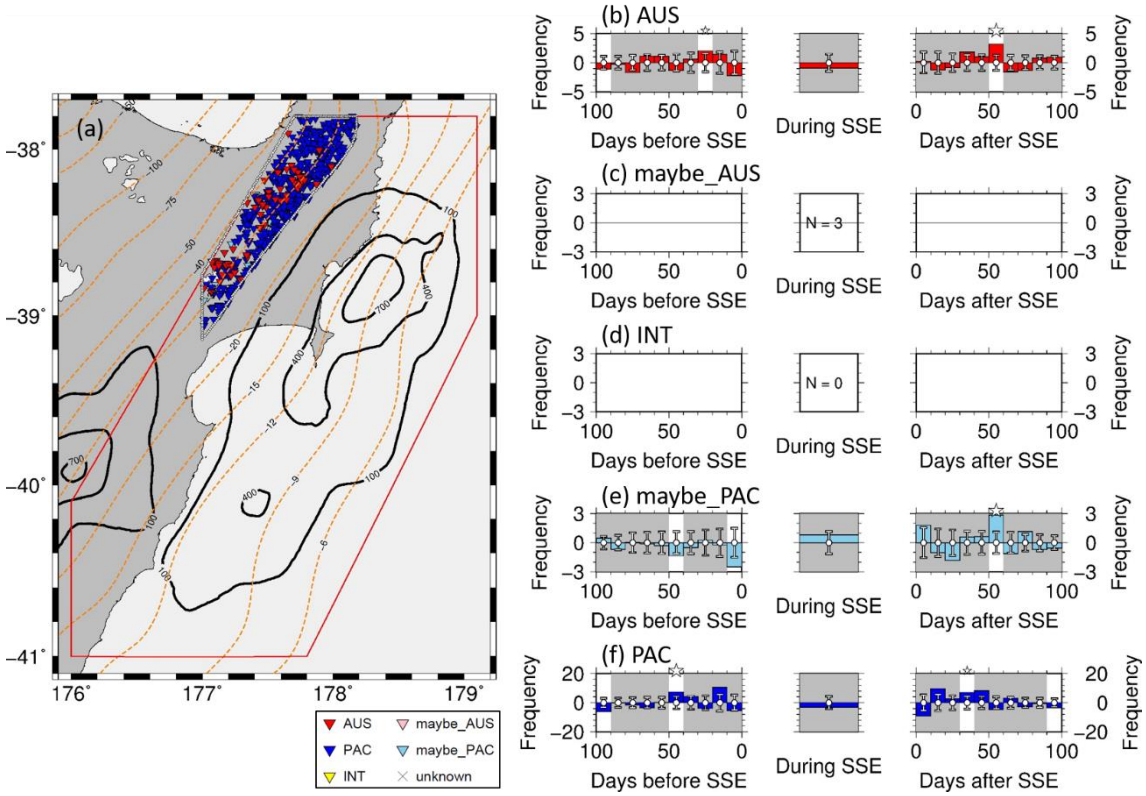

Figure 3.14. Same as Figure 3.11 but for earthquakes northwest of the SSE source in the northern Hikurangi margin.

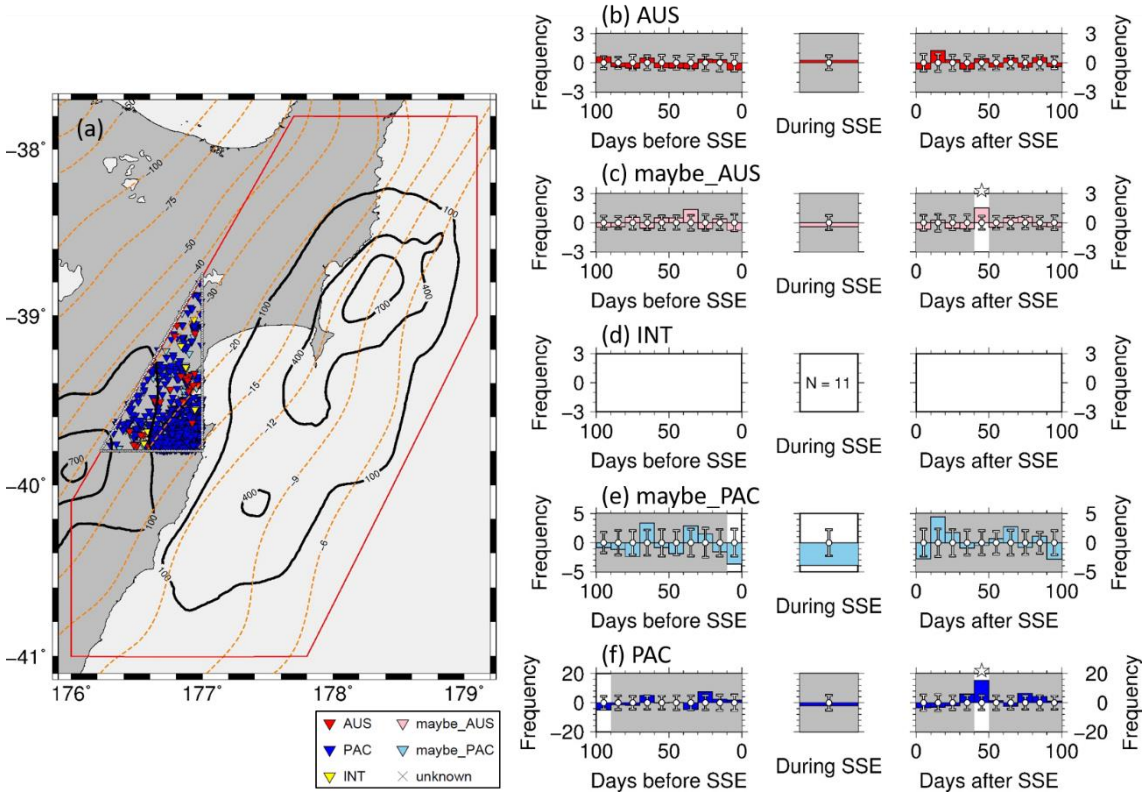

Figure 3.15. Same as Figure 3.11 but for earthquakes west of the SSE source in the northern Hikurangi margin.

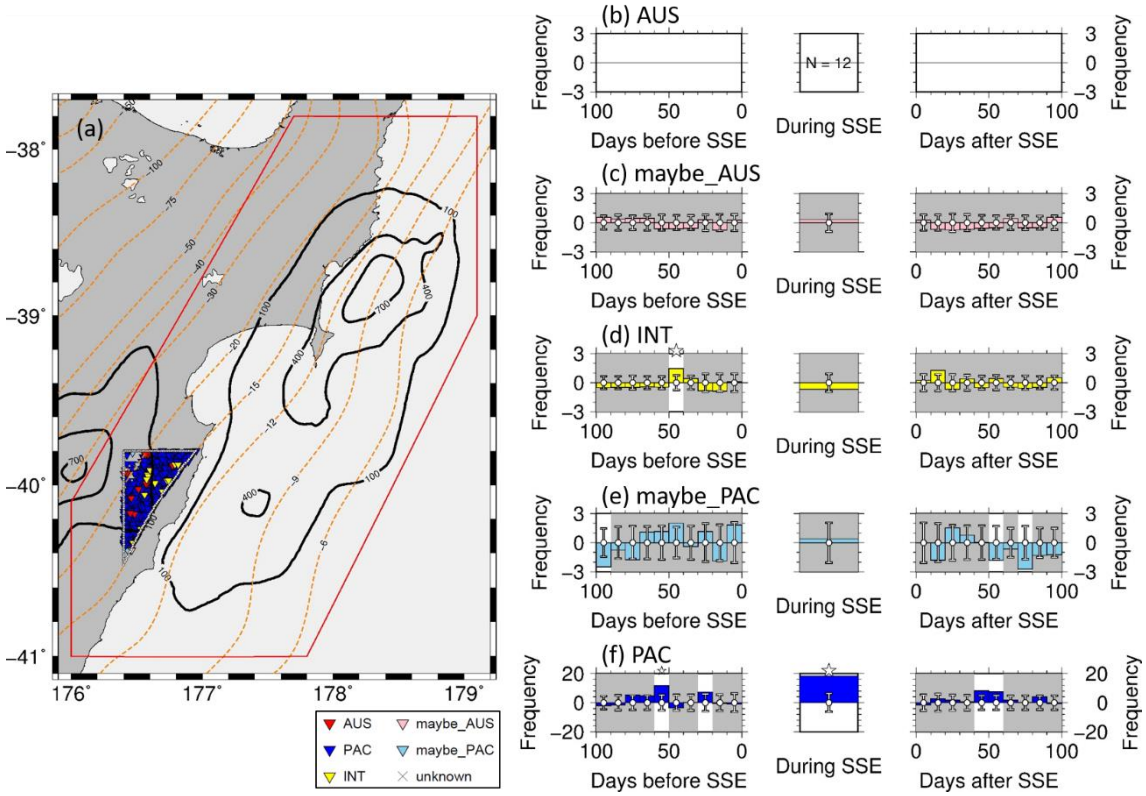

Figure 3.16. Same as Figure 3.11 but for earthquakes west of the SSE source in the central Hikurangi margin.

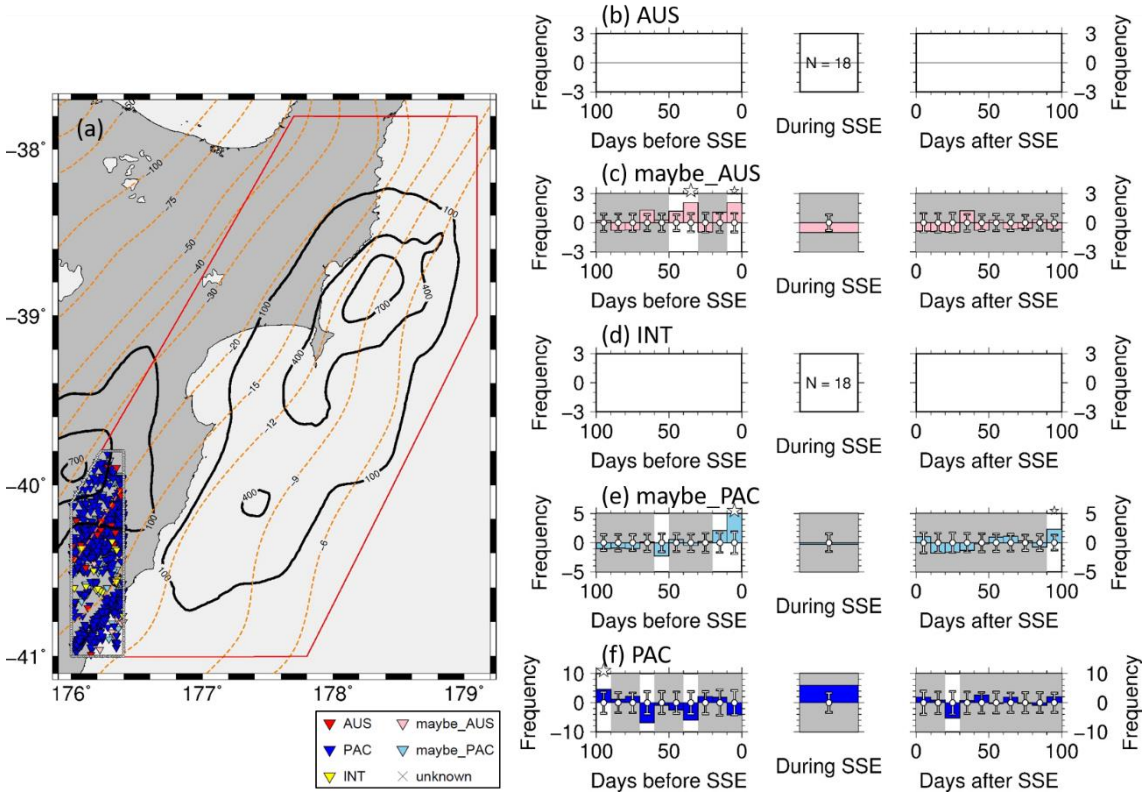

Figure 3.17. Same as Figure 3.11 but for earthquakes west and southwest of the SSE source in the central Hikurangi margin.

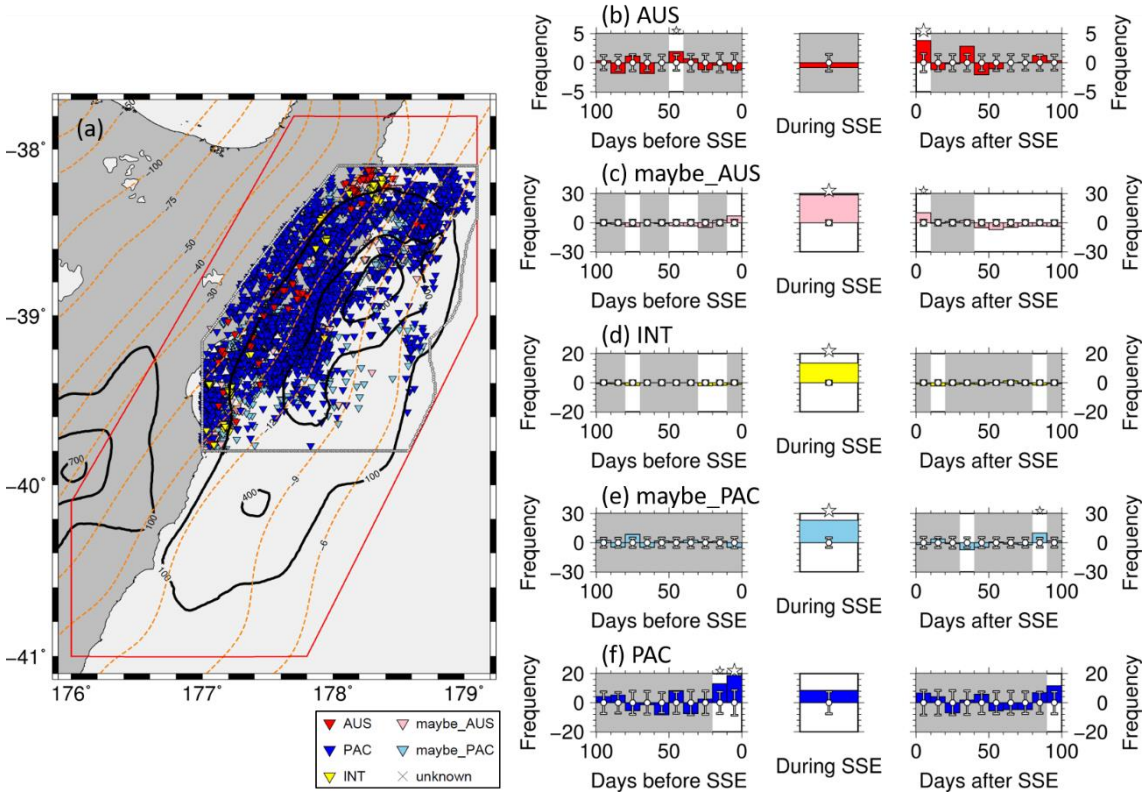

Figure 3.18. Same as Figure 3.11 but for SSE signals with a ground displacement greater than the median.

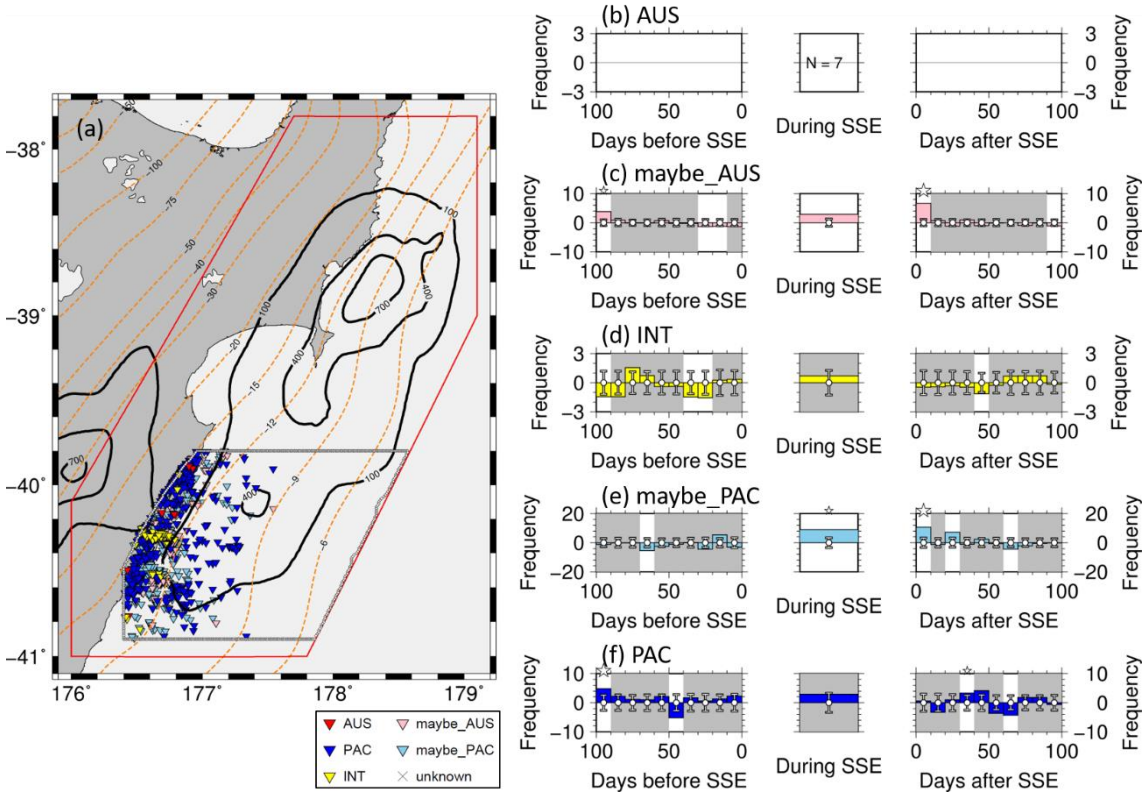

Figure 3.19. Same as Figure 3.12 but for SSE signals with a ground displacement greater than the median.

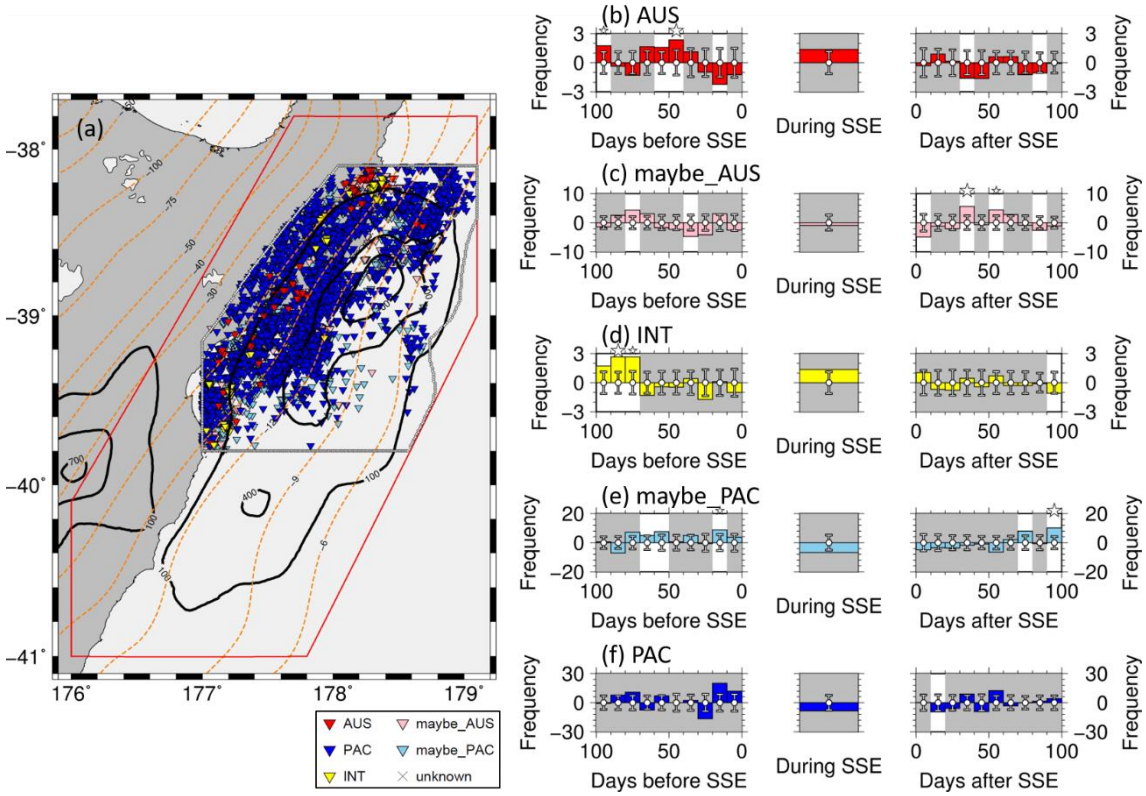

Figure 3.20. Same as Figure 3.11 but for SSE signals with a ground displacement smaller than the median.

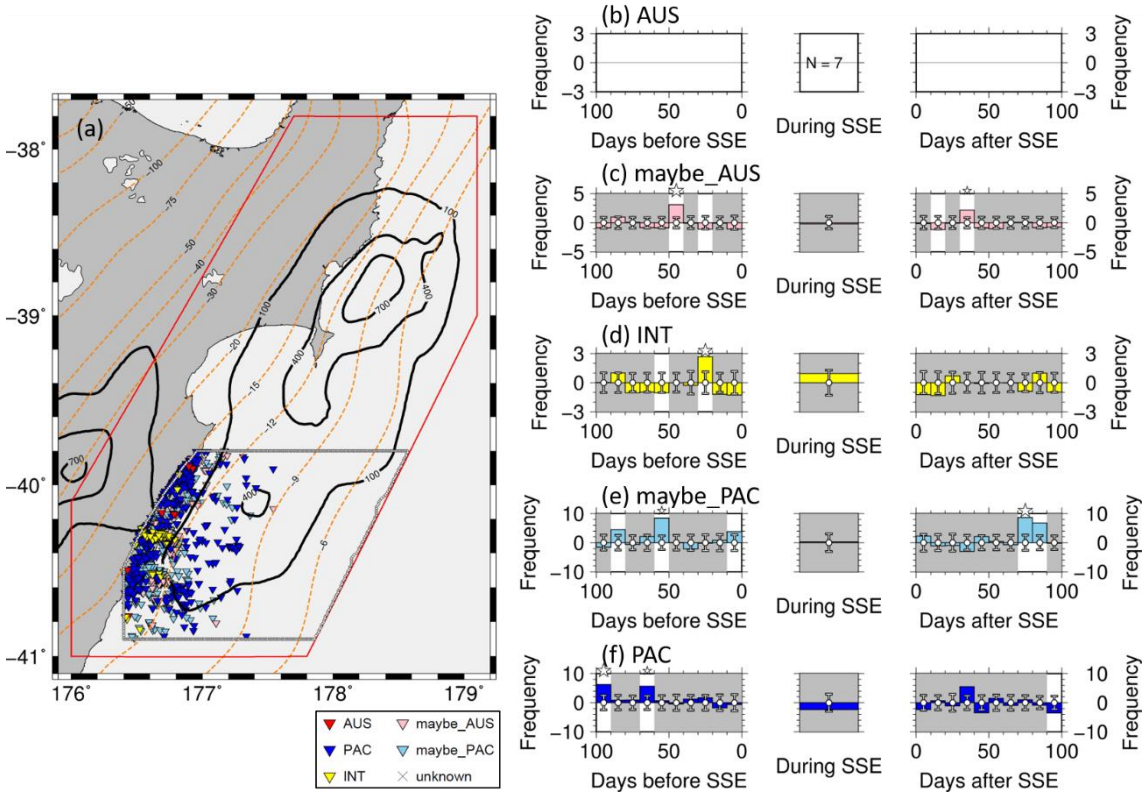

Figure 3.21. Same as Figure 3.12 but for SSE signals with a ground displacement smaller than the median.

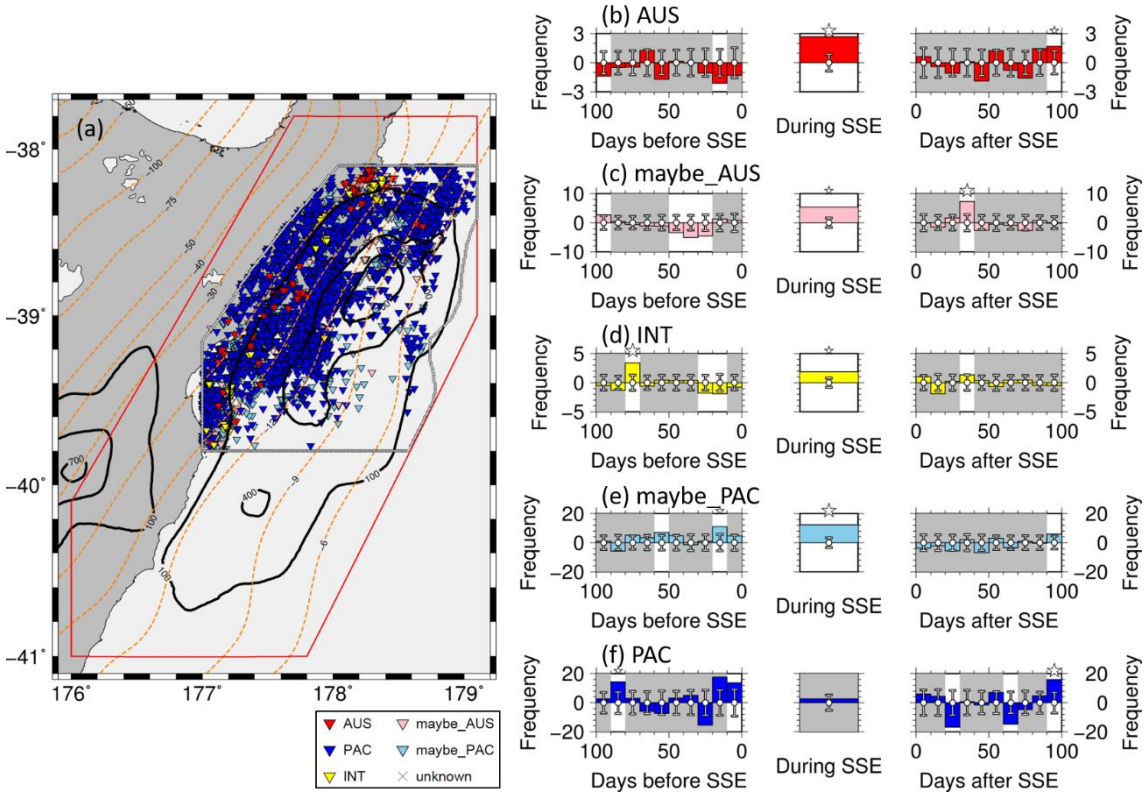

Figure 3.22. Same as Figure 3.11 but for SSE signals with a duration greater than the median.

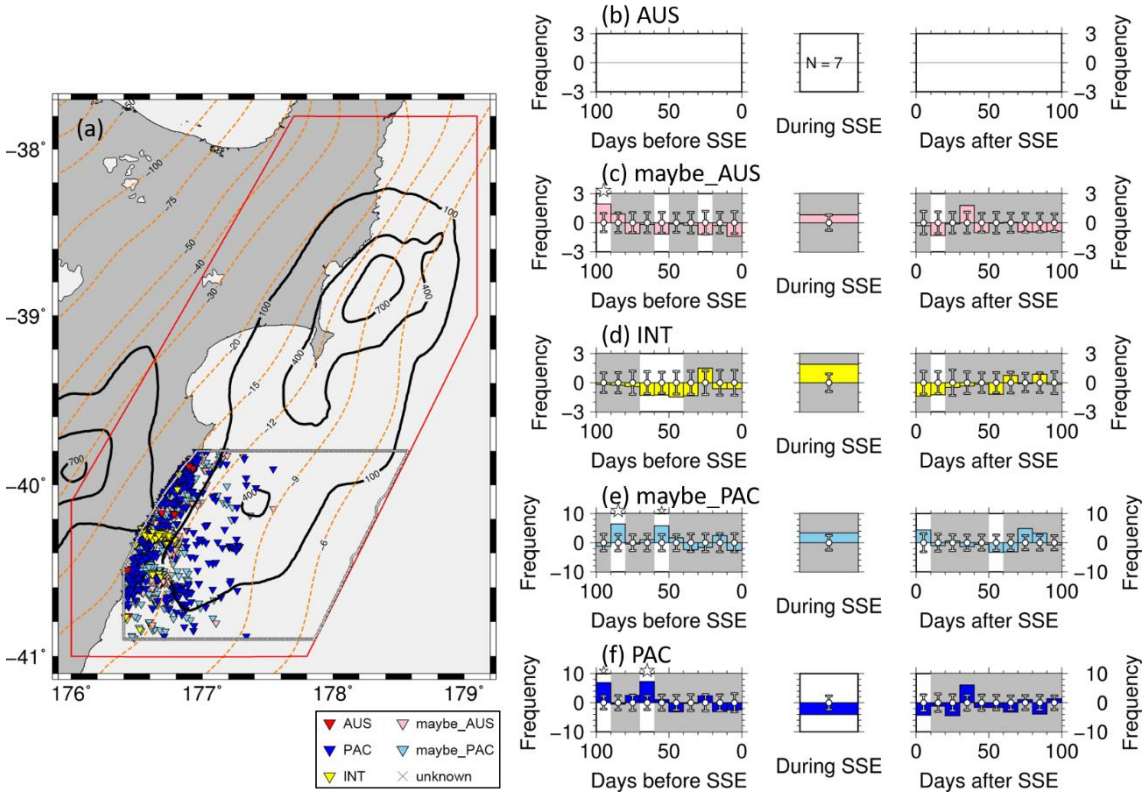

Figure 3.23. Same as Figure 3.12 but for SSE signals with a duration greater than the median.

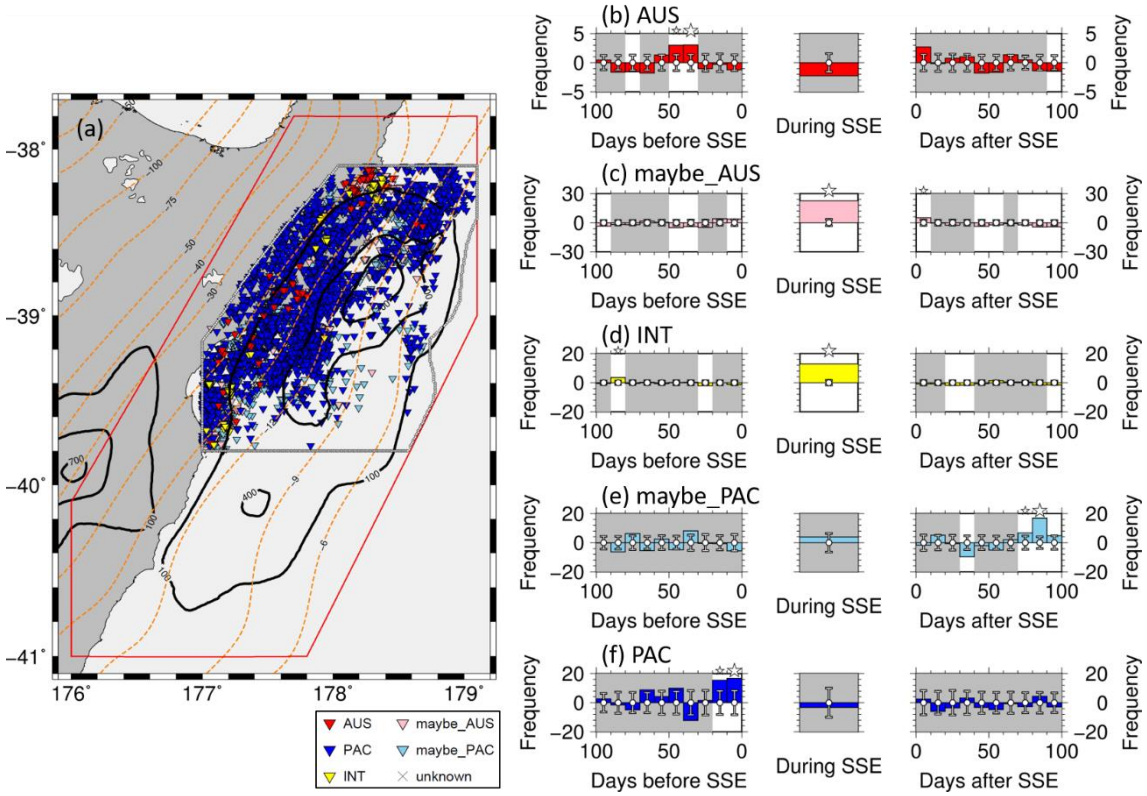

Figure 3.24. Same as Figure 3.11 but for SSE signals with a duration smaller than the median.

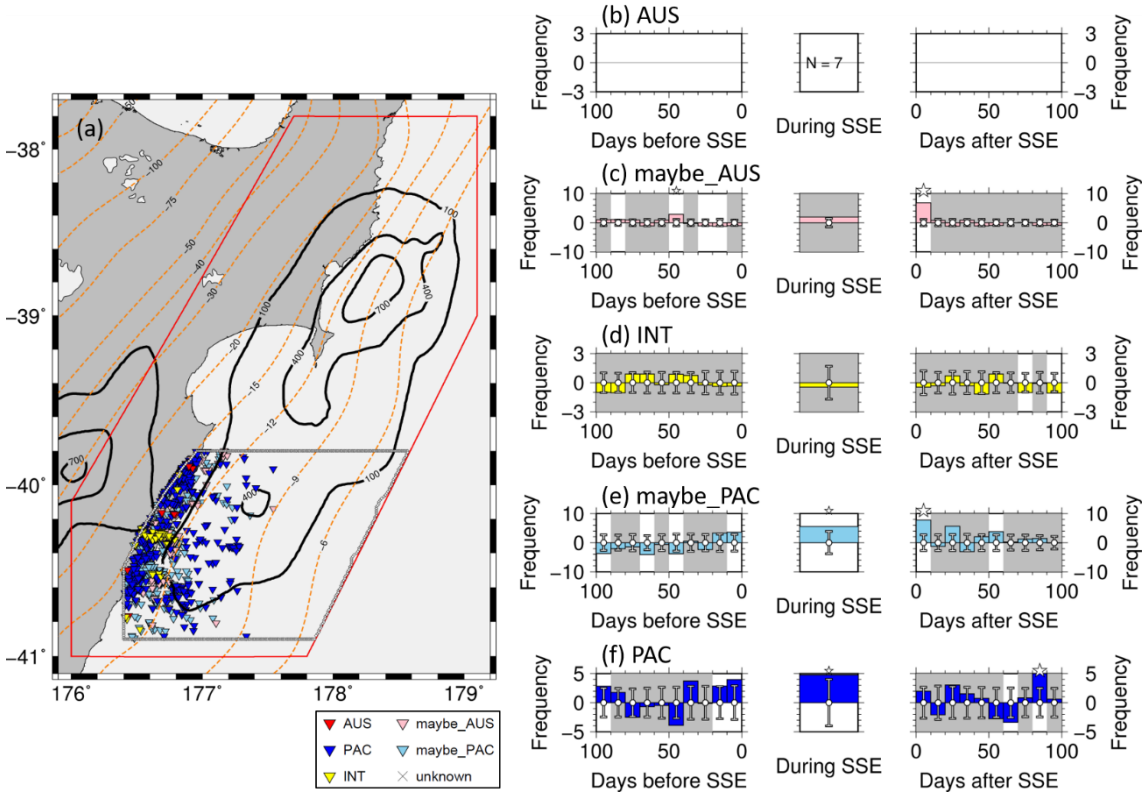

Figure 3.25. Same as Figure 3.12 but for SSE signals with a duration smaller than the median.

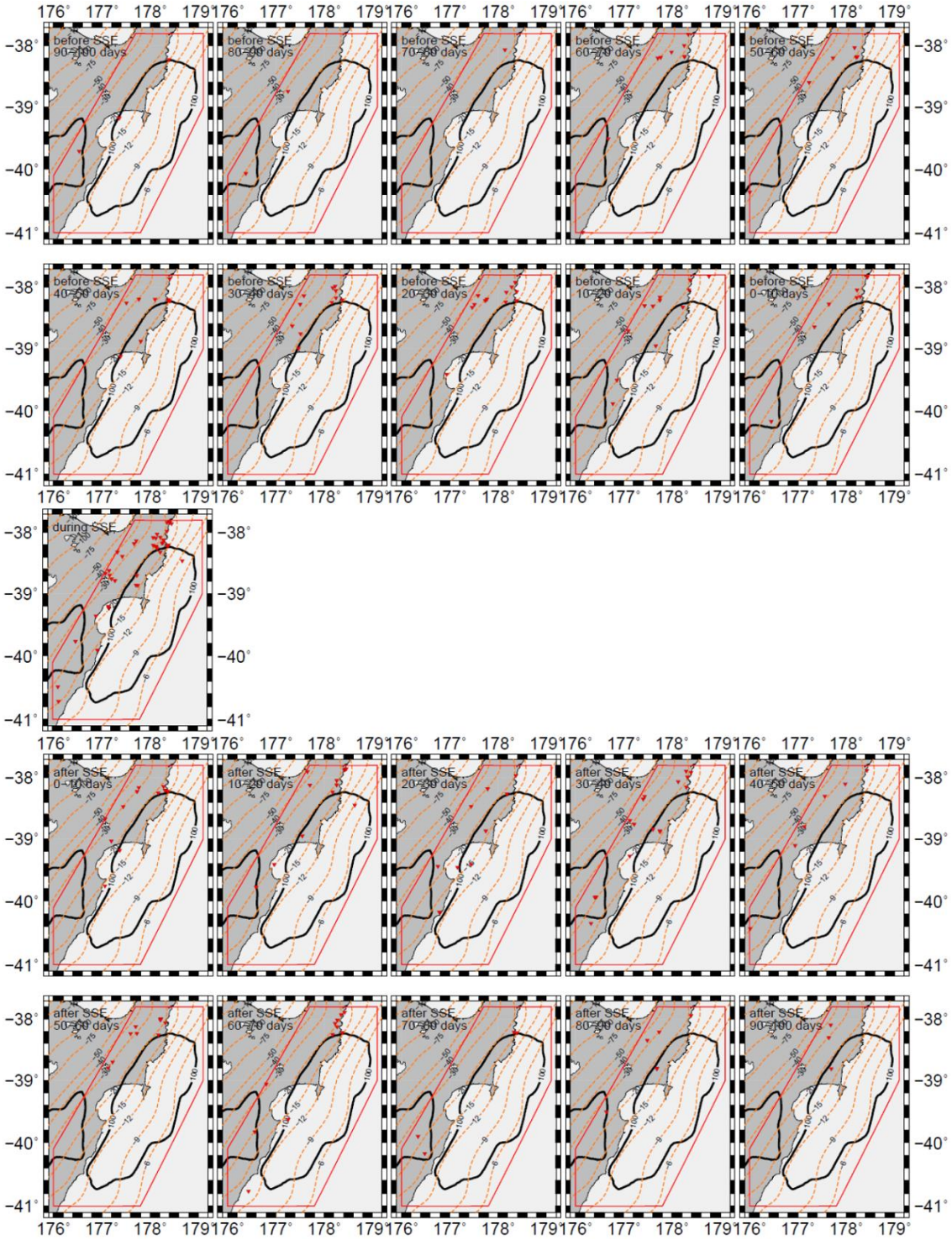

Figure 3.26. Distribution of AUS earthquakes in each period.

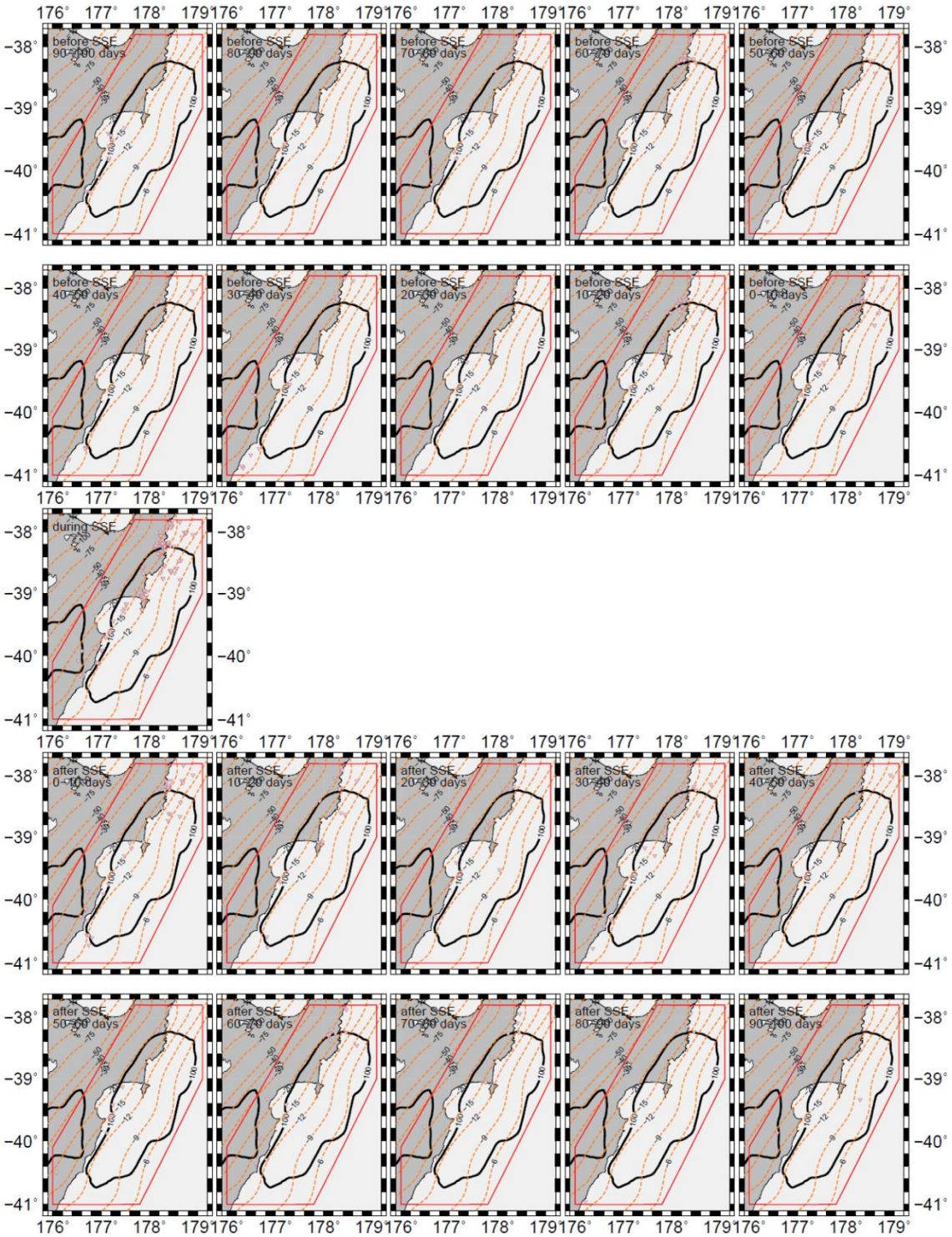

Figure 3.27. Distribution of maybe_AUS earthquakes in each period.

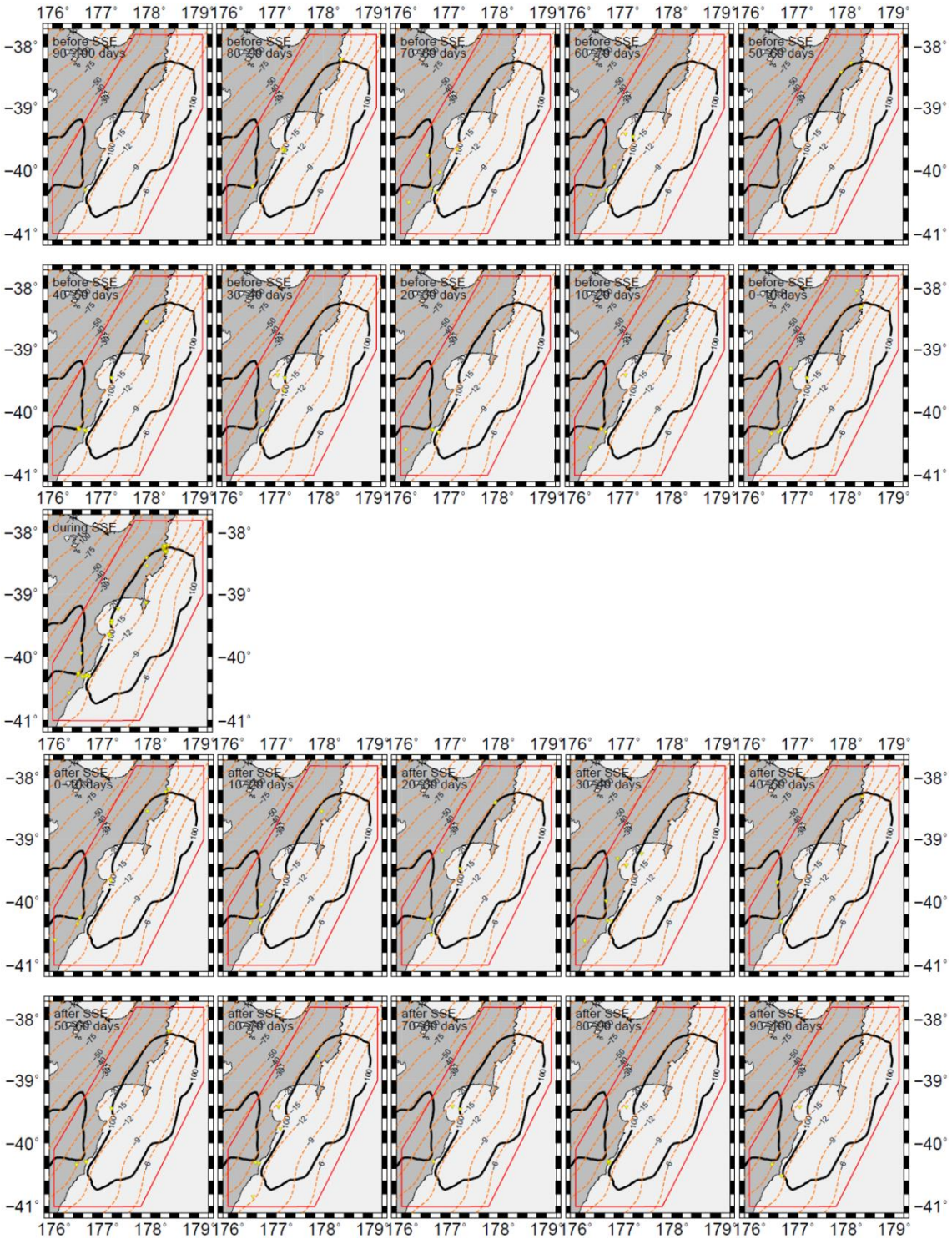

Figure 3.28. Distribution of INT earthquakes in each period.

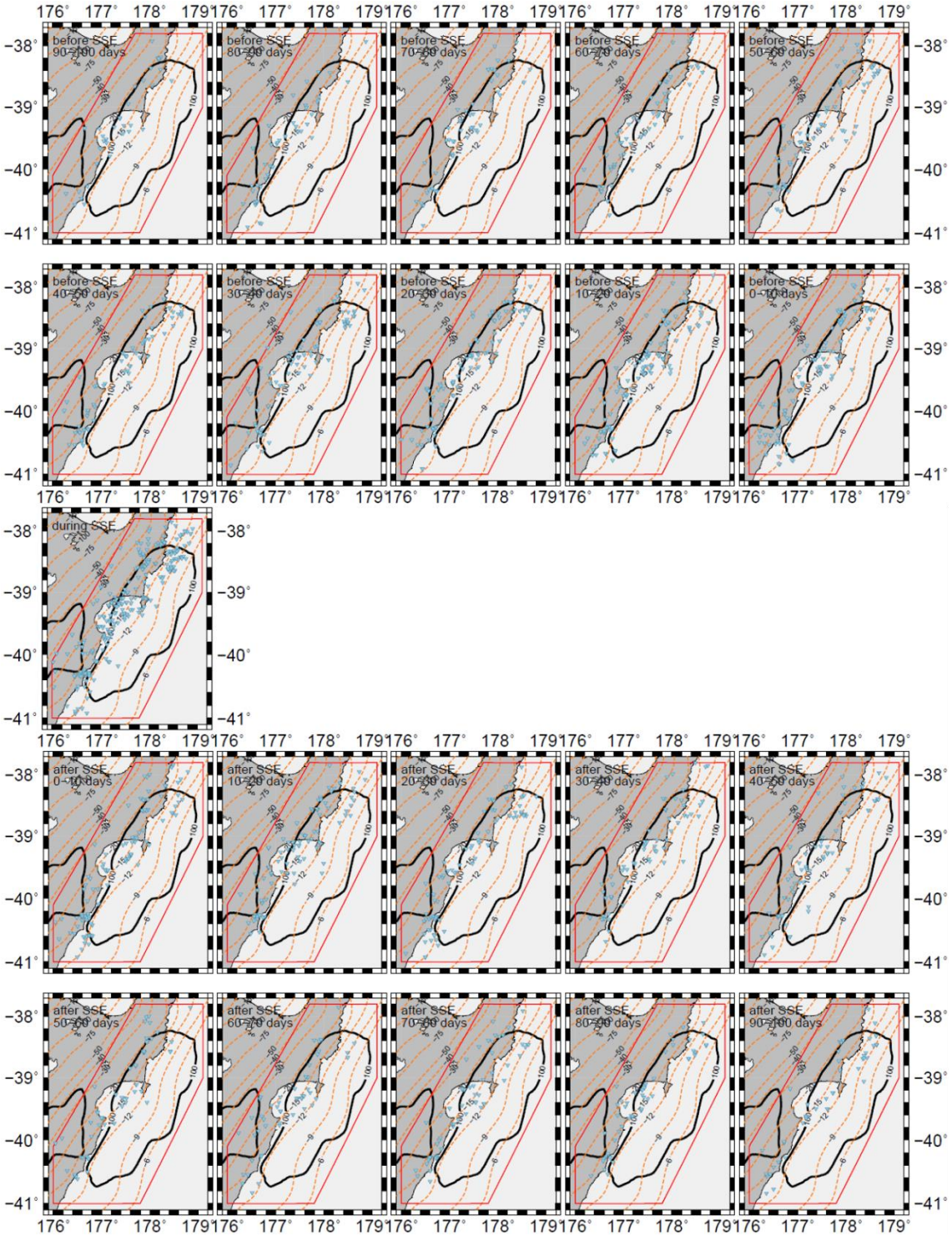

Figure 3.29. Distribution of maybe_PAC earthquakes in each period.

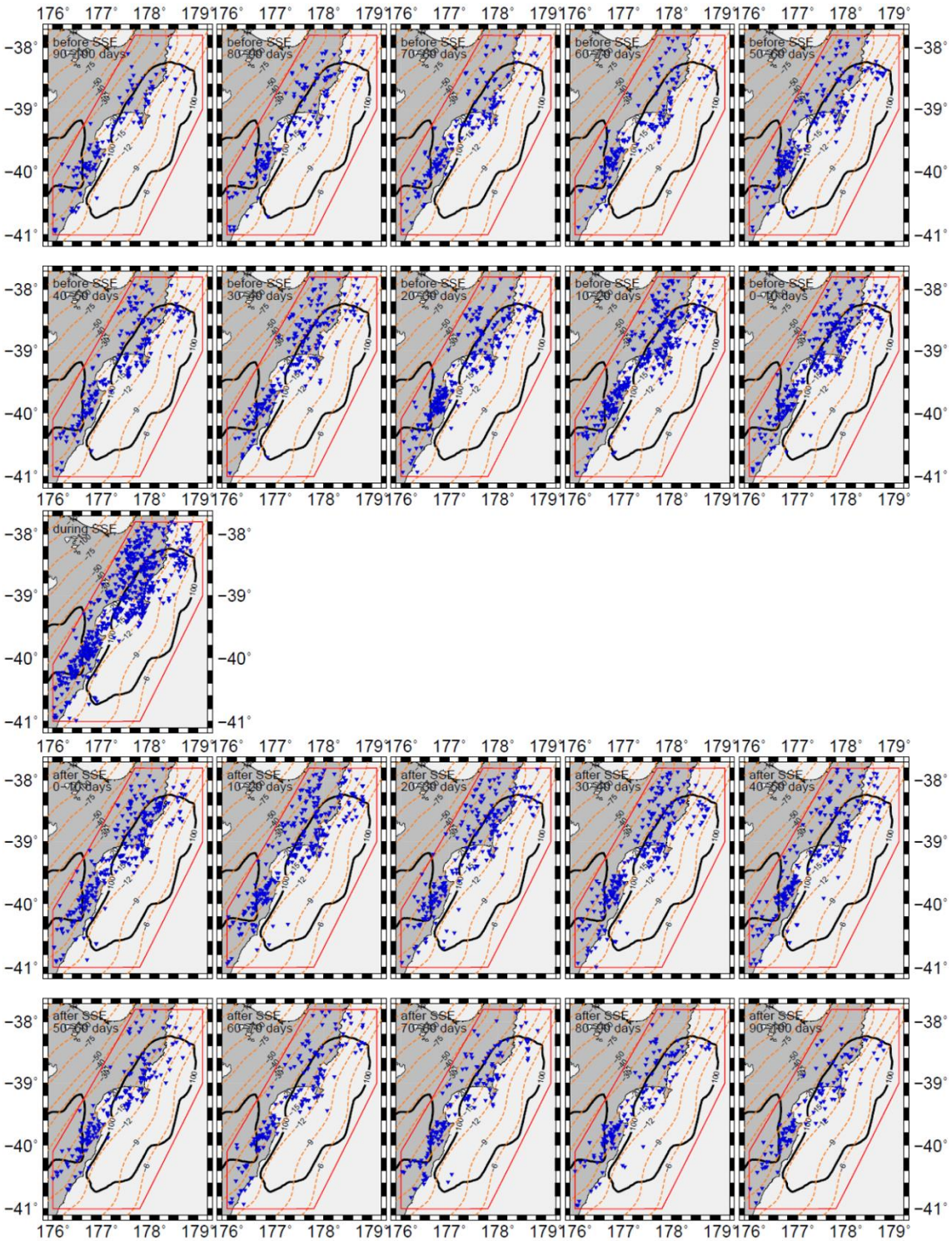

Figure 3.30. Distribution of PAC earthquakes in each period.

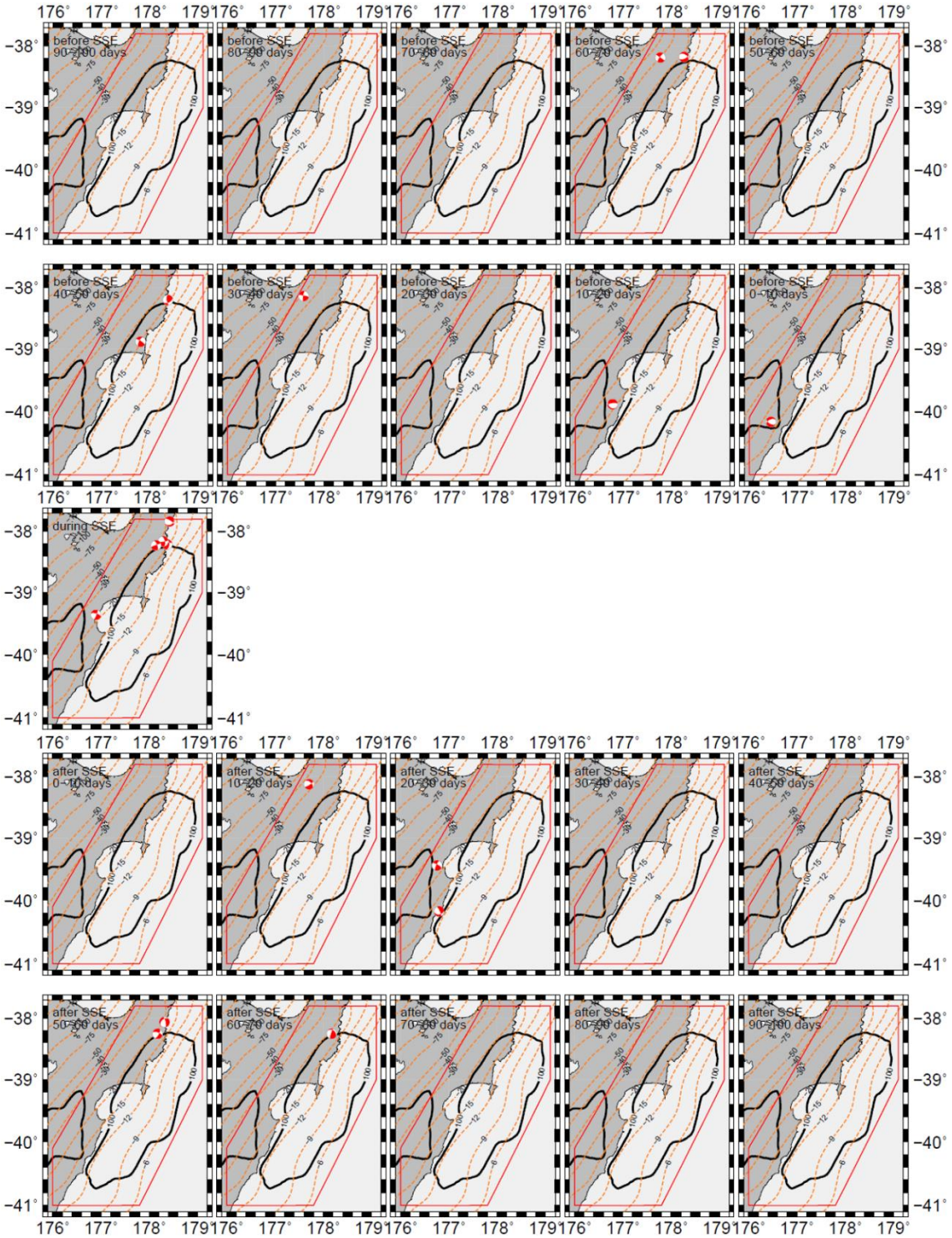

Figure 3.31. Focal mechanisms of AUS earthquakes in each period.

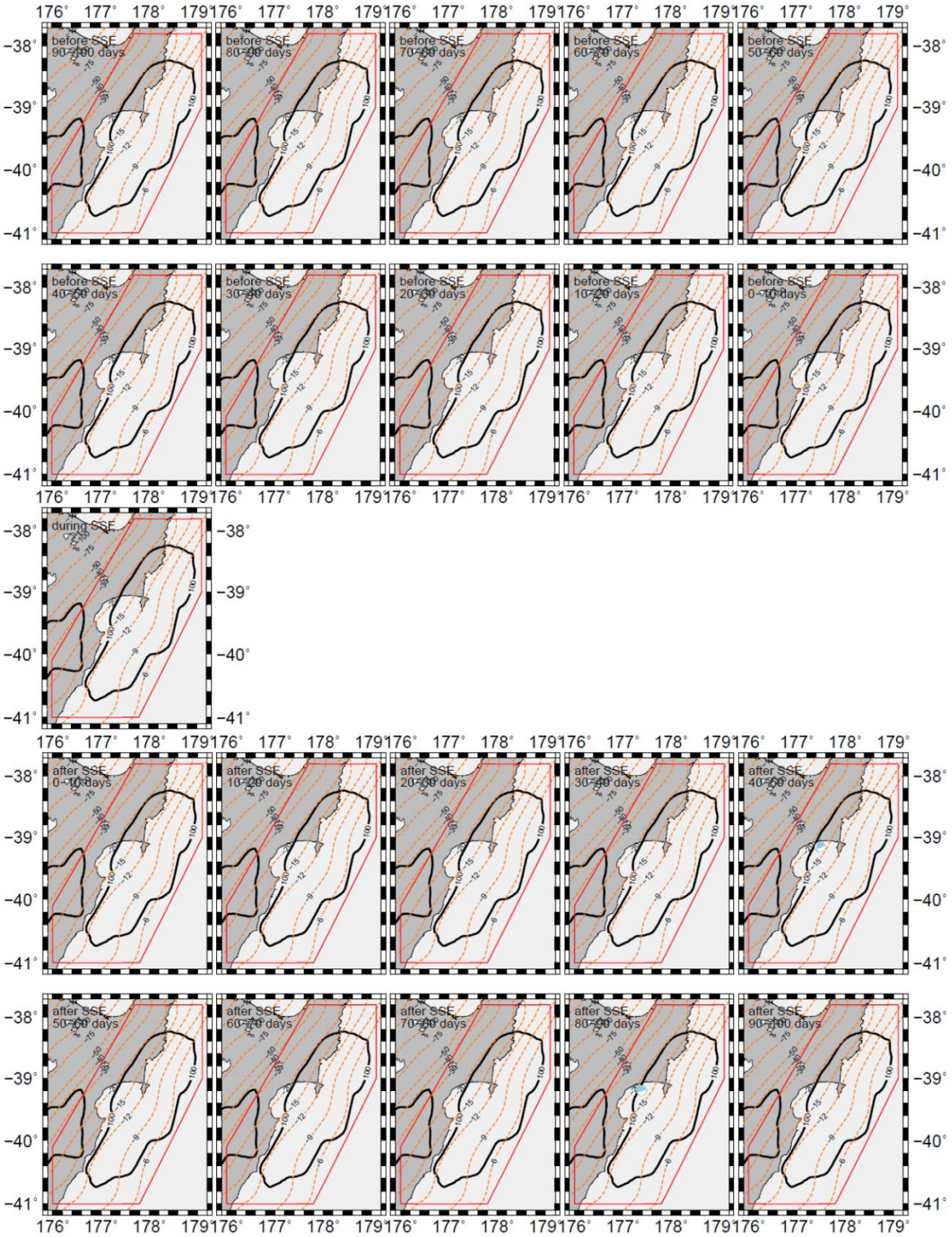

Figure 3.32. Focal mechanisms of maybe_AUS earthquakes in each period.

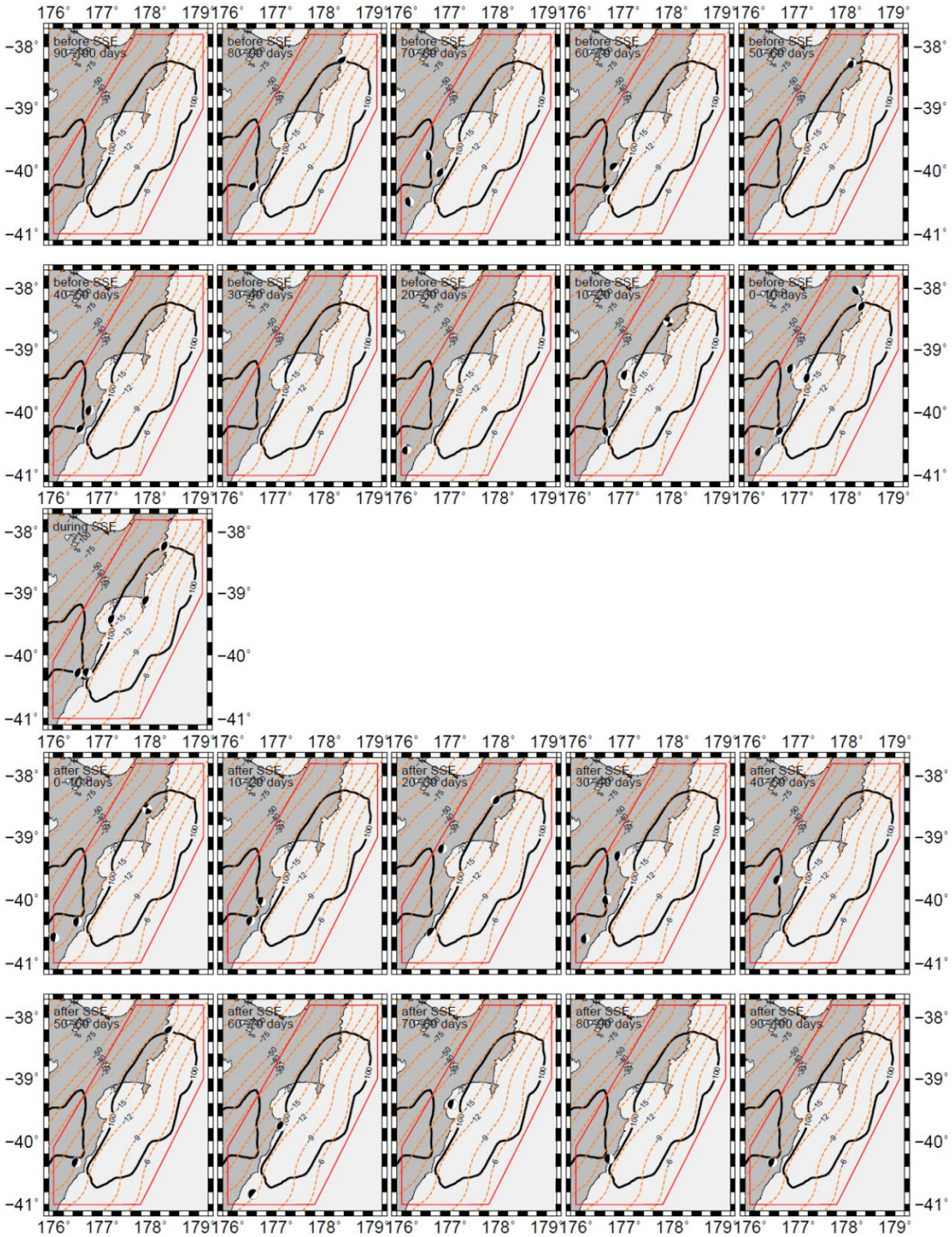

Figure 3.33. Focal mechanisms of INT earthquakes in each period.

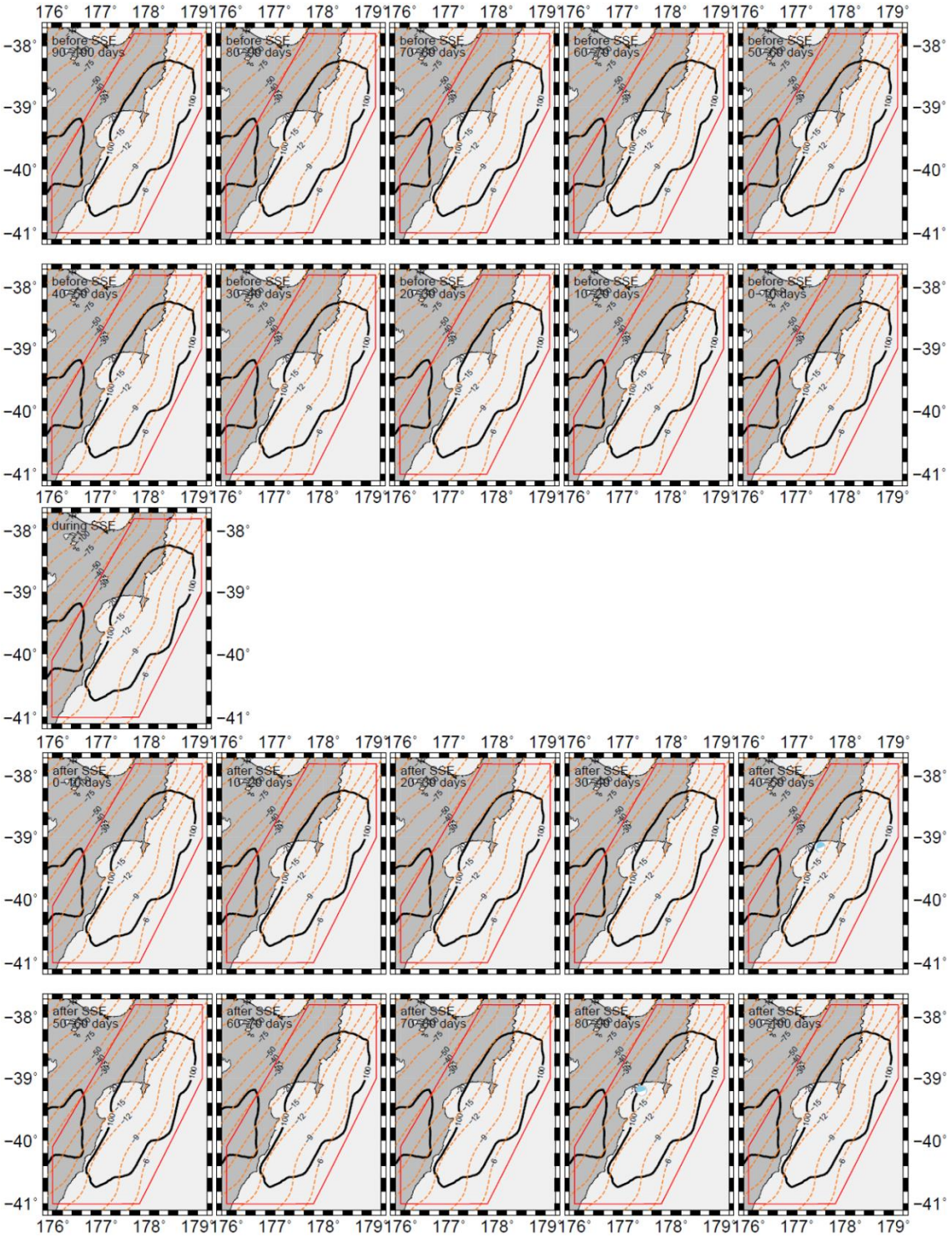

Figure 3.34. Focal mechanisms of maybe_PAC earthquakes in each period.

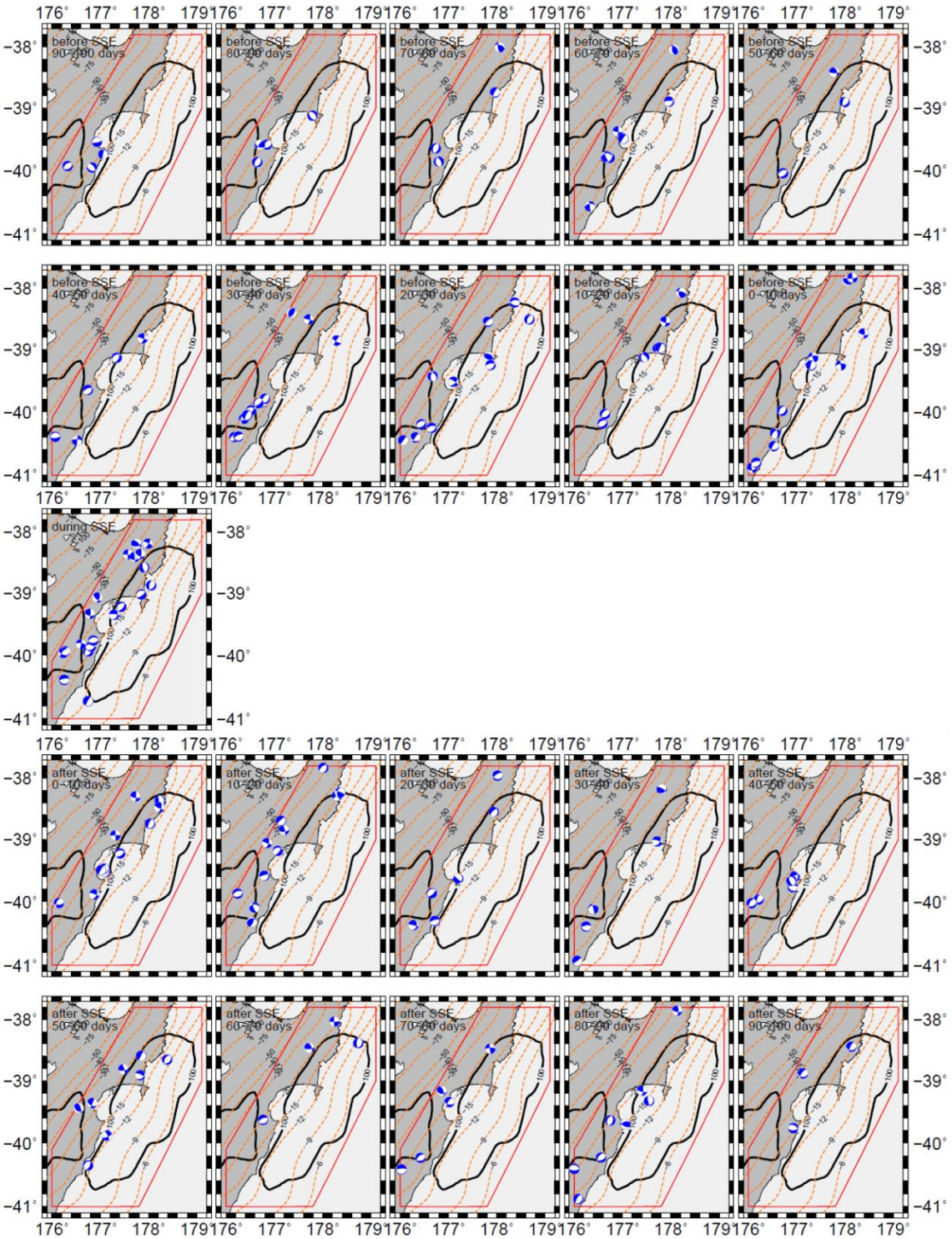

Figure 3.35. Focal mechanisms of PAC earthquakes in each period.

Chapter 4.

Discussion

4.1. What controls the activation pattern of seismicity?

We found that many earthquakes, classified as AUS, maybe_AUS, INT, maybe_PAC, and PAC, were activated with SSEs across the northern and central Hikurangi margin. However, activation patterns of seismicity in and around the SSE sources differed between the northern and central Hikurangi margin. In the northern Hikurangi margin (Figure 3.11), deeper (PAC) earthquakes were dominantly activated prior to SSEs (~38%), shallower (AUS) earthquakes were dominantly activated after SSEs (~53%), and earthquakes at or close to the plate boundary (INT, maybe_AUS, and maybe_PAC) were dominantly activated during SSEs (~76%, 51%, and 40%, respectively). In the central Hikurangi margin (Figure 3.12), earthquakes at or close to the plate interface (INT, maybe_AUS, and maybe_PAC) were activated during or after the SSEs (~35-64%). Since such characteristic activation patterns were observed, which we demonstrated cannot be explained by random occurrence, some driving forces are likely to generate the observed patterns.

In the northern Hikurangi margin, some studies recently suggested fluid movement related to SSEs on the Hikurangi margin interface. Warren-Smith et al. (2019) inferred a fault-valving model to explain their observations of stress-ratio variations throughout the SSE cycle at the northern Hikurangi margin. In this model, the accumulated fluid pressure within the subducting oceanic crust triggers SSEs, which open fluid pathways that allow these fluids to escape into the plate boundary and upper plate. Zal et al. (2020) proposed a similar model to explain their observations of temporal variations in shear-wave splitting parameters and changes in Vp/Vs measured between 2014 and 2015 around the northern Hikurangi margin. Nishikawa et al. (2021) proposed intraplate fluid migration before and after SSEs based on observations of earthquake swarms between 1997 and 2015 in the northern and central Hikurangi margins. Wang et al. (2022) again inferred a similar model to Warren-Smith et al. (2019) based on their observations of seismic velocity variations measured using ambient seismic noise between 2014 and 2015 around the northern Hikurangi margin.

Considering these previous studies that inferred fluid movement before and after SSEs in the northern Hikurangi margin, the earthquake activation patterns we observed in the northern Hikurangi margin might also be related to fluid movement. The fault-valving model suggests that fluid pressure accumulates within the subducting oceanic crust until an SSE occurs. As discussed by Nishikawa et al. (2021), this accumulated fluid pressure might break a low permeability seal (Tenthorey et al., 2003), allowing fluid migration along pre-existing faults in the subducting oceanic crust prior to SSEs, which then weaken the shear strength of the fault (e.g., Yamashita, 1998),

potentially triggering pre-SSE PAC seismicity. When the fluid pressure reaches the threshold to trigger an SSE, a slow slip occurs at the plate boundary, and fluid might move along the plate boundary, which can trigger and activate earthquakes at the plate interface (INT) during the SSE. The failure of a low permeability seal at the plate boundary during SSEs or INT events might drain the pressurized fluid and saturate the rock with fluid above (Nakajima and Uchida, 2018), which can trigger and activate earthquakes within the upper plate (AUS) after SSEs. SSEs can produce an extended increase in dilation (Rivet et al., 2011), increasing porosity (Wang et al., 2022) and permeability, which might also contribute to the activated post-SSE seismicity.

Another possible mechanism for SSE-earthquake interactions is that SSEs can alter the stress field and load surrounding seismic patches on the plate boundary. Fukuda (2018) found a strong correlation between earthquake swarm seismicity rates and SSE slip rates in Boso-oki, Japan, suggesting that the SSE-induced stress loading rate probably triggered swarms. This can account for co-SSE or post-SSE seismicity but not pre-SSE seismicity; such a characteristic differs from the fluid movement model above. SSEs introduce the change of Coulomb failure stress not only along the fault plane of the SSE source but also around the source. Segall et al. (2006) showed that earthquakes within the Kīlauea volcano, Hawaii, which occurred in January 2005, were located in the region of positive Coulomb stress change due to an ongoing SSE, indicating that the SSE likely triggered the earthquakes.

This chapter examines what driving force(s) causes the observed activation patterns in the northern and central Hikurangi margins. We evaluate fluid movement inferred from earthquake swarms, b-values of the magnitude-frequency distribution, and SSE-induced Coulomb stress changes and propose the mechanisms of SSE-related earthquakes in the Hikurangi margin.

4.2. Fluid movement inferred from earthquake swarms

4.2.1. Introduction

Earthquake swarms, commonly defined as earthquake sequences in a short time without a remarkable mainshock, are often considered to be related to fluid movement processes (e.g., Hill, 1977). For example, the Yamagata-Fukushima border earthquake swarms in Japan migrated after the 2011 M9 Tohoku-oki earthquake, indicating that fluid movement triggered the swarms (Okada et al., 2015; Yoshida and Hasegawa, 2018). In the Main Ethiopian Rift, day-to-month-long swarms were detected with increases in seismicity and magnitude, which was interpreted as fluid-induced seismicity (Raggiunti et al., 2023). Numerical simulations with pore pressure diffusion can reproduce observed features of earthquake swarms, including their space-time distribution (Hainzl, 2004). In this section, we assume that earthquake swarms, especially swarm migration, can be an indicator of fluid movement, and we discuss fluid movement from swarm activities.

4.2.2. Swarm detection

We used the space-time ETAS model (Zhuang et al., 2002) to detect earthquake swarms following the previous studies (Nishikawa and Ide, 2018; Nishikawa et al., 2019; Nishikawa et al., 2021). In this ETAS model, the seismicity rate (conditional intensity rate) λ at location (x, y) and time t can be written as

$$\lambda(t,x,y) = \mu(x,y) + \sum_{t_i<t} \kappa(M_i) g(t-t_i) f(x-x_i, y-y_i; M_i). \tag{4.1}$$

The first and second terms on the right hand of Equation (4.1) represent the background seismicity rate and the aftershock rate, respectively: $\mu(x,y)$ is the background seismicity rate at location (x,y), $\kappa(M)$ is the expected number of aftershocks from the magnitude M of a preceding earthquake, $g(t)$ is the probability density of the aftershock lag times, which is independent of the magnitude of a preceding earthquake, and $f(x,y;M)$ is the probability density of aftershock locations. Specific forms of each function are expressed as

$$\mu(x,y) = \nu u(x,y), \tag{4.2}$$

$$\kappa(M) = Ae^{\alpha(M-M_c)}, \tag{4.3}$$

$$g(t) = \begin{cases} (p-1)c^{p-1}(t+c)^{-p} & \cdots \text{for } t>0 \\ 0 & \cdots \text{otherwise,} \end{cases} \tag{4.4}$$

and

$$f(x,y;M) = \frac{q-1}{\pi D^2 e^{\gamma(M-M_c)}} \left(1 + \frac{x^2+y^2}{D^2 e^{\gamma(M-M_c)}}\right)^{-q}, \tag{4.5}$$

where $u(x,y)$ and M_c are the spatial intensity function and the magnitude of completeness, and ν, A, c, α, p, D, q, and γ are ETAS parameters. These parameters are positive, and p is greater than one. Since the magnitude of completeness decreased with time (Figure 2.2) probably due to an increase in the number of seismic stations and automated picking of arrival times, as discussed in section 2.2, we estimated these eight ETAS parameters for four periods with different M_c: 2004-2007 (M_c=2.8), 2008-2011 (M_c=2.6), 2012-2015 (M_c=2.5), and 2016-2020 (M_c=2.5). The periods after 2011 were divided so that the length of each period was almost the same. We estimated ETAS parameters with the maximum likelihood method using the code for the space-time ETAS model and stochastic declustering (Zhuang et al., 2002; Zhuang et al., 2004; Zhuang, 2006) (Table 4.1). Swarms were detected as earthquake sequences that were more intense than expected from the ETAS model. We estimated the expected number of earthquakes from the ETAS model on a 10 km $\times$ 10 km grid using earthquakes of which distance from the grid point was shorter than 10 km (Figure 4.1a). The expected number of earthquakes N_i from time 0 to t_i, the occurrence time of earthquake i, is written as

$$N_i = \int_0^{t_i} \iint_S \lambda(t,x,y) dx dy dt, \tag{4.6}$$

where S is the detection circle. Thus the expected number of earthquakes between two earthquakes i and $i+1$ is

$$N_{i+1} - N_i = \int_{t_i}^{t_{i+1}} \iint_S \lambda(t,x,y)dxdydt. \quad (4.7)$$

Under the assumption that N_i follows a Poisson process, the standard deviation σ of the expected number of earthquakes is

$$\sigma = \sqrt{N_{i+1} - N_i}. \quad (4.8)$$

If the observed seismicity completely follows the ETAS model, $N_{i+1} - N_i$ equals one. If earthquakes occur more than expected based on the ETAS model (the case of potential swarms), $N_{i+1} - N_i$ should be less than one. Following Nishikawa et al. (2021), we detected earthquake swarm sequences as a series of earthquakes that satisfy the condition $N_{i+1} - N_i + 1.5\sigma < 1$ for four or more successive events (Figure 4.1b). We considered a sequence containing aftershocks of the 2007 M6.7 Gisborne earthquake as an "aftershock swarm," which is potentially triggered by an afterslip of preceding large earthquakes. Thus, we removed a sequence that includes aftershocks of the 2007 M6.7 Gisborne earthquake, as also removed by Nishikawa et al. (2021). We obtained 194 swarm sequences composed of 1,794 swarm events. Many swarm events were located in the shallower part of the background seismicity (Figure 4.2).

4.2.3. Diffused swarms

We classified the 194 detected swarm sequences into three types: "diffused" that shows swarm migration which can be explained by a fluid diffusion theory, "not-diffused" that shows migration which cannot be explained by the fluid diffusion theory, and "undefined" that shows an unclear migration pattern. The classification consisted of two steps (Figure 4.3). If the earthquake classification type of the first event in a sequence was unknown, or the number of events in the sequence excluding the type of unknown was five or less, the sequence was classified as "undefined." For other sequences, the relationships between the time t and distance r from the first event were examined. Sequences with $\min_{i \neq j}\{|r_i - r_j|;\ i,j = 1,\cdots,N\}$ > 10 km, where N is the number of events in the sequence, were classified into "not-diffused" sequences. Sequences not following a characteristic fluid diffusion expansion were also classified into "not-diffused" sequences. The "diffused" sequences are expected to be well fit by the function

$$r = \sqrt{4\pi D t}, \quad (4.9)$$

where D is the hydraulic diffusivity (Shapiro et al., 1997). Thus, if the correlation coefficient between r^2 and t ($CC_{\sqrt{t}}$) was less than 0.5, the sequences were classified into "not-diffused" ones. Using a linear function, we also fitted the r – t relationships and calculated the correlation coefficient between r and t (CC_t). The subscript of CC means the time dependence of distance r. Since a negatively large $CC_{\sqrt{t}} - CC_t$ value means that the sequence is well-explained by the linear function in linear time rather than by the square-root function, we removed sequences which can be well

explained by the square-root function. The $CC_{\sqrt{t}}$ vs. $CC_{\sqrt{t}} - CC_t$ plot shows that the maximum of $CC_{\sqrt{t}} - CC_t$ for $CC_{\sqrt{t}} > 0.5$ is less than 0.1 and the minimum less than -0.1 (Figure 4.4). Simply assuming that sequences with $\left|CC_{\sqrt{t}} - CC_t\right| > 0.1$ can be explained by a linear function or square-root function, we determined the threshold of $CC_{\sqrt{t}} - CC_t$ as -0.1. We classified the sequences with $CC_{\sqrt{t}} - CC_t < -0.1$ as "not-diffused." Finally, we visually checked other sequences and classified them into "not-diffused" if they seemed to deviate from the migration pattern expressed in Equation (4.9). Appendix B shows examples of "diffused," "not-diffused," and "undefined" sequences. Since the number of events in a sequence detected in this study was small (~5), we simply fitted Equation (4.9) to the observed relationships between r and t rather than their envelopes. This might miss the sequences that really followed fluid diffusion, and they would be classified as "not-diffused" sequences. We checked the swarms that were defined as "not-diffused" and whether they can be within the envelope of the fluid diffusion curve, but the time-distance distributions of most swarms were complex, and it was difficult to classify them as "diffused" sequences (Figure B3, B4). However, the "diffused" sequences were well fitted by Equation (4.9), and the fitted curves were like the envelopes, we can say that the "diffused" sequences followed the fluid diffusion. We obtained twelve "diffused" swarm sequences, 75 "not-diffused" swarm sequences, and 78 "undefined" swarm sequences (Figure 4.5). Although the distribution of each type of sequence depends on the detectability, ten out of twelve "diffused" swarm sequences were located around the northern Hikurangi subduction interface (Figure 4.5a), which, if we assume that these swarms were related to fluid migration, indicates that fluid movement occurs more easily in the northern Hikurangi margin than the central Hikurangi margin.

We tested if our method detects "diffused" swarms for random seismicity. We generated ten random earthquake catalogs, where the latitude and longitude of earthquakes are random, and the origin time, depth, and magnitude of earthquakes are the same as the original catalog. We applied swarm detection and swarm classification methods for these ten random catalogs. Our method detected four "diffused" swarm sequences, 355 "not-diffused" swarm sequences, and 490 "undefined" swarm sequences in total (Table 4.2). The ratio of the number of "diffused" to "not-diffused" is 0.011, much smaller than the observed ratio of 0.160, indicating that the detected "diffused" swarms are not apparent.

Some "diffused" swarm sequences in the northern Hikurangi margin occurred around the SSE occurrence time: a sequence consisting of AUS, INT, and maybe_AUS events started about one day after an SSE (Figure 4.6a), a sequence consisting of INT and maybe_AUS events started during an SSE (Figure 4.6b), and a sequence consisting of PAC events started about 25 days before an SSE (Figure 4.6c). Under the assumption that "diffused" swarms were caused by fluid migration, these results indicate that fluid might migrate within the Australian plate after SSEs, at the plate boundary during SSEs, and within the Pacific plate before SSEs. We note that the timing of swarm migration and hence fluid movement is not limited to the abovementioned periods. Figure 4.6d shows the

migration of AUS events 41 days before an SSE, indicating that swarms and fluid migration in the upper plate were not always associated with SSEs.

4.2.4. Discussions

Permeability is one of the most important parameters to evaluate the properties of porous rocks. We estimated the permeability k from the obtained diffusivity values (D) for "diffused" swarm sequences (Saar and Manga, 2004; Ingebritseni and Manning, 2010). The permeability k is written as

$$k = \frac{\nu_{\mathrm{w}} D S_{\mathrm{S}}}{g}, \tag{4.10}$$

where ν_{w} is the kinematic viscosity of the fluid, S_{S} is the specific storage (= 10^{-6} m^{-1} for igneous fracture rock according to Saar and Manga, 2004), and g is the gravitational acceleration (= 9.8 m/s^2). Since the value of S_{S} might not be optimized for the Hikurangi margin, it can produce some bias for estimating k, however, the relative k would be less biased if we assume that S_{S} does not spatially change so much. The kinematic viscosity ν_{w} is expressed as

$$\nu_{\mathrm{w}} = \frac{0.032}{\rho(1 - \alpha_{\mathrm{w}} T)(15.4 + T)}, \tag{4.11}$$

where ρ is the density of water (= 1,000 kg/m^3), α_{w} is the coefficient of thermal expansion of water (= 10^{-3} $°C^{-1}$), and T is the temperature (°C). In this study, the temperature was expressed as a function of the depth. We assumed the mean surface temperature of 10 °C and geothermal gradient of 10 °C/km (the red curve in Figure 4.7) from the results of a numerical study at the shallow Hikurangi subduction zone (Antriasian et al., 2019). Using the depth-dependent ν_{w} (the blue curve in Figure 4.7) and diffusivity D obtained from Equation (4.9), which ranges between 2 and 200 m^2/s (Table 4.3), we estimated the permeability k (Figure 4.8). Estimated permeability in the northern Hikurangi margin decreased with depth (Figure 4.8b), consistent with previous studies (e.g., Ingebritseni and Manning, 2010). Perez-Silva et al. (2023) estimated the range of diffusivity as 10-100 m^2/s to reproduce SSEs in the Hikurangi margin from numerical models using the rate-and-state friction law (Dieterich, 1979; Ruina, 1983; Marone, 1998) and fluid diffusion along the fault plane. This is very close to our estimation for the northern Hikurangi margin (~10-180 m^2/s). Permeability estimated from the diffusivity of Perez-Silva et al. (2023) (an orange line in Figure 4.8b) overlapped the range of permeability estimated in this study. The results of relatively high permeability in the upper plate in the northern Hikurangi margin might be due to the extensional strain rate field here (Haines and Wallace, 2020). Note that since the permeability depends on many parameters described above, the absolute value of the estimated permeability probably has a large uncertainty. However, the relative value of the estimated permeability might be small if we assume that the constants in Equation (4.11) and the value of S_{S} do not change from place to place in the study area. Although the estimated

permeability has large uncertainty due to the uncertainty of other parameters, our permeability estimation indicates that high permeability (10^{-13}-10^{-11} m^2) was needed for fluid movement in the northern Hikurangi margin.

As discussed in section 2.4, the concentration and gap of AUS events corresponded to the area of extensional and contractional regions of areal strain rates (Dimitrova et al., 2016; Haines and Wallace, 2020), respectively, in the north of our study area (Figure 2.22a, f). One of the possibilities to explain this is the permeability. The contractional strain is expected to decrease permeability (Gangi, 1978), making it difficult to induce fluid-related AUS events. In contrast, the extensional strain may lead to large permeability, thereby enabling fluid movement and fluid-related AUS events.

4.3. b-value

Montuori et al. (2010) estimated the b-value, a parameter describing the magnitude-frequency distribution, in the southern Hikurangi margin. They compared the b-value distribution with previously determined 3-D distributions of Vp, Vp/Vs, and Qp from seismic tomography (Eberhart-Phillips et al., 2005; Reyners and Eberhart-Phillips, 2009). From a comparison between b-value and tomography results, they concluded that material inhomogeneity, caused by fluid-filled cracks resulting from dehydration of the subducted slab and subducted sediments, is the predominant cause of b-value variation in the shallow part of the margin. Using the reconstructed catalog, we estimated the b-value of each earthquake type if the number of earthquakes was greater than 100 and examined its regionality. Using the maximum likelihood method (Equation (3.3); Utsu, 1965), we estimated the b-value as 1.40 ± 0.02 for all events except earthquakes type of "unknown," 1.05 ± 0.07 for AUS events, 1.29 ± 0.07 for maybe_AUS events, 0.73 ± 0.03 for INT events, 1.66 ± 0.05 for maybe_PAC events, and 1.33 ± 0.02 for PAC events (Figure 4.9, 4.10). The goodness-of-fit (e.g., Liu et al., 2017) estimated smaller b-values than the maximum likelihood method, but the relationship among the b-values for respective event types (maybe_PAC > PAC ~ maybe_AUS > AUS > INT) did not change. Such high b-values (> 1.0) were also obtained in the shallow southern Hikurangi margin with the maximum likelihood method (Montuori et al., 2010). We obtained (1) higher b-values in the northern Hikurangi margin than the central Hikurangi margin, especially for PAC and maybe_PAC events (red and blue dots in Figure 4.10), (2) the highest b-value for maybe_PAC events (~1.8 and ~1.4 in the northern and central Hikurangi margin, respectively), and (3) the lowest b-value for INT events (~0.8 in the northern and central Hikurangi margins) (Figure 4.10). The fluid pressure can explain the first feature of the estimated b-values, that is, the faults in the northern Hikurangi margin might be more pressurized by fluids than those in the central Hikurangi margin. Since the maybe_PAC events include earthquakes on the plate interface or just below it, the second feature of the estimated b-values might arise from overpressured oceanic crust just below the plate interface. The third feature, the lowest b-values for INT events, is probably due to their reverse faulting (Schorlemmer et al., 2005). The b-value also

depends on other factors, including the deviatoric stress (Lockner, 1993), the confining pressure (Lockner, 1993), and the state of patches (Schorlemmer and Wiemer, 2005). Although we cannot rule out these other possibilities, the results of the b-value analysis are consistent with the presence of fluid inferred from swarm activities, indicating that the fluid pressure probably affects b-values in the northern and central Hikurangi margins probably due to material heterogeneity caused by variations in crack fluid content like the southern Hikurangi margin (Montuori et al., 2010).

4.4. Coulomb stress change

4.4.1. Introduction

Faulting causes crust deformation, leading to changes in normal and shear stresses acting on the surrounding faults depending on the fault geometry and sense of slip. In this study, Coulomb stress change or Coulomb Failure Function (CFF) change is defined as

$$\Delta CFF = \Delta\tau + \mu\Delta\sigma, \tag{4.12}$$

where $\Delta\tau$, $\Delta\sigma$, and μ are the change of shear stress (positive in the inferred direction of slip), the change of normal stress (positive for fault unclamping), and frictional coefficient, respectively (Harris, 1998; Toda et al., 2011). SSEs also can produce Coulomb stress change for surrounding faults (e.g., Segall et al., 2006), indicating the possibility of triggering earthquakes.

In the northern Hikurangi margin, AUS events were activated immediately after SSEs, and INT, maybe_AUS, and maybe_PAC events were activated during SSEs (Figure 3.11). In the central Hikurangi margin, maybe_AUS events were activated immediately after SSEs, and maybe_PAC events were activated during and immediately after SSEs (Figure 3.12). Since the activation pattern of maybe_AUS and maybe_PAC events was the same as that of INT events in the northern Hikurangi margin, we considered many of maybe_AUS and maybe_PAC events as INT events not only in the northern Hikurangi margin but also in the central Hikurangi margin. In this section, we examine how the Coulomb stress changed for AUS and INT events by SSEs and assess the potential for triggering earthquakes.

4.4.2. Computing Coulomb stress change

We computed SSE-induced Coulomb stress change using Coulomb 3.3 program (Toda et al., 2005; Lin and Stein, 2004) assuming rectangular source faults and a frictional coefficient of 0.4 that is a mean for carbonates and volcaniclastics in the northern Hikurangi margin (Shreedharan et al., 2022) and also adopted by Warren-Smith et al. (2019). We considered the location and geometry of SSE sources to fit the source inverted by previous studies. The location and geometry of earthquakes (receiver faults) were determined in Chapter 2 from relocation obtained by NonLinLoc and the focal mechanism obtained by HASH. We computed Coulomb stress changes if the location and geometry of both source and receiver were known. In the northern Hikurangi margin, three AUS events during

SSEs were already estimated for their locations and geometries and accompanied with SSEs documented by previous studies (Figure 4.11c). Table 4.4 shows these AUS events' location and fault geometry, and Table 4.5 shows the location and fault geometry of corresponding SSEs. We found that Coulomb stress change for these AUS events was negative or neutral independent of the assumed receiver nodal plane (Figure 4.12), indicating that AUS events during SSEs in the northern Hikurangi margin were probably not triggered by SSE-induced Coulomb stress change. Although AUS events immediately after SSEs in the northern Hikurangi margin did not have well-resolved focal mechanisms, some of them (in the north of the northern Hikurangi margin) were possibly not triggered by SSE-induced Coulomb stress change under the assumption that their focal mechanisms were similar to those of AUS events during SSEs (A, B, and C in Figure 4.11c). This assumption may be valid because they occurred close to each other. We cannot estimate other AUS events during SSEs (in the south of the northern Hikurangi margin) because no AUS events were nearby with resolved focal mechanisms. Thus we cannot rule out the possibility that AUS events immediately after SSEs in the northern Hikurangi margin were triggered by SSE-induced Coulomb stress change, however, such stress triggering would also need to explain the delayed nature of AUS events because AUS events were not activated during SSEs (Figure 3.11b).

Earthquakes that occur on the same fault plane and have the same slip sense as SSEs can be triggered by SSE-induced Coulomb stress change, indicating that INT events (including maybe_AUS and maybe_PAC events) might have been triggered by SSEs in the northern and central Hikurangi margin (Figure 4.13).

4.5. Models for earthquakes and SSEs

The activation period in the northern Hikurangi margin depends on the classification type: PAC events before SSEs, maybe_PAC, INT, and maybe_AUS events during SSEs, and AUS events immediately after SSEs (Figure 3.11). Many of the "diffused" swarm sequences were detected in the northern Hikurangi margin, and a PAC migration occurred before an SSE, an INT migration during an SSE, and an AUS migration after an SSE. These results indicate that fluid movement from the subducting Pacific plate before SSEs to the upper Australian plate after SSEs is possibly a driving force of earthquakes in the northern Hikurangi margin (Figure 4.14a). We note that not all SSE signals accompanied earthquakes and that only a few swarm sequences were accompanied with SSEs. About 25% of SSE signals were accompanied with pre-SSE PAC events; 17%, 9%, and 10% of SSE signals accompanied with co-SSE maybe_PAC, INT, and maybe_AUS events, respectively; and 2% of SSE signals accompanied with post-SSE AUS events. These facts may suggest that fluid movement and/or its related seismicity do not always occur with SSEs. This would be in case the decrease in shear strength by the increase of pore fluid pressure changes or the shear stress accumulated when an SSE occur is too small to cause instability as an earthquake. The observation that larger ground

displacement signals, or larger SSEs, were accompanied with more active seismicity (Figure 3.18, 3.19) might mean the decrease in shear strength by the increase of pore fluid pressure change is larger when a larger SSE occurs. We also note that the SSE-induced stress loading likely triggers earthquakes at the plate boundary and that we cannot rule out the possibility that the SSE-induced Coulomb stress change triggers AUS events after SSEs. Swarm migration analysis estimated high permeability (10^{-13}-10^{-11} m^2) for fluid movement in the northern Hikurangi margin. The concentration and gap of AUS events north of the northern Hikurangi margin (Figure 2.22a, f) might be generated by permeable and impermeable structures caused by extensional and contractional strain, respectively.

In contrast, in the central Hikurangi margin, the activation period differed from that of the northern Hikurangi margin: maybe_PAC events during and immediately after SSEs, and maybe_AUS events immediately after SSEs (Figure 3.12). Only one "diffused" swarm sequence was observed in the central Hikurangi margin, suggesting that driving forces other than fluid movement might trigger earthquakes. Coulomb stress change analysis showed that SSEs can trigger earthquakes at the plate boundary. These results indicate that SSE-induced stress loading might be the main driving force of earthquakes in the central Hikurangi margin (Figure 4.14b).

This study revealed the mechanisms of triggered earthquakes and their regional dependence. The difference between the northern and central Hikurangi margin corresponds to the seismic velocity structure (Eberhart-Phillips and Bannister, 2015; Eberhart-Phillips et al., 2017; Chow et al., 2022), electrical resistivity (Heise et al., 2017; Heise et al., 2019), and geological features (Reyes et al., 2022) (Table 4.6).

Reyes et al. (2022) measured fluid flow in springs and geochemically and isotopically evaluated the fluid flow in the subaerial Hikurangi forearc. They found that 95% of aqueous fluids, by volume, across the subaerial Hikurangi forearc were being discharged in the creeping zone (referred to slipping zone by Reyes et al., 2022) where a low slip deficit rate was estimated (Wallace et al., 2012), which partly overlaps the northern Hikurangi margin defined in this study. Reyes et al. (2022) also estimated the ascent rates of cold waters to find that the rate in the northern creeping zone was three times higher than in the southern locked zone. These results from venting fluids indicate the existence of structures that enable fluid movement in the upper plate above the shallow SSEs in the slipping zone (~the northern Hikurangi margin).

The Vp/Vs systematically changes across the Hikurangi margin (Eberhart-Phillips and Bannister, 2015; Eberhart-Phillips et al., 2017). The Vp/Vs at or near the plate boundary is relatively higher in the creeping zone (Vp/Vs > 1.8) than locked zone (Vp/Vs < 1.8) (Figure 15 in Reyes et al., 2022), indicating more fluid-rich sources in the creeping zone (the northern Hikurangi margin). Electrical resistivity is widely estimated across the Hikurangi margin (Heise et al., 2017; Heise et al., 2019). Resistivity at the plate interface was estimated to be lower in the northern Hikurangi margin (> 6 Ωm) than in the central Hikurangi margin (> 60 Ωm), indicating that fluid-rich sediment might lie

on the subducting oceanic crust in the northern Hikurangi margin. These studies suggest a higher possibility of fluid-related events in the northern Hikurangi margin than in the central Hikurangi margin, supporting our results and discussions.

4.6 Suggestions for future work

Since this study used seismic stations inland, relocated hypocenters offshore had large uncertainties and were classified as "unknown," making it almost impossible to discuss how the activation patterns vary offshore. The accuracy of relocation will improve by using HOBITSS ocean bottom seismometers, depth-phase (e.g., Ma and Eaton, 2011), machine-learning-based phase-picking (e.g., Zhu and Beroza, 2019), and polarity-picking (e.g., Hara et al., 2019), leading to increase the number of AUS, INT, and PAC events with reducing the number of unknown events. This study analyzed earthquakes with magnitude greater than 2.8 between 2004 and 2007, 2.6 between 2008 and 2011, and 2.5 between 2012 and 2020. Detecting smaller earthquakes (e.g., Chamberlain et al., 2017) not included in the GeoNet catalog and investigating the temporal relationship with SSEs will provide us with the magnitude dependence of triggering mechanisms. An analysis of smaller earthquakes will enable us to detect precise swarm migrations caused by fluid diffusion. We did not invert individual SSE sources in this study. Evaluating the space-time evolution of individual SSEs and surrounding seismicity would allow us to test our interpretation of the triggering mechanism of fluid movement and stress loading.

Table 4.1. Estimated ETAS parameters for four time periods.

	2004 - 2007	2008 - 2011	2012 - 2015	2016 - 2020
ν	1.03	1.02	1.02	1.03
A	0.496	0.485	0.485	0.487
c	4.72×10^{-3}	8.27×10^{-3}	6.18×10^{-3}	7.05×10^{-3}
α	1.66	1.54	1.56	1.26
p	1.03	1.04	1.03	1.04
D^2	7.35×10^{-4}	3.59×10^{-4}	0.46×10^{-4}	1.79×10^{-4}
q	2.34	1.97	1.33	1.70
γ	0.979	0.695	0.083	0.249

Table 4.2. The number of "diffused," "not-diffused," and "undefined" swarm sequences for ten random earthquake catalogs.

	Diffused	Not-diffused	Undefined
Catalog 1	0	31	50
Catalog 2	0	40	58
Catalog 3	0	31	45
Catalog 4	0	32	48
Catalog 5	0	30	44
Catalog 6	0	36	51
Catalog 7	1	36	55
Catalog 8	1	42	34
Catalog 9	1	43	52
Catalog 10	1	34	53
Total	4	355	490

Table 4.3. Estimated diffusivity for “diffused” swarm sequences. The left column corresponds to the sequence number in Figure 4.5.

Number	Diffusivity (m^2/s)
1	2.9±1.2
2	29.1±1.2
3	18.1±1.3
4	181.1±1.1
5	79.3±1.1
6	59.5±1.4
7	42.4±1.2
8	14.6±1.3
9	27.0±1.4
10	62.2±1.1
11	32.1±1.3
12	16.4±1.3

Table 4.4. Location and geometry of AUS events in the northern Hikurangi margin during SSEs.

	Date	Depth (km)	Mw	Strike (°)	Dip (°)	Rake (°)
A	Sep. 2011	12.2±1.4	2.88	256	64	142
				5	56	32
B	Jul. 2013	13.0±0.8	3.29	81	83	-150
				347	60	-8
C	Sep. 2014	11.5±0.8	3.21	248	85	161
				340	71	5

Table 4.5. Source properties of rectangular SSEs corresponding to AUS events in the northern Hikurangi. The leftmost column is AUS events during the SSEs in Table 4.3. The rightmost column is the previous studies to which we referred. a: Wallace et al. (2012), b: Gomberg et al. (2020), c: Warren-Smith et al. (2019).

Corresponding AUS events	Width (km)	Length (km)	Top depth (km)	Slip (mm)	Mw	Strike (°)	Dip (°)	Rake (°)	Ref.
A	50	40	8	45	6.2	207	8	107	*a
B	50	50	8	100	6.8	207	8	107	*b
C	18	60	13	10	5.6	207	8	107	*c

Table 4.6. The difference in physical and geological properties between the northern and central Hikurangi margins. The rightmost column is the previous studies to which we referred. a: Eberhart-Phillips and Bannister (2015), b: Eberhart-Phillips et al. (2017), c: Heise et al. (2017), d: Heise et al. (2019), e: Reyes et al. (2022).

	Slipping zone (~Northern Hikurangi margin)	Locked zone (~Central Hikurangi margin)	Reference
Vp/Vs	> 1.8	< 1.8	*a, *b
Electrical resistivity	> 6 Ωm	> 60 Ωm	*c, *d
Ratio of vented aqueous fluids by volume	95%	5%	*e
Ascent rates of cold waters	3 times larger than locked zone	-	*e

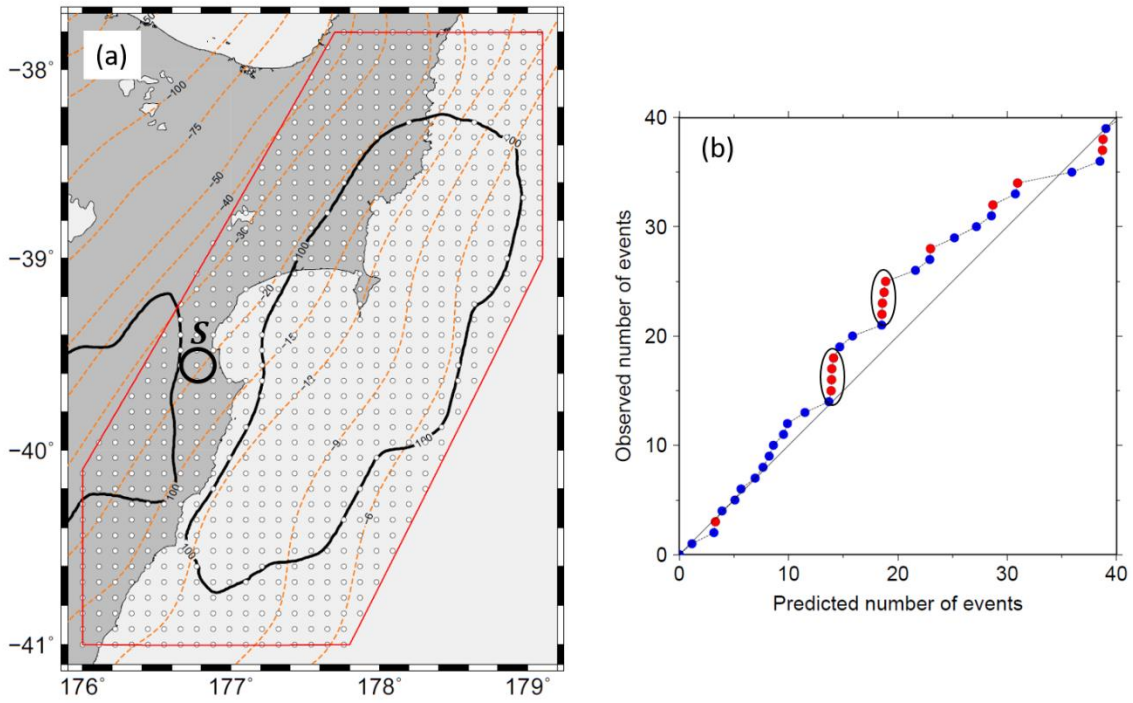

Figure 4.1. Swarm detection conditions. (a) Detection grid point. White dots are points for swarm detection and are located every 10 km. The black circle is the detection circle with a radius of 10 km. (b) An example of the relationship between observed and predicted number of earthquakes. Blue and red dots represent earthquakes that do not satisfy and satisfy the condition $N_{i+1} - N_i + 1.5\sigma < 1$. Black circles indicate earthquake sequences that satisfy the condition for four or more successive events.

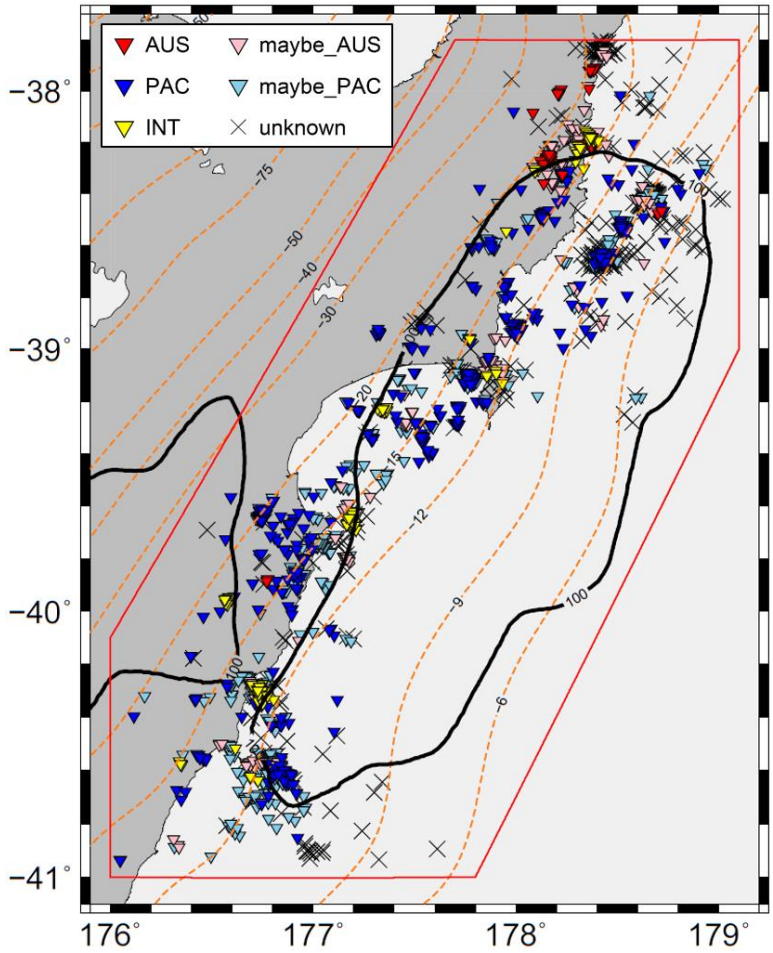

Figure 4.2. Distribution of detected swarm events. Red, blue, yellow, pink, and light blue inverted triangles are AUS, PAC, INT, maybe_AUS, and maybe_PAC earthquakes, respectively. Black crosses are unknown earthquakes. Black contours are cumulative SSE slips of 100 mm between 2002-2020 (Wallace, 2020; Woods, 2022). Orange dashed line contours are the iso-depth of the subducted Pacific plate surface (in kilometers) estimated by Williams et al. (2013). The red line indicates the study area.

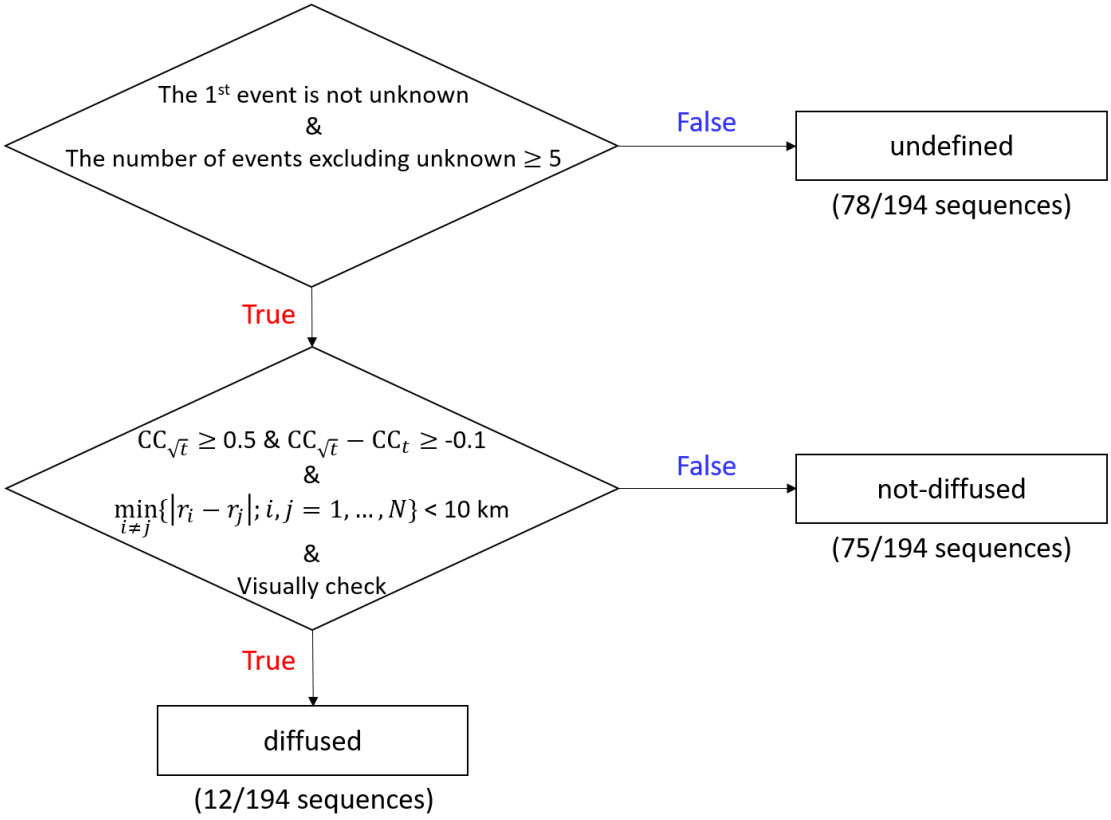

Figure 4.3. Flowchart for classification of swarm sequences.

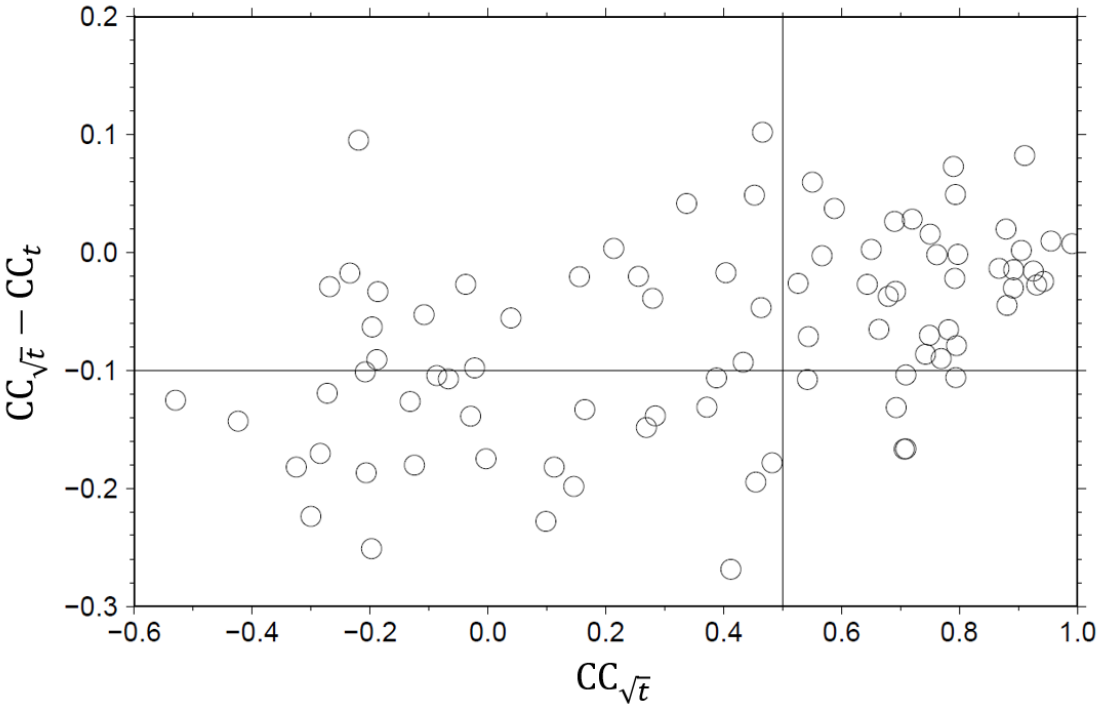

Figure 4.4. The relationship between $CC_{\sqrt{t}} - CC_t$ and $CC_{\sqrt{t}}$. The vertical and horizontal lines indicate the threshold of $CC_{\sqrt{t}}$ = 0.5 and $CC_{\sqrt{t}} - CC_t$ = -0.1, respectively.

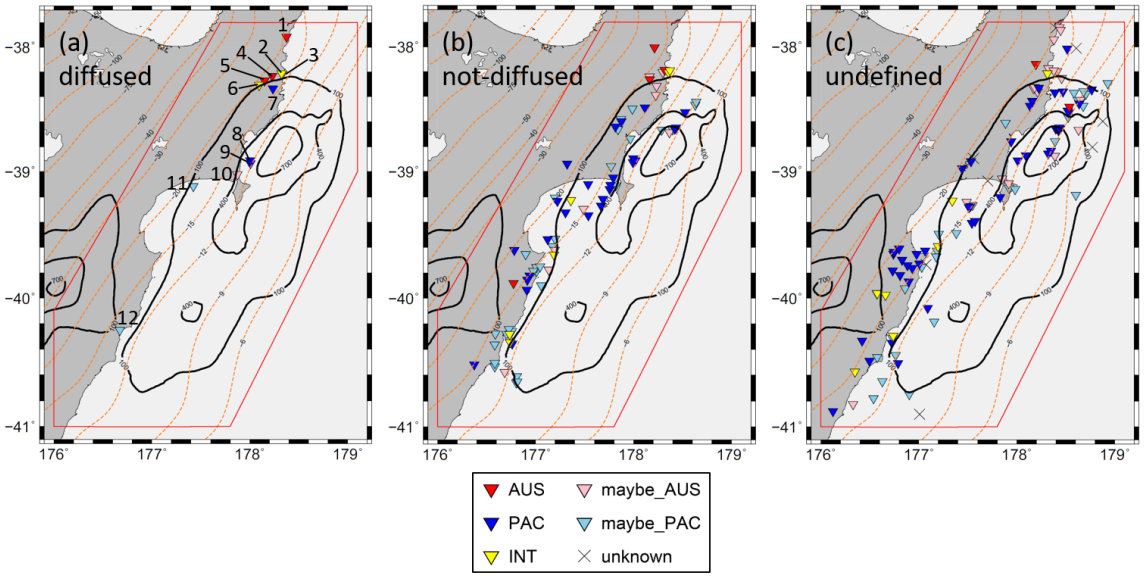

Figure 4.5. Distribution of three types of swarm sequences. (a) Distribution of "diffused" sequences. The number corresponds to the event number in Table 4.2. (b) Distribution of "not-diffused" sequences. (c) Distribution of "undefined" sequences. The location of a sequence represents the mean location of all events in the sequence. The type of sequence (AUS, INT, or PAC) is the most common classification type in the sequence.

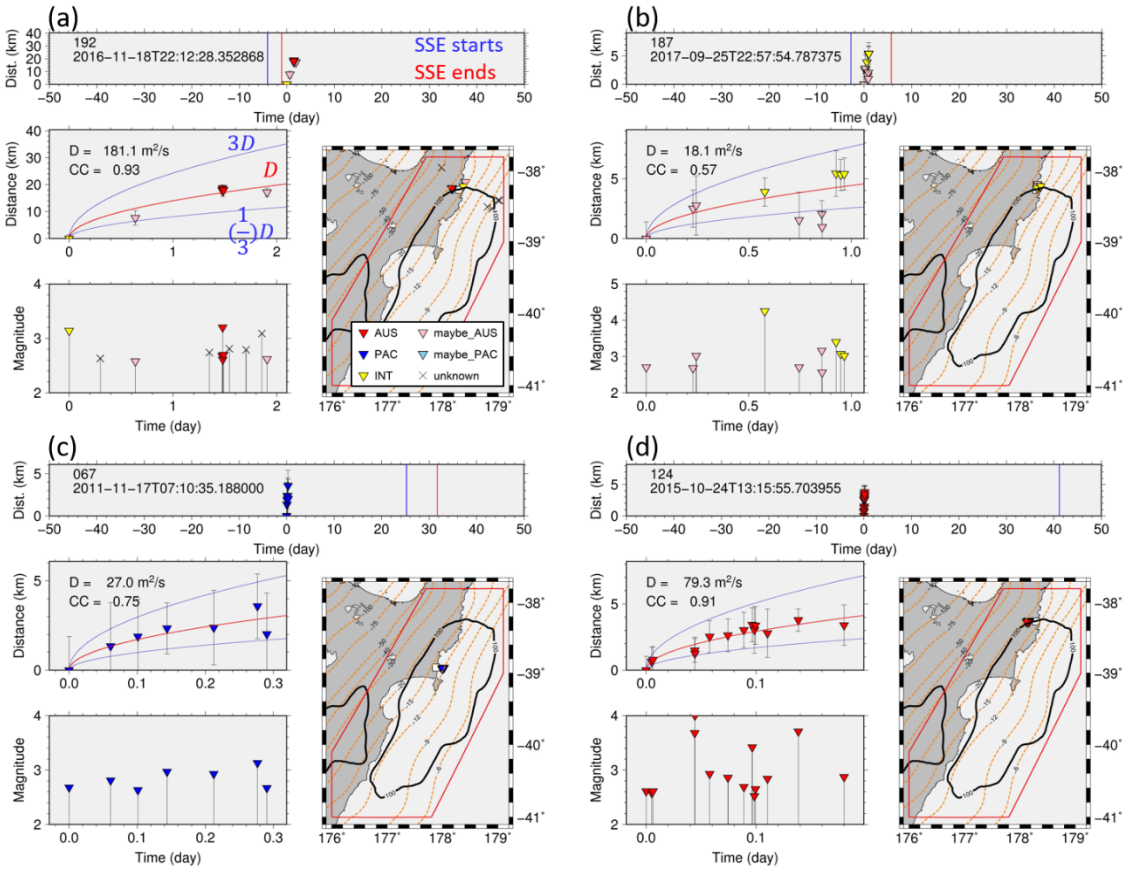

Figure 4.6. Four examples of "diffused" sequences. (a) The swarm sequence consisted of AUS, INT, and maybe_AUS events. (b) The swarm sequence consisted of INT and maybe_AUS events. (c) The swarm sequence consisted of PAC events. (d) The swarm sequence consisted of AUS events. (Upper left panel) The relationship between the time and distance from the first event in the sequence. The vertical blue and red lines indicate estimated SSE start and end times, respectively. The number and date on the left are the sequence number and the date of the first event, respectively. (Middle left panel) The enlarged figure of the upper left panel. A red curve is the diffusion curve with estimated diffusivity D. Blue curves are diffusion curves with diffusivity of $3D$ and $\frac{1}{3}D$. (Lower left panel) Magnitude-time diagram. (Lower right panel) Distribution of events in the sequence.

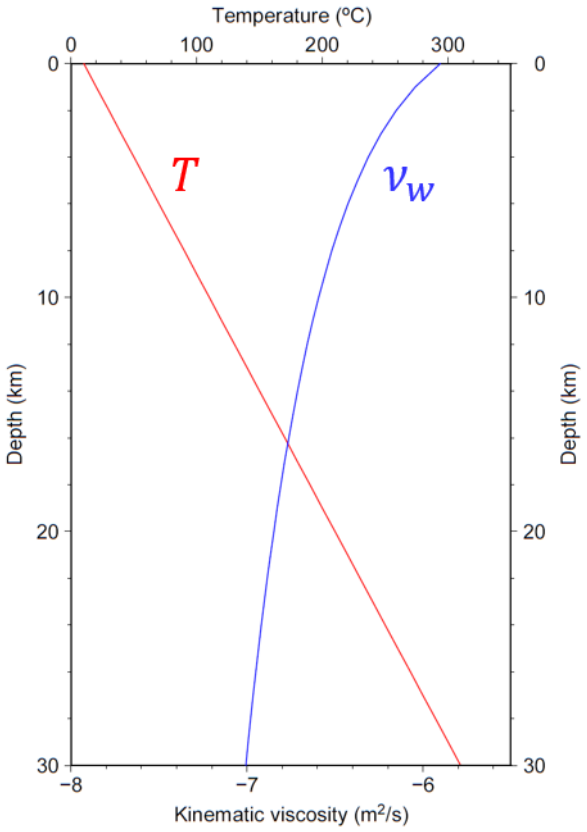

Figure 4.7. Depth-dependent temperature T and kinematic viscosity ν_w.

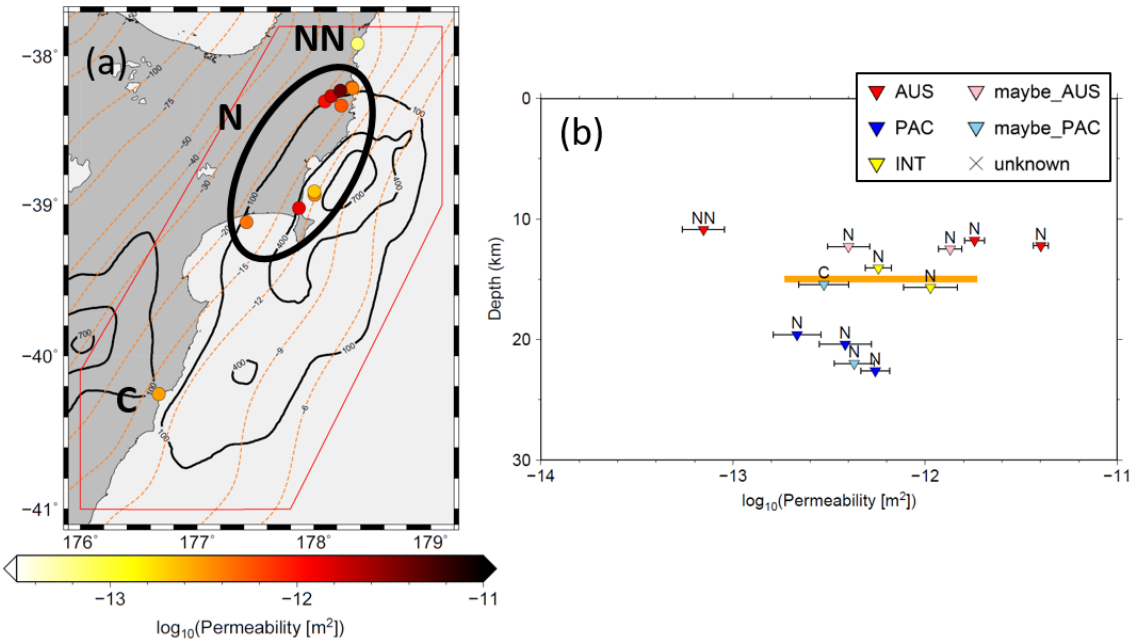

Figure 4.8. Estimated permeability for "diffused" swarm sequences. (a) Distribution of permeability. Sequences are divided into three regions: NN, N, and C. (b) The relationship between estimated permeability and depth of the sequence. Characters above each triangle correspond to the region. A horizontal orange bar indicates the permeability range from Perez-Silva et al. (2023).

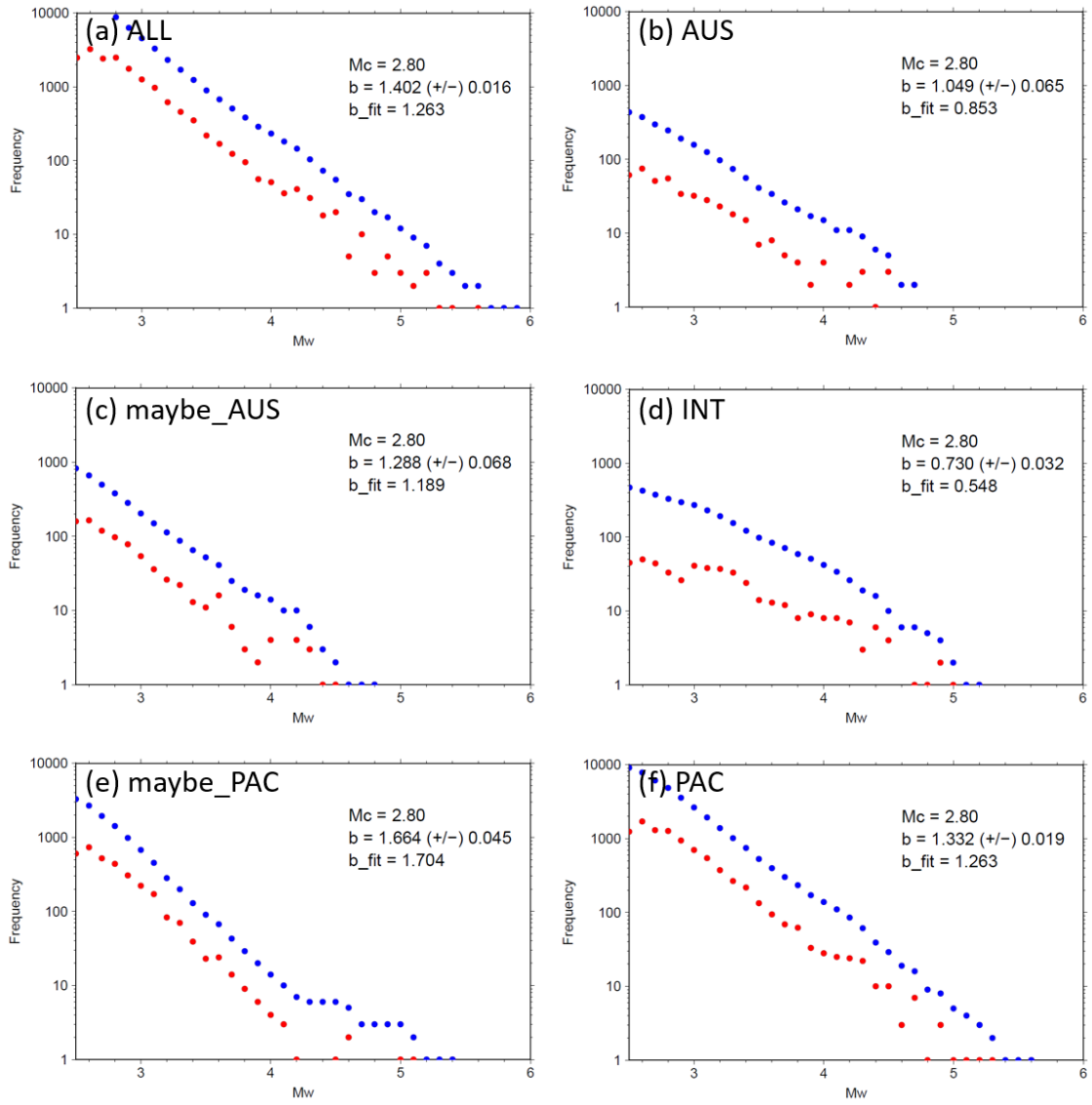

Figure 4.9. The magnitude-frequency distribution using (a) all events, (b) AUS events, (c) maybe_AUS events, (d) INT events, (e) maybe_PAC events, and (f) PAC events in the whole study area. The red dots indicate the number of earthquakes in the magnitude bin 0.1. The blue dots indicate the cumulative number of earthquakes greater than the magnitude. The Mc is the magnitude of completeness estimated. The b and b_fit are the estimated b-values with the maximum likelihood and the goodness-of-fit, respectively.

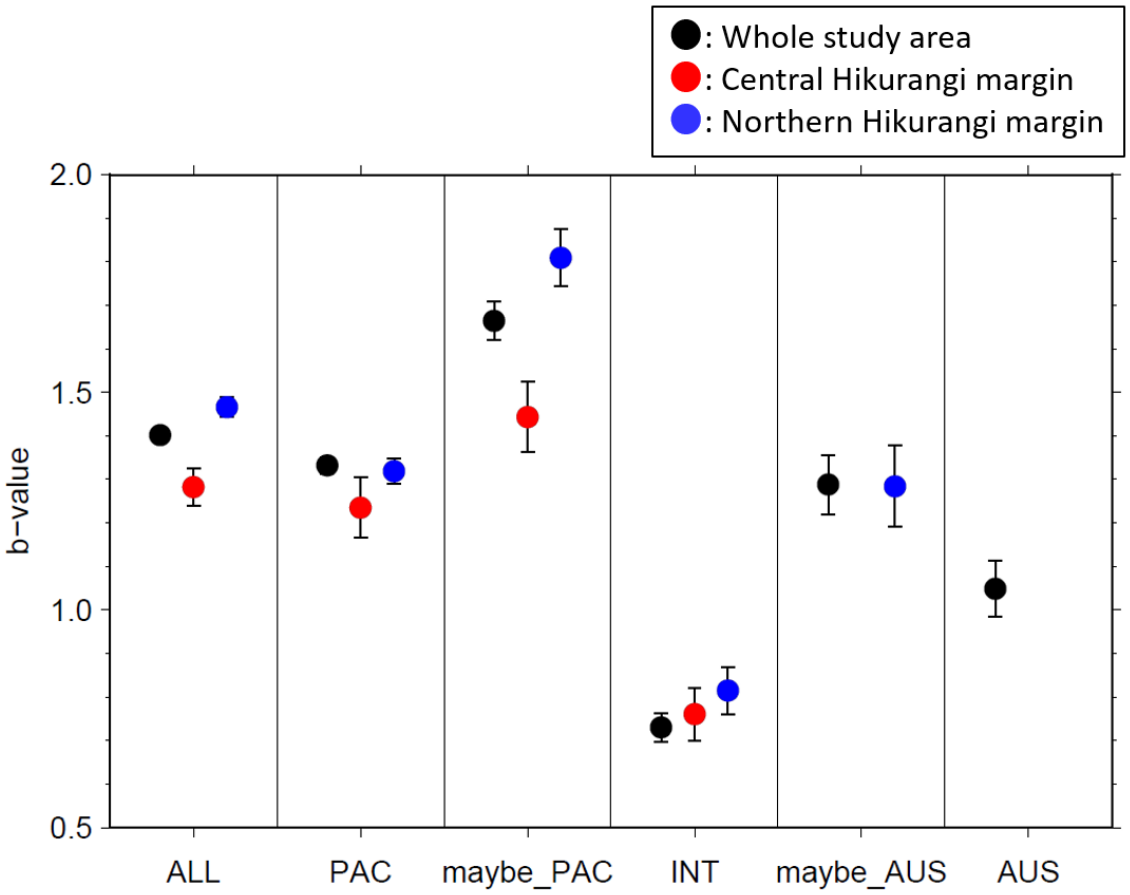

Figure 4.10. The b-values estimated from the maximum likelihood method. Black, red, and blue circles indicate the b-value for the whole study area, central Hikurangi margin, and northern Hikurangi margin, respectively. The b-values are estimated and plotted if the number of events is greater than 100.

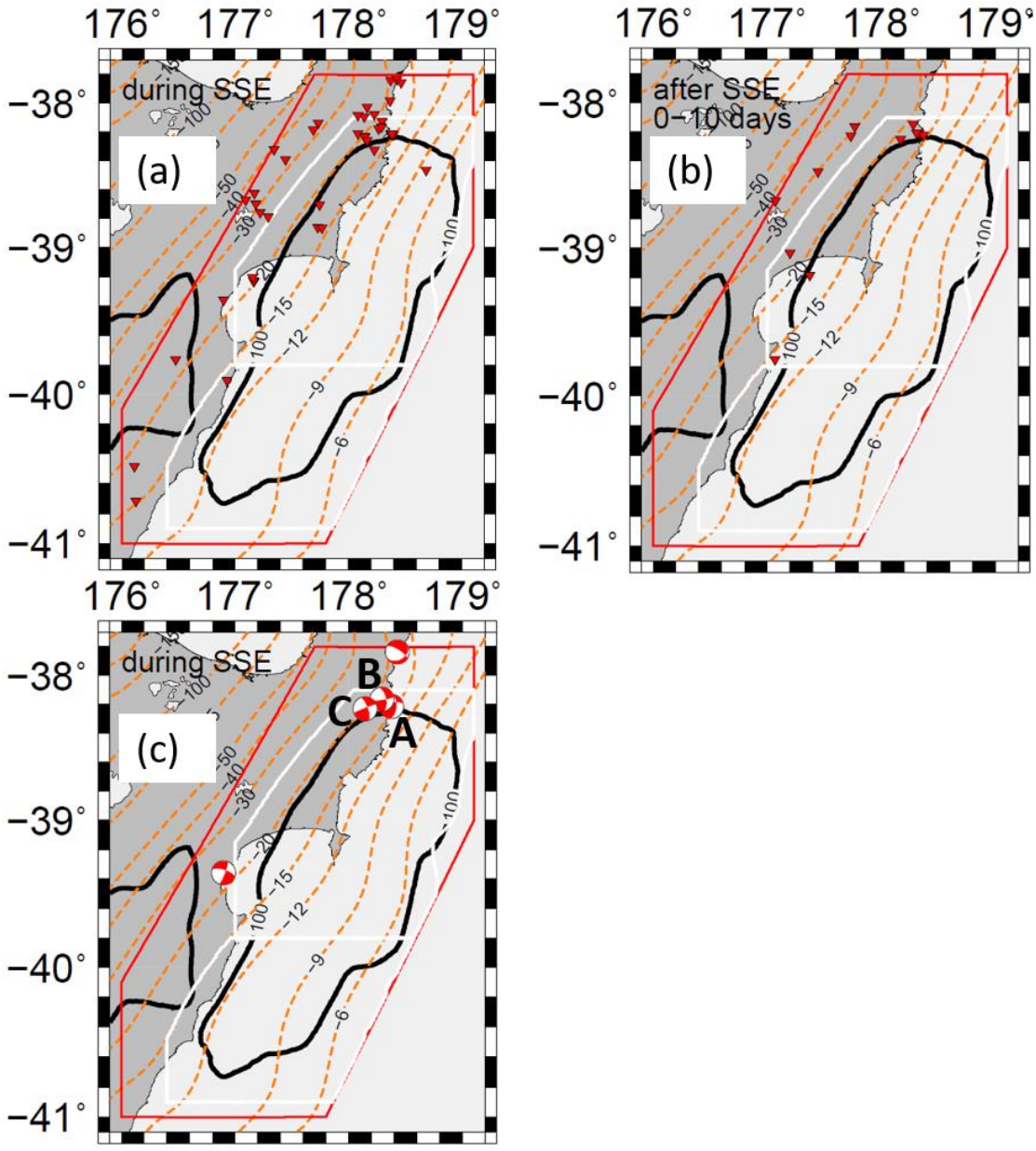

Figure 4.11. Distribution of AUS events. (a) AUS events during SSEs. (b) AUS events 0-10 days after SSEs. (c) Focal mechanisms of AUS events during SSEs. Events A, B, and C occurred in northern Hikurangi and were accompanied with known SSEs. White lines indicate the area of northern and central Hikurangi. No events were obtained for their focal mechanisms 0-10 days after SSEs.

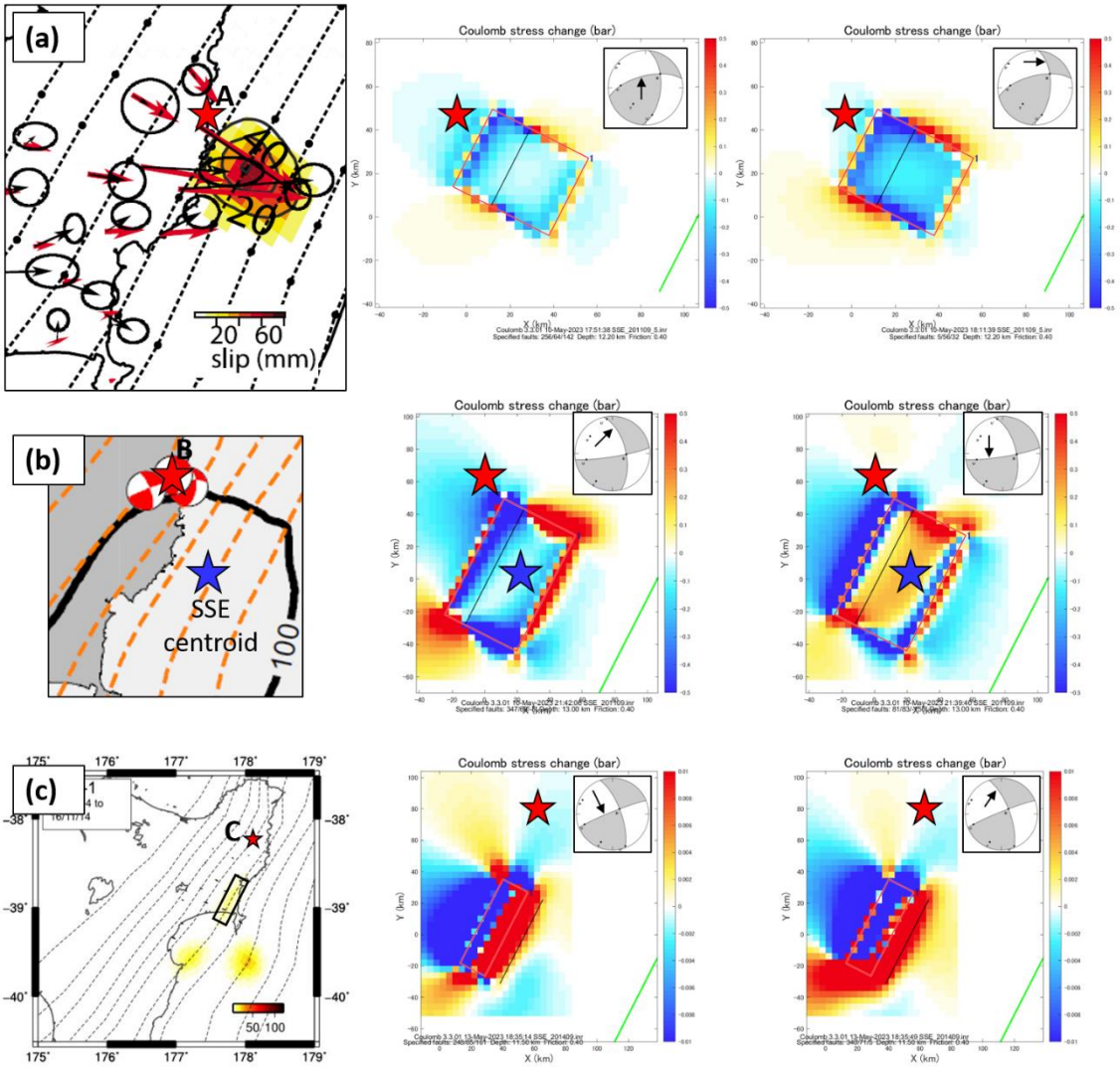

Figure 4.12. Computed Coulomb stress change for AUS events during SSEs. (a) For AUS event A. (Left panel) The SSE slip contour from Wallace et al. (2012). The red star is the epicenter of event A. (Middle and right panels) Coulomb stress change (in bar) at the depth of event A. The red rectangular is the SSE source. The inserted beach ball and arrow indicate the nodal plane used to compute Coulomb stress change. (b) For AUS event B. The blue star indicates the centroid of SSE from Gomberg et al. (2020). (c) For AUS event C. The SSE slip contour is from Warren-Smith et al. (2019). Focal mechanisms were created using Earthquake Focal Mechanism software (Zimmermann, 2009).

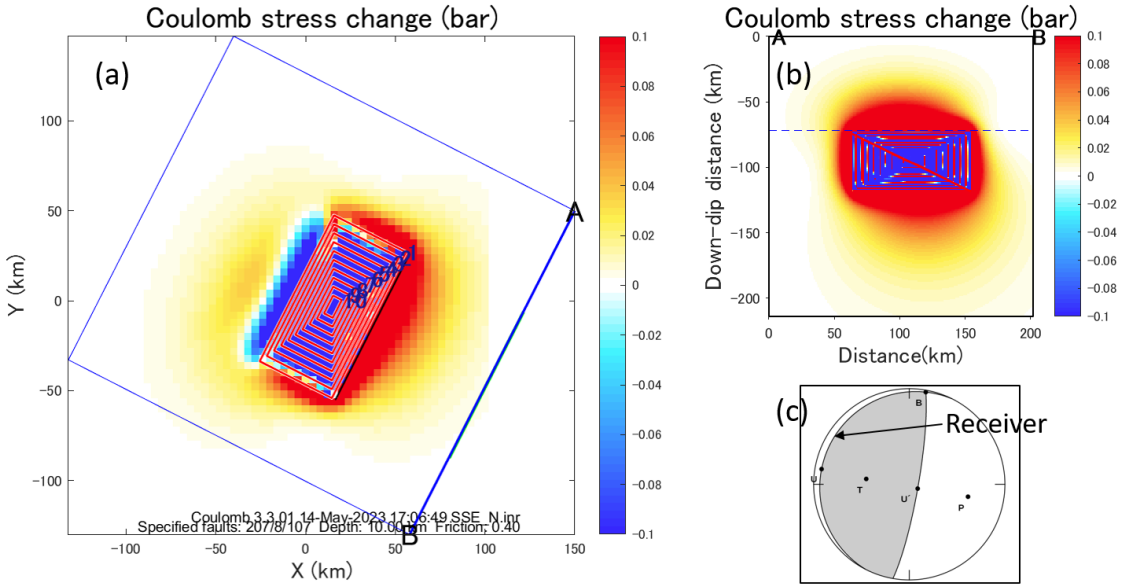

Figure 4.13. Coulomb stress change for favorable INT events. (a) Coulomb stress change at the top depth of the SSE source. Red rectangles are nested-SSE sources with a maximum slip of 150 mm and magnitude of 6.5. The blue rectangle indicates the area for the along-dip view. (b) Coulomb stress change along the SSE source fault. (c) Receiver fault geometry that is the same as the SSE source. Focal mechanisms were created using Earthquake Focal Mechanism software (Zimmermann, 2009).

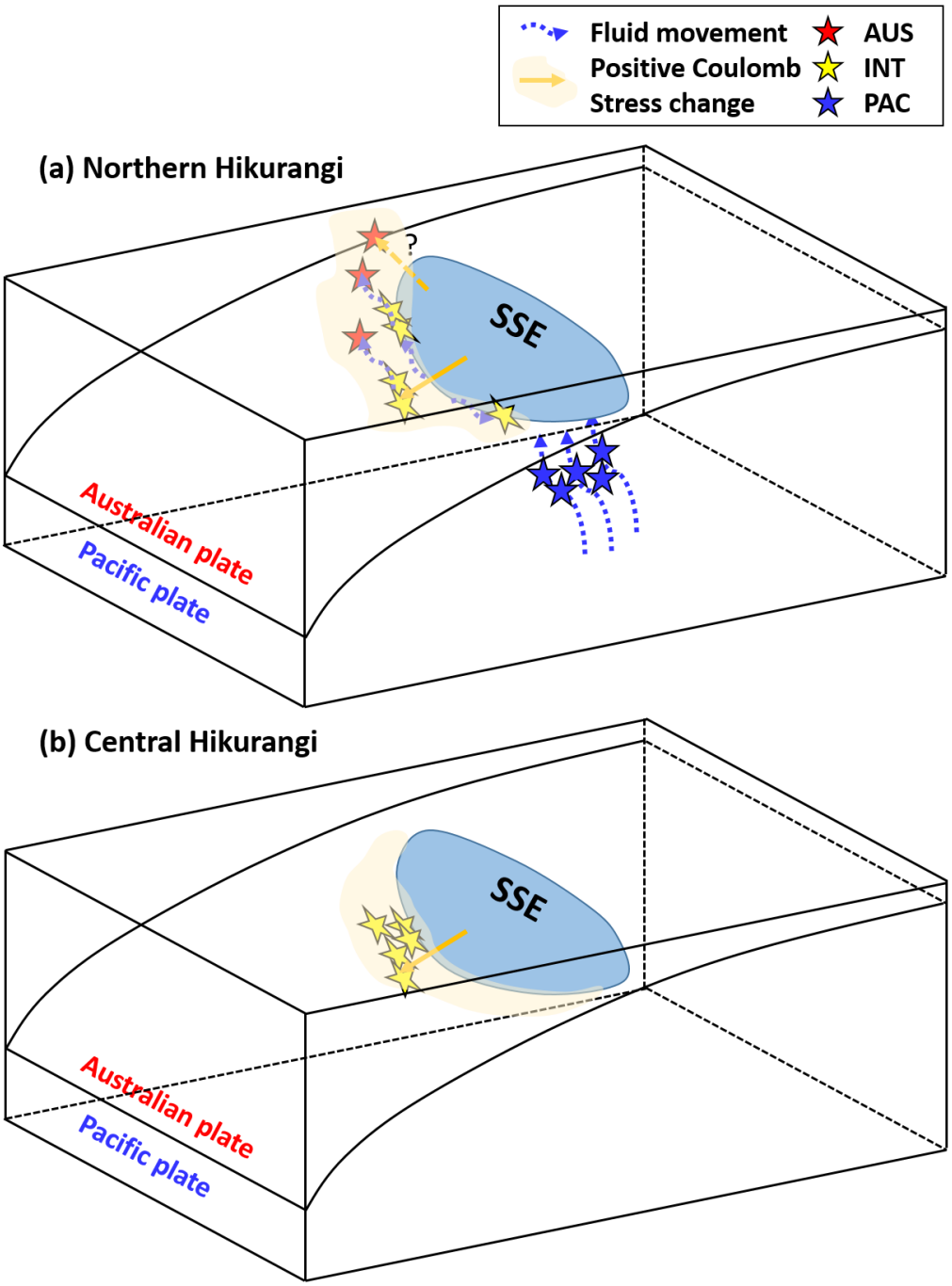

Figure 4.14. Conceptual model of earthquake mechanisms related to SSEs (a) for the northern Hikurangi margin and (b) the central Hikurangi margin. Red, yellow, and blue stars indicate AUS, INT, and PAC events, respectively. The blue arrow indicates fluid movement. The orange arrow and light yellow shade indicate positive Coulomb stress change induced by SSEs.

Chapter 5.
Conclusion

In many subduction zones around the world SSEs regularly occur almost simultaneously with inter-plate, intra-slab, and overriding plate earthquakes surrounding SSEs. This study revealed how the earthquakes were triggered and related to SSEs in the northern and central Hikurangi margins, New Zealand, a region known for repeated SSE activities. Our detailed spatiotemporal earthquake analysis showed the differences between the northern and central Hikurangi margins as follows.

1. The northern Hikurangi margin

   PAC events (earthquakes in the Pacific plate) were activated 0-20 days before SSEs, INT events (earthquakes at the plate boundary) and their candidates were activated during SSEs, and AUS events (earthquakes in the Australian plate) were activated 0-10 days after SSEs. We detected "diffused" earthquake swarm sequences which showed migration patterns consistent with fluid diffusion. Ten out of the twelve "diffused" swarm sequences were located here. We detected a "diffused" swarm sequence mainly including AUS events, INT events, and PAC events immediately after, during, and before an SSE, respectively. These results indicate that fluid movement from before SSEs to after SSEs is a possible mechanism of earthquake-triggering in the northern Hikurangi margin.

2. The central Hikurangi margin

   Candidates of INT events were activated during and 0-10 days after SSEs. Unlike the northern Hikurangi margin, activated AUS events after SSEs or activated PAC events before SSEs were not detected in the central Hikurangi margin. We detected only one diffusion-consistent earthquake swarm sequence. These results suggest that the main mechanism of earthquake-triggering in the central Hikurangi margin may be different from that in the northern Hikurangi margin, that is, not the fluid movement but stress loading induced by SSEs.

The difference in earthquake-triggering mechanisms between the northern and central Hikurangi margins is consistent with the volume and ascent rate of vented aqueous fluid (Reyes et al., 2022), velocity structures near the plate boundary (Eberhart-Phillips et al., 2017), and electrical resistivity at the plate interface (Heise et al., 2017; Heise et al., 2019). Further study using earthquakes with smaller magnitudes and evaluating the space-time evolution of SSEs will enable a more detailed view of changes in earthquake-triggering mechanisms along the Hikurangi subduction zone. It would allow us to test the interpretations of this study and its comparison with other subduction zones in the world.

Appendix

A. Parameter dependence of activation patterns

A1. The Kagan angle

The threshold of the Kagan angle to classify INT events was originally 60°. We examined this angle as 50° (Figures A.1, A2) and 70° (Figures A.3, A4). When the threshold was 50°, the activation patterns were almost the same as the original (Kagan angle of 60°). However, when the threshold was 70°, laxer condition, AUS activity of 40-50 days in the northern Hikurangi margin was suppressed.

A2. Cross-correlation

When computing the waveform cross-correlation, 1-10 Hz bandpass filtering was applied, and the threshold of CC was 0.65. We examined the case of 1-20 Hz bandpass filtered cross-correlation with a CC threshold of 0.65 (Figures A.5, A.6) and the case of 1-10 Hz bandpass filtered cross-correlation with a CC threshold of 0.60 (Figures A.7, A.8) and 0.70 (Figures A.9, A.10). The case of 1-20 Hz bandpass filtered CC and the case of CC threshold of 0.70 showed almost the same activation patterns as the case in the main text. When the CC threshold was 0.60, AUS activity of 40-50 days in the northern Hikurangi margin was suppressed, and INT events during SSEs in the central Hikurangi margin were activated.

A3. The GNSS-epicenter distance

The distance between GNSS stations and epicenters was constrained to be shorter than 50 km. We examined the GNSS-epicenter distance of 30 km (Figures A.11, A.12) and 70 km (Figures A.13, A.14). When the distance was 30 km, we cannot find activated AUS events immediately after the SSEs in the northern Hikurangi margin. The activation patterns for the case of 70 km were almost the same as the original ones in the main text.

A4. The b-value, d_f, and η

The b-value and d_f for declustering were estimated and used as 1.41 and 1.71, respectively. We examined activation patterns with b-value of 1.20 (Figures A.15, A.16) and 1.60 (Figures A.17, A.18) and d_f of 1.50 (Figures A.19, A20) and 1.90 (Figures A.21, A.22). The threshold of η for declustering was originally $10^{-6.5}$. We varied this as $10^{-6.2}$ (Figures A.23, A.24) and $10^{-6.8}$ (Figures A.25, A.26). We found that b-value, d_f, and threshold of η did not largely affect the activation patterns in the northern and central Hikurangi margins.

A5. Random SSEs and fixed seismicity

We investigated activation patterns for fixed SSEs and random seismicity in the main text. Here, we tested random SSEs and fixed seismicity (Figure A27, A28). The activation patterns were almost the same as the original ones in the main text. However, maybe_PAC events in the northern

Hikurangi margin were most activated 10-20 days before SSEs, probably indicating that these maybe_PAC events were PAC events.

B. Migration patterns of detected earthquake swarms

We demonstrate the migration patterns of “diffused” sequences (Figure B.1, B.2), which probably follow the fluid migration, “not-diffused” sequences (Figure B.3, B.4), which might not follow the fluid migration, and “undefined” sequences (Figure B.5, B.6), which we cannot evaluate their activities. A sequence in Figure B.3 was not classified as a “diffused” sequence due to the large distance between events (> 30 km). A sequence in Figure B.4 was not classified as the “diffused” sequence due to the large distance between events (> 30 km) and small cross-correlation coefficient. Sequences in Figure B.5 and B.6 were not classified as the “diffused” sequence due to the small number of events in the sequence (< 5).

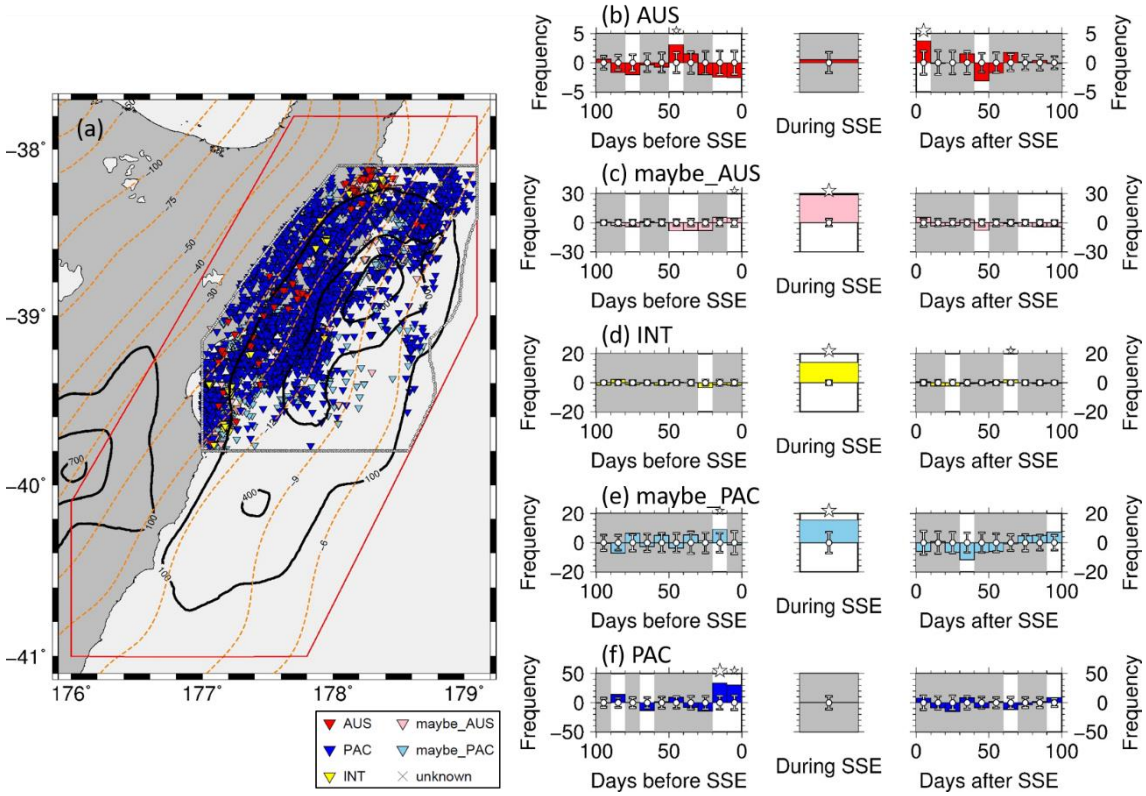

Figure A.1. Activation pattern in the northern Hikurangi margin using a Kagan angle of 50° to classify INT.

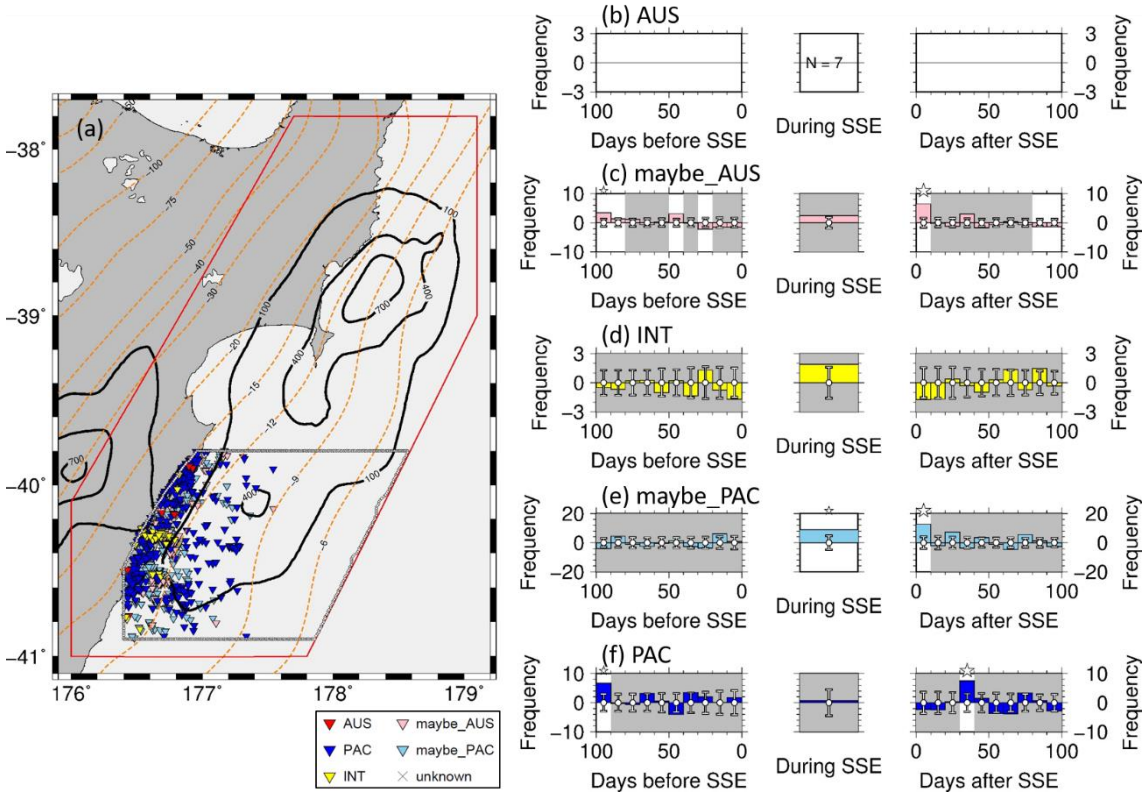

Figure A.2. Activation pattern in the central Hikurangi margin using a Kagan angle of 50° to classify INT.

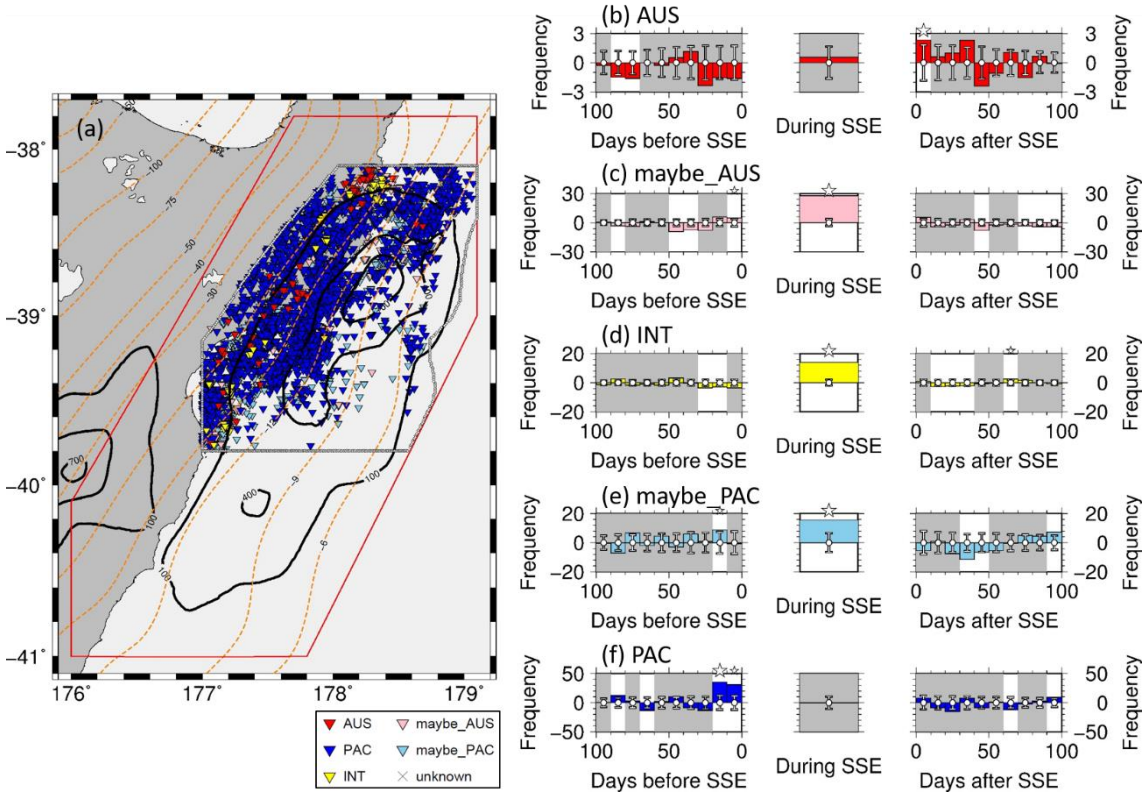

Figure A.3. Activation pattern in the northern Hikurangi margin using a Kagan angle of 70° to classify INT.

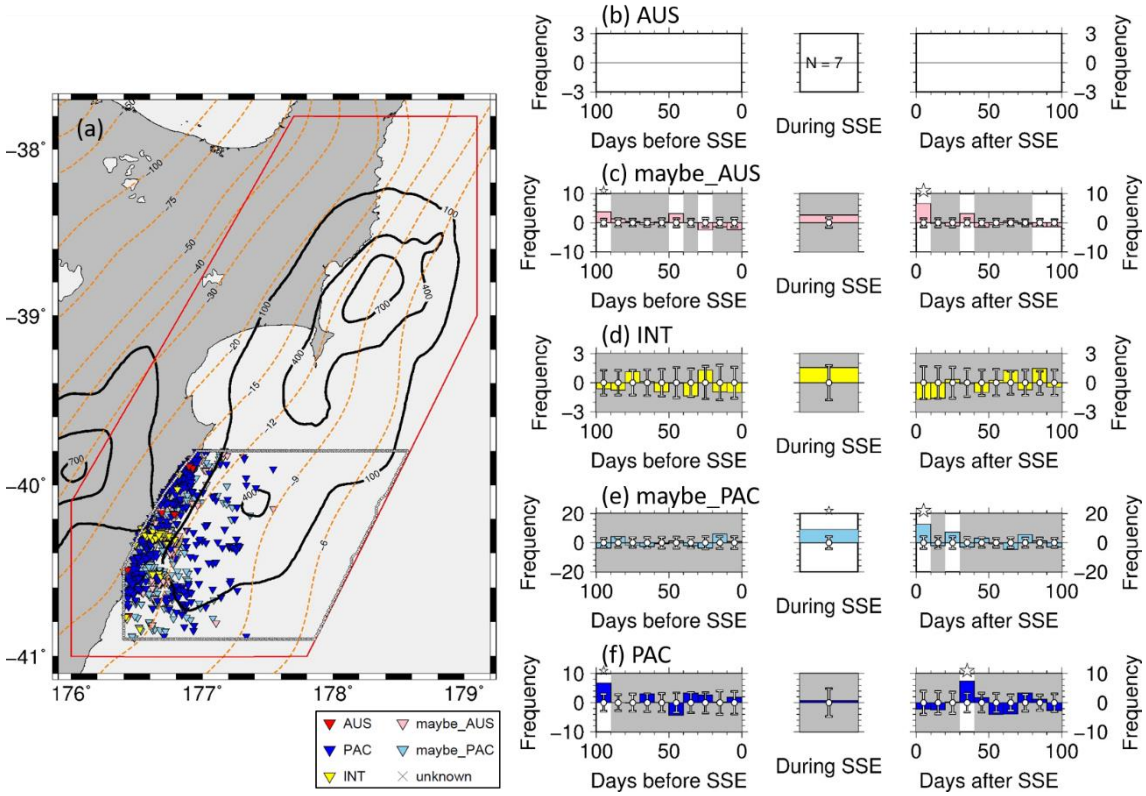

Figure A.4. Activation pattern in the central Hikurangi margin using a Kagan angle of 70° to classify INT.

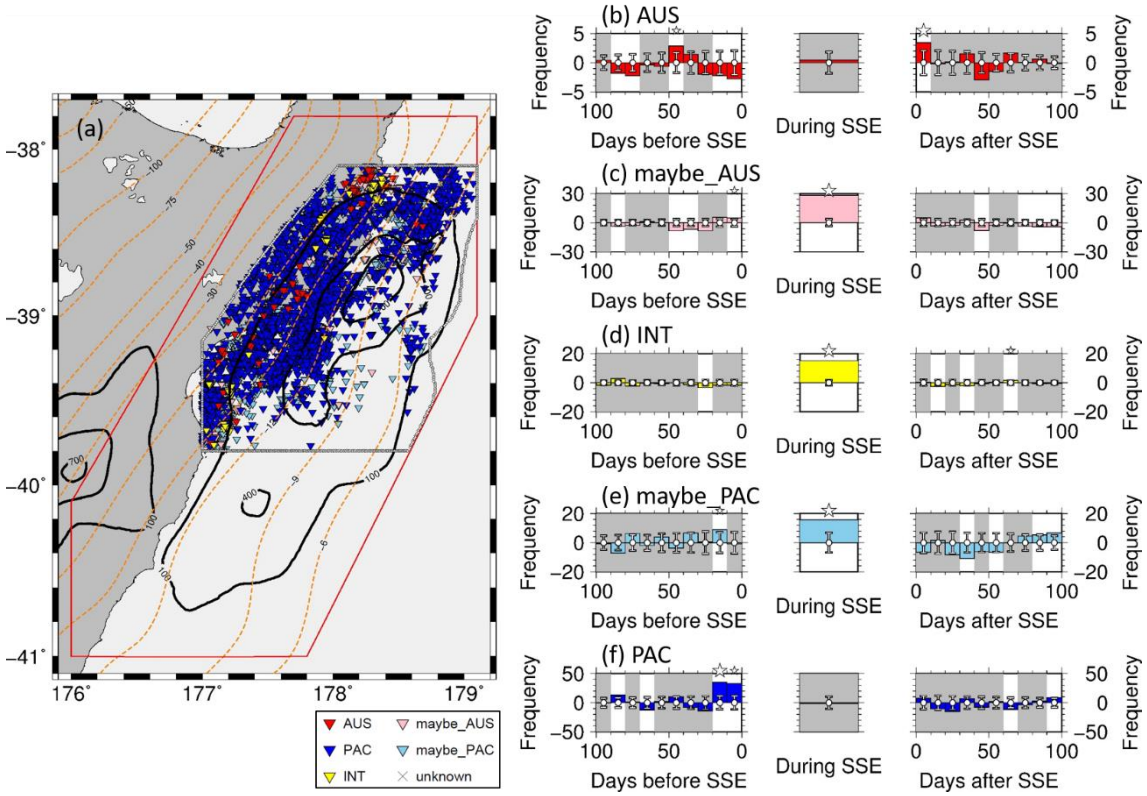

Figure A.5. Activation pattern in the northern Hikurangi margin after applying 1-20 Hz bandpass filter.

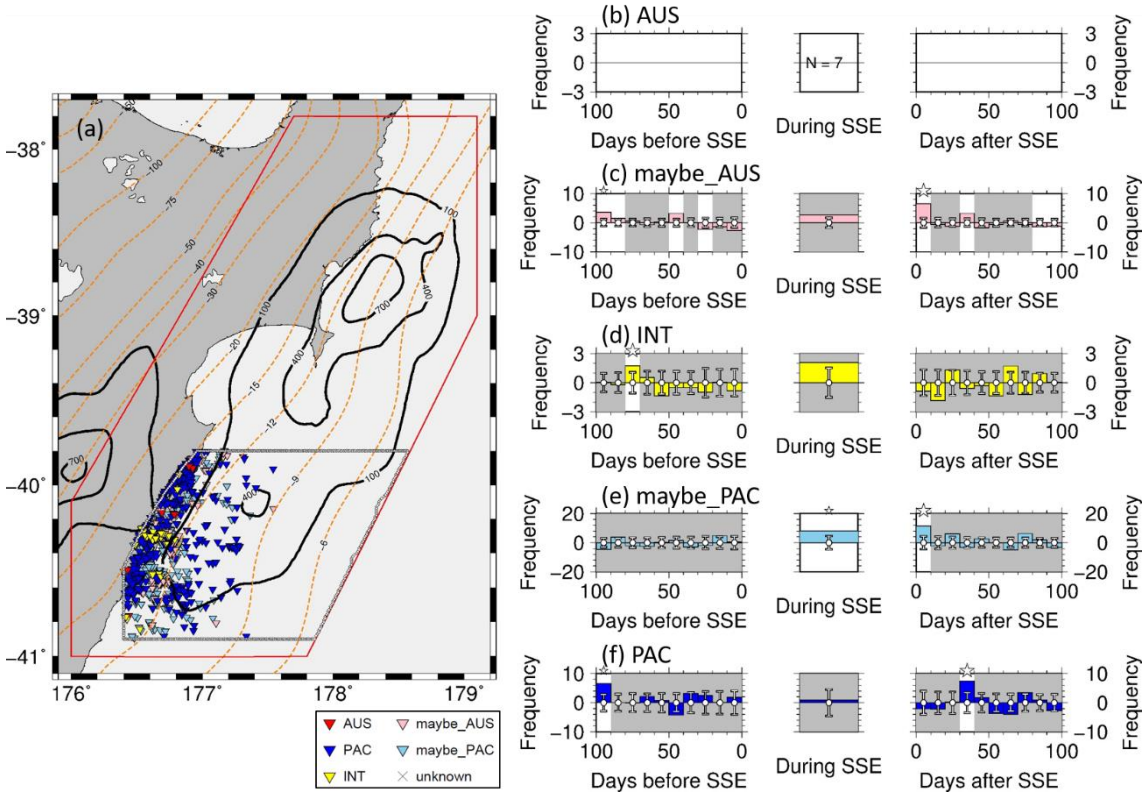

Figure A.6. Activation pattern in the central Hikurangi margin after applying 1-20 Hz bandpass filter.

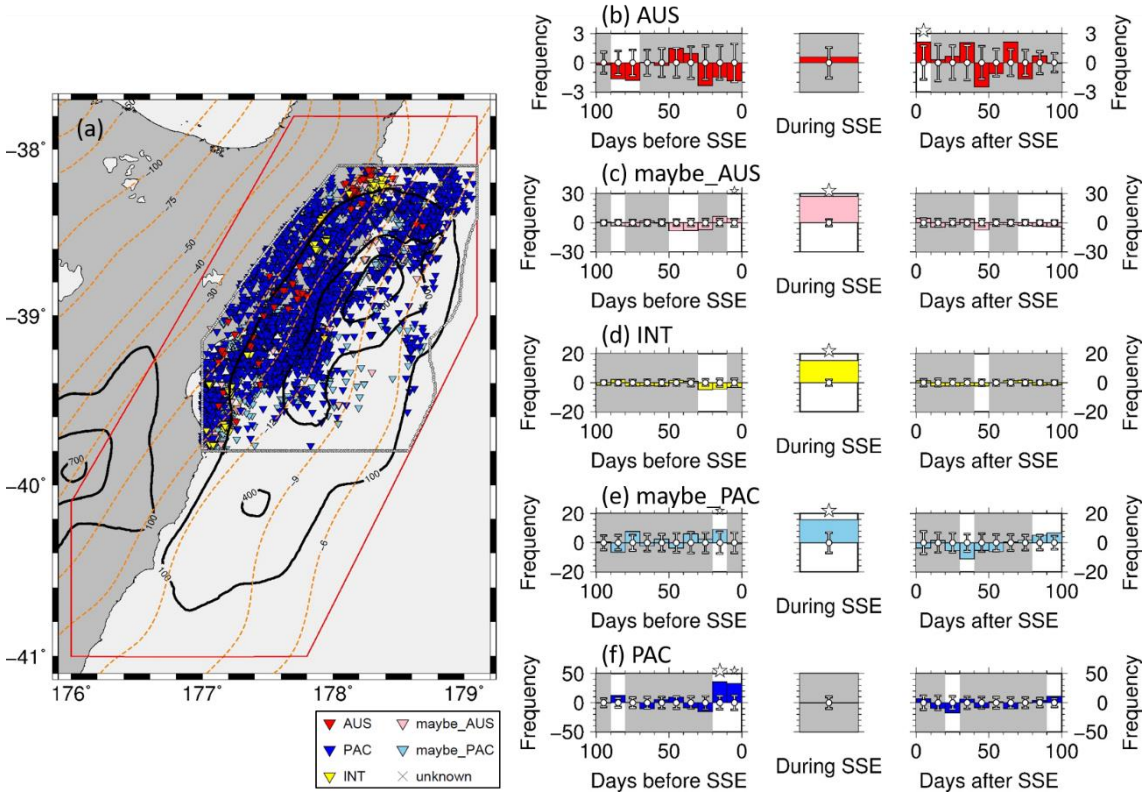

Figure A.7. Activation pattern in the northern Hikurangi margin using a CC threshold of 0.60.

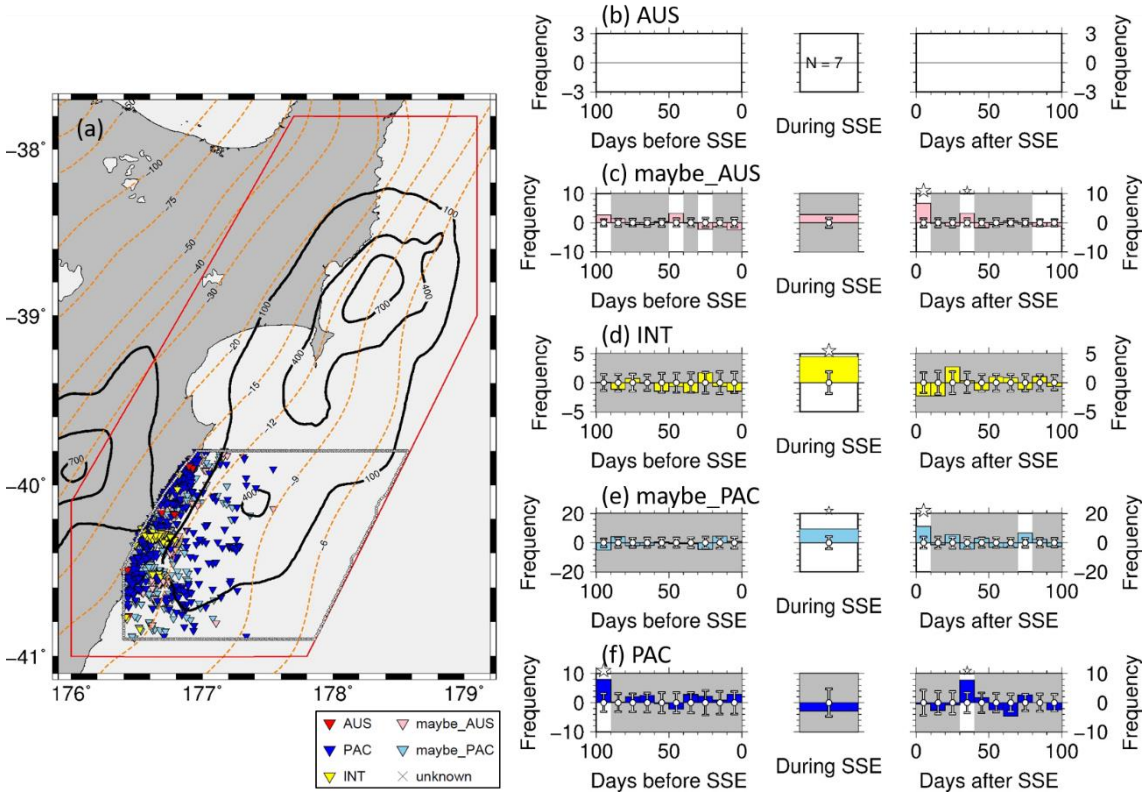

Figure A.8. Activation pattern in the central Hikurangi margin using a CC threshold of 0.60.

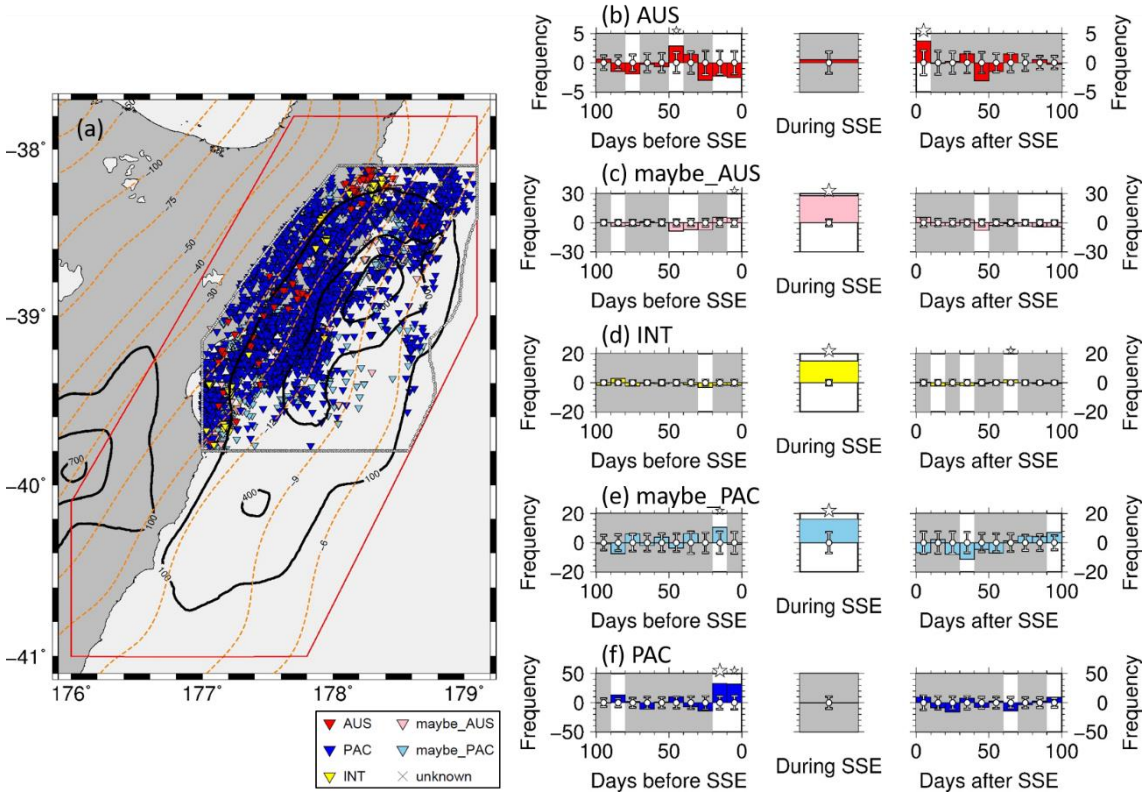

Figure A.9. Activation pattern in the northern Hikurangi margin using a CC threshold of 0.70.

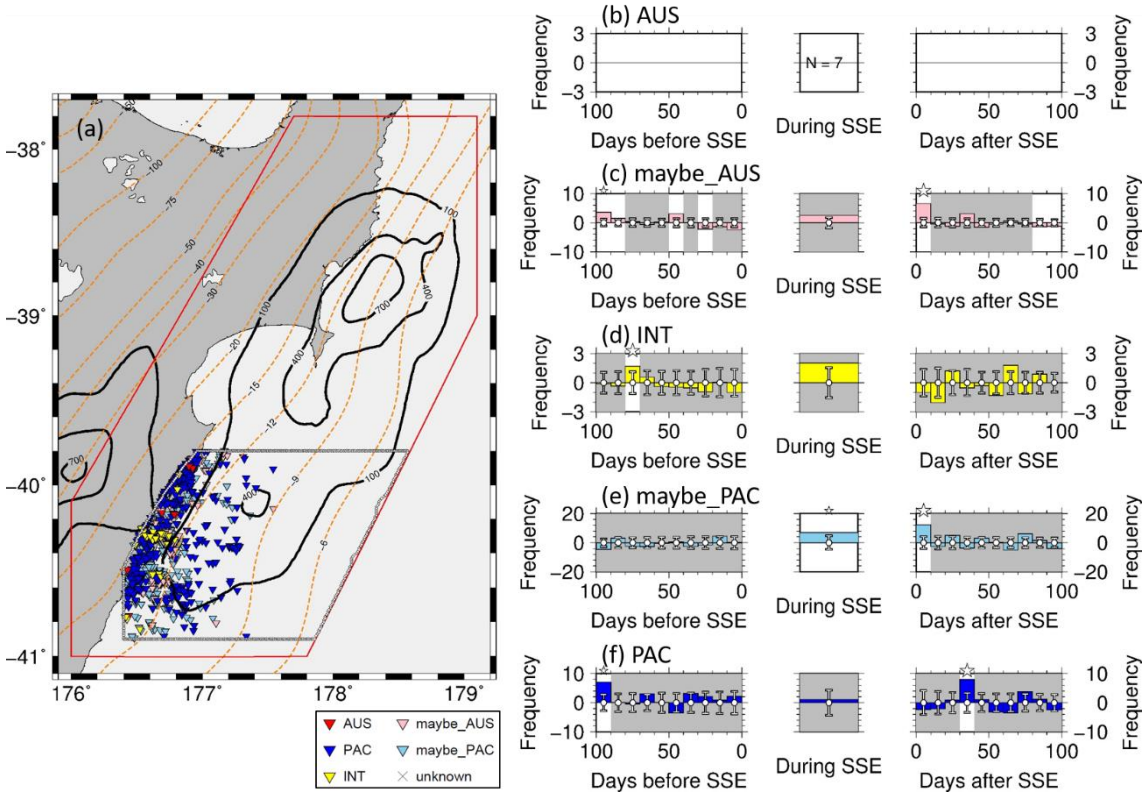

Figure A.10. Activation pattern in the central Hikurangi margin using a CC threshold of 0.70.

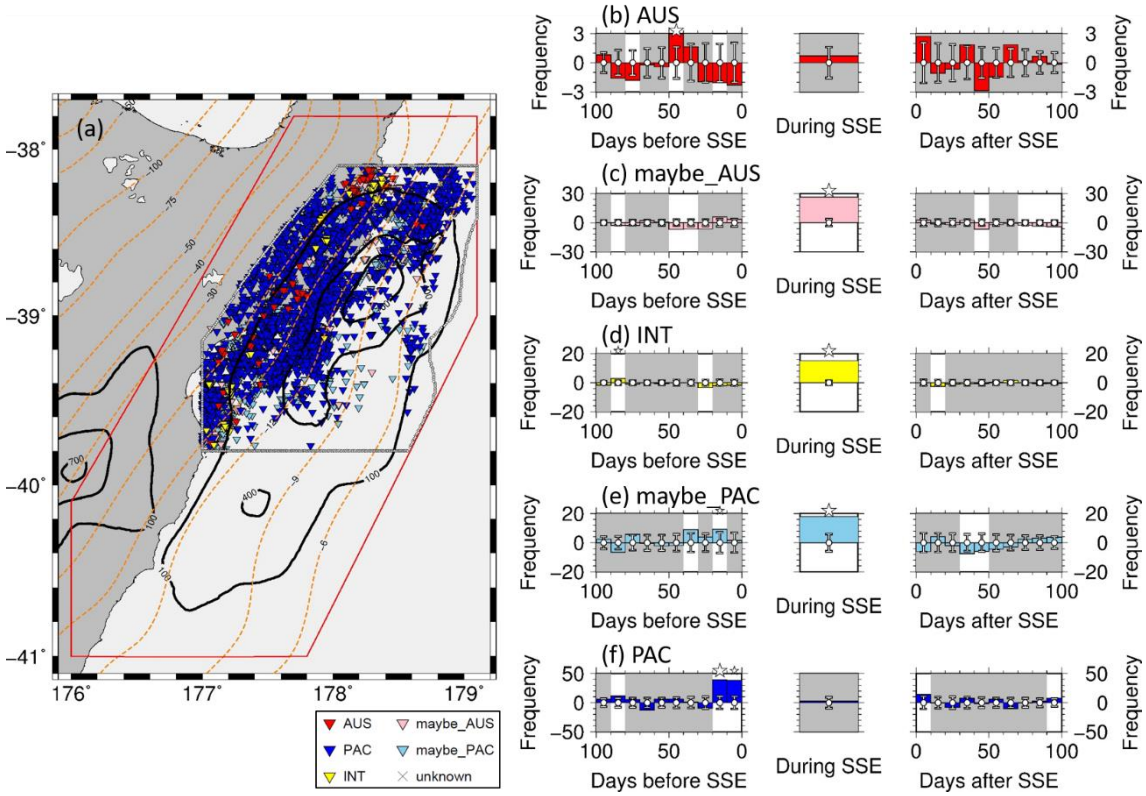

Figure A.11. Activation pattern in the northern Hikurangi margin using GNSS-epicenter distance shorter than 30 km.

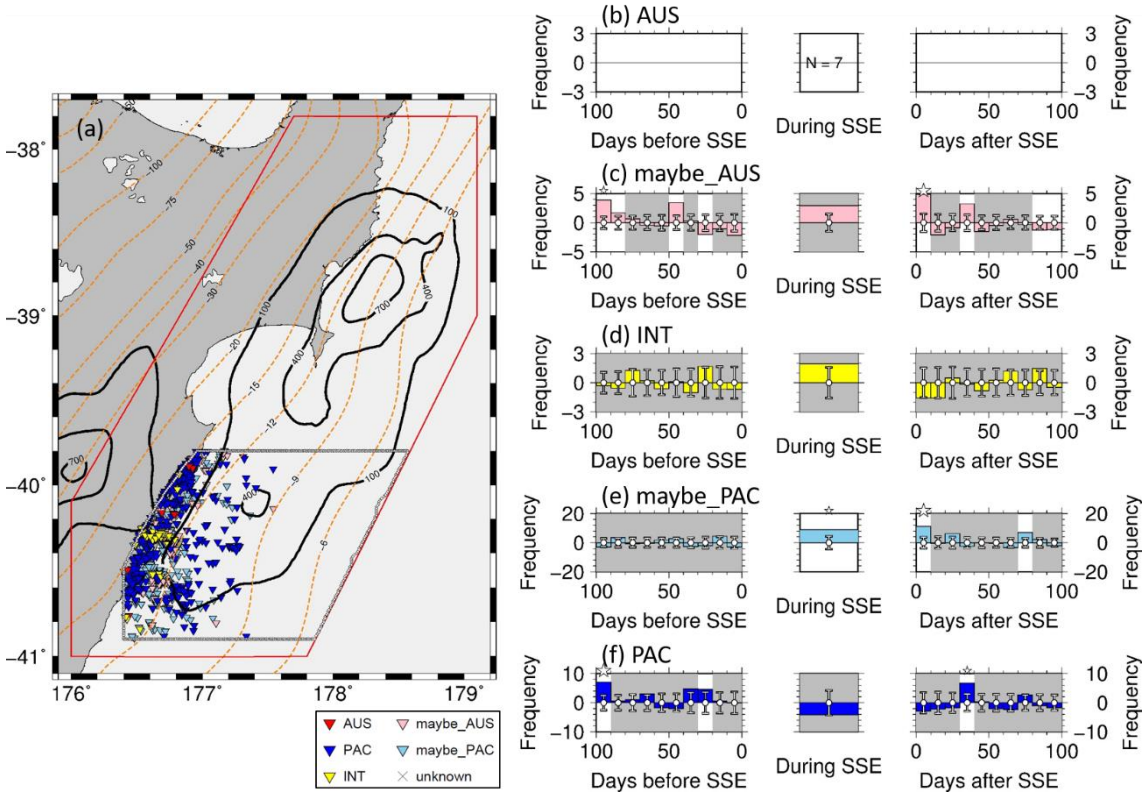

Figure A.12. Activation pattern in the central Hikurangi margin using GNSS-epicenter distance shorter than 30 km.

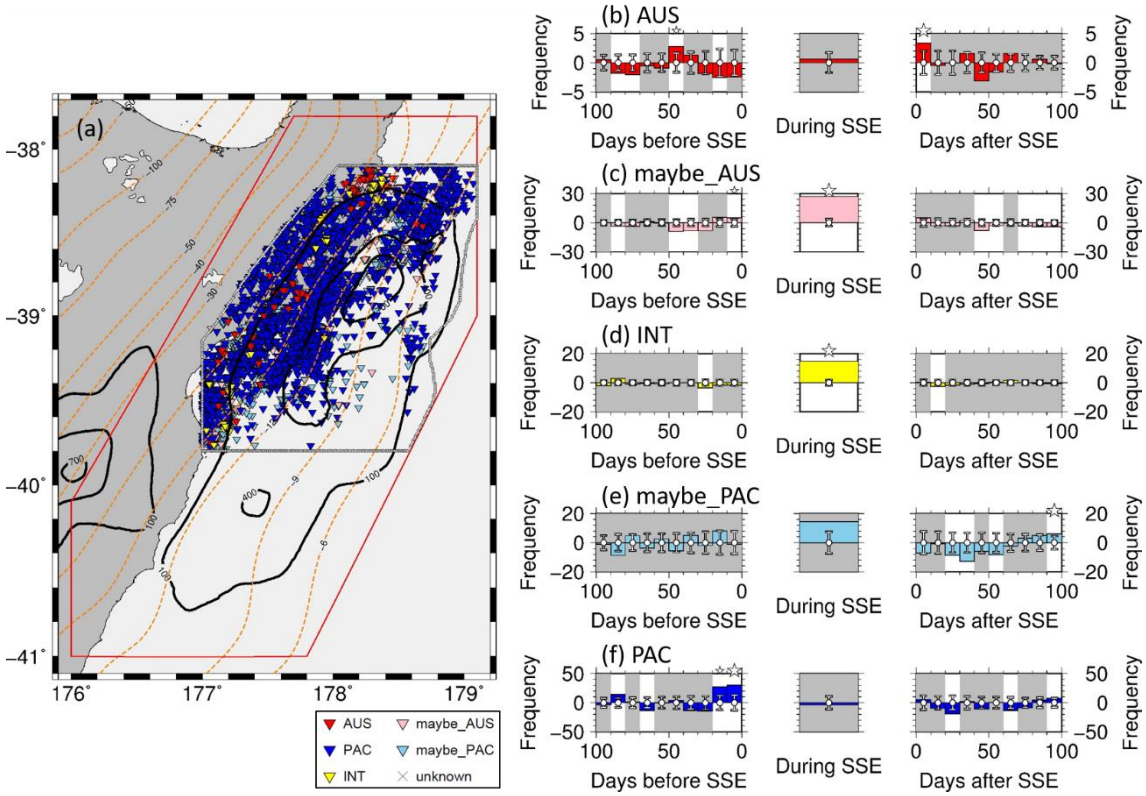

Figure A.13. Activation pattern in the northern Hikurangi margin using GNSS-epicenter distance shorter than 70 km.

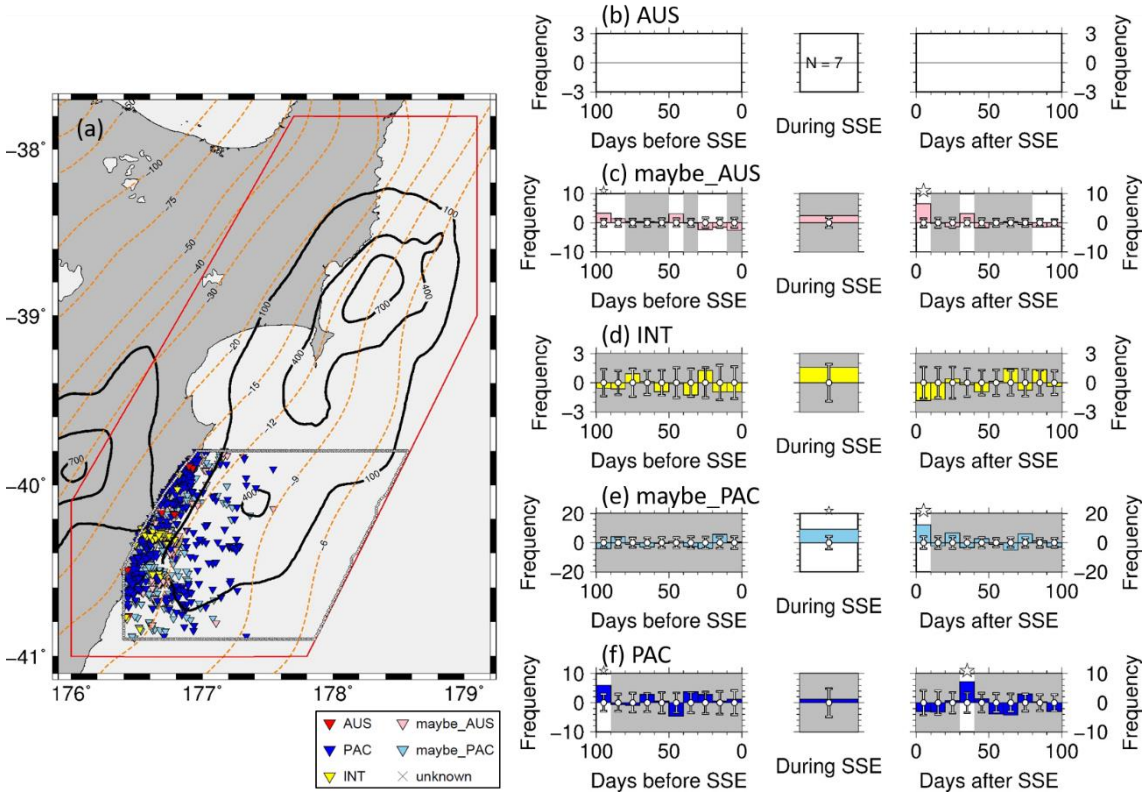

Figure A.14. Activation pattern in the central Hikurangi margin using GNSS-epicenter distance shorter than 70 km.

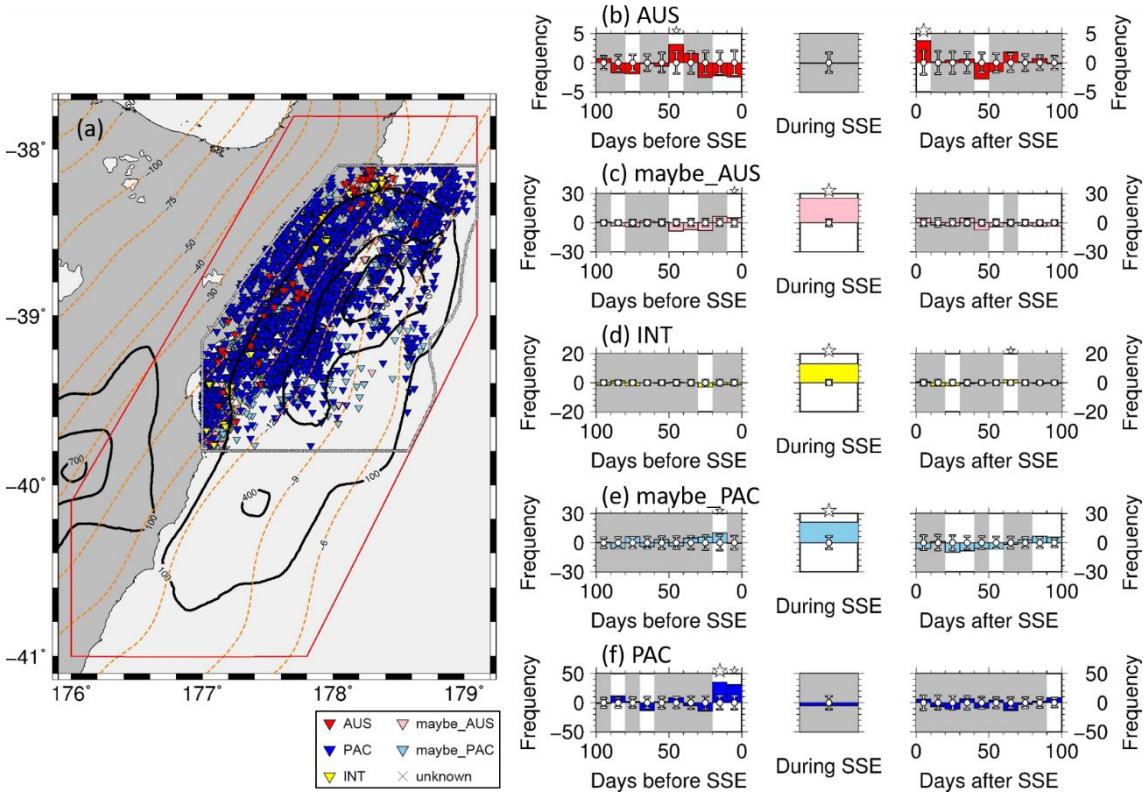

Figure A.15. Activation pattern in the northern Hikurangi margin with a b-value of 1.20 calculating space-time distance.

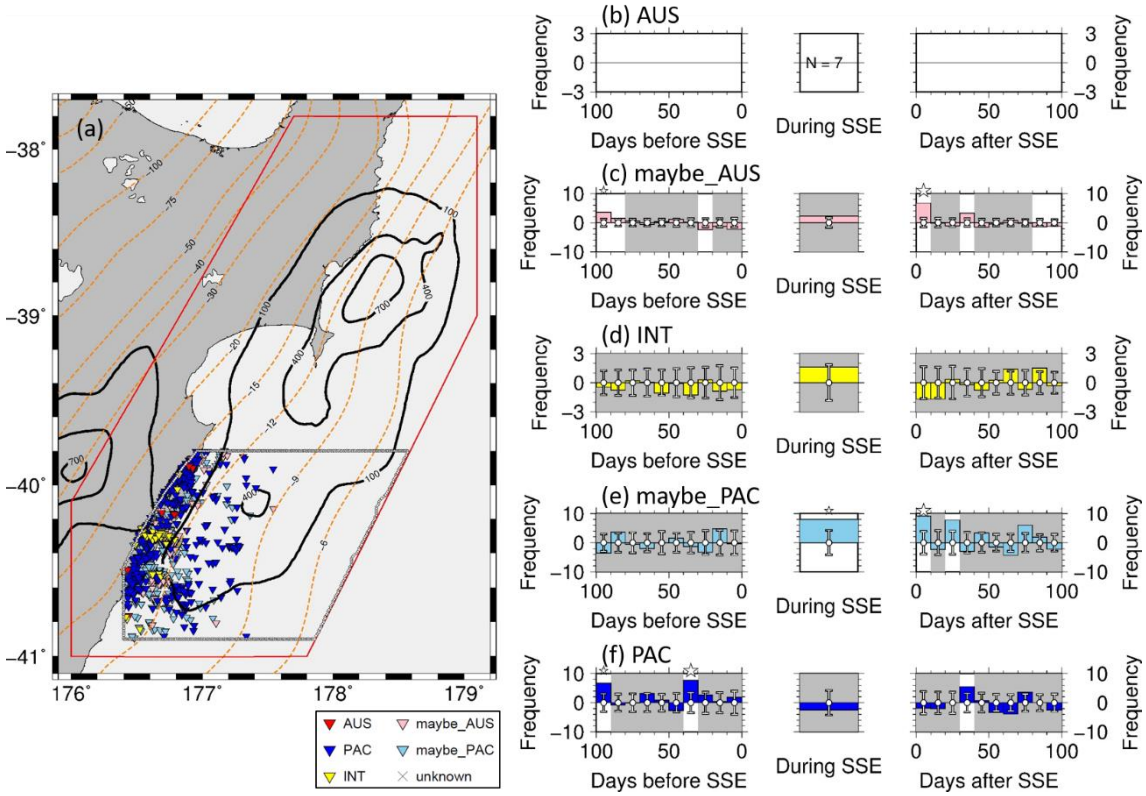

Figure A.16. Activation pattern in the central Hikurangi margin with a b-value of 1.20 calculating space-time distance.

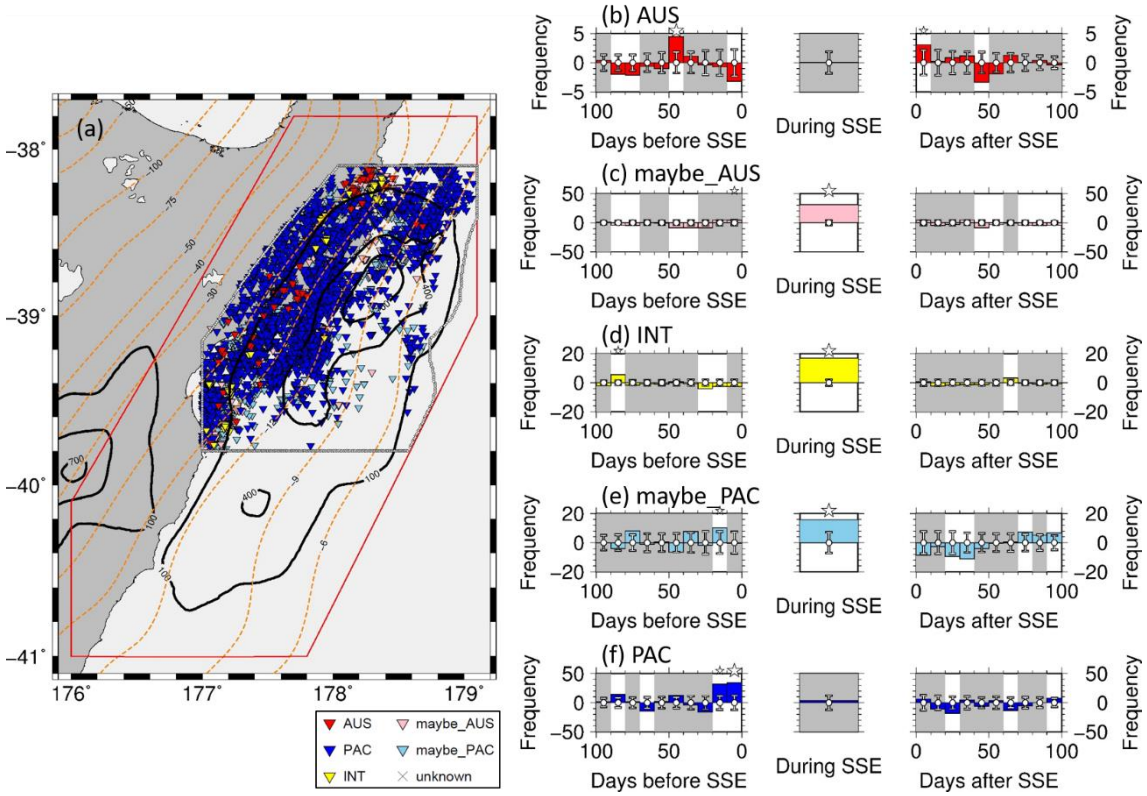

Figure A.17. Activation pattern in the northern Hikurangi margin with a b-value of 1.60 calculating space-time distance.

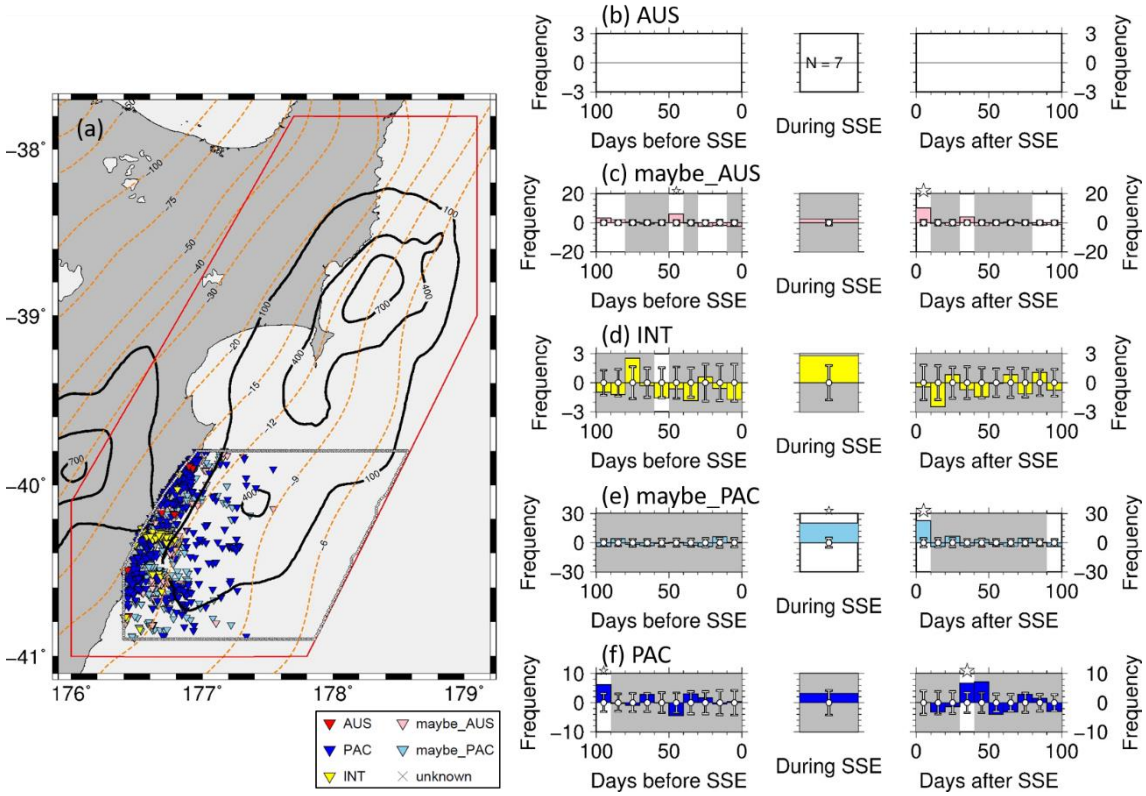

Figure A.18. Activation pattern in the central Hikurangi margin with a b-value of 1.60 calculating space-time distance.

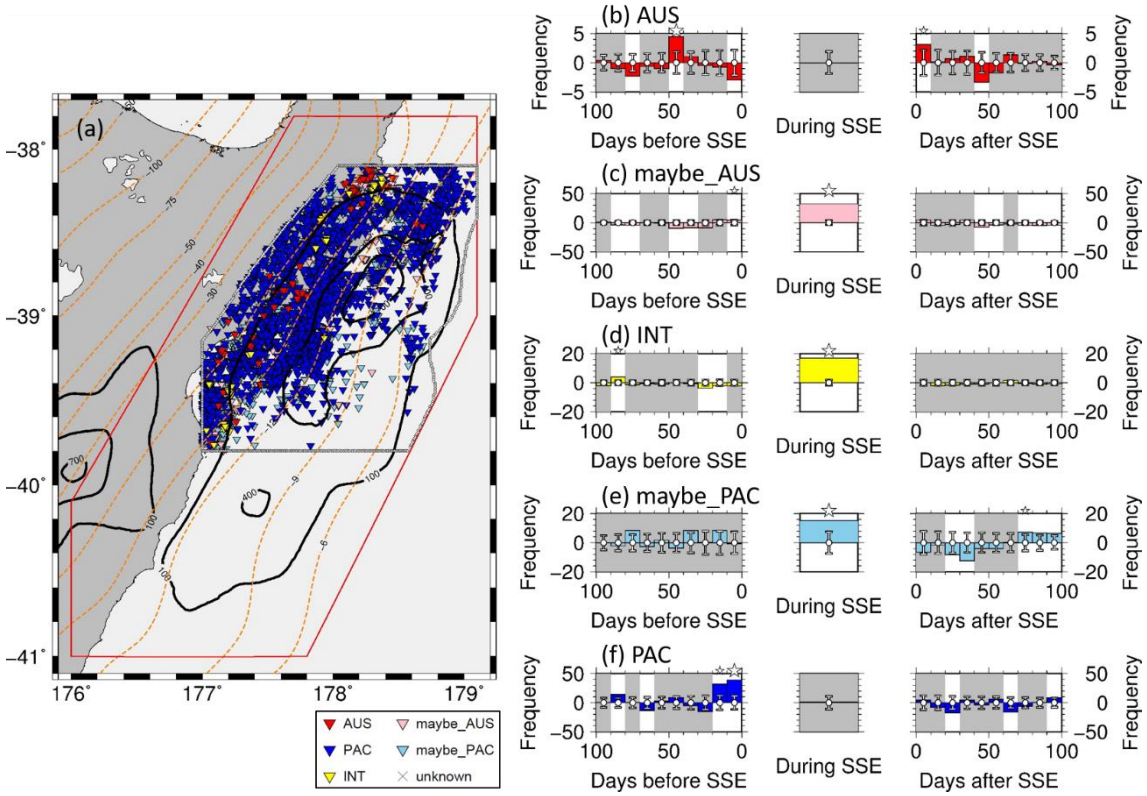

Figure A.19. Activation pattern in the northern Hikurangi margin with d_f of 1.50 calculating space-time distance.

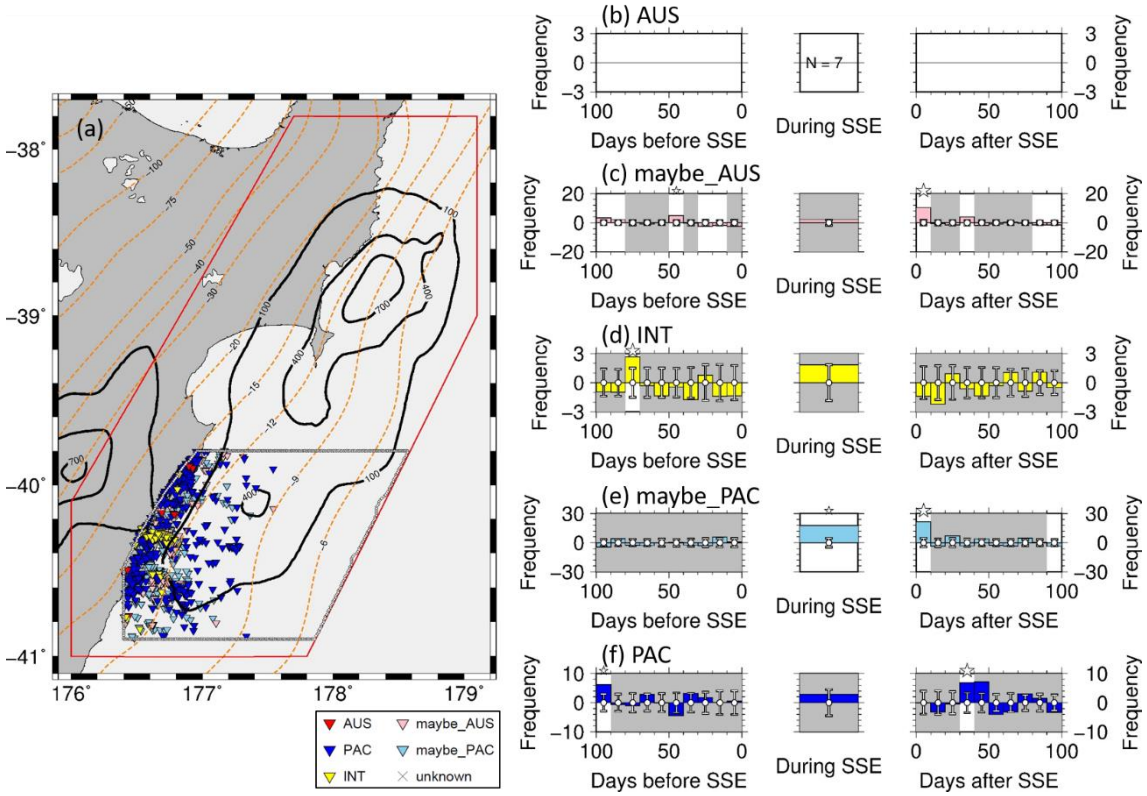

Figure A.20. Activation pattern in the central Hikurangi margin with d_f of 1.50 calculating space-time distance.

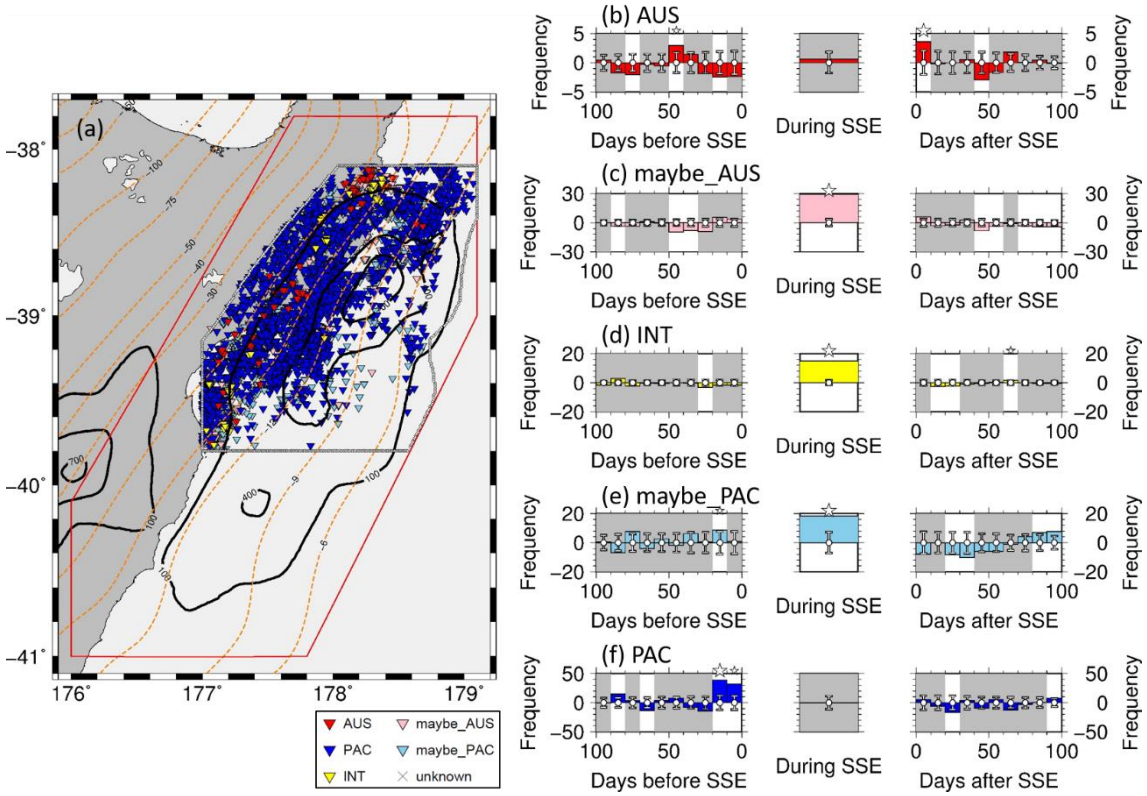

Figure A.21. Activation pattern in the northern Hikurangi margin with d_f of 1.90 calculating space-time distance.

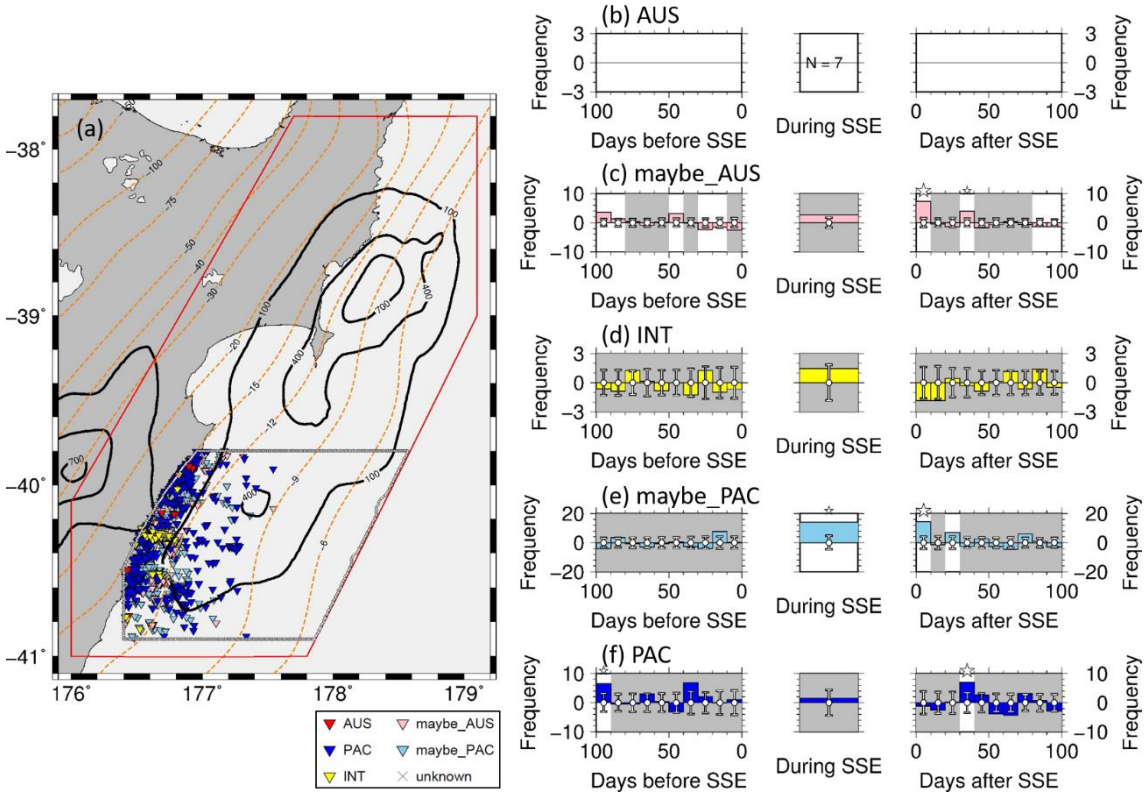

Figure A.22. Activation pattern in the central Hikurangi margin with d_f of 1.90 calculating space-time distance.

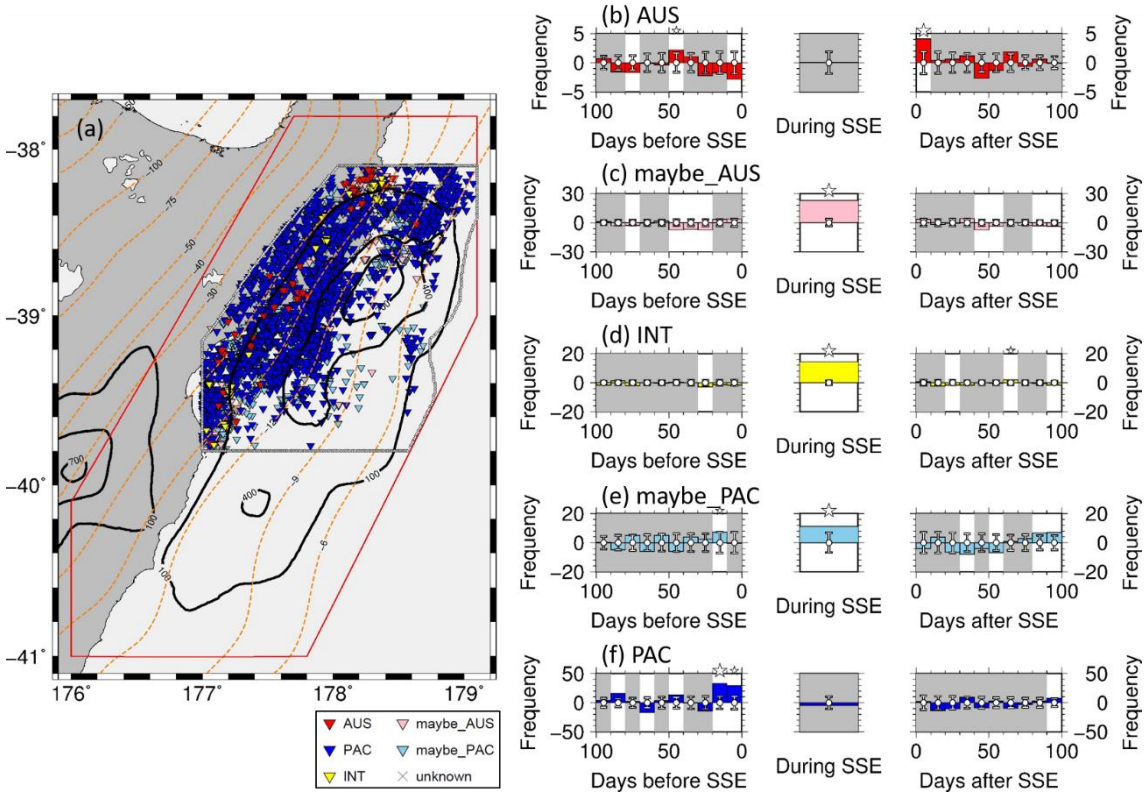

Figure A.23. Activation pattern in the northern Hikurangi margin using $\log_{10}\eta$ greater than -6.2.

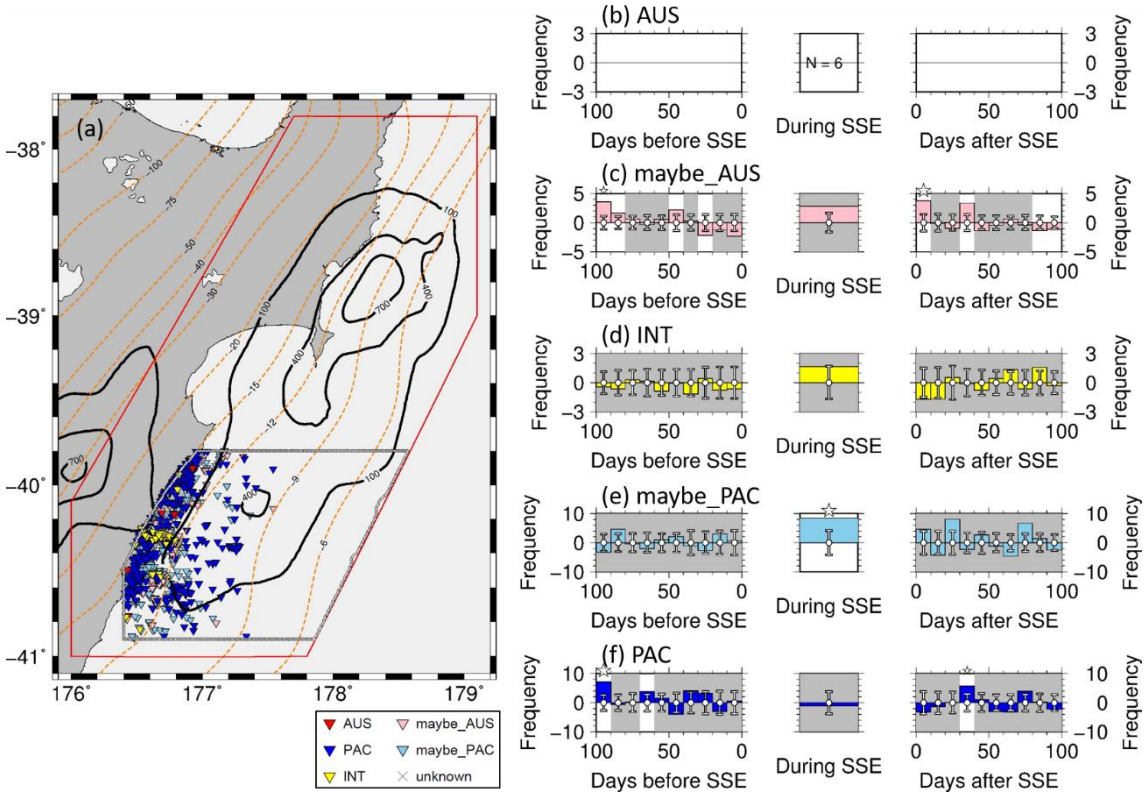

Figure A.24. Activation pattern in the central Hikurangi margin using $\log_{10}\eta$ greater than -6.2.

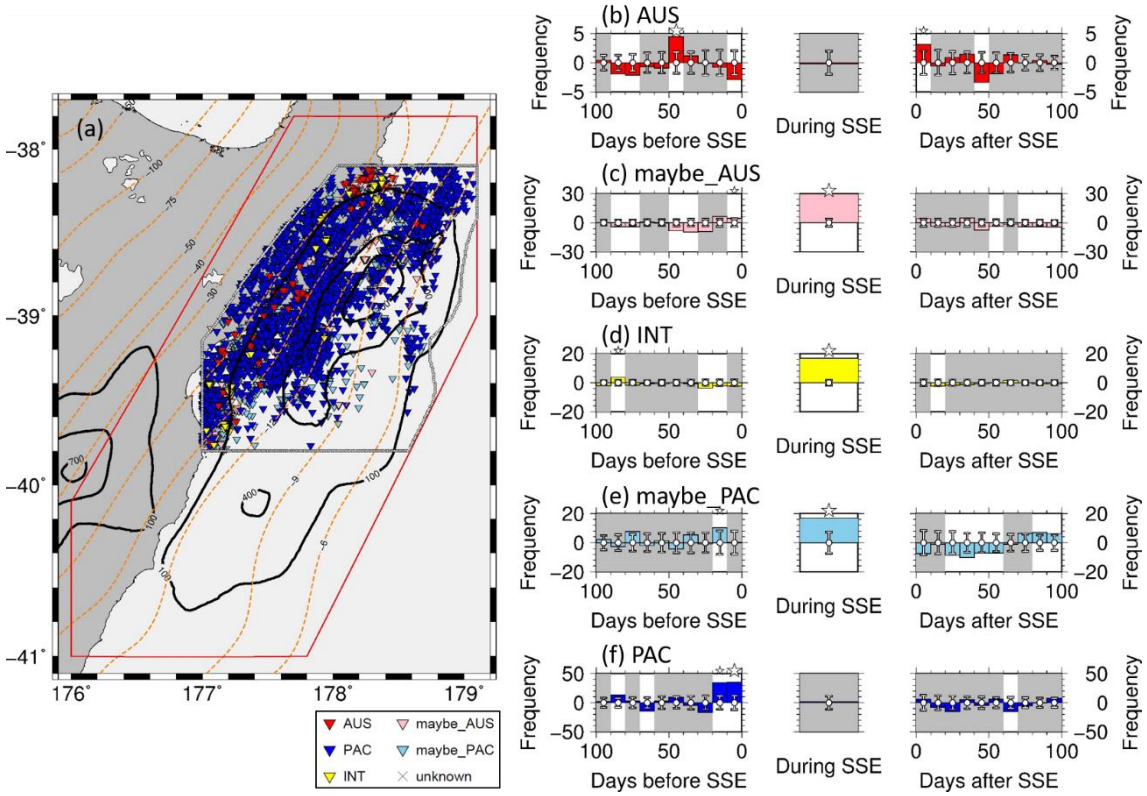

Figure A.25. Activation pattern in the northern Hikurangi margin using $\log_{10}\eta$ greater than -6.8.

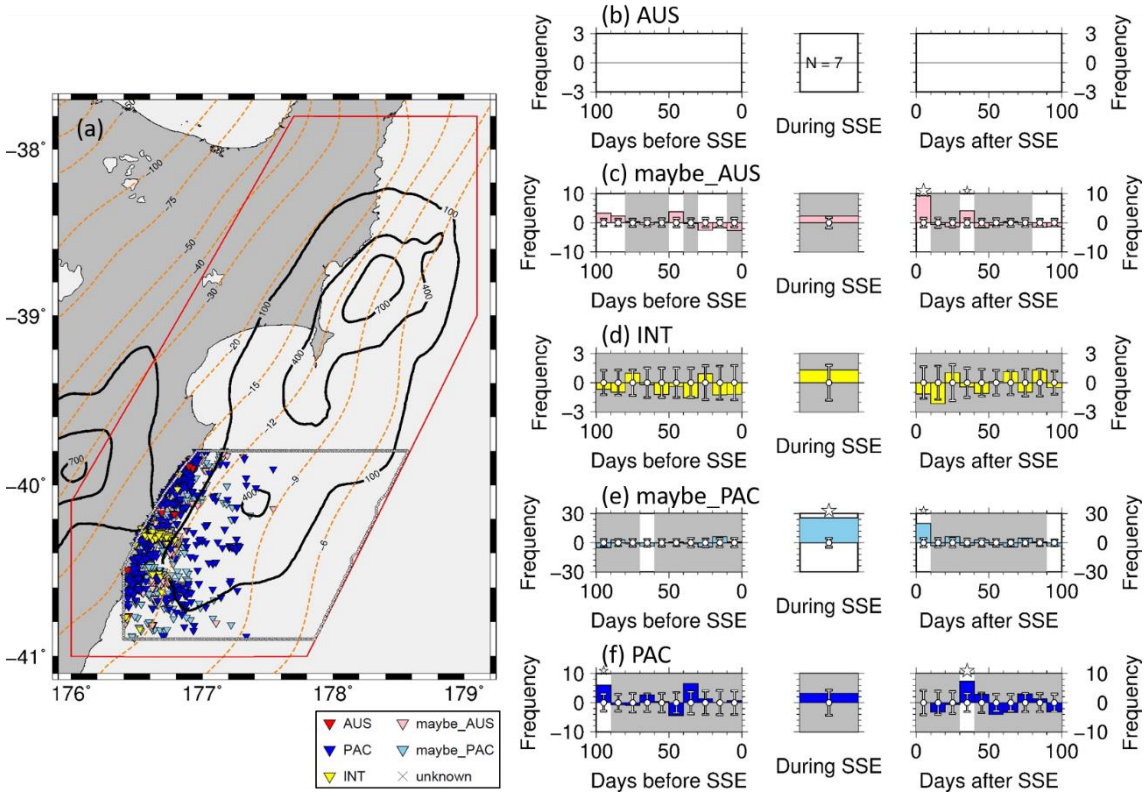

Figure A.26. Activation pattern in the central Hikurangi margin using $\log_{10}\eta$ greater than -6.8.

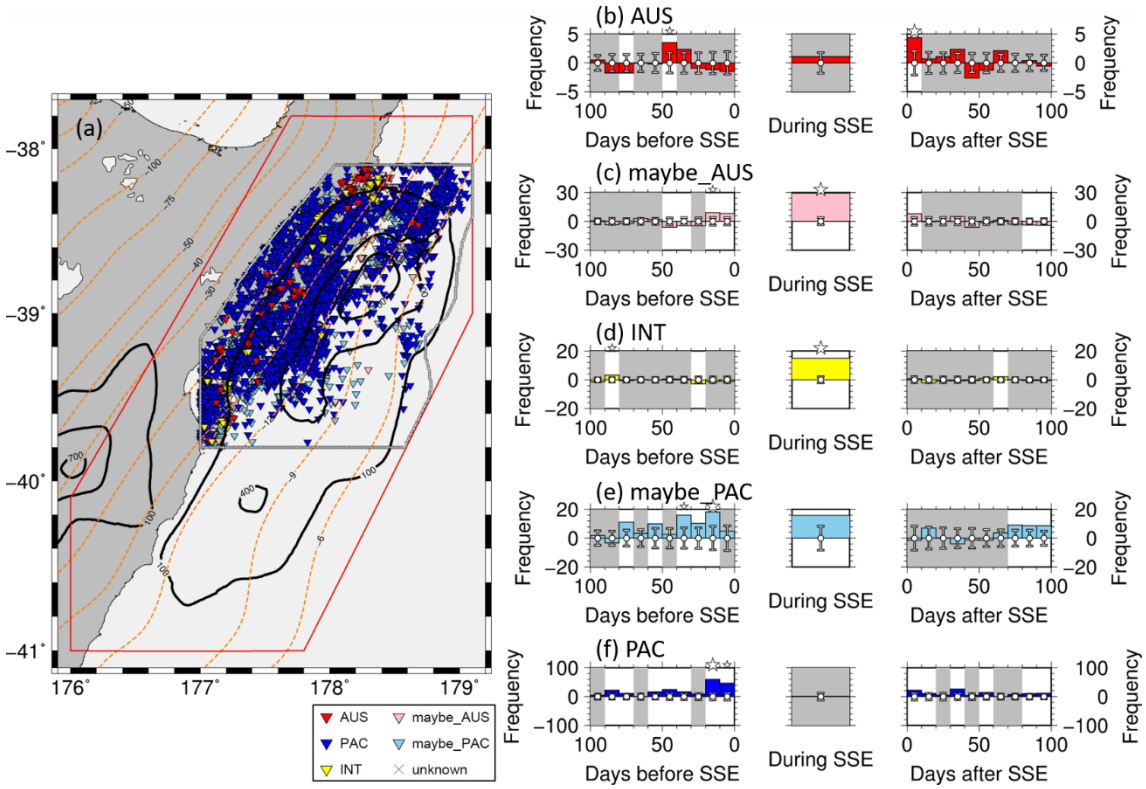

Figure A.27. Activation pattern in the northern Hikurangi for random SSEs and fixed seismicity.

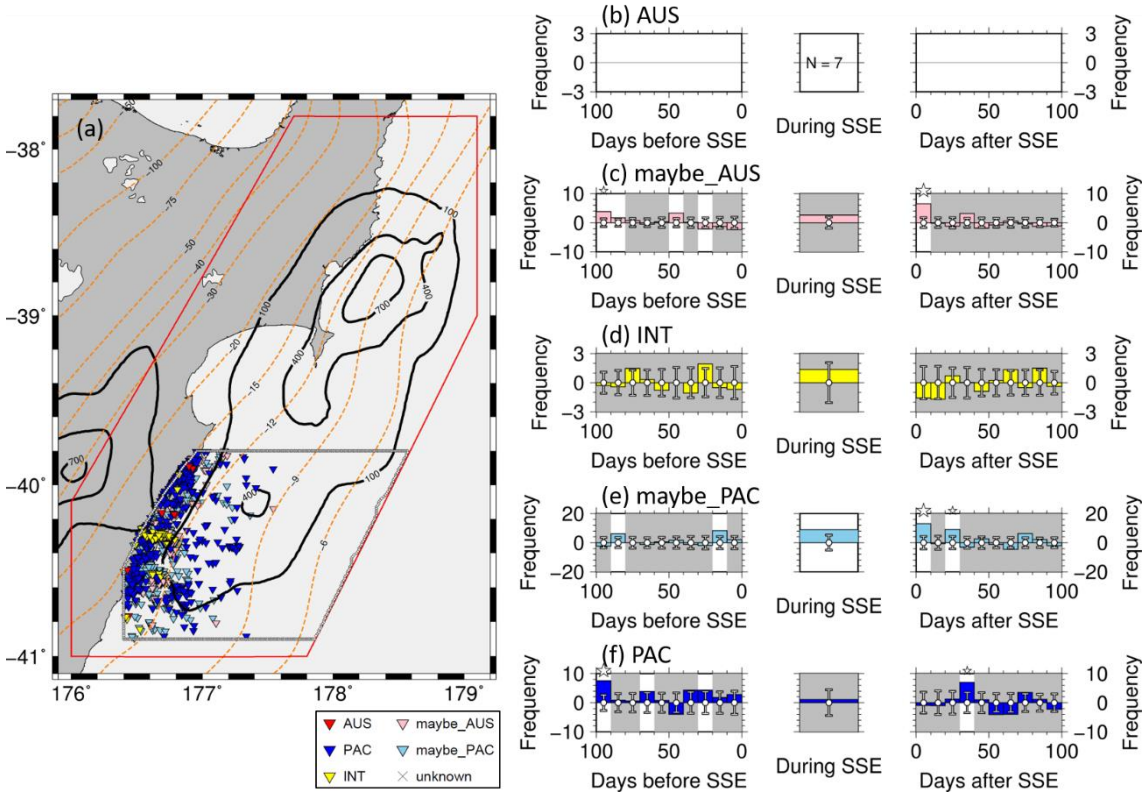

Figure A.28. Activation pattern in the central Hikurangi for random SSEs and fixed seismicity.

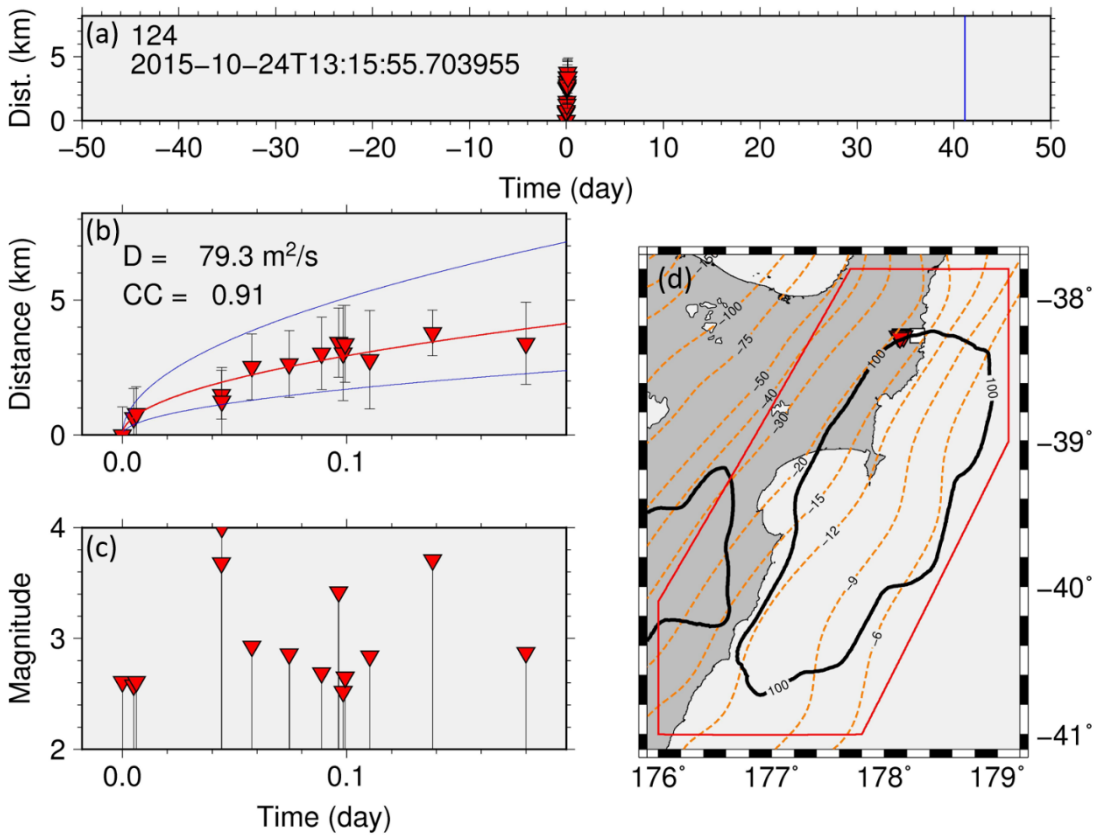

Figure B.1. A "diffused" swarm sequence occurred in October 2015. (a) The relationship between the time and distance from the first event in the sequence. The vertical blue and red lines indicate estimated SSE start and end times, respectively. The number and date on the left are the sequence number and the date of the first event, respectively. (b) The enlarged figure of the upper left panel. A red curve is the diffusion curve with estimated diffusivity D. Blue curves are diffusion curves with diffusivity of $3D$ and $\frac{1}{3}D$. (c) Magnitude-time diagram. (d) Distribution of events in the sequence.

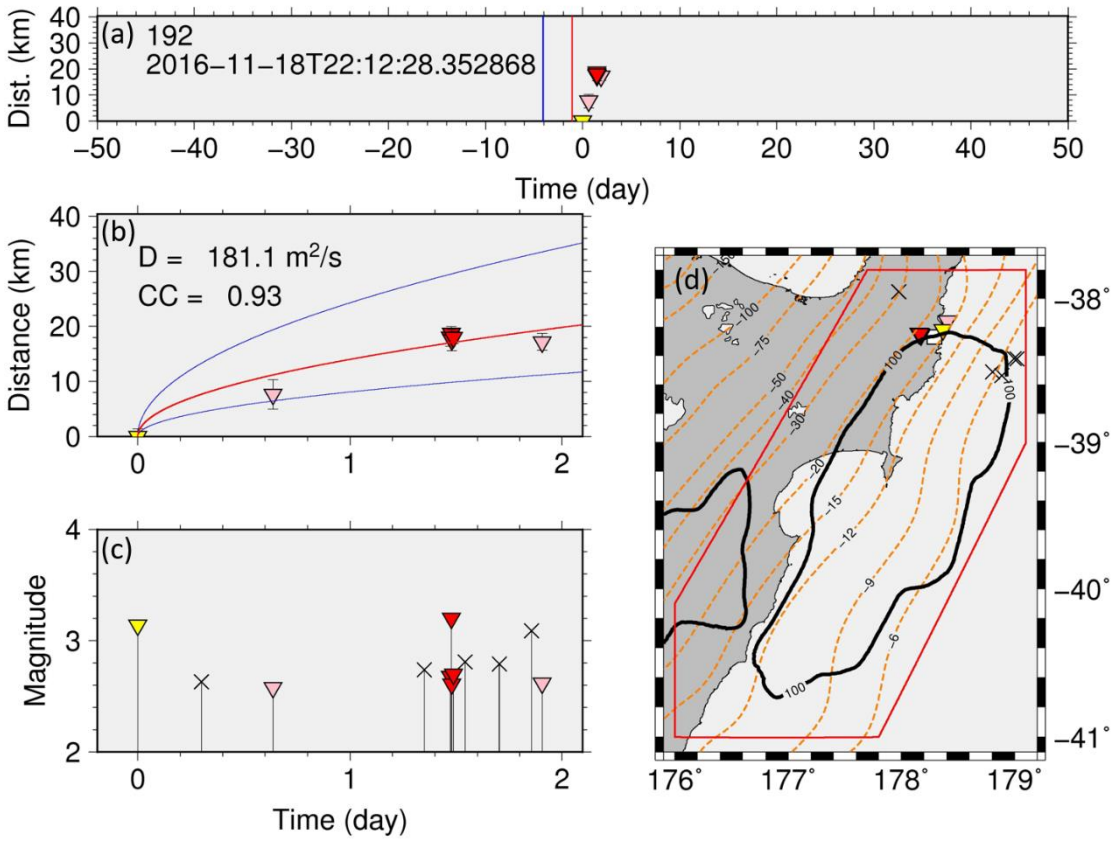

Figure B.2. A "diffused" swarm sequence occurred in November 2016. The diagrams are the same as in Figure B.1.

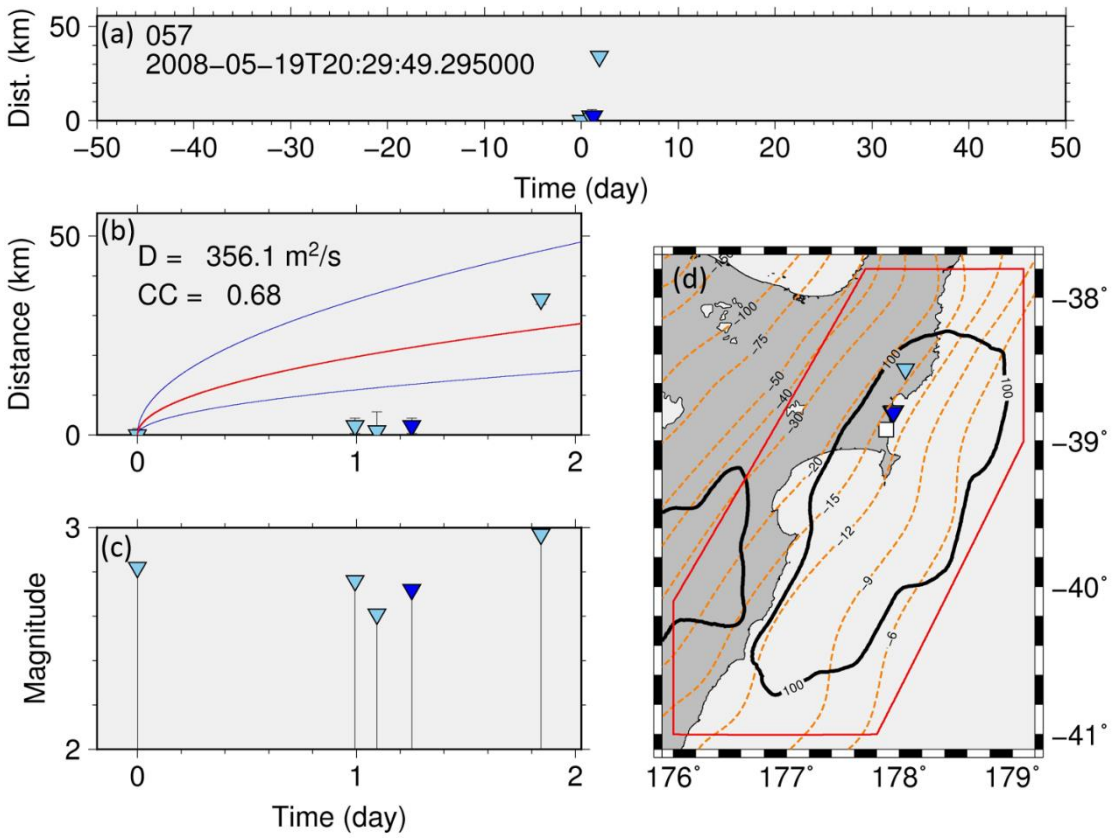

Figure B.3. A "not-diffused" swarm sequence occurred in May 2008. The diagrams are the same as in Figure B.1.

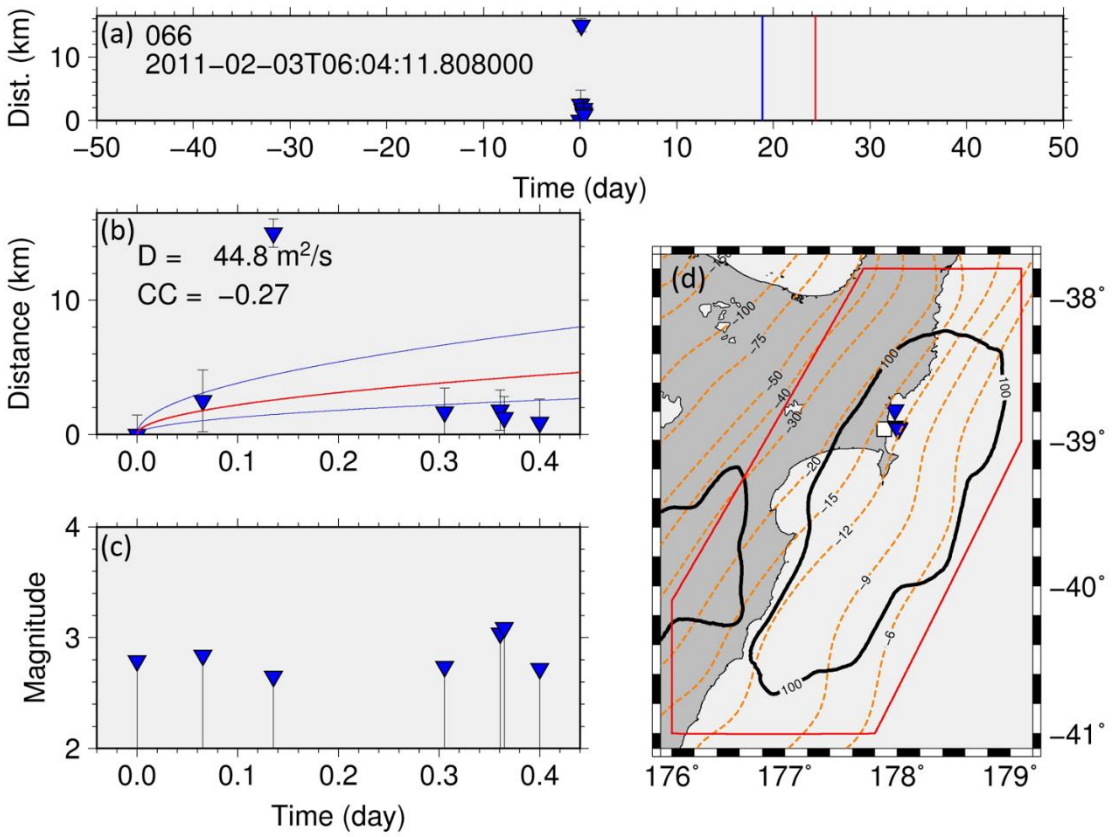

Figure B.4. A "not-diffused" swarm sequence occurred in February 2011. The diagrams are the same as in Figure B.1.

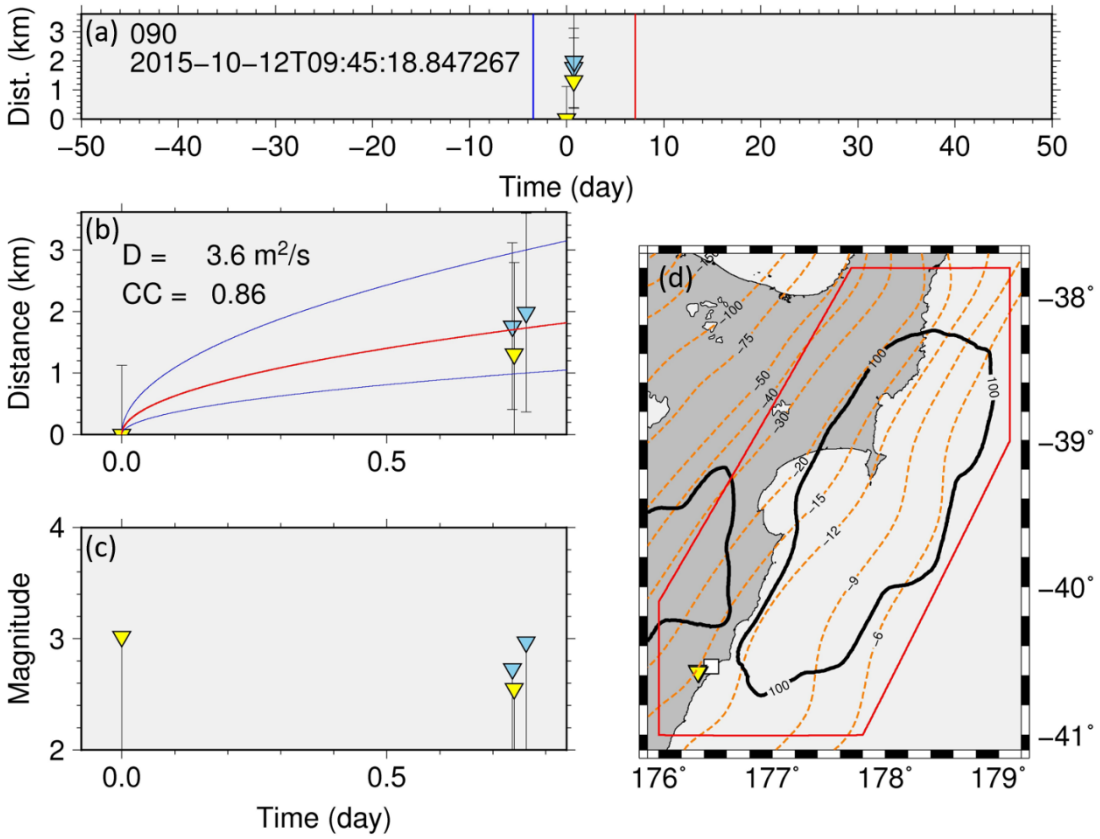

Figure B.5. An "undefined" swarm sequence occurred in October 2015. The diagrams are the same as in Figure B.1.

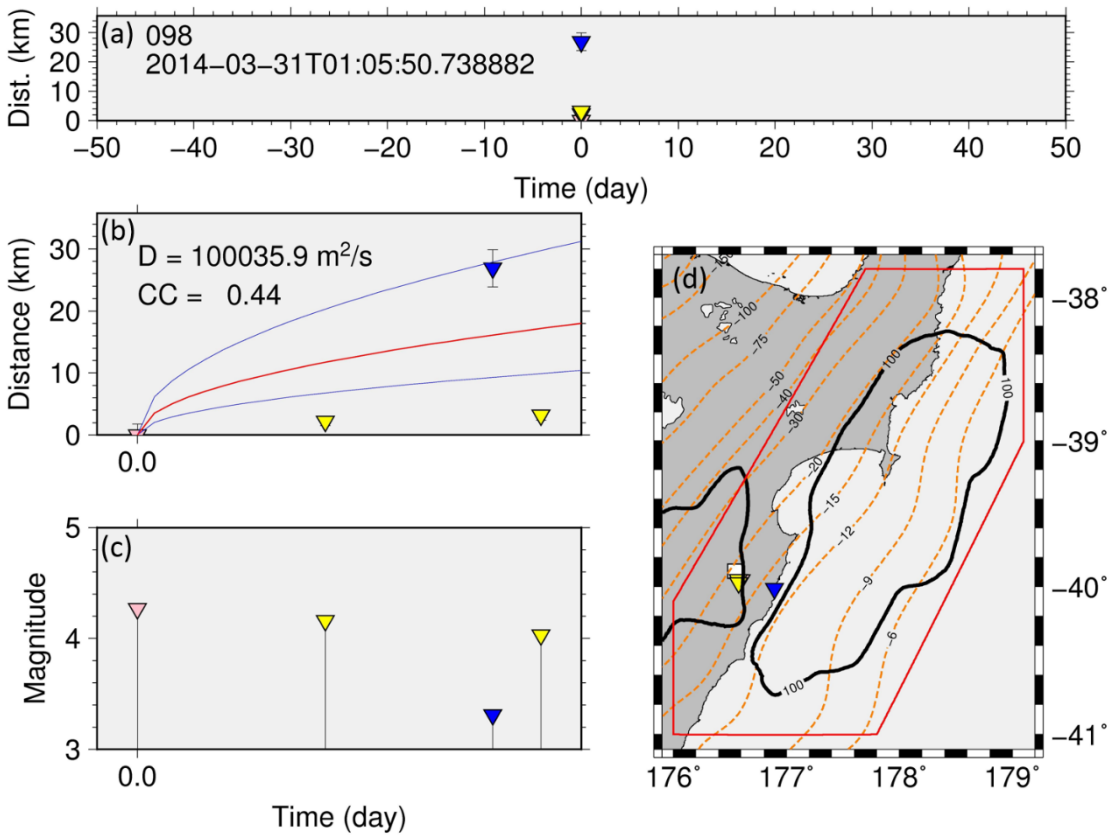

Figure B.6. An "undefined" swarm sequence occurred in March 2014. The diagrams are the same as in Figure B.1.

References

Akaike, H. (1974). A new look at the statistical model identification. *IEEE Transactions on Automatic Control*, *19*(6), 716–723. https://doi.org/10.1109/TAC.1974.1100705

Álvarez-Gómez, J.A. (2019). FMC - Earthquake focal mechanisms data management, cluster and Classification. *SoftwareX*, *9*, 299–307. https://doi.org/10.1016/j.softx.2019.03.008

Antriasian, A., Harris, R.N., Tréhu, A.M., Henrys, S.A., Phrampus, B.J., Lauer, R., Gorman, A.R., IPecher, I.A., & Barker, D. (2019). Thermal regime of the Northern Hikurangi margin, New Zealand. *Geophysical Journal International*, *216*(2), 1177–1190. https://doi.org/10.1093/gji/ggy450

Barnes, P.M., Lamarche, G., Bialas, J., Pecher, I., Henrys, S., Pecher, I., Netzeband, G.L., Greinert, J., Mountjoy, J.J., Pedley, K., & Crutchley, G. (2010). Tectonic and geological framework for gas hydrates and cold seeps on the Hikurangi subduction margin, New Zealand. *Marine Geology*, *272*(1–4), 26-48. https://doi.org/10.1016/j.margeo.2009.03.012

Beanland, S., & Haines, J. (1998). The kinematics of active deformation in the North Island, New Zealand, determined from geological strain rates. *New Zealand Journal of Geology and Geophysics*, *41*(4), 311-323. https://doi.org/10.1080/00288306.1998.9514813

Bell, R., Sutherland, R., Barker, D.H.N., Henrys, S., Bannister, S., Wallace, L., & Beavan, J. (2010). Seismic reflection character of the Hikurangi subduction interface, New Zealand, in the region of repeated Gisborne slow slip events. *Geophysical Journal International*, *180*(1), 34–48. https://doi.org/10.1111/j.1365-246x.2009.04401.x

Bormann, P., & Saul, J. (2008). The New IASPEI Standard Broadband Magnitude mB. *Seismological Research Letters*, *79*(5), 698–705. https://doi.org/10.1785/gssrl.79.5.698

Boulton, C., Niemeijer, A.R., Hollis, C.J., Townend, J., Raven, M.D., Kulhanek, D.K., & Shepherd, C.L. (2019). Temperature-dependent frictional properties of heterogeneous Hikurangi Subduction Zone input sediments, ODP Site 1124. *Tectonophysics*, *757*, 123–139. https://doi.org/10.1016/j.tecto.2019.02.006

Bratt, S.R., & Nagy, W. (1991). The LocSAT Program, Science Applications International Corporation (SAIC), San Diego.

Chamberlain, C.J., Boese, C.M., & Townend, J. (2017). Cross-correlation-based detection and characterisation of microseismicity adjacent to the locked, late-interseismic Alpine Fault, South Westland, New Zealand. *Earth and Planetary Science Letters*, *457*, 63-72. https://doi.org/10.1016/j.epsl.2016.09.061

Chamberlain, C.J., Frank, W.B., Lanza, F., Townend, J., & Warren-Smith, E. (2021). Illuminating the Pre-, Co-, and Post-Seismic Phases of the 2016 M7.8 Kaikōura Earthquake With 10 Years of Seismicity. *Journal of Geophysical Research: Solid Earth*, *126*(8), e2021JB022304.

https://doi.org/10.1029/2021JB022304

Chow, B., Kaneko, Y., Tape, C., Modrak, R., Mortimer, N., Bannister, S., & Townend, J. (2022). Strong upper-plate heterogeneity at the Hikurangi subduction margin (North Island, New Zealand) imaged by adjoint tomography. *Journal of Geophysical Research: Solid Earth*, *127*, e2021JB022865. https://doi.org/10.1029/2021JB022865

Delahaye, E.J., Townend, J., Reyners, M.E., & Rogers, G. (2009). Microseismicity but no tremor accompanying slow slip in the Hikurangi subduction zone, New Zealand, *Earth and Planetary Science Letters*, *277*(1–2), 21-28. https://doi.org/10.1016/j.epsl.2008.09.038

Dieterich, J.H. (1979). Modeling of rock friction: 1. Experimental results and constitutive equations. *Journal of Geophysical Research: Solid Earth*, *84*(B5), 2161–2168. https://doi.org/10.1029/JB084iB05p02161

Dimitrova, L., Wallace, L.M., Haines, J., & Williams, C. (2016). High resolution view of active tectonic deformation along the Hikurangi subduction margin and the Taupo Volcanic Zone, New Zealand. *New Zealand Journal Geology and Geophysics*, *59*(1), 70–85. https://doi.org/10.1080/00288306.2015.1127825

Eaton, J.P. (1996). Microearthquake Seismology in USGS Volcano and Earthquake Hazards Studies: 1953-1995.

Eberhart-Phillips, D., & Bannister, S. (2015). 3–D imaging of the northern Hikurangi subduction zone, New Zealand: variations in subducted sediment, slab fluids and slow slip. *Geophysical Journal International*, *201*(2), 838–855. https://doi.org/10.1093/gji/ggv057

Eberhart-Phillips, D., Bannister, S., & Reyners, M. (2017). Deciphering the 3–D distribution of fluid along the shallow Hikurangi subduction zone using P- and S-wave attenuation. *Geophysical Journal International*, *211*(2), 1032–1045. https://doi.org/10.1093/gji/ggx348

Eberhart-Phillips, D., Bannister, S., Reyners, M., & Henrys, S. (2020). New Zealand Wide model 2.2 seismic velocity and Qs and Qp models for New Zealand [Data set]. *Zenodo*. https://doi.org/10.5281/zenodo.3779523

Eberhart-Phillips, D., Reyners, M., Bannister, S., Chadwick, M., & Ellis, S. (2010). Establishing a Versatile 3-D Seismic Velocity Model for New Zealand. *Seismological Research Letters*, *81*(6), 992–1000. https://doi.org/10.1785/gssrl.81.6.992

Eberhart-Phillips, D., Reyners, M., Chadwick, M., & Chiu, J.M. (2005). Crustal heterogeneity and subduction processes: 3-D Vp, Vp/Vs and Q in the southern North Island, New Zealand. *Geophysical Journal International*, *162*(1), 270–288. https://doi.org/10.1111/j.1365-246X.2005.02530.x

Evanzia, D., Lamb, S., Savage, M.K., & Stern, T. (2019). Illumination of deformation by bending stresses within the southern Hikurangi double Benioff zone. *New Zealand Journal of Geology and Geophysics*, *62*(1), 111-120. https://doi.org/10.1080/00288306.2018.1532439

Fukuda, J.I. (2018). Variability of the space-time evolution of slow slip events off the Boso Peninsula, central Japan, from 1996 to 2014. *Journal of Geophysical Research: Solid Earth*, *123*(1), 732–760. https://doi.org/10.1002/2017JB014709

Gale, N., Gledhill, K., Chadwick, M., & Wallace, L.M. (2015). The Hikurangi Margin Continuous GNSS and Seismograph Network of New Zealand. *Seismological Research Letters*, *86*(1), 101–108. https://doi.org/10.1785/0220130181

Gangi, A.F. (1978). Variation of whole and fractured porous rock permeability with confining pressure. *International Journal of Rock Mechanics and Mining Sciences & Geomechanics Abstracts*, *15*(5), 249-257. https://doi.org/10.1016/0148-9062(78)90957-9

GeoNet. (no date a). Historical Location Information GROPE. Retrieved June 20, 2023, from https://www.geonet.org.nz/data/supplementary/earthquake_location_grope

GeoNet. (no date b). Historical Location Information GROPE. Retrieved June 20, 2023, from https://www.geonet.org.nz/data/supplementary/earthquake_location

GeoNet. (no date c). GNSS Time Series Notes. Retrieved July 4, 2023, from https://www.geonet.org.nz/data/supplementary/gnss_time_series_notes

GNS Science. (2023a). GeoNet Aotearoa New Zealand Earthquake Catalogue [Dataset]. *GNS Science*, *GeoNet*. https://doi.org/10.21420/0S8P-TZ38

GNS Science. (2023b). GeoNet Aotearoa New Zealand Earthquake Moment Tensor Solutions [Dataset]. *GNS Science*, *GeoNet*. https://doi.org/10.21420/MMJ9-CZ67

GNS Science. (2023c). GeoNet Aotearoa GeoNet Aotearoa New Zealand Seismic Digital Waveform Dataset [Dataset]. *GNS Science*, *GeoNet*. https://doi.org/10.21420/G19Y-9D40

GNS Science. (2023d). GeoNet Aotearoa New Zealand Continuous GNSS Network - Time Series Dataset [Dataset]. *GNS Science*, *GeoNet*. https://doi.org/10.21420/30F4-1A55

Gomberg, J., Baxter, P., Smith, E., Ariyoshi, K., & Chiswell, S.M. (2020). The ocean's impact on slow slip events. *Geophysical Research Letters*, *47*(14), e2020GL087273. https://doi.org/10.1029/2020GL087273

Gutenberg, B., & Richter, C.F. (1941). Seismicity of the earth. *Geological Society Of America*, Special Papers, 34.

Haines, A.J. (1981). A local magnitude scale for New Zealand earthquakes. *Bulletin of the Seismological Society of America*, *71*(1), 275-294. https://doi.org/10.1785/BSSA0710010275

Haines, A.J., & Wallace, L.M. (2020). New Zealand-wide geodetic strain rates using a physics-based approach. *Geophysical Research Letters*, *47*, e2019GL084606. https://doi.org/10.1029/2019GL084606

Hainzl, S. (2004). Seismicity patterns of earthquake swarms due to fluid intrusion and stress triggering. *Geophysical Journal International*, *159*(3), 1090-1096. https://doi.org/10.1111/j.1365-246X.2004.02463.x

Hara, S., Fukahata, Y., & Iio, Y. (2019). P-wave first-motion polarity determination of waveform data in western Japan using deep learning. *Earth, Planets and Space*, *71*, 127. https://doi.org/10.1186/s40623-019-1111-x

Hardebeck, J.L., & Shearer, P.M. (2002). A new method for determining firstmotion focal mechanisms. *Bulletin of the Seismological Society of America*, *92*(6), 2264-2276. https://doi.org/10.1785/0120010200

Hardebeck, J.L., & Shearer, P.M. (2003). Using S/P Amplitude Ratios to Constrain the Focal Mechanisms of Small Earthquakes. *Bulletin of the Seismological Society of America*, *93*(6), 2434-2444. https://doi.org/10.1785/0120020236

Harris, R.A. (1998). Introduction to Special Section: Stress Triggers, Stress Shadows, and Implications for Seismic Hazard. *Journal of Geophysical Research: Solid Earth*, *103*(B10), 24347– 24358. https://doi.org/10.1029/98JB01576

Heise, W., Caldwell, T.G., Bannister, S., Bertrand, E.A., Ogawa, Y., Bennie, S.L., & Ichihara, H. (2017). Mapping subduction interface coupling using magnetotellurics: Hikurangi margin, New Zealand. *Geophysical Research Letters*, *44*(18), 9261–9266. https://doi.org/10.1002/2017GL074641

Heise, W., Ogawa, Y., Bertrand, E.A., Caldwell, T.G., Yoshimura, R., Ichihara, H., Bennie, S.L., Seki, K., Saito, Z., Matsunaga, Y., Suzuki, A., Kishita, T., & Kinoshita, Y. (2019). Electrical resistivity imaging of the inter-plate coupling transition at the Hikurangi subduction margin, New Zealand. *Earth and Planetary Science Letters*, *524*, 115710. https://doi.org/10.1016/j.epsl.2019.115710

Hill, D.P. (1977). A model for earthquake swarms, *Journal of Geophysical Research*, *82*(8), 1347–1352. https://doi.org/10.1029/JB082i008p01347

Hirata, T. (1989). A correlation between the b value and the fractal dimension of earthquakes. *Journal of Geophysical Research: Solid Earth*, *94*(B6), 7507–7514. https://doi.org/10.1029/JB094iB06p07507

Hughes, L., Chamberlain, C.J., Townend, J., & Thomas, A.M. (2021). A repeating earthquake catalog from 2003 to 2020 for the Raukumara Peninsula, northern Hikurangi subduction margin, New Zealand. *Geochemistry, Geophysics, Geosystems*, *22*, e2021GC009670. https://doi.org/10.1029/2021GC009670

Ide, S. (2010). Striations, duration, migration and tidal response in deep tremor. *Nature*, *466*, 356–359. https://doi.org/10.1038/nature09251

Ide, S., Beroza, G., Shelly, D., & Uchide, T. (2007). A scaling law for slow earthquakes. *Nature*, *447*, 76–79. https://doi.org/10.1038/nature05780

Igarashi, T. (2010). Spatial changes of inter-plate coupling inferred from sequences of small repeating earthquakes in Japan. *Geophysical Research Letters*, *37*(20), L20304. https://doi.org/10.1029/2010GL044609

Ingebritsen, S.E., & Manning, C.E. (2010). Permeability of the continental crust: dynamic variations inferred from seismicity and metamorphism. *Geofluids*, *10*, 193-205. https://doi.org/10.1111/j.1468-8123.2010.00278.x

Kagan, Y.Y. (1991). 3-D rotation of double-couple earthquake sources. *Geophysical Journal International*, *106*(3), 709–716. https://doi.org/10.1111/j.1365-246x.1991.tb06343.x

Kato, A., & Nakagawa, S. (2014). Multiple slow-slip events during a foreshock sequence of the 2014 Iquique, Chile Mw 8.1 earthquake. *Geophysical Research Letters*, *41*(15), 5420–5427. https://doi.org/10.1002/2014GL061138

Kato, A., Obara, K., Igarashi, T., Tsuruoka, H., Nakagawa, S., & Hirata, N. (2012). Propagation of Slow Slip Leading Up to the 2011 Mw 9.0 Tohoku-Oki Earthquake. *Science*, *335*(6069), 705-708. https://doi.org/10.1126/science.1215141

Kennet, B.L.N. (1991). IASPEI 1991 Seismological Tables. *Terra Nova*, *3*(2), 122-122. https://doi.org/10.1111/j.1365-3121.1991.tb00863.x

Lin, J., & Stein, R.S. (2004). Stress triggering in thrust and subduction earthquakes, and stress interaction between the southern San Andreas and nearby thrust and strike-slip faults. *Journal of Geophysical Research: Solid Earth*, *109*(B2), B02303. https://doi.org/10.1029/2003JB002607

Liu, X., Pan, M., Li, X., & Wang, J. (2017). B-Value Characteristics of Rock Acoustic Emission Under Impact Loading. In: Shen, G., Wu, Z., Zhang, J. (eds) *Advances in Acoustic Emission Technology*, *Springer Proceedings in Physics*, *179*, *Springer*, *Cham*. https://doi.org/10.1007/978-3-319-29052-2_12

Liu, Y., & Rice, J.R. (2007). Spontaneous and triggered aseismic deformation transients in a subduction fault model. *Journal of Geophysical Research*, 112(B09404). https://doi.org/10.1029/2007JB004930

Lockner, D. (1993). The role of acoustic emission in the study of rock fracture. *International Journal of Rock Mechanics and Mining Sciences & Geomechanics Abstracts*, *30*(7), 883-899. https://doi.org/10.1016/0148-9062(93)90041-B

Lomax, A., Virieux, J., Volant, P., & Berge-Thierry, C. (2000). Probabilistic earthquake location in 3D and layered models. In *Advances in seismic event location* (pp. 101–134). Springer. https://doi.org/10.1007/978-94-015-9536-0_5

Ma, S., & Eaton, D.W. (2011). Combining double-difference relocation with regional depth-phase modelling to improve hypocentre accuracy. *Geophysical Journal International*, *185*(2), 871–889. https://doi.org/10.1111/j.1365-246X.2011.04972.x

Marone, C. (1998). Laboratory-derived friction laws and their application to seismic faulting. *Annual Review of Earth and Planetary Sciences*, *26*(1), 643–696. https://doi.org/10.1146/annurev.earth.26.1.643

Matsuno, M., Tagami, A., Okada, T., Matsumoto, S., Kawamura, Y., Iio, Y., Sato, T., Nakayama, T.,

Hirahara, S., Bannister, S., Ristau, J., Savage, M.K., Thurber, C.H., & Sibson, R.H. (2022). Spatial and temporal stress field changes in the focal area of the 2016 Kaikōura earthquake, New Zealand: A multi-fault process interpretation. *Tectonophysics*, *835*, 229390. https://doi.org/10.1016/j.tecto.2022.229390

Miyazawa, M., & Mori, J. (2005). Detection of triggered deep low-frequency events from the 2003 Tokachi-oki earthquake. *Geophysical Research Letters*, *32*(10), L10307. https://doi.org/10.1029/2005GL022539

Mochizuki, K., Sutherland, R., Henrys, S., Bassett, D., Van Avendonk, H., Arai, R., Kodaira, S., Fujie, G., Yamamoto, Y., Bangs, N., & Barker, D. (2019). Recycling of depleted continental mantle by subduction and plumes at the Hikurangi Plateau large igneous province, southwestern Pacific Ocean. *Geology*, *47*(8), 795–798. https://doi.org/10.1130/G46250.1

Montuori, C., Falcone, G., Murru, M., Thurber, C., Reyners, M., & Eberhart-Phillips, D. (2010). Crustal heterogeneity highlighted by spatial b-value map in the Wellington region of New Zealand. *Geophysical Journal International*, *183*(1), 451-460. https://doi.org/10.1111/j.1365-246X.2010.04750.x

Mortimer, N., & Parkinson, D. (1996). Hikurangi Plateau: A Cretaceous large igneous province in the southwest Pacific Ocean. *Journal of Geophysical Research: Solid Earth*, *101*(B1), 687– 696. https://doi.org/10.1029/95JB03037

Müller, R.D., Sdrolias, M., Gaina, C., & Roest, W.R. (2008). Age, spreading rates, and spreading asymmetry of the world's ocean crust. *Geochemistry, Geophysics, Geosystems*, *9*(4), Q04006. https://doi.org/10.1029/2007GC001743

Nakajima, J., & Uchida, N. (2018). Repeated drainage from megathrusts during episodic slow slip. *Nature Geoscience*, *11*, 351–356. https://doi.org/10.1038/s41561-018-0090-z

Nishikawa, T., & Ide, S. (2018). Recurring slow slip events and earthquake nucleation in the source region of the M 7 Ibaraki-Oki earthquakes revealed by earthquake swarm and foreshock activity. *Journal of Geophysical Research: Solid Earth*, *123*(9), 7950–7968. https://doi.org/10.1029/2018JB015642

Nishikawa, T., Matsuzawa, T., Ohta, K., Uchida, N., Nishimura, T., & Ide, S. (2019). The slow earthquake spectrum in the Japan Trench illuminated by the S-net seafloor observatories. *Science*, *365*(6455), 808–813. https://doi.org/10.1126/science.aax5618

Nishikawa, T., Nishimura, T., & Okada, Y. (2021). Earthquake swarm detection along the Hikurangi Trench, New Zealand: Insights into the relationship between seismicity and slow slip events. *Journal of Geophysical Research: Solid Earth*, *126*, e2020JB020618. https://doi.org/10.1029/2020JB020618

Nishimura, T. (2014). Short-term slow slip events along the Ryukyu Trench, southwestern Japan, observed by continuous GNSS. *Progress in Earth and Planetary Science*, *1*(1), 22.

https://doi.org/10.1186/s40645-014-0022-5

Nishimura, T., Matsuzawa, T., & Obara, K. (2013). Detection of short-term slow slip events along the Nankai Trough, southwest Japan, using GNSS data. *Journal of Geophysical Research: Solid Earth*, *118*(6), 3112–3125. https://doi.org/10.1002/jgrb.50222

Obara, K. (2020). Characteristic activities of slow earthquakes in Japan. *Proceedings of the Japan Academy, Series B*, *96*(7), 297-315. https://doi.org/10.2183/pjab.96.022

Obara, K., & Kato, A. (2016). Connecting slow earthquakes to huge earthquakes. *Science*, *353*, 253-257. https://doi.org/10.1126/science.aaf1512

Okada, T., Iio, Y., Matsumoto, S., Bannister, S., Ohmi, S., Horiuchi, S., Sato, T., Miura, T., Pettinga, J., Ghisetti, F., & Sibson, R.H. (2019). Comparative tomography of reverse-slip and strike-slip seismotectonic provinces in the northern South Island, New Zealand. *Tectonophysics*, *765*, 172–186. https://doi.org/10.1016/j.tecto.2019.03.016

Okada, T., Matsuzawa, T., Umino, N., Yoshida, K., Hasegawa, A., Takahashi, H., et al. (2015). Hypocenter migration and crustal seismic velocity distribution observed for the inland earthquake swarms induced by the 2011 Tohoku-Oki earthquake in NE Japan: Implications for crustal fluid distribution and crustal permeability. *Geofluids*, *15*(1–2), 293–309. https://doi.org/10.1111/gfl.12112

Perez-Silva, A., Kaneko, Y., Savage, M., Wallace, L., & Warren-Smith, E. (2023). Characteristics of slow slip events explained by rate-strengthening faults subject to periodic pore fluid pressure changes. *Journal of Geophysical Research: Solid Earth*, *128*(6), e2022JB026332. https://doi.org/10.1029/2022JB026332

Petersen, T., Gledhill, K., Chadwick, M., Gale, N.H., & Ristau, J. (2011). The New Zealand national seismograph network. *Seismological Research Letters*, *82*(1), 9–20. https://doi.org/10.1785/gssrl.82.1.9

Raggiunti, M., Keir, D., Pagli, C., & Lavayssière, A. (2023). Evidence of fluid induced earthquake swarms from high resolution earthquake relocation in the Main Ethiopian Rift. *Geochemistry, Geophysics, Geosystems*, *24*(4), e2022GC010765. https://doi.org/10.1029/2022GC010765

Reyes, A.G., Ellis, S.M., Christenson, B.W., & Henrys, S. (2022). Fluid flowrates and compositions and water–rock interaction in the Hikurangi margin forearc, New Zealand. *Chemical Geology*, *614*, 121169. https://doi.org/10.1016/j.chemgeo.2022.121169

Reyners, M., & Eberhart-Phillips, D. (2009). Small earthquakes provide insight into plate coupling and fluid distribution in the Hikurangi subduction zone, New Zealand. *Earth and Planetary Science Letters*, *282*(1–4), 299-305. https://doi.org/10.1016/j.epsl.2009.03.034

Reyners, M., Eberhart-Phillips, D., & Bannister, S. (2017). Subducting an old subduction zone sideways provides insights into what controls plate coupling. *Earth and Planetary Science Letters*, *466*, 53–61. https://doi.org/10.1016/j.epsl.2017.03.004

Reyners, M., & McGinty, P. (1999). Shallow subduction tectonics in the Raukumara Peninsula, New Zealand, as illuminated by earthquake focal mechanisms. *Journal of Geophysical Research: Solid Earth*, *104*(B2), 3025–3034. https://doi.org/10.1029/1998JB900081

Ristau, J. (2013). Update of Regional Moment Tensor Analysis for Earthquakes in New Zealand and Adjacent Offshore Regions. *Bulletin of the Seismological Society of America*, *103*(4), 2520–2533. https://doi.org/10.1785/0120120339

Rivet, D., Campillo, M., Shapiro, N.M., Cruz-Atienza, V., Radiguet, M., Cotte, N., & Kostoglodov, V. (2011). Seismic evidence of nonlinear crustal deformation during a large slow slip event in Mexico. *Geophysical Research Letters*, *38*(8), L08308. https://doi.org/10.1029/2011GL047151

Romanet, P., & Ide, S. (2019). Ambient tectonic tremors in Manawatu, Cape Turnagain, Marlborough, and Puysegur, New Zealand. *Earth Planets and Space*, *71*(1), 1–9. https://doi.org/10.1186/s40623-019-1039-1

Ruina, A. (1983). Slip instability and state variable friction laws. *Journal of Geophysical Research: Solid Earth*, *88*(B12), 10359–10370. https://doi.org/10.1029/JB088iB12p10359

Saar, M.O., & Manga, M. (2004). Depth dependence of permeability in the Oregon Cascades inferred from hydrogeologic, thermal, seismic, and magmatic modeling constraints. *Journal of Geophysical Research: Solid Earth*, *109*(B4), B04204. https://doi.org/10.1029/2003JB002855

Sato, R. (1967). Attenuation of Seismic Waves. Journal of Physics of the Earth, 15(2), 32-61. https://doi.org/10.4294/jpe1952.15.32

Schorlemmer, D., & Wiemer, S. (2005). Microseismicity data forecast rupture area. *Nature*, *434*, 1086. https://doi.org/10.1038/4341086a

Schorlemmer, D., Wiemer, S., & Wyss, M. (2005). Variations in earthquake-size distribution across different stress regimes. *Nature*, *437*, 539–542. https://doi.org/10.1038/nature04094

Segall, P., Desmarais, E., Shelly, D., Miklius, A., & Cervelli, P. (2006). Earthquakes triggered by silent slip events on Kīlauea volcano, Hawaii. *Nature*, *442*, 71–74. https://doi.org/10.1038/nature04938

Shaddox, H.R., & Schwartz, S.Y. (2019). Subducted seamount diverts shallow slow slip to the forearc of the northern Hikurangi subduction zone, New Zealand. *Geology*, *47*(5), 415–418. https://doi.org/10.1130/g45810.1

Shapiro, S.A., Huenges, E., & Borm, G. (1997). Estimating the crust permeability from fluid-injection-induced seismic emission at the KTB site. *Geophysical Journal International*, *131*(2), 15-18. https://doi.org/10.1111/j.1365-246X.1997.tb01215.x

Shreedharan, S., Ikari, M., Wood, C., Saffer, D., Wallace, L., & Marone, C. (2022). *Geochemistry, Geophysics, Geosystems*, *23*, e2021GC010107. https:doi.org/10.1029/2021GC010107

Takahashi, H. (2021). A study on characteristics of tectonic tremor activity along the Japan Trench. PhD thesis, Tohoku University, Japan.

Tenthorey, E., Cox, S.F., & Todd, H.F. (2003). Evolution of strength recovery and permeability during

fluid–rock reaction in experimental fault zones. *Earth and Planetary Science Letters*, *206*(1–2), 161–172. https://doi.org/10.1016/S0012-821X(02)01082-8

Toda, S., Lin, J. & Stein, R.S. (2011). Using the 2011 Mw 9.0 off the Pacific coast of Tohoku Earthquake to test the Coulomb stress triggering hypothesis and to calculate faults brought closer to failure. *Earth, Planets and Space*, *63*, 725–730. https://doi.org/10.5047/eps.2011.05.010

Toda, S., Stein, R.S., Richards-Dinger, K., & Bozkurt, S. (2005). Forecasting the evolution of seismicity in southern California: Animations built on earthquake stress transfer. *Journal of Geophysical Research: Solid Earth*, *110*(B5), B05S16. https://doi.org/10.1029/2004JB003415

Todd, E.K., & Schwartz, S.Y. (2016). Tectonic tremor along the northern Hikurangi Margin, New Zealand, between 2010 and 2015. *Journal of Geophysical Research: Solid Earth*, *121*(12), 8706–8719. https://doi.org/10.1002/2016JB013480

Todd, E.K., Schwartz, S.Y., Mochizuki, K., Wallace, L.M., Sheehan, A.F., Webb, S.C., et al. (2018). Earthquakes and tremor linked to seamount subduction during shallow slow slip at the Hikurangi margin, New Zealand. *Journal of Geophysical Research: Solid Earth*, *123*(8), 6769–6783. https://doi.org/10.1029/2018JB016136

Uchida, N. (2019). Detection of repeating earthquakes and their application in characterizing slow fault slip. *Progress in Earth and Planetary Science*, *6*(40). https://doi.org/10.1186/s40645-019-0284-z

Uchida, N., & Matsuzawa, T. (2013). Pre- and postseismic slow slip surrounding the 2011 Tohoku-oki earthquake rupture. *Earth and Planetary Science Letters*, *374*, 81-91. https://doi.org/10.1016/j.epsl.2013.05.021

Utsu, T. (1965). A Method for Determining the Value of b in a Formula log n=a-bM showing the Magnitude-Frequency Relation for Earthquakes. *Geophysical bulletin of the Hokkaido University*, *13*, 99-103. https://doi.org/10.14943/gbhu.13.99

Wallace, L.M. (2020). Slow slip events in New Zealand. *Annual Review of Earth and Planetary Sciences*, *48*(1), 175–203. https://doi.org/10.1146/annurev-earth-071719-055104

Wallace, L.M., & Beavan, J. (2010). Diverse slow slip behavior at the Hikurangi subduction margin, New Zealand. *Journal of Geophysical Research: Solid Earth*, *115*(B12), 1–20. https://doi.org/10.1029/2010jb007717

Wallace, L.M., Beavan, J., Bannister, S., & Williams, C. (2012). Simultaneous long-term and short-term slow slip events at the Hikurangi subduction margin, New Zealand: Implications for processes that control slow slip event occurrence, duration, and migration. *Journal of Geophysical Research: Solid Earth*, *117*(B11), 1–18. https://doi.org/10.1029/2012jb009489

Wallace, L.M., Beavan, J., McCaffrey, R., & Darby, D. (2004). Subduction zone coupling and tectonic block rotation in the North Island, New Zealand. *Journal of Geophysical Research: Solid Earth*, *109*, B12406. https://doi.org/10.1029/2004JB003241

Wallace, L.M., & Eberhart-Phillips, D. (2013). Newly observed, deep slow slip events at the central Hikurangi margin, New Zealand: Implications for downdip variability of slow slip and tremor, and relationship to seismic structure. *Geophysical Research Letters*, *40*(20), 5393–5398. https://doi.org/10.1002/2013gl057682

Wallace, L.M., Hreinsdóttir, S., Ellis, S., Hamling, I., D'Anastasio, E., & Denys, P. (2018). Triggered slow slip and afterslip on the southern Hikurangi subduction zone following the Kaikōura earthquake. *Geophysical Research Letters*, *45*(10), 4710–4718. https://doi.org/10.1002/2018gl077385

Wallace, L.M., Kaneko, Y., Hreinsdóttir, S., Hamling, I., Peng, Z., Bartlow, N., D'Anastasio, E., & Fry, B. (2017). Large-scale dynamic triggering of shallow slow slip enhanced by overlying sedimentary wedge. *Nature Geoscience*, *10*(10), 765–770. https://doi.org/10.1038/ngeo3021

Wallace, L.M., Reyners, M., Cochran, U., Bannister, S., Barnes, P.M. et al. (2009). Characterizing the seismogenic zone of a major plate boundary subduction thrust: Hikurangi margin, New Zealand. *Geochemistry, Geophysics, Geosystems*, *10*(10), Q10006. https://doi.org/10.1029/2009GC002610

Wallace, L.M., Webb, S.C., Ito, Y., Mochizuki, K., Hino, R., Henrys, S., Schwartz, S.Y., & Sheehan, A.F. (2016). Slow slip near the trench at the Hikurangi subduction zone, New Zealand. *Science*, *352*(6286), 701–704. https://doi.org/10.1126/science.aaf2349

Wang, W., Savage, M.K., Yates, A., Zal, H.J., Webb, S., Boulton, C., Warren-Smith, E., Madley, M., Stern, T., Fry, B., Mochizuki, K., & Wallace, L. (2022). Temporal velocity variations in the northern Hikurangi margin and the relation to slow slip. *Earth and Planetary Science Letters*, *584*, 117443. https://doi.org/10.1016/j.epsl.2022.117443

Warren-Smith, E., Fry, B., Wallace, L., Chon, E., Henrys, S., Sheehan, A., et al. (2019). Episodic stress and fluid pressure cycling in subducting oceanic crust during slow slip. *Nature Geoscience*, *12*(6), 475–481. https://doi.org/10.1038/s41561-019-0367-x

Wiemer, S., & Wyss, M. (2000). Minimum magnitude of completeness in earthquake catalogs: Examples from Alaska, the western United States, and Japan. *Bulletin of the Seismological Society of America*, *90*(4), 859–869. https://doi.org/10.1785/0119990114

Williams, C.A., Eberhart-Phillips, D., Bannister, S., Barker, D.H.N., Henrys, S., Reyners, M., & Sutherland, R. (2013). Revised Interface Geometry for the Hikurangi Subduction Zone, New Zealand. *Seismological Research Letters*, *84*(6), 1066–1073. https://doi.org/10.1785/0220130035

Woessner, J., & Wiemer, S. (2005). Assessing the quality of earthquake catalogues: Estimating the magnitude of completeness and its uncertainty. *Bulletin of the Seismological Society of America*, *95*(2), 684–698. https://doi.org/10.1785/0120040007

Woods, K. (2022). Investigation of Hikurangi subduction zone slow slip events using onshore and onshore geodetic data. PhD thesis, Victoria University of Wellington, Wellington, New Zealand.

Yamashita, T. (1998). Simulation of seismicity due to fluid migration in a fault zone. *Geophysical*

Journal International, *132*(3), 674–686. https://doi.org/10.1046/j.1365-246X.1998.00483.x

Yarce, J., Sheehan, A.F., Nakai, J.S., Schwartz, S.Y., Mochizuki, K., Savage, M.K. et al. (2019). Seismicity at the northern Hikurangi Margin, New Zealand, and investigation of the potential spatial and temporal relationships with a shallow slow slip event. *Journal of Geophysical Research: Solid Earth*, *124*, 4751–4766. https://doi.org/10.1029/2018JB017211

Yarce, J., Sheehan, A.F., & Roecker, S. (2023). Temporal relationship of slow slip events and microearthquake seismicity: Insights from earthquake automatic detections in the northern Hikurangi margin, Aotearoa New Zealand. *Geochemistry, Geophysics, Geosystems*, *24*, e2022GC010537. https://doi.org/10.1029/2022GC010537

Yoshida, K., & Hasegawa, A. (2018). Hypocenter migration and seismicity pattern change in the Yamagata-Fukushima border, NE Japan, caused by fluid movement and pore pressure variation. *Journal of Geophysical Research: Solid Earth*, *123*, 5000–5017. https://doi.org/10.1029/2018JB015468

Zal, H.J., Jacobs, K., Savage, M.K., Yarce, J., Mroczek, S., Graham, K., Todd, E.K., Nakai, J., Iwasaki, Y., Sheehan, A., Mochizuki, K., Wallace, L., Schwartz, S., Webb, S., & Henrys, S. (2020). Temporal and spatial variations in seismic anisotropy and VP/VS ratios in a region of slow slip. *Earth and Planetary Science Letters*, *532*, 115970. https://doi.org/10.1016/j.epsl.2019.115970

Zaliapin, I., & Ben-Zion, Y. (2013). Earthquake clusters in southern California I: Identification and stability. *Journal of Geophysical Research: Solid Earth*, *118*, 2847–2864. https://doi.org/10.1002/jgrb.50179

Zhu, W., & Beroza, G.C. (2019). PhaseNet: a deep-neural-network-based seismic arrival-time picking method. *Geophysical Journal International*, *216*(1), 261–273. https://doi.org/10.1093/gji/ggy423

Zhuang, J. (2006). Second-order residual analysis of spatiotemporal point processes and applications in model evaluation. *Journal of the Royal Statistical Society: Series B (Statistical Methodology)*, *68*(4), 635-653. https://doi.org/10.1111/j.1467-9868.2006.00559.x

Zhuang, J., Ogata, Y., & Vere-Jones, D. (2002). Stochastic declustering of space-time earthquake occurrences. *Journal of the American Statistical Association*, *97*(458), 369–380. https://doi.org/10.1198/016214502760046925

Zhuang, J., Ogata, Y., & Vere-Jones, D. (2004). Analyzing earthquake clustering features by using stochastic reconstruction. *Journal of Geophysical Research: Solid Earth*, *109*(B5), B05301. https://doi.org/10.1029/2003JB002879

Zimmermann, B. (2009). Earthquake Focal Mechanism. Retrieved July 6, 2023, from http://demonstrations.wolfram.com/EarthquakeFocalMechanism/